Design and Implementation of High Gain 60 GHz Antennas for Imaging/Detection Systems

Zouhair Briqech

A Thesis
in
The Department
of
Electrical and Computer Engineering

Presented In Partial Fulfillment of the Requirements
for the Degree of Doctor of Philosophy
Concordia University
Montreal, Quebec, Canada

December 2015

CONCORDIA UNIVERSITY

SCHOOL OF GRADUATE STUDIES

This is to certify that the thesis prepared

By: Zouhair Briqech

Entitled: Design and Implementation of High Gain 60 GHz Antennas for Imaging/Detection Systems

and submitted in partial fulfillment of the requirements for the degree of

Doctor of Philosophy (Electrical & Computer Engineering)

complies with the regulations of the University and meets the accepted standards with respect to originality and quality.

Signed by the final examining committee:

_____ Chair
Dr. T. Zayed

_____ External Examiner
Dr. M.C.E. Yagoub

_____ External to Program
Dr. M. Bertola

_____ Examiner
Dr. A.A. Kishk,

_____ Examiner
Dr. R. Paknys

_____ Examiner
Dr. T. A. Denidni,

_____ Thesis Supervisor
Dr. A.R. Sebak

Approved by: _____

Dr. A.R. Sebak, Graduate Program Director

_____

Dr. A. Asif, Dean

Faculty of Engineering and Computer Science

Abstract

Design and Implementation of High Gain 60 GHz Antennas for Imaging/Detection Systems

Zouhair Briqech, Ph.D.
Concordia University.

Recently, millimeter wave (MMW) imaging detection systems are drawing attention for their relative safety and detection of concealed objects. Such systems use safe non-ionizing radiation and have great potential to be used in several applications such as security scanning and medical screening. Antenna probes, which enhance system performance and increase image resolution contrast, are primarily used in MMW imaging sensors. The unlicensed 60 GHz band is a promising band, due to its wide bandwidth, about 7 GHz (57 - 64 GHz), and lack of cost. However, at 60 GHz the propagation loss is relatively high, creating design challenges for operating this band in MMW screening. A high gain, low profile, affordable, and efficient probe is essential for such applications at 60 GHz.

This thesis's focus is on design and implementation of high gain MMW probes to optimize the performance of detection/imaging systems. First, single-element broadside radiation microstrip antennas and novel probes of endfire tapered slot high efficient antennas are presented. Second, a 57-64 GHz, 1 × 16-element beam steering antenna array with a low-cost piezoelectric transducer controlled phase shifter is presented. Then, a mechanical scanner is designed specifically to test proposed antenna probes utilizing low-

power 60 GHz active monostatic transceivers. The results for utilizing proposed 60 GHz probes show success in detecting and identifying concealed weapons and explosives in liquids or plastics.

As part of the first research theme, a 60 GHz circular patch-fed high gain dielectric lens antenna is presented, where the prototype's measured impedance bandwidth reaches 3 GHz and a gain of 20 dB. A low cost, 60 GHz printed Yagi antenna array was designed, optimized, fabricated and tested. New models of the antipodal Fermi tapered slot antenna (AFTSA) with a novel sine corrugated (SC) shape are designed, and their measured results are validated with simulated ones. The AFTSA-SC produces a broadband and high efficiency pattern with the capacity for high directivity for all ISM-band. Another new contribution is a novel dual-polarized design for AFTSA-CS, using a single feed with a pair of linearly polarized antennas aligned orthogonally in a cross-shape. Furthermore, a novel 60 GHz single feed circularly polarized (CP) AFTSA-SC is modeled to radiate in the right-hand circularly polarized antenna (RHCP). A RHCP axial ratio bandwidth of < 3dB is maintained from 59 to 63 GHz. In addition, a high gain, low cost 60 GHz Multi Sin-Corrugations AFTSA loaded with a grooved spherical lens and in the form of three elements to operate as the beam steering antenna is presented. These probes show a return loss reduction and sidelobes and backlobe suppression and are optimized for a 20 dB or higher gain and radiation efficiency of ~90% at 60 GHz.

The second research theme is implementing a 1 × 16-element beam steering antenna array with a low-cost piezoelectric transducer (PET) controlled phase shifter. A power divider with a triangular feed which reduces discontinuity from feed lines corners is introduced. A 1 × 16-element array is fabricated using 60 GHz AFTSA-SC antenna

elements and showed symmetric E-plane and H-plane radiation patterns. The feed network design is surrounded by electromagnetic band-gap (EBG) structures to reduce surface waves and coupling between feed lines. The design of a circularly polarized 1 × 16-element beam steering phased array with and without EBG structures also investigated.

A target detection investigation was carried out utilizing the proposed 60GHz antennas and their detection results are compared to those of V-band standard gain horn (SGH). System setup and signal pre-processing principle are introduced. The multi-corrugated MCAFTSA-SC probe is evaluated with the imaging/detection system for weapons and liquids concealed by clothing, plywood, and plastics. Results show that these items are detectable in clear 2D image resolution. It is believed that the 60 GHz imaging/detection system results using the developed probes show potential of detecting threatening objects through screening of materials and public.

Dedication

To my family.

Acknowledgement

I would like to express sincere gratitude to my supervisor, Prof. Abdel Razik Sebak, for guiding me in this research. Many thanks for the invaluable supervision, motivation, and encouragement. I also appreciated your approachability, trust, and patience. Thank you for offering me teaching positions and capstone roles, which helped me gain skills. Thank you for much thorough feedback. In addition, I must thank my co-supervisor Prof. Tayeb Denidni. Thank you for your encouragement and insightful suggestions. I am also grateful to you for the use of INRS facilities.

Special thanks go to Vincent Mooney Chopin for your technical support and warmth. Thanks for the invaluable assistance with imaging/detection system setup. I will also extend gratitude to Jeffrey Landry. Thank you for the hours and days you spent antenna prototyping, making the impossible happen. I must also express appreciation to Dave Chu; thanks for your helpful technical assistance. I'm also indebted to Maxime Thibault, Dr. David Dousset, and Dr. Ali Doghri who provided technical help and assistance in antenna measurements at École Polytechnique. Likewise, thanks to Prof. François Boone and his technician team for their antenna fabrication and help at the University of Sherbrooke.

I would like to express sincere appreciation to colleagues Ayman Elboushi, Tiago Freire Carneiro Leao, Abdulhadi Shalaboda, Ahmed Abumazwed, Issa Mohamed, Mohamed Hassan, and the Electromagnetics and Microwave group for your help and friendship. I also appreciate S. Lougheed's help in correcting this thesis.

I am very obliged to my dissertation committee for reading my thesis. Thank you to Prof. A. Kishk, Prof. T. A. Denidni , Prof. R. Paknys, Prof. M. Bertola, to the defence chair Prof. T. Zayed, and to external examiner Prof. M. Yagoub. I appreciate your participation and valuable suggestions.

I would like to express a deep sense of gratitude to my family — my mother, Hakima Filali, and father, Mohammed Briqech, sister, Shadia, and brothers, Younis, Abdu-Ellah, Esmail, Yasin - and my friends. Thank you for your support, prayers, and inspiration. I am much indebted to my parents; your affection and perseverance are always with me on my life's journey. Finally, and most of all, my thanks goes to God - for being with me and guiding me to knowledge and kind blessings.

Table of Contents

List of Figures

List of Tables

List of Abbreviations

2D	Two-Dimentional
3D	Three-Dimensional
ADS	Advanced Design System
AFTSA	Antipodal Tapered Slot Antenna
ALTSA	Antipodal Linearly Tapered Slot Antenna
AR	Axial Ratio
BLTSA	Broken Linearly Tapered Slot Antenna
BW	Bandwidth
CMOS	Complementary Metal–Oxide–Semiconductor
CP	Circular Polarized
CAD	Computer Aided Design
CSTMWS	Computer Simulation Technology Microwave Studio
CWSA	Constant Width Slot Antenna
DETSA	Dual Exponentially Tapered Slot Antenna
EBG	Electromagnetic Band-Gap
EM	Electro-magnetic
ETSA	Exponentially Tapered Slot Antenna
FCC	Federal Communications Commission
FDTD	Finite Difference Time Domain
FEM	Finite Element Method
FIT	Integration Technique
FMM	Fast Multipole Method
FOV	field Of View
GO	Geometrical Optics
GS	Grooved Spherical
HFSS	High Frequency Structure Simulator
HPBW	Half Power Beamwidth
HS	Hemispherical Lens

IEEE	Institute of Electrical and Electronics Engineers
IFFT	Inverse Fast Fourier Transform
ISM	Industrial, Scientific and Medical
LCP	Liquid Crystal Polymer
LHCP	Left-Hand Circular Polarization
LNA	Low Noise Amplifier
LTCC	Low Temperature Cofired Ceramic
LTSA	Linearly Tapered Slot Antenna
MMW	Millimeter-Wave
MIMO	Multi- Input Multi-Output
MMIC	Monolithic Microwave Integrated Circuit
MoM	Method of Moment
MPMAA	Multilayer Parasitic Microstrip Array Antennas
MSC	Multi Sin-Corrugation
MSL	Microstrip Line
NDL	Nonlinear Delay Line
OUT	Object Under Test
PAA	Phased Antenna Array
PCB	Printed Circuit Board
PET	Piezoelectric Transducer
PMMA	Polymethyl Methacrylate
PMMW	Passive Millimeter Wave Imaging
PNA	Performance Network Analyzer
RHCP	Right-Hand Circular Polarization
RF	Radio Frequency
SC	*Sine*-Corrugation
SAR	Synthetic Aperture Radar
SFCW	Stepped Frequency Continuous Wave
SGH	Standard Gain Horn
SIW	Surface Integrated Waveguide
SKA	Square Kilometer Array

SLR	Sidelobe Level Ratio
TLM	Transmission Line Matrix
TM	Transverse Magnetic
TMG	Microstrip Feeder With Large Ground
TML	Microstrip Transition Feed Line
TMS	Transition Slot Mode
TPX	Polymethylpentene
TRL	Through-Reflect-Line
UTD	Uniform Theory Of Diffraction
VSWR	Voltage Standing Wave Ratio

Chapter 1: Introduction

1.1 Introduction

Millimeter-Wave (MMW) is a well-known technology operating in the frequency band of 30 GHz to 300 GHz. The band belongs to the Extremely High Frequency (EHF) class [1]. Generally, imaging technology for security applications is one of the major applications in the millimeter wave band. Visible or infrared (IR) imaging systems are not able to see concealed objects or through poor visibility weather. However, an advantage of MMW is that it is able to penetrate through dust and smoke [2]-[3]. As well, the propagation nature of MMW is considered non-ionizing radiation, so the band is potentially useful and safe for human body scanning. For these reasons, this band offers a remarkable opportunity to perform surveillance. Furthermore, the band's ability to penetrate dielectrics, such as cloth and plastic materials, has opened up the chance for detecting concealed weapons or explosive materials under people's clothing especially at airport and border checkpoints.

In MMW imaging, there are two major techniques [2], [4], [7]-[24]: passive and active systems. The first, passive MMW, receives the blackbody millimeter-wave signal; an energy source radiated by all objects based on their temperature and composition [10] - [12]. The second technique, active MMW, consists of a transceiver system which sends a signal toward an object and receives the reflected signal, while measuring reflections of the illumination sources that come from the target. The active imaging system depends on the arrangement of the transmitter and the receiver antenna probe, which can be formed as monostatic, bistatic, or multistatic. An example of the monostatic MMW imaging /

detection system is illustrated in Fig. 1.1 - this model is similar to the technique adopted in this thesis.

Consequently, MMW wireless technology is considered an attractive field for the next generation of wireless communication systems, especially the unlicensed V-band around 60 GHz [2]. However, the attenuation loss at 60 GHz around 13dB/km caused by absorption in the air [4] may limit the system wireless range even for short-distance communications. Implementation of the antenna design and fabrication of a high-performance model present significant challenges in the categories of millimeter imaging, detection of concealed objects, and wireless communications. Important requirements of 60 GHz antenna designs are: wide impedance bandwidth, directive beam with low sidelobes, and - to overcome high attenuation- high gain antennas are required.

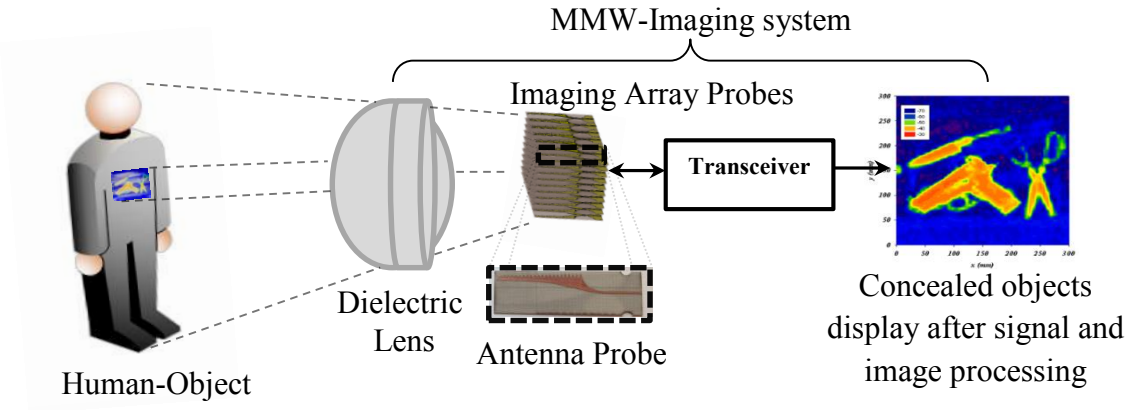

Figure 1.1 Monostatic MMW imaging / detection system

1.2 Motivation

MMW-imaging technology is highly in demand for the increasing development of the sensitivity of the receiver system. The probe mainly includes the implementation of antenna design. Notably, MMW has two major advantages: it is non-ionizing and able to

penetrate clothing. On the contrary, the X-Ray is considered an ionizing frequency that is hazardous to the human body, even though this technology has been the leading technique among imaging systems, and is still the most utilized for medical imaging applications. However, for safe body scanning, it is not an ideal choice. Moreover, the visible or infrared (IR) image systems are not able to see concealed objects or through poor visibility weather conditions. Therefore, the advantages of MMW radiation are that it is potentially safe for human body scanning, since it has a very low penetration of living tissues, and it is able to penetrate through clothing, fire, dust and smoke.

The frequency band from 57 GHz to 64 GHz, called the Industrial, Scientific and Medical (ISM) band, is not considered a choice for MMW imaging systems for commercial applications because of its higher effect of atmospheric absorption. Therefore, most applications of MMW imaging systems are operating within atmospheric transmission windows around 35 GHz, 94GHz, 140GHz, and 220GHz, where their attenuation losses are relatively low. The ISM–band is a free band of charge, and the technology operating in this band is rapidly developing, ranging from a single component of the full transceiver system, such as LNA under Monolithic Microwave Integrated Circuit (MMIC) technology, to the full MMIC transceiver. These advances are very promising for enhancing the system's performance and increasing the image system sensitivity.

Several MMW antenna probes have been implemented to be integrated within imaging systems. The on-chip patch antenna uses complementary metal–oxide–semiconductor (CMOS) technology for remote sensing and advanced imaging, [5]. In [6], a slot-loaded patch antenna has a 3-D array frame imaging system. However, these patch antennas lack a directive beam, which is essential for imaging and detection applications.

A wideband three-dimensional (3-D) imaging system for the detection of concealed weapons and contraband formed from data over a 2-D aperture was implemented at the Pacific Northwest National Laboratory, in Richland, WA, [7]; the scanner uses a linear sequentially switched array. Moreover, an active 2D multistatic array design using a beamforming scanning technique, developed by Rohde and Schwarz, was employed for human body scanning, as shown in [8], [41], and [42]. It uses balanced-fed patch-excited horn antenna integrated to interface directly with differential MMICs of the system [43], [44]. A dielectric rod antenna array fed by WR-28 metal waveguides was presented by [45] for the 3D holographic imaging system. A reconfigurable reflectarray antenna that has 25600 reflecting elements with electronically controllable phase shifters was designed for the MMW imaging system [46]. A linear one-dimensional imaging array that uses quasi-mono-static reflection mode as a synthetic aperture radar technique was presented by [19]. It also uses a taper slot antenna array as transition to waveguides.

Despite the adequate performance of these antenna sensors, the majority are classified as heavy weight, large, or lacking a directive beam which considers the general realization of a MMW imaging system. In this viewpoint, the following characteristics: low profile, compact size, easy to fabricate, easy to integrate with the system, low cost, and efficient antenna probe are considered essential design principles for MMW imaging and detection systems. Furthermore, the antenna element is considered as an eye of the system - in most imaging systems the implementation relies on the active components and signal or imaging processing, but is lacking the study and the understanding of the antenna sensor design in terms of the sensing spot for each element in an array system. Therefore, the motivation of this thesis is to carefully study and design antennas characterized for imaging

system applications, with regard to: antenna mainbeam to increase sensing of the target and surpassing the sidelobe levels and backlobe to eliminate the sensing out of the target spot, and wide bandwidth design. All of these features are essential for reducing the signal to noise level and enhancing the system's image resolution with state of the art antenna probes.

1.3 Thesis Objectives

The objectives of this thesis are divided into three main aspects as follows:

I. The primary objective is improving the performance of an antenna elements at 60GHz desired for MMW imaging/detection applications including (a) in-depth implementation optimization, fabrication and testing of several antenna probes and (b) study their geometrical shapes in order to optimize sensing performance.

II. Investigating a 1 × 16-element beam steering antenna array with a low-cost piezoelectric transducer (PET) controlled phase shifter which provide significant enhancements of system performance for imaging detection. This includes an alternative power divider as a Y-junction which has a wide impedance bandwidth and low insertion loss compared with conventional T-junction type. Furthermore, investigating the feed network design surrounded by electromagnetic band-gap (EBG) structures in order to reduce the surface wave and mutual coupling between the antenna array elements.

III. As a proof of concept, the chosen fabricated designs of antipodal Fermi tapered slot antenna probes will be used as scanning sensor in an imaging/ detection system at a band of 57-64 GHz. Several experiments will be conducted in order to test and

evaluating the performance of different selected probes in different scenarios to detect and identify concealed conventional weapons, such as handguns - whether plastic or metal, ceramic knives, and explosives in liquid form or plastics with similar properties.

1.4 Thesis Outline

The thesis presents new multiple antenna probes, fabrication and testing, wideband phased antenna array using PET, and experiments to evaluate probes in imaging/detection of hidden weapons and other threatening items. The organization of this thesis is as follows:

Chapter 2 presents a literature review and an introduction to the millimeter-wave band and to imaging system technology. First, there is a clarification of the concepts to operate an imaging system with a discussion of the reasons to choose 60 GHz. Then, the background of phased antenna array is introduced, as well as methods of beam shaping, and the piezoelectric transducer-controlled phase shifter on microstrip lines. Then we present a literature review for millimeter wave antenna probes. Also, a literature review of active and passive millimeter-wave imaging systems is presented. Finally, we give background information and methodology for the imaging/detection system performance.

Chapter 3 discusses the theoretical background and associated methodology of the presented probes. This includes design procedure, equations, and guideline techniques used in modeling antenna probes. These techniques include antipodal Fermi tapered slot antennas and dielectric lens antenna configurations. Also, EM numerical modeling techniques used in the simulation software for designing antennas will be discussed.

Chapter 4 presents the implemented 60 GHz antenna probe results, which are discussed in detail. First, we will discuss the results of a 60 GHz circular patch-fed high gain dielectric lens antenna, and the importance of adding a lens to the antenna, and the experimental results. Then, measured results for a novel antenna structure with low-cost 60 GHz printed Yagi antenna array which has been fabricated will be presented. Several new models of the antipodal Fermi tapered slot antenna AFTSA with a novel sine corrugated (SC) shape are designed, and the measured results are validated with simulated results. Also, a novel dual-polarized design of AFTSA-CS, using a single feed with a pair of linearly polarized antennas aligned orthogonal to each other as a cross shape, is presented. Furthermore, a novel 60 GHz single feed circularly polarized (CP) AFTSA-SC is modeled to radiate in RHCP wave as well in LHCP wave. Finally, a 60 GHz Multi Sin-Corrugations AFTSA loaded with a grooved spherical lens is presented.

Chapter 5 presents the analytical results of 57-64 GHz, 1 × 16-element beam steering antenna arrays with PET-controlled phase shifter. First, the principle of Y-junction unequal power is presented. Second, the 1 × 16-element beam steering phased array designed with a 60 GHz AFTSA-SC is presented with EBG. Third, the design of a circularly polarized 1 × 16-element beam steering phased array without and with EBG structures, is further investigated. Finally, a wide-Scan AFTSC-MSC array fed with grooved spherical lens antenna as form of three elements to operate as the beam steering antenna is presented.

Chapter 6 introduces the experimental results of the imaging detection of a target, comparing a V-band standard gain horn (SGH) with the proposed 60 GHz antenna probes.

The chapter then presents imaging/detection results for concealed weapons and liquids behind clothing, plywood, and plastics using the MC-AFTSA probe.

Chapter 7 summarizes the research accomplishments as well as thesis contributions, and presents conclusions, recommendations, and suggestions for further research.

Chapter 2: Literature Review

2.1 Introduction

In this chapter, the millimeter-wave band, the concepts of the MMW antenna design, and phased antenna array techniques for the mm-wave imaging system are presented. Furthermore, descriptions of active and passive MMW system principles will be discussed. As well, there will be an overview of the main tools and methods to consider when designing an imaging system, with most necessary formulas that explain the design procedure.

2.1.1 Millimeter-Wave Band

Millimeter-Wave (MMW) is classified as technology operating in the frequency band of 30 GHz to 300 GHz, which corresponds to wavelengths of 10-mm to 1-mm. The band belongs to the Extremely High Frequency (EHF) class [1]. The IEEE classifications of MMW frequency bands are shown in Table 2.1.

Millimeter-wave has a wide band portion of the electromagnetic spectrum, therefore this band is able to transfer high density data through wireless communication systems [47]. Meanwhile, MMW signals cannot propagate over great distances and have weak penetration through solid material - these characteristics are not considered disadvantageous, and, notably, MMW is very efficient at increasing the security of communication transmissions [48], [49].

Nowadays, MMW technology is presented beside the antenna design extensively, in many fields of research. These research fields include: wireless communication systems, imaging technology, medical and security scanners, directed energy weapons, high resolution radar sensors, radar mining applications, and radiometer astronomy.

Table 2.1: Millimeter-Wave Band Classifications [1]

Specific Frequency Ranges For Radar Based on ITU Assignments (GHz)	Nominal Frequency Range (GHz)	Band Designation
33.4 to 36	27 to 40	Ka
59 to 64	40 to 75	V
76 to 81	75 to 110	W
92 to 100		
126 to 142	110 to 300	Mm
144 to 149		
231 to 235		
238 to 248		

2.1.2 What and Why 60 GHz?

The 60 GHz technology has been well known since 2001, when the Federal Communications Commission (FCC) set the new unlicensed band range at 57 to 64 GHz. Note that for many years mm-wave technology has mainly been deployed for military applications. A free of charge, 7 (GHz) band has opened the chance and challenge for all fields of research to utilize 60 GHz in ISM-band, which stands for "Industrial, Scientific and Medical" band. Other countries are assigned their own 60 GHz unlicensed bands and this is illustrated in Fig. 2.1.

2.1.2.1 Atmospheric Losses

The main source of transmission loss is free-space loss; additionally, there are the atmospheric loss factors that affect millimeter wave propagation [34]. At 60 GHz, there are high levels of atmospheric loss that occur when millimeter waves travelling through the atmosphere are absorbed by molecules of oxygen, water vapor, and other gases. Therefore,

at a certain frequency the wavelength matches the resonant frequencies of the gas molecules where it absorbs the radiation energy and increase the path loss in that frequency, as shown in Fig. 2.2

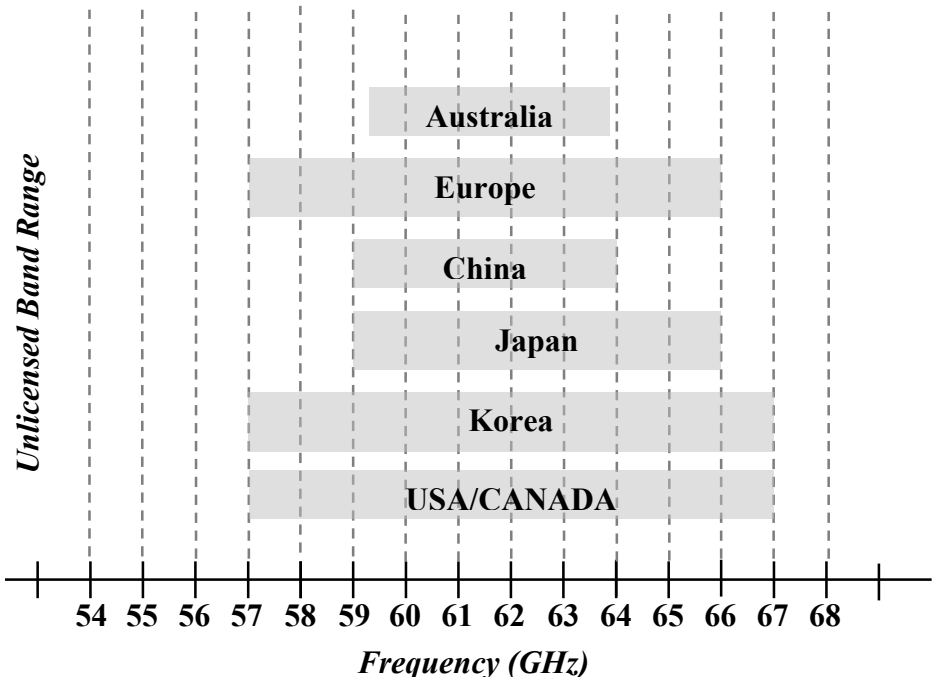

Figure 2.1 Worldwide unlicensed band allocations for 60 GHz.

There is a 13dB/Km to 15dB/km atmospheric loss at 60 GHz, which includes oxygen, normal water vapor, other gaseous atmospheric constituents and average rain. In a long distance communication situation, 60 GHz is an unreliable frequency. On the other hand, it is considered a secure frequency and is able to reuse the same band in the same short-range communication area. The effect of the atmospheric loss is considered an advantage in 60 GHz. In the MMW range there is a low atmospheric loss in relatively transparent windows centered at 35, 94, 140 and 220 GHz.

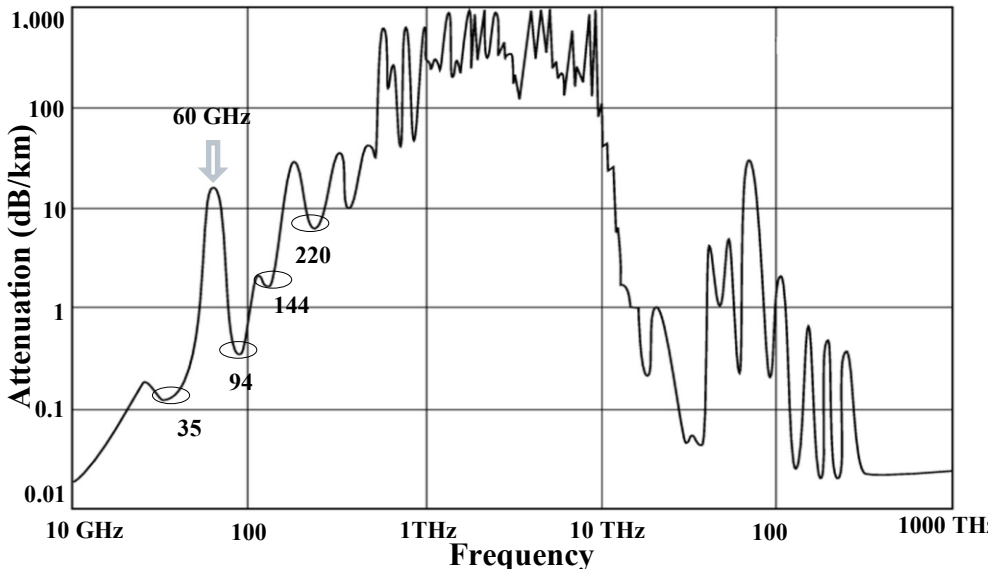

Figure 2.2 Atmospheric Propagation Loss [34].

2.2 Millimeter-Wave Antenna Probes

In general, there are many kinds of MMW antennas: in fact, most types of antennas could be utilized at MMW, but with high frequencies shrinking the scaling dimension these antennas could present a challenge for design optimization, efficiency, metallic loss, fabrication and cost. In forgotten research, in 1895 at Residency College, in Calcutta, India, Jagadish Chandra Bose was the first pioneer to demonstrate MMW transmission and to receive a signal at 60 GHz, over 23 meters of distance to ring a bell [52]. Recently, several antennas of different types have been investigated for MMW applications, such as for microwave imaging detection systems and for wireless communication systems [7], [53]-[67]. As in many applications, antennas that are low profile, low cost, high performance, easy to fabricate, and weigh less, are preferable commercially to traditional designs, such as conventional horn antennas and metallic waveguides. The waveguide antennas are known to provide higher performance and lower losses [53], [55], but they are not suitable for low profile and their approach is to make it compact. There are also other approaches which have been explored to reduce costs, such as metalized plastics [56]. Recently, certain

antennas are recognized for having a high performance and low profile, such as, Yagi-Uda based antennas [57], stacked antennas [58], hybrid antennas [59], tapered Slot Antennas [60], DRA-based antennas [61], Bow-tie antennas [62], lens antennas [54], [J1], [C10] and dielectric rod end-fired antennas [63]. Fig. 2.3 shows some photographs of these antennas. The antennas with an endfire characteristic are preferable for millimeter wave imaging scanning to the broadside ones, since they have high gain performance and high sensibility to detect the target. Therefore, for designing a MMW imaging scanning, tapered slot antennas are considered the optimum choice, as they have endfire radiation characteristics, including low profile, high efficiency, easy to fabricate, high gain and low cost [60].

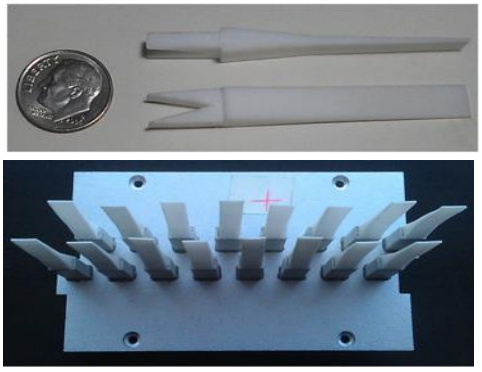

(a) The top; Antenna units made of Teflon, the bottom; Module of antenna array [13].

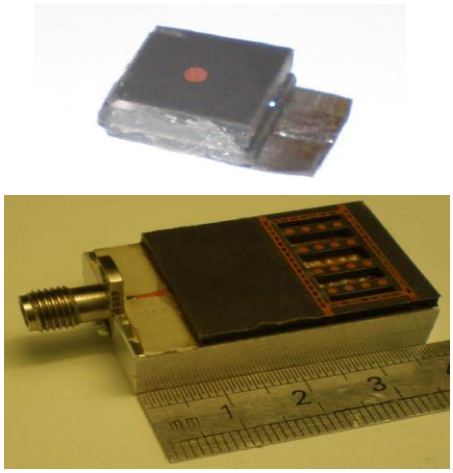

(b) The top; circular patch-based Yagi antenna, the bottom; the 4×4 stacked Yagi antenna array [58].

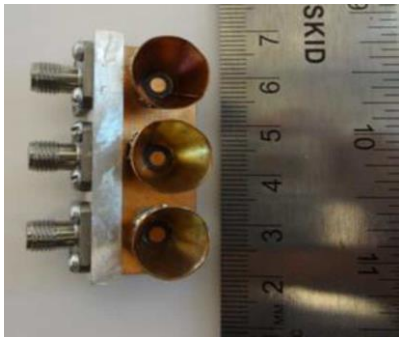

(c) Triple Hybrid microstrip antenna sensor [59].

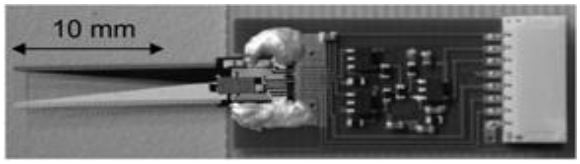

(d) TSA antenna in compact receiver PMMW imaging system [60].

Figure 2.3 Photograph of varied types of MMW antenna probes.

In MMW the wavelength that makes the antennas applicable to be on chips to employ in mobile compact devices is very short. The three most common technologies are: low temperature co-fired ceramic (LTCC), liquid crystal polymer (LCP), and silicon. LTCC and LCP are usually used in the printed planar MMW antennas with a command substrate and transceiver [49]. Other advantages of the printed planar antenna are that it is compact, and high-gain multilayer parasitic microstrip array antennas (MPMAA) operate in the 60 GHz band. The antenna consists of three layers with a 2 X 2 parasitic array on each layer [64]. The wideband dipole antenna, when dealing with MMW familiar printed antenna, is the Bowtie [65]. For multi-frequency image scanning at 90GHz it is suitable to utilize the Bowtie antenna with Teflon substrate.

Since MMW antennas are physically very small, they have more ability to build On-Chip or packaging techniques. With On-Chip antennas, as presented in [66], there are a number of approaches to minimize dielectric and metal losses, as well as to improve the common substrate for on-chip antenna integration, such as Silicon. For instance, [67], a Double-Dipole Antenna with parasitic elements for 122 GHz System in-Package Radar Sensors utilizes On-chip antenna. Parasitic patches suppress the radiation parallel to the substrate surface and thus eliminate surface waves and reduce the return loss.

2.3 Phased Antenna Array

The conventional beam scanning technique involves mechanically rotating a single antenna or an array with fixed phase to the element. The most current technique involves electronically scanning antennas which are known as phased array antennas. This is done by a sweep in the direction of the main beam and electronically varying the phase of the

radiating elements, that is producing a moving antenna element radiation pattern without moving any antenna elements. Millimeter wave propagation characteristics are required for steering of the beam to increase the insight of the antenna, while enhancing system sensitivity. Furthermore, phased array antennas are known for their capability to steer the beam pattern electronically with high effectiveness, managing to get minimum side-lobe levels [35], [36]. The phased array antenna consists of a power distribution network, antenna elements, and phase shifters, as illustrated in Fig. 2.4.

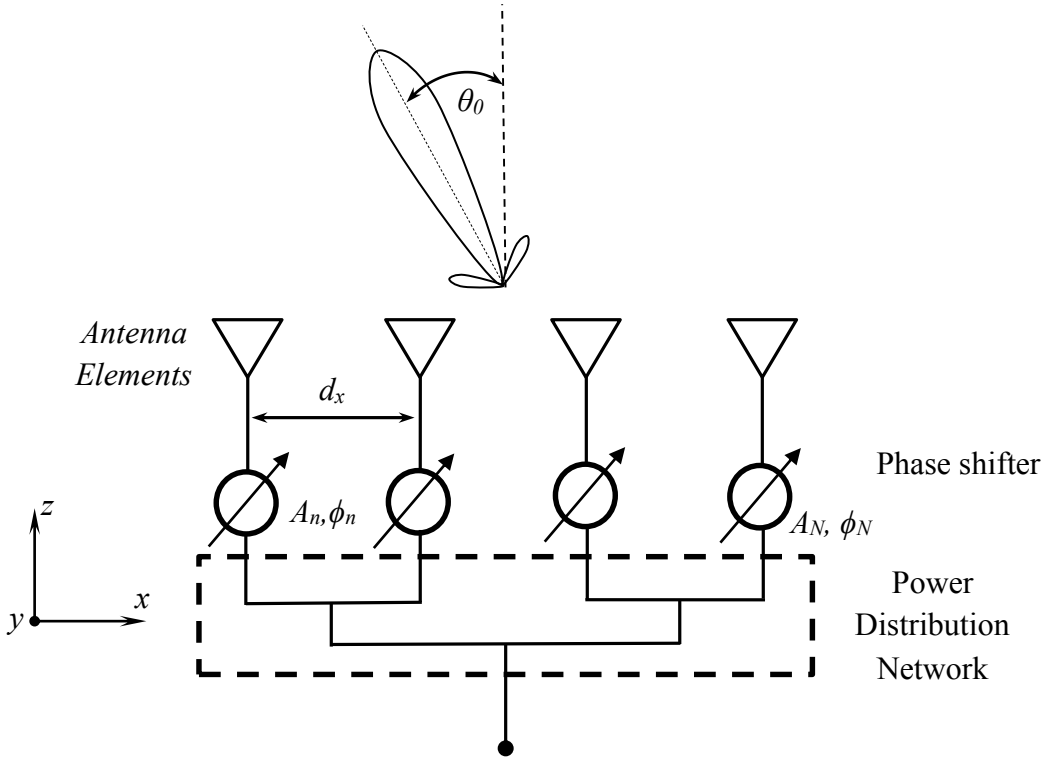

Figure 2.4 Linear phased antenna array.

In the Fig. 2.4, a linear array in a one-dimensional structure consists of $1 \times N$ antenna elements. It is assumed that the output ports of the power distribution network connected to the phase shifters and then connected to the antenna elements, as illustrated in the figure. The output signal at each phase shifter is with a phase taper, ϕ_n, and an amplitude coefficient, A_n. The combination of the transmitted or received signal at the

antenna elements is in phase to achieve maximum beam response at the scanned direction, θ_o. The phase scanning in single dimension, with a linear phase taper, and the phase difference between adjacent radiators is constant, thus the phase of each shifter element, ϕ_n, is expressed as [36]

$$\phi_n = -nkd_x \sin\theta_0 \tag{2.1}$$

where d_x is the spacing between the elements, k is the free space wave number ($2\pi/\lambda_0$), λ_0 is wavelength, and n is indicated to n^{th} element of the array. The required amount of the delay time $\Delta\tau_n$ provides a true time delay of the beam scanning, and is given by [36]

$$\Delta\tau_n = \frac{-2\pi n d_x \sin\theta_0}{\lambda_0} \tag{2.2}$$

The calculation of the far field pattern of an array (E_{Array}) is equivalent to the far field of a single element (E_s) multiplied by the spatial array factor, E_a , and is given as

$$E_{Array} = E_s \; E_a \tag{2.3}$$

The spatial factor depends on the amplitude coefficient of each element and angular position θ_o. In the case of the linear array structured in xz-plane, it is expressed as

$$E_a(\theta) = \sum_{n}^{N-1} A_n \, e^{jnkd_x(\sin\theta - \sin\theta_0)} \tag{2.4}$$

Also, the spatial factor is simplified when the array in uniform excitation is given by

$$E_a(\theta) = \frac{\sin\left[N\pi\frac{d_x}{\lambda_0}(\sin\theta - \sin\theta_0)\right]}{N\sin\left[\pi\frac{d_x}{\lambda_0}(\sin\theta - \sin\theta_0)\right]} \tag{2.5}$$

For a uniform excitation linear array, the half power beamwidth (HPBW) for large N is given as [36]

$$\theta_{HPBW} \approx \frac{0.8858\lambda_0}{N d_x \cos\theta_0} \tag{2.6}$$

where N is the total number of the antenna elements. The HPBW is inversely proportional to, N, d_x, θ_0, and to the operated frequency; generally, as the frequency increases the HPBW become narrower.

The grating lobes (GL) in the array factor occur when spacing between the elements exceeds a critical dimension, which leads to reducing the power in the main lobe, and accordingly reduces the gain of the antenna array [36]. The grating lobes are defined by

$$\frac{d_x}{\lambda_0} = \frac{n}{\sin\theta_0 - \sin\theta_{gl}} \tag{2.7}$$

Therefore, when the spacing $d_x = 0.5\ \lambda_0$, a grating lobe is at -90° for a beam scanned to +90°. In the case of the main beam at broadside and $d_x = \lambda_0$, the grating lobes appear at ±90°. Accordingly, for wide angle scanning range, half-wavelength or a slightly larger spacing between the antenna elements is chosen.

2.3.1 Methods of Beam Shaping

The design of an antenna array to obtain a desired beam shape can be achieved with a conventional method using a power distribution synthesis method. Such a method is based on the array size and its single elements. The size of an array controls both the beam shape and the directivity. A large size array is expensive, and a smaller size is preferable. On the other hand, a large size offers more degree of design parameters and may improve the array performance. The tolerance in the array design, sidelobe levels and efficiency can be controlled using different synthesis methods. Several pattern synthesis methods maybe

employed to obtain a specific beam shape and they depend on the antenna element type [35], and leads to form a desired radiation characteristic in terms of the main beam shape, pattern nulls, and sidelobe level. A typical low sidelobe level is defined as ≤ -30dB leading to increase spectrum congestion as in satellite transmissions, which also reduces radar clutter, jammer vulnerability, and communications and radar intercept probability. There are well known methods that have the advantage of suppressing side lobe levels, such as, Dolph-Chebyshev distribution, Hamming distribution, Taylor one-parameter distribution, Taylor N-bar distribution, and Villeneuve n distribution. Chebyshev distributions are similar to Taylor distributions. However, using Chebyshev distribution one can obtain the narrowest possible mainlobe at a specified sidelobe level. On the other hand, when a Taylor distribution is used, it is able to make tradeoffs between the sidelobe level and the mainlobe width. In addition, a Taylor distribution avoids edge discontinuities, which leads to sidelobes decrease monotonically in the Taylor distribution. Therefore, Taylor distributions are ordinarily utilized in radar applications, for example, weighting feeding network of the antenna array design [50] and for synthetic aperture radar images. In order to achieve a lower sidelobe level and the highest directivity, the Taylor N-bar distribution is very often chosen [37].

2.3.2 Piezoelectric Transducer-Controlled Phase Shifter on MSL

The electronics beam steering and beamforming techniques are derived from a phase shifter forming a phased- array antenna system. The number of phase shifter in PAA structure in most designs is proportional to the number of antenna elements, or even more. This fact makes the system loss and the power efficiency of PAA difficult and challenging to enhance. There many types of phase shifters that have been published, such as the

ferroelectric [38], waveguide semiconductor [39] and monolithic microwave integrated circuit (MMIC) [40] which typically are lossy and narrow-band of phase shifting. As well as their design complexity, a large number of phase –shifters can cost about 50% of a system's total expenditure. Low-complexity and low-cost important aspects in system design. On the other hand, there are several new trending technologies with high efficiency performance in the MMW regime such as the MMIC; however, the cost and prototyping difficulty is still uncompensated [41], [42].

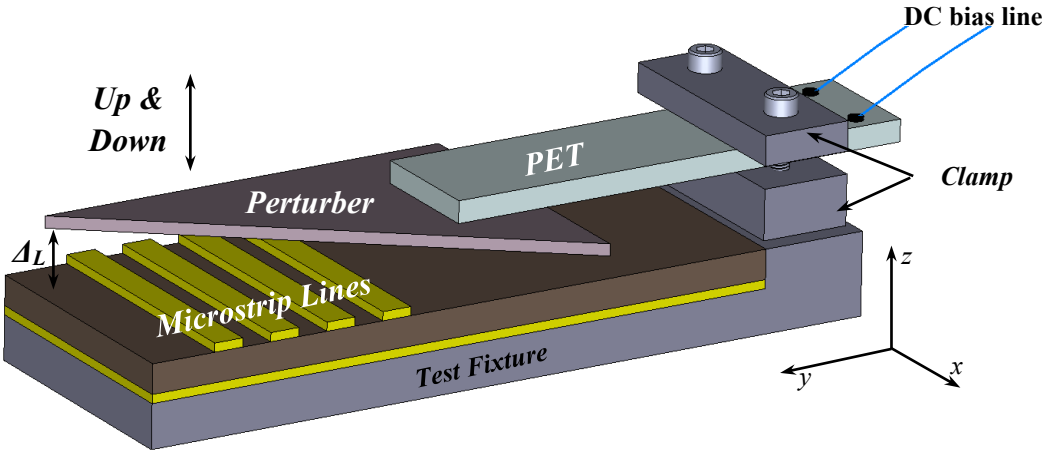

Figure 2.5 Schematic of the phase shifter is controlled by a PET on microstrip lines.

A low cost PAA system used as a true time delay device was developed by T. Y. Yun and K. Chang [43] - [49], and achieved with the idea of the Piezoelectric Transducer (PET) controlled delay microstrip line (MSL) to steer the beam in the PAA system. This method is considered low cost to employ in millimeter wave PAA applications as seen in [50]. In this technique, a layer of dielectric material is placed above a microstrip line separated by a small air gap. The piezoelectric transducer is attached to the dielectric material, and a DC voltage drives the PET as shown in Fig. 2.5. The PET is a piezoelectric ceramic actuated by applying a DC-voltage [51], and the movements of perturber can be controlled electronically or manually. Accordingly, depending upon the polarity of the DC

bias voltage, the transducer moves up or down varying the air gap between the perturber and the microstrip line. Any changes in the air gap that vary the value of the effective dielectric constant, consequently, change the wave propagation constant that causes a phase shift to generate a true-time delay at microstrip line.

Fig. 2.6 illustrates the multilayer structure of the PET controlled phase shifter for one microstrip line. The substrate of the grounded microstrip line has a thickness h_1 and dielectric constant ε_{r1}. A perturber with the certain length L, the dielectric constant ε_{r3} and thickness h_3 , is utilized to perturb the electromagnetic wave field of the microstrip line. The PET controls the variation of the air gap between the perturber and the substrate (h_2), this variation changes the effective dielectric constant (ε_{eff}). The phase shift difference $\Delta\phi$ caused by perturbation is defined as [44]

$$\Delta\phi = L_p \times \Delta\beta \tag{2.8}$$

where the length of the microstrip line under perturbation is L_p and the difference between the perturbed and unperturbed propagation constant is $\Delta\beta$ which can be expressed as [44]

$$\Delta\beta = \frac{2\pi}{\lambda_0}\left(\sqrt{\varepsilon'_{eff}(f)} - \sqrt{\varepsilon_{eff}(f)}\right. \tag{2.9}$$

where $\varepsilon'_{eff}(f)$ is the effective dielectric constant without perturbation *when* $\varepsilon_{r2} = 1$, and $\varepsilon_{r2} \neq 1$ when the effective dielectric constant is perturbed, then it is $\varepsilon_{eff}(f)$, f is the frequency, and λ_0 is the wavelength in free space. Accordingly, the delay time Δt caused by the perturbation is defined as

$$\Delta t = \frac{\Delta\phi}{360 \cdot f} \tag{2.10}$$

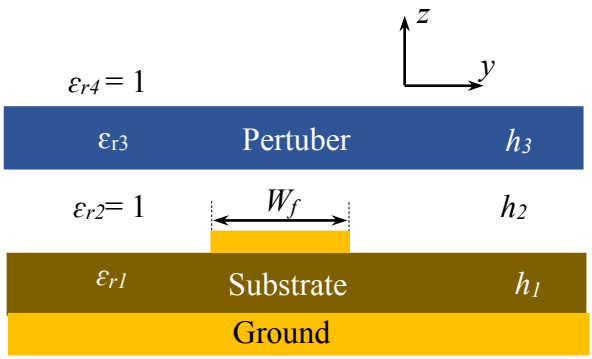

Figure 2.6 The multilayer structure of the PET controlled phase shifter for one microstrip line.

2.4 Millimetre Wave Imaging Detection

The MMW-imaging system is a highly in-demand technology for homeland security applications. Accordingly, MMW has two major advantages: it is non-ionizing and able to penetrate clothing [2], [4], [7], [8], [9] - [24]. On the contrary, high quality X-Ray images have been widely used in luggage and goods scanning at border and airport checkpoints. However, the X-Ray's ionizing frequency is hazardous to the human body. Moreover, for contrast, the visible or infrared (IR) image systems are not able to see concealed objects or through poor visibility weather conditions. The advantage with MMW radiation is that it is safe for human body scanning, and able to penetrate through fog, smoke, heavy dust, or nonmetal obstacles [9]. Consequently, natural applications of MMW imaging systems include surveillance, security, ideally suited for detecting concealed weapons or explosives [10]. Medical and biometrics imaging is also starting to be a field for investigation [11]. As well, low visibility navigation is another application for MMW imaging [12]. Table 2.2 shows the electrical properties of the human body's tissue parameters at 60 GHz [13]. The MMW band has high penetration for clothing and some other materials.

Table 2.2 Human Body's Tissue Parameters at 60 GHz [13]

Tissue	**Relative permittivity (ε_r)**	**Loss tangent (**$\tan\delta$**)**
Skin (Dry)	7.98	1.37
Skin (Wet)	10.2	1.16
Muscle	12.9	1.23
Fat	3.13	0.27

Passive MMW imaging system [16]

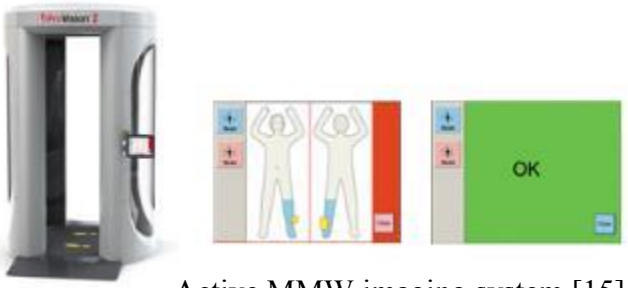

Active MMW imaging system [15]

Figure 2.7 Photographs of various types of MMW systems.

MMW imaging scanning of passengers at checkpoints seems to be mandatory at airports in most developed countries worldwide. Several MMW imaging systems are deployed globally to enhance airport security, for example, the ProVision 2 active MMW system in [15] eliminates privacy concerns as an image-free solution, automatically able to detect concealed objects made of both metallic and non-metallic materials. As a further example, Brijot's GEN 2 is a passive MMW imaging system [16] operating as a real-time scanner that images with an integrated full-motion video camera. The photographs of these MMW imaging systems are shown in Fig. 2.7.

MMW imaging detection can be an active or passive system. An active MMW imager mode is considered a transceiver system, since the transmitter source illuminates

the target and the receiver scans the scattered wave that reflects off the target. A passive mode considered as a receiver system scans the energy that is naturally emitted by the target, where the receiver senses the blackbody radiation as a form of temperature differences.

2.4.1 Active Millimeter-Wave Imaging Systems

In [7], an active MMW imaging system has been developed to detect concealed weapons and contraband at airports and other secure locations, using a holographic linear array of sequentially switched transmitter receivers scanned over an aperture to actively illuminate objects. In [17], the authors describe a 60-GHz active imaging radar, which uses a Yagi–Uda antenna array. This 60-GHz imaging system incorporates multilayered feedforward neural-network signal processing under coherent illumination in order to reconstruct images. A 60 to 66 GHz active three dimensional MMW imaging sparse array configuration for personnel security screening, is introduced in [18]. A 72 to 80 GHz active MMW imaging system with a planar multistatic array design using a beamforming scanning technique, is illustrated in [8]. The array is developed due to its exceptional reduction in the number of RF modules while maintaining high image quality. A linear one-dimensional 30 GHz imaging array uses quasi-mono-static reflection mode as a synthetic aperture radar technique, as presented in [19], which is based on PIN diode-loaded switchable resonant slot antennas in linear array form.

The active system depends on illumination of the target by transmitting the source and then receiving the scattered signal. This process could be formed as monostatic,

bistatic, and multistatic, which stands on the mechanism of the transmitter and the receiver antenna configurations.

2.4.1.1 Monostatic Imaging System

A system configured to receive and transmit the microwave signals from a single antenna indicated to be a monastic imaging system is shown in Fig. 2.8. This system consists of a transceiver, antenna, dielectric lens, analog to digital converter, and data acquisition to process and display the image. The transceivers transmit a signal passing through the lens to focus the waves and narrow the beam, then strike the target. The scattered signal reflected back also passes through the lens and the transceiver antenna receives the signal at the focal point. This signal is down-converted to intermediate frequency and passes through an analog to digital converter, then data acquisition processing takes place to filter the desired data into an image.

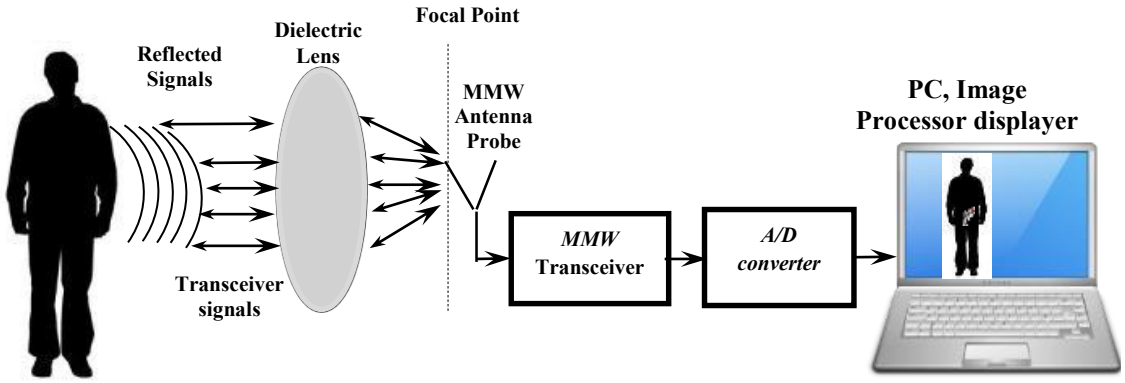

Figure 2.8 Active monostatic type Millimeter-Wave imaging system.

2.4.1.2 Bistatic Imaging System

A system is configured of two antennas, one that transmits a microwave signal, while the other antenna receives the signal - this form is a bistatic imaging system, shown in Fig. 2.9. The transmitter antenna illuminates the target, then the scattered signal passes

through the lens to magnify and narrow the beam, then at the focal point the antenna receives the signal. The signal is down-converted to intermediate frequency and then passes to a data acquisition after it is converted to digital form. This data is filtered and processed to form an image.

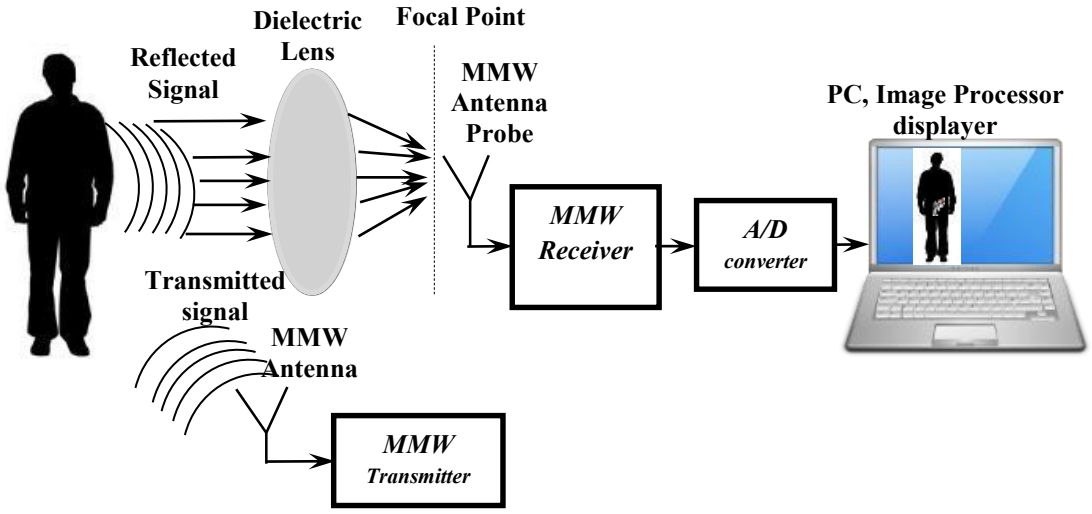

Figure 2.9 Active bistatic type Millimeter-Wave imaging system.

2.4.2 Millimeter-Wave Imaging Systems

In [12], PMMW array with optical up conversion are implemented to be an effective aid for guidance at landings and takeoffs under fog and low visibility conditions. Also in [20], PMMW image is implemented to be considered for tactical aircraft air force, army, navy, and aerospace research. The applications for remote sensing have a vast implementation and use of PMMW imaging [21]. A Compact receiver module for passive millimeter-wave imaging presented in [60], the MMIC receiver module is compacted with an antipodal linearly tapered slot antenna to achieve high efficiency performance. Furthermore, as in [22], complementary metal oxide semiconductor (CMOS) technology based on both simple detector and pre-amplified detector is implemented to employ in PMMW systems. The substrate integrated waveguide (SIW) technology as a platform

developed for the PMMW imaging system is reported in [23]. PMMW with Dual-Polarization, in [24], presents a polarization diversity of MMW radiation used for enhanced discrimination of targets and surfaces. In [11], a potential use of PMMW techniques in microscopy, where scanning near-field microscopy enables direct observation of *Ka*-band signals thermally emitted from the object, is presented.

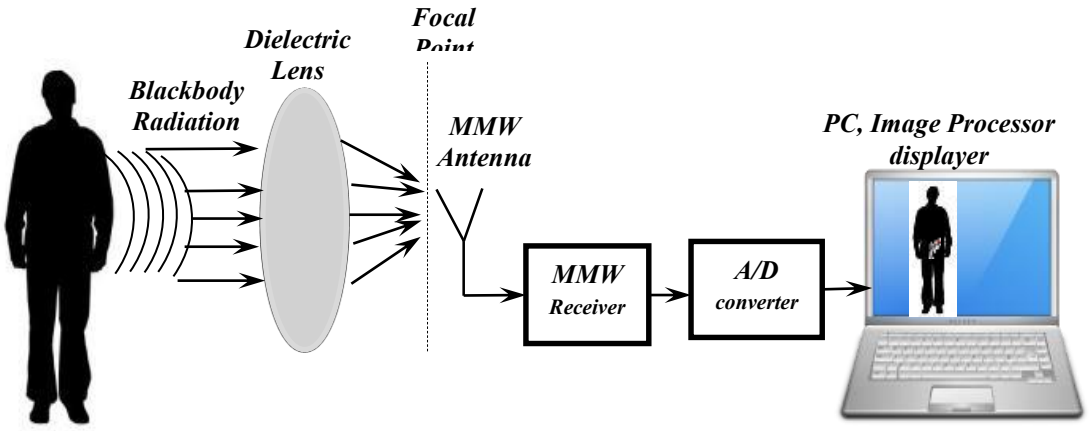

Figure 2.10 Passive Millimeter-Wave imaging system.

The Passive MMW imaging system is a receiver system, as shown in Fig. 2.10, which is receiving the millimeter-wave illuminations signals that radiate from any object at a temperature higher than 0 K. The radiation from the object is classified as blackbody radiation, which is an energy source that is radiated by all objects based on their temperature and composition [2], [4].

2.4.3 Imaging System performance

This section introduces the imaging scanning principle and it is equation drive a monostatic synthetic aperture radar (SAR) as transceiver system without and with lens structure.

2.4.3.1 Spatial Resolution

Spatial resolution means the point pixel size of the image object, expressed as pixels per line, dots per inch (dpi), or lines per millimeter (lp/mm), etc. The resolution of the antenna detects a picture which depends on the main beam of the antenna, a narrower beam that guides to the largest antenna. The spatial resolution of an imaging system is also known as a field of view (FOV), and is controlled by the angle θ_N as shown in Fig. 2.11.

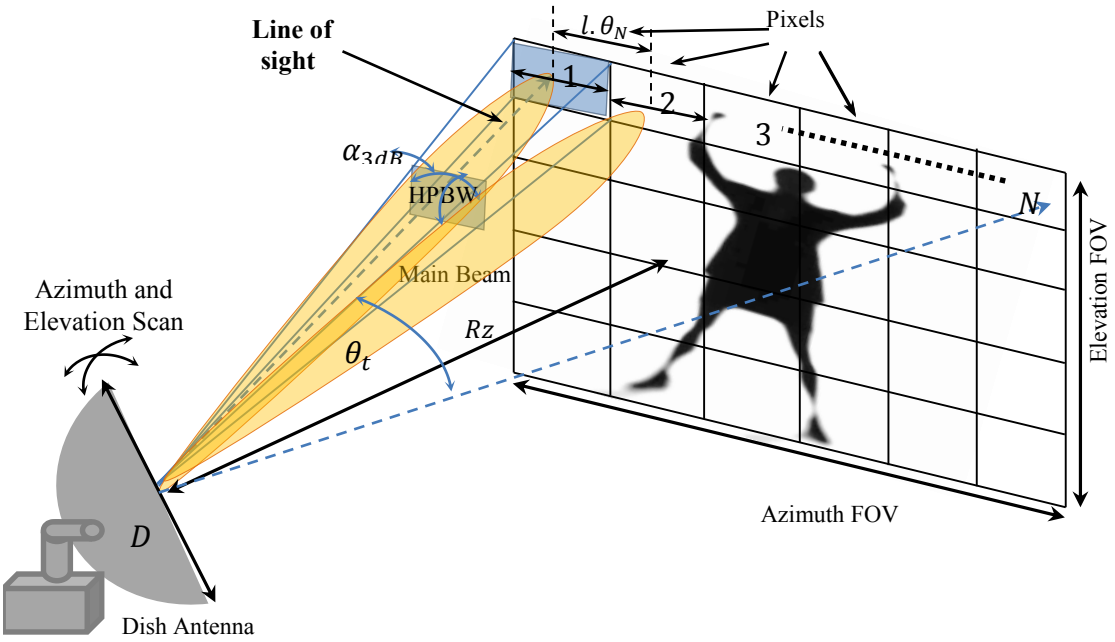

Figure 2.11 Imaging system scanning principle.

The pixel that defines the resolution of the image is a the angle, α. Then the scene spot is given by

$$\alpha = \frac{\lambda}{D} \tag{2.11}$$

where; λ is the wavelength of the incident radiation, and D: the diameter of the antenna. The scan point steps are related to the image processing scan [167], while the antenna is moving along the azimuth and the elevation plane.

The half power beamwidth (α_{3dB}) is a constant value for each N picture point across the horizontal FOV= θ_t.

$$\alpha_{3dB} = \frac{\theta_t}{N} \tag{2.12}$$

The Eq. (2. 13) can verify the total number of picture points across the horizontal FOV.

$$N = \frac{D\theta_t}{\lambda} \tag{2.13}$$

While, in the case of using a dielectric lens in front of the antenna, the refractive index of the lens medium is taken into account.

$$N = \frac{nD\theta_t}{\lambda} \tag{2.14}$$

Where; n : Refractive index of the dielectric lens.

The antenna diameter times the step angle ($D\theta_N$) is known as the Lagrange invariant and it is a constant parameter throughout an imaging system process.

2.4.3.2 Lens Scanning

Consider a dielectric lens of diameter D and focal length f_p and an object at a distance R_Z from the lens. The side view is detailed in Fig. 2.12. The spot size (A) of the beam at a distance (R_Z) is;

$$A = R_Z.\alpha \tag{2.15}$$

Substitute the value of α_{3dB}

$$A = R_Z.\frac{\lambda}{D} \tag{2.16}$$

The angular shift of the beam θ_N with the vertical shift of the lens by a distance y_a from the center is expressed as:

$$\theta_N = \arctan\left(\frac{y_a}{f_p}\right) \tag{2.17}$$

The shift in beam reflected on the partial field of view y_o along the vertical dimension of the target at distance R_Z is

$$y_o = \frac{y_a}{f_p} . R_Z \tag{2.18}$$

Any shift in (y_a) of the lens from the center of the focal antenna, therefore, causes a shift (y_o) of the beam spot from the field of view on the object target.

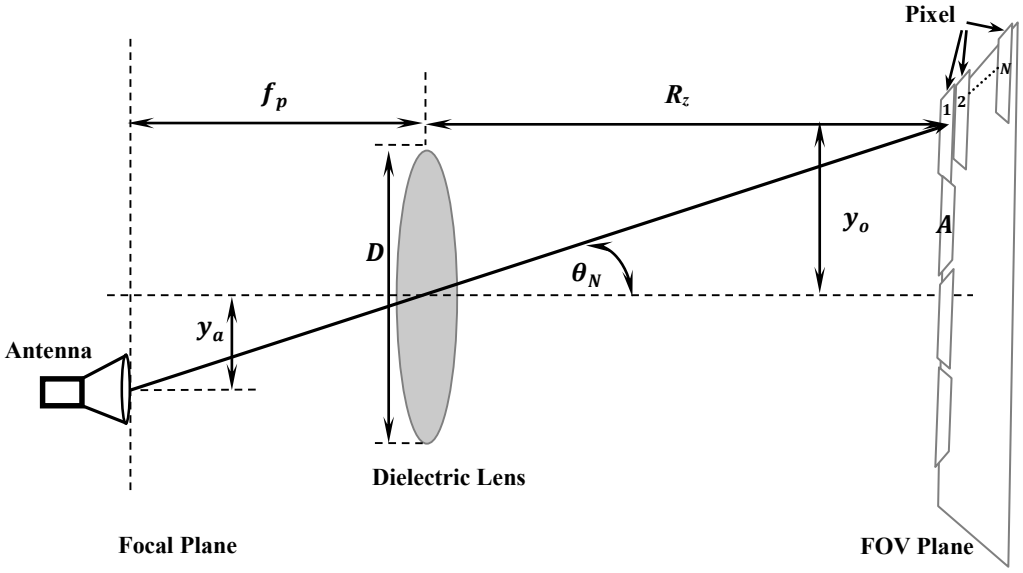

Figure 2.12 Principle diagram of lens scanning for imaging system.

2.4.3.3 Real-time Scanning Operation

In the case of the array receiver's imaging detector, each receiver has an integration time. The performance of the image receiver is measured by integration times during the scanning process and speed in displaying the scene. The integration time (τ) calculated during the required time (t) of the full image per total number of picture points in the one image frame (m) multiplied by the number of receiver image detectors (n_r) is given by

$$\tau = n_r \frac{t}{m} \tag{2.19}$$

2.5 Summary

In this chapter, the concepts of the millimeter wave band and the possibility to utilize 60 GHz in MMW applications were introduced. In addition, the designing principle of the phased antenna array and the designing procedure in utilizing the piezoelectric transducer-controlled phase shifter on microstrip line were introduced. Also, a survey explaining different millimeter-wave antennas utilized as probes for imaging applications was presented. Finally, there was a literature review of various MMW imaging detection applications, as well as different imaging detection types. The literature review also included the methodology and theoretical background required for designing the system.

Chapter 3: Theoretical Background and Analysis

3.1 Introduction

This chapter presents the theoretical background and methodology required for designing the high performance MMW antenna needed for imaging/detection systems. Section 3.2 describes the analysis of electromagnetic waves in antenna radiated fields, and introduces an overview and definition of basic antenna parameters. In Section 3.3, we will try to introduce a methodology behind antenna design prospect needed for a MMW imaging/detection system. Section 3.4 introduces the spherical dielectric lens antenna and design equations. In Section, 3.5 we will start to introduce a literature review of the tapered slot antenna showing its advantages and disadvantages, and we will introduce the antipodal tapered slot (AFTSA) antenna's design formula, as well as the *sin*-corrugation design's empirical equations. Section 3.6 introduces antenna array design requirements and the inquiry to consider for the 60 GHz imaging/detection system. Finally, there is an overview of numerical techniques used by simulation software tools used in antenna design and analyzed in this thesis.

3.2 Theoretical background and antenna parameters

The solutions for electromagnetic fields and waves are keys to solve for the radiation characteristics of antennas as well as for microwave devices and components such as feed networks, phase shifters, filters, and transitions. Such solutions are based on Maxwell's equations, either in time or frequency domain, subject to proper boundary conditions [68], [98]. Maxwell's equations can be described in two forms, and differential

and integral form as in Eq. (3.1), Eq. (3.2), Eq. (3.3), and Eq. (3.4). Details of Maxwell's equations and appropriate boundary conditions are discussed in details in [68].

Differential form		***Integral form***	
$\nabla \cdot \vec{D} = \rho_v$	$\leftrightarrow$	$\oiint \vec{D} \cdot d\vec{S} = Q_{enc}$	(3.1)
$\nabla \cdot \vec{B} = 0$	$\leftrightarrow$	$\oiint \vec{B} \cdot d\vec{S} = 0$	(3.2)
$\nabla \times \vec{E} = -j\omega\mu\vec{H}$	$\leftrightarrow$	$\oint \vec{E} \cdot d\vec{l} = -j\,\omega \iint \vec{B} \cdot dS$	(3.3)
$\nabla \times \vec{H} = j\omega\varepsilon\vec{E} + \sigma\vec{E} + \vec{J}$	$\leftrightarrow$	$\oint \vec{H} \cdot d\vec{l} = j\omega \iint \vec{D} \cdot dS + \iint \sigma\vec{E} \cdot dS + \iint \vec{J} \cdot dS$	(3.4)

Eq. (3.1) is Gauss' Law for electric fields, where $\vec{D}$ presents the electrical flux density, ρ_v is the volume charge density, and Q_{enc} is the total enclosed charge. Eq. (3.2) is Gauss' Law for magnetic fields, where $\vec{B}$ is the magnetic flux density. Eq. (3.3) is Faraday's Law, and Eq. (3.4) is Ampere's Law, where $\vec{E}$ is the electrical field intensity, $\vec{H}$ is the magnetic field intensity, σ is the conductivity, and $\vec{J}$ is the source's current density.

Maxwell's equations are applied under the proper boundary conditions to obtain a necessary solution. These boundary conditions to evaluate each point along the boundary between the two media are summarized as follows [68]:

$$\hat{n} \times \left(\vec{H}_2 - \vec{H}_1\right) = \vec{J}_s \tag{3.5}$$

$$\left(\vec{E}_2 - \vec{E}_1\right) \times \hat{n} = \vec{M}_s \tag{3.6}$$

$$\hat{n} \cdot \left(\vec{D}_2 - \vec{D}_1\right) = \rho_s \tag{3.7}$$

$$\hat{n} \cdot \left(\vec{B}_2 - \vec{B}_1\right) = 0 \tag{3.8}$$

where $\vec{H}_2, \vec{H}_1$ is the magnetic field intensity at the medium 1 and medium 2, respectively; $\vec{J}_s$ is the electrical surface current; $\vec{E}_1 and\ \vec{E}_2$ are the electrical field intensity at medium 1 and medium 2, respectively; $\vec{M}_s$ is the magnetic surface current; $\vec{D}_1$ and $\vec{D}_2$ present the electrical flux density at medium 1 and medium 2, respectively; ρ_s is the electrical charge density; $\vec{B}_1$ and $\vec{B}_2$ are the magnetic flux density and $\hat{n}$ is the unit vector normal to the boundary between the two media, from medium 1 to medium 2, as illustrated in Fig. 3.1.

The boundary condition equations are applied at each point between the two media along the boundary.

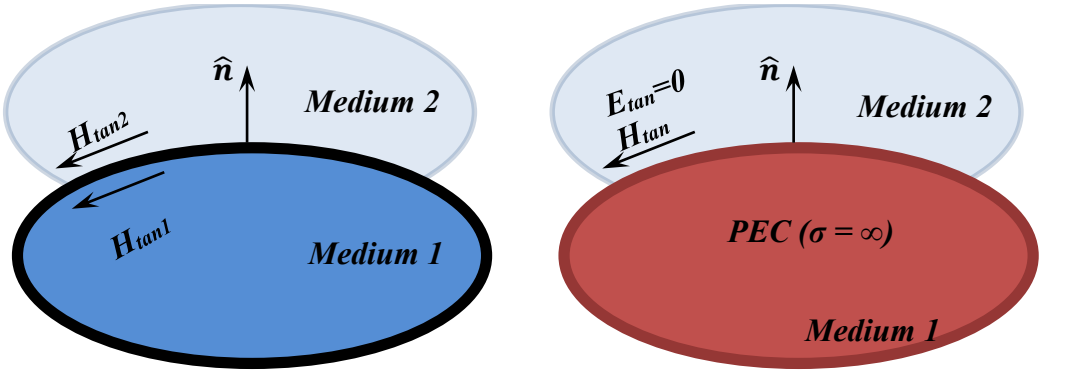

(a) General Case (b) Perfect Electric Conductor (PET) Case

Figure 3.1 The two media boundary conditions.

The parameters that describe the performance of an antenna, whether on the transmitting or receiving mode, are summarized as follow [68]:

- **Radiation Pattern**

  The radiation pattern describes a graphical representation of the antenna's radiation properties, and can be obtained mathematically as a function of space coordinates. Depending on the antenna design, the radiation pattern can be classified as an

isotropic radiator (equal radiation in all directions), directional radiator, broadside radiator, and/or omnidirectional radiator (often described as "doughnut shaped").

- **Field Regions**

Generally, there are three field regions as boundaries surrounding the antenna. First, reactive-near-field regions are bounded in the distance as $R < 0.62\sqrt{D^3/\lambda}$ from the antenna surface, where D is the largest antenna dimension, and λ is the wavelength. The second region, the near-field region, is that portion of an antenna field between the reactive-near-field regions and far field region as in $0.62\sqrt{D^3/\lambda} \leq R < 2D^2/\lambda$, and it is also called the Fresnel region. Third, the far-field region is the antenna field at $R \geq 2D^2/\lambda$.

- **Antenna Efficiency**

Antenna efficiency is the measure to evaluate antenna performance in radiated power (P_r) respecting to the input power (P_{in}) as in

$$e_{total} = \frac{P_r}{P_{in}} \tag{3.9}$$

$$e_{total} = e_c e_d e_{ref} \tag{3.10}$$

$$e_{total} = e_c e_d (1 - |\Gamma|^2) \tag{3.11}$$

where e_{total} represents total antenna efficiency, and e_c is the conduction efficiency, e_d dielectric efficiency, e_{ref} mismatch efficiency, and Γ reflection coefficient.

- **Directivity and Gain**

The Directivity D defines the ratio the maximum radiation intensity ($U\ (\theta, \phi)$) to the average radiation intensity (U_{ave}) given by

$$D(\theta,\phi) = \frac{U(\theta,\phi)}{U_{ave}} = \frac{U(\theta,\phi)}{\frac{1}{4\pi}\iint U(\theta,\phi)d\Omega}. \quad (3.12)$$

The gain of an antenna is directivity by a factor of total antenna efficiency as in

$$G(\theta,\phi) = e_{total}\, D(\theta,\phi) \quad (3.13)$$

- **Sidelobe**

  The far-field radiation patterns of an antenna consists of mainlobe and sidelobes. The sidelobe level describe the power dissipated by the antenna beside the mainlobe. The sidelobe at 180° from the mainlobe is called the backlobe.

- **Half Power Beamwidth**

  The half power beamwidth (HPBW) is the angular separation at -3 dB from the peak of the mainbeam. Where it is 50% (half power) the radiation pattern decreases in magnitude. The HPBW is usually expressed in degrees.

- **Antenna Polarization**

  The polarization of an antenna is described in the orientation of the electric field or E-plane with respect to Earth's surface. The antenna polarization can be linear (horizontal or vertical), elliptical, and circular.

- **Axial Ratio**

  The axial ratio AR refers to the ratio of two orthogonal components for an electric-field. In a CP antenna, the electrical-field components are equal in magnitude; therefore, the axial ratio is 1 or 0 dB. An AR less than 3 dB often describes the circular polarization at frequency range or bandwidth of a CP antenna.

- **Impedance Matching and Bandwidth**

  The impedance matching is the frequency range in which the antenna obtains a low reflection coefficient at the input antenna port as acceptable as $S_{11} \leq$ -10 dB. The bandwidth describes the frequency range where the radiation characteristics and matching impedance of an antenna have an adequate performance and meet the desire requirements.

3.3 Methodology of Antenna Design for MMW Imaging/Detection System

MMW propagation basically requires a high gain antenna and high efficiency. Line of sight alignment is also mandatory for direct communication between two systems. Furthermore, the antennas for imaging/detection systems require a very delicate design; with a passive imaging system, the temperature of blackbody radiation has very low electromagnetic wave energy, and the image system requires a higher gain antenna to reach the minimum input sensitivity of the radiometer receiver. Accordingly, two antenna types frequently used in imaging scanning are the parabolic and lens antenna, which both provide a high gain antenna performance. However, these antennas are bulky and associated with inefficient cost and complicated manufacturing - the low profile PCB antenna design is preferable for commercial systems.

Modern imaging systems use lenses in front of the antenna to increase gain, while the lens naturally behaves as a concentrate for the main-beam of the feed element. Thus, the endfire radiation pattern antenna has a narrower bandwidth and this antenna is a suitable choice for enhancing the coupling between antenna and lens. Furthermore, the radiation pattern is a critical part in the MMW antenna design, wherein the scanning techniques depend on signals that are collected by the main-beam of the antenna, however, the signals

collected from sidelobes and backlobe are considered unwanted singles. In order to suppress sidelobes and backlobe level as much as possible and optimize the performance of the imaging/detection system a proper antenna design is required. The challenge to design an antenna for an imaging/detection system is maintaining the balance to obtain the optimum antenna requirement such as wide bandwidth impedance, high gain, and high efficiency, and maintaining the radiation pattern characteristic stable with low sidelobes level. Therefore, the proposed antipodal Fermi tapered slot antennas in this recent research are implemented and investigated to satisfy the imaging/detection system requirements.

3.4 Spherical Dielectric Lens Antennas

Many techniques exist for the purpose of increasing the gain of an antenna. For example, antenna arrays are constructed from several antenna elements to increase the associated gain [55]. However, there is a loss that occurs due to the mutual coupling phenomenon, and more loss in the feeding structures [69], [70]. Another technique that can be implemented to increase the gain of the antenna is the dielectric lens, as focus on the radiation energy [71]. It is very useful for imaging and mining systems that need to enhance the directivity of the antenna. The design of a spherical dielectric lens is such that, if a point source is located on the surface, the lens transforms the resulting spherical waves into a plane wave with the propagating vector, aligned along the diameter and passing through the feed point. The variation of the relative dielectric constant (ε_r) as a function of the normalized radius (r/R), with the position of the feed (ro/R) as the parameter, illustrated in Fig. 3.2, can be expressed in Eq. (3.14), and (3.15).

$$\varepsilon_r = 2 - \left(\frac{r}{R}\right)^2 \tag{3.14}$$

The refractive index of the lens is given by

$$n(r) = n_R \left[2 - \left(\frac{r}{R}\right)^2\right]^{1/2} \tag{3.15}$$

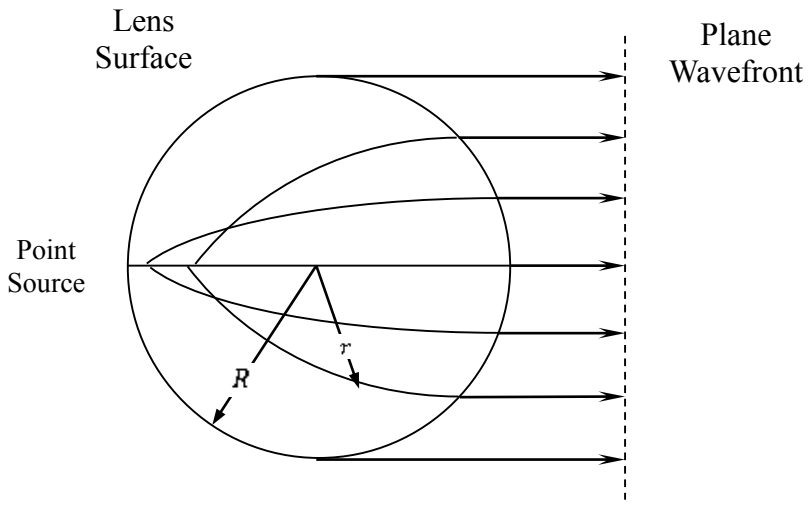

Figure 3.2 Spherical dielectric lens concepts.

3.5 Taper Slot Antennas

In this section we will start to introduce an updated literature review for the tapered slot antenna, and the advantages of using this antenna in an imaging system. A new design of antipodal Fermi tapered slot antenna is presented. Meanwhile, we will try to introduce the design formula for the most up to date design in this research for the antipodal tapered slot (AFTSA) antenna. These design equations are presented to simplify this model design procedure.

The tapered slot antenna (TSA) is considered a broadband antenna. TSAs are a class of endfire antenna, with their radiation patterns capable of obtaining high directivity while maintaining a wide bandwidth; furthermore, they are well known as surface wave antennas. TSAs are completely planar antennas that can be easily printed on a dielectric substrate. These types of antennas have been intensely investigated through the MMW band design. This antenna consists of a very thin substrate and low permittivity, in order to optimize the

gain and antenna bandwidth. Table 3.1 shows the advantages and disadvantages of tapered slot antennas. Therefore, this wide bandwidth model is of great interest due to its low cost, ease of fabrication, usefulness in scaling model design into higher frequency, low sidelobes, and high gain - all these features are important requirements for MMW imaging systems.

Table 3.1 The Advantages and Disadvantages of TSAs.

Advantages of TSAs	**Disadvantages of TSAs**
- Thin Structure	- High cross-polarization level in the diagonal plane
- Low Weight	- The same types of TSAs have a broad main beam in both azimuth and elevation planes
- Easy to Fabricate	- High backlobes
- Broadband	- Non-planar architecture when used as a circular polarization antenna
- Directional Antenna	- Low performance for dual-multifrequency or dual polarization
- High Gain	
- Low Sidelobe Levels	
- Suitable for Microwave Integrated Circuits	

Generally, the TSA consists of a tapered slot of different shapes [47], [72], cut out of a thin film of metal with or without a thin dielectric substrate. The TSA is approximately the shape of the ridge horn antenna. There are many types of TSA's, which are mainly classified depending on the taper slot shape. These models are:

- Fermi Tapered Slot Antenna (FTSA) [73] – [79]

- Constant Width Slot Antenna (CWSA) [80]
- Linearly Tapered Slot Antenna (LTSA) [81] – [85]
- Broken Linearly Tapered Slot Antenna (BLTSA) [86]
- Antipodal Linearly Tapered Slot Antenna (ALTSA) [87], [88]
- Exponentially Tapered Slot Antenna (ETSA) also called Vivaldi Antenna [89] – [94]
- Dual Exponentially Tapered Slot Antenna (DETSA) also called Vivaldi Antenna [95], [96]
- Elliptically Tapered Slot Antenna (ETSA) [97]

3.5.1 Antipodal Fermi Taper Slot Antennas

The Antipodal Fermi Taper Slot Antenna (AFTSA) has a new slot shape which is curved using the Fermi Dirac equation - presented by Sugawara [77], [78]. Meanwhile, Sugawara added to this design a rectangular corrugation [74] – [77] to decrease the effect of the surface wave in the edges of the substrate, to enhance radiation characteristics and return loss, and to decrease the sidelobes level. In fact, the design shape of the antipodal model makes the microstrip feed line better at exciting the radiating element of the tapered slot. On the other hand, the distance between the tapered slots is controlled by the substrate thickness and the size of the aperture slot. This distance generates a surface wave in the dielectric and that creates radiation which causes cross-polarization. Even so, the cross-polarization is within an acceptable level compared to the dominant radiation of co-polarization. Therefore, the receiver antennas in the passive MMW imaging system received non-uniform polarization from the target, which is presented as a blackbody radiation that is propagating in random polarization. Finally, the AFTSA is the ultimate model and is practically suitable for the modern passive MMW imaging systems.

3.5.2 Design of the Antipodal Fermi Tapered Slot Antenna with *Sin*-Corrugation

This research presents a novel corrugation shape design for the Fermi TSA. This corrugation is designed in a sine wave shape. Notably, this model has provided the flexibility to control surface current waves that flow in the side edges of the substrate. In addition, the smooth curve shape of the sine wave reduces the radiation that comes from the sharp edges. Those facts provide better enhancement compared with the conventional corrugation type [74] –[77], for instance they enhance matching impedance which makes the antenna have broader bandwidth, they have high gain, low side lobe levels, and almost the same E-plane and H-plane has been achieved.

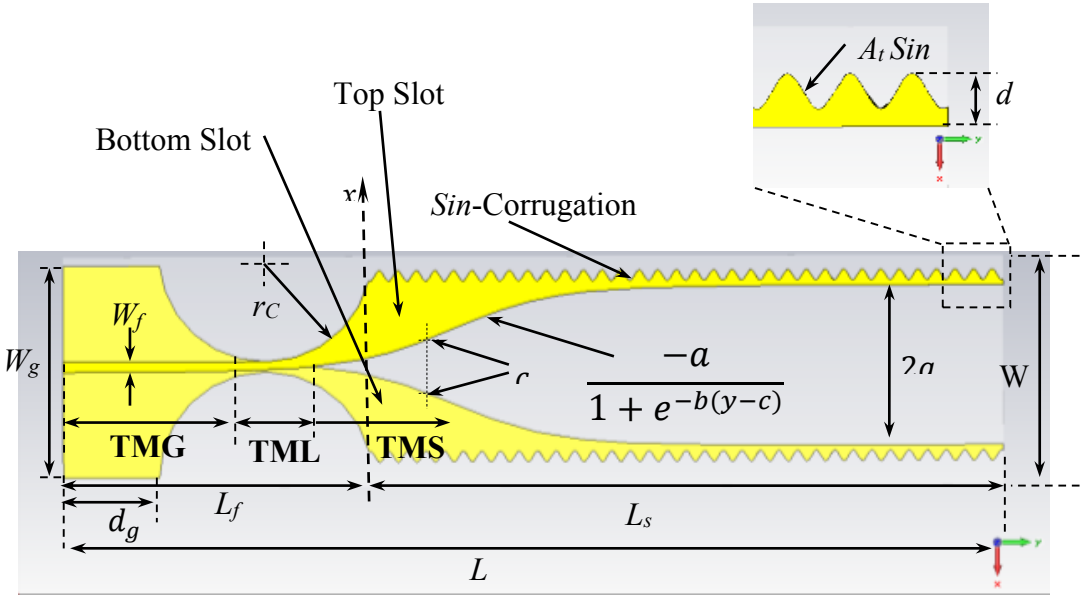

Figure 3.3 Antipodal Fermi tapered slot antenna configuration with *sin*-shaped corrugation.

The antipodal tapered slot radiator is configured with two conducting tapered slots; they are positioned symmetrically on opposite sides of the substrate with respect to the normal for the substrate (y-axis), as shown in Fig. 3.3. The antenna is fed by a gradually circle slot r_C, and it is symmetric to the back side of the ground tapered slot, this circle slot

is important for achieving high impedance matching. The feed line is excited by a waveguide port and optimized to satisfy the input impedance with width W_f, and the feed line is grounded with width W_g. The gain of the antenna is in direct proportion to the length of the tapered slot L_s.

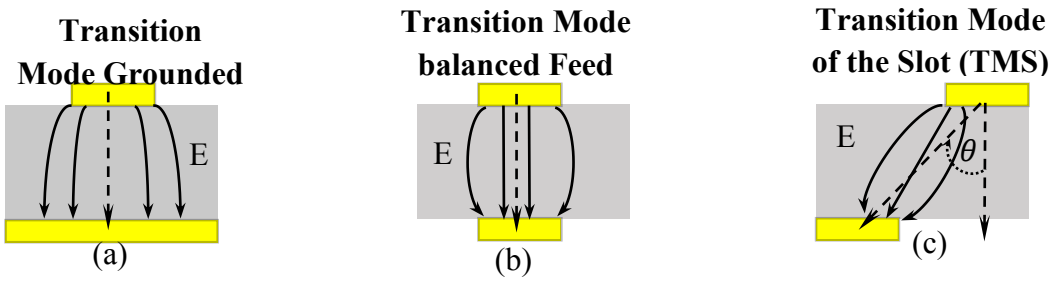

Figure 3.4 Distribution of the electric field lines at (a) the input of microstrip feeder grounded; (b) the balanced Microstrip transition feed line; and (c) the antenna transition slot mode.

Fig. 3.4 illustrates the behavior distribution of the electric field lines for each transition region. The first region, presented in Fig. 3.4 (a), shows the input of a microstrip feeder with large ground (TMG), and then Fig. 3.4 (b) shows the balance transition of the microstrip transition feed line (TML). The last transition region, illustrated in Fig. 3.4 (c), an imbalance region pushing the wave to propagate, is called the transition slot mode (TMS); as one can see, the electric field transfers with angle θ. Furthermore, this distance between the two conductors generates a surface wave in the dielectric substrate that causes cross-polarized radiation, due to the imbalance between the feed and the ground plane, as illustrated in Fig. 3.3. The following will concentrate on the design of each parameter in detail. This antenna model at E -plane is in the *xy*-plane ($\theta = 90^o$), and the H-plane is in the *yz*-plane ($\phi = 90^o$). The shape of the taper slot curve is defined mathematically by the Fermi-Dirac function as in Eq. (3.16).

$$f(y) = \frac{-a}{1 + e^{-b(y-c)}} \tag{3.16}$$

$$f(c) = \frac{a}{2} \tag{3.17}$$

$$f'(c) = \frac{ab}{4} \tag{3.18}$$

$$L_s \geq y \geq -L_f \tag{3.19}$$

Where *y* is a variable of the Fermi-Dirac function and starts from $-L_f$ to L_s, L_f is the length from input feed line to the start point of the corrugation, and L_s is the length from the start point of the corrugation to the end of the slot. The other constants, *a*, *b*, and *c*, affect the antenna's radiation performance. a is the asymptotic value of the taper's width, and it has a range of $5\lambda_g \geq a \geq 3\lambda_g$, where λ_g is the guided wavelength. The value of c is related to *y*-coordinates at the inflection point of the Fermi-Dirac function, which has a range of$2\lambda_g \geq c \geq \lambda_g$, and b is related to the gradient at the inflection point c, which takes a range of $1.5\lambda_g \geq b \geq 0.8\lambda_g$.

The design of the FTSA basically depends on trial-and-error optimization approaches. For years, the design of the TSA has been primarily based on an empirical approach, which was an initial step for designing the Femi tapered slot model. This research examined several models to simplify the design formulas, which initiating a start point for designing this antenna model. As a results, the following equations provide simple guidelines:

As a first step, we have to identify the operating frequency, and then from the value of the lowest operating frequency of the desired band, f_1, we calculate the thickness, h, of the substrate using an empirical approach as follows:

$$h = \frac{c_o}{20\, f_1(\sqrt{\varepsilon_r} - 1)} \tag{3.20}$$

where c_o is the speed of light, and ε_r is the relative dielectric constant of the substrate. For the second step, starting by calculating the microstrip feed line, W_f, is required to satisfy the input characteristic impedance of the system, Z_o, which in our case is equal to 50 Ω and can be calculated using the following equations:

For $W_f/h \leq 1$:

$$Z_o = \frac{60}{\sqrt{\varepsilon_f}} \ln\left(\frac{8h}{W_f} + \frac{W_f}{4h}\right) \tag{3.21}$$

ε_f is the effective dielectric constant for the transmission line, and is given by

$$\varepsilon_f = \frac{\varepsilon_r + 1}{2} + \frac{\varepsilon_r - 1}{2 \times \sqrt{1 + 12h/W_f}} \tag{3.22}$$

For $W_f/h \geq 1$:

$$Z_o = \frac{120\pi}{\sqrt{\varepsilon_f}\left[W_f/h + 1.39 + 0.67\ln\left(W_f/h + 1.44\right)\right]} \tag{3.23}$$

The third step, chosen the circular slot of the feeding transition, where the circular slot in the top layer and the two circle slots in the bottom layer are formed with the same radius r_c . They are chosen depending on the ground plane W_g and W_f as in the following equations:

$$r_c = \frac{W_g}{2} - \frac{W_f}{2} \tag{3.24}$$

$$W_g = 2a + d \tag{3.25}$$

$$2.5\lambda_o \geq r_c \geq 1.5\lambda_o \tag{3.26}$$

Where L_f can also be found with two values, r_c, and d_g - d_g is the ground distance.

$$L_f = 2r_c + d_g \tag{3.27}$$

$$1.5\lambda_g \geq d_g \geq \lambda_g \tag{3.28}$$

$$L = L_s + L_f \tag{3.29}$$

In the fourth step, the gain of the model is directly proportional to the length of the tapered slot, L_s, which increases the length that increases the gain of the antenna. This is typically chosen between $2\lambda_o$ to $N\lambda_o$, where *N* is the number of the traveling wavelength through the substrate.

$$L_s = N\lambda_o \tag{3.30}$$

3.5.2.1 Sine-Wave Corrugation Design

The corrugation structure consists of a periodic sine-wave shaped at the edges of the FTSA substrate. The corrugation is the last step in the design procedure. This corrugation is a new flexible shape, described in Eq. (3.31), which contains two constants; A_t is the amplitude of the corrugation, and *k* affects the angle variation of the sine-wave. When it increases, the other shrinks, and when it decreases, is the other expands in a sine-wave shape. These two variables control the surface wave characteristic behaviour on both side edges of the substrate.

$$A_t \sin kt \tag{3.31}$$

$$k \geq 1.5\lambda_g \tag{3.32}$$

$$\frac{\lambda_g}{3} \geq A_t \geq \frac{\lambda_g}{10} \tag{3.33}$$

Consequently, in the small antennas undesired surface currents on the outlines create a near-field radiation and this reduces the gain of the antenna as well as increases sidelobes level. Thus, the sin-corrugation model influences the influx of the current

distribution, and that creates a flexibility to control the flow of the electric field in the propagation direction. Thus, this decreases the reflection coefficient toward the feed line, meanwhile guiding the propagation wave in the desired direction that increases antenna gain. Moreover, the radiation pattern is affected by those changes, A_t and k in Eq. (3.32) and (3.33) are varied to obtain optimum control to suppress the sidelobes and backlobe characteristics.

Fig. 3.5 illustrates a design method flowchart for an Antipodal Fermi tapered slot antenna. This flowchart is a summary of the proposed methodology for designing any model of AFTSA-SC. In Millimeter-wave frequencies, any small variation in a model parameter affects the results generated in the simulation. Therefore, each step of the process is considered time-consuming for obtaining the desired results; in fact, the proposed design methodology provides a guideline to establish a starting point - the methodology outlines the model parameter adjustments that can be made to optimize AFTSA-SC performance.

3.6 Antenna Array Design Requirements

When looking ahead to design a probe for an imaging/detection system, it is required to choose and implement a suitable antenna element and phased antenna array structure to obtain the optimum system performance.

3.6.1 Bandwidth

A high range resolution performance is required for a millimeter-wave imaging/ detection system with a wide bandwidth, as mentioned in Eq. (3.34). In order to obtain a wide bandwidth phase array probe, in the first place, it is important to determine a wide bandwidth antenna element, as well as a high gain element to increase spatial resolution, which depends on HPBW. These features can be achieved using a single tap-

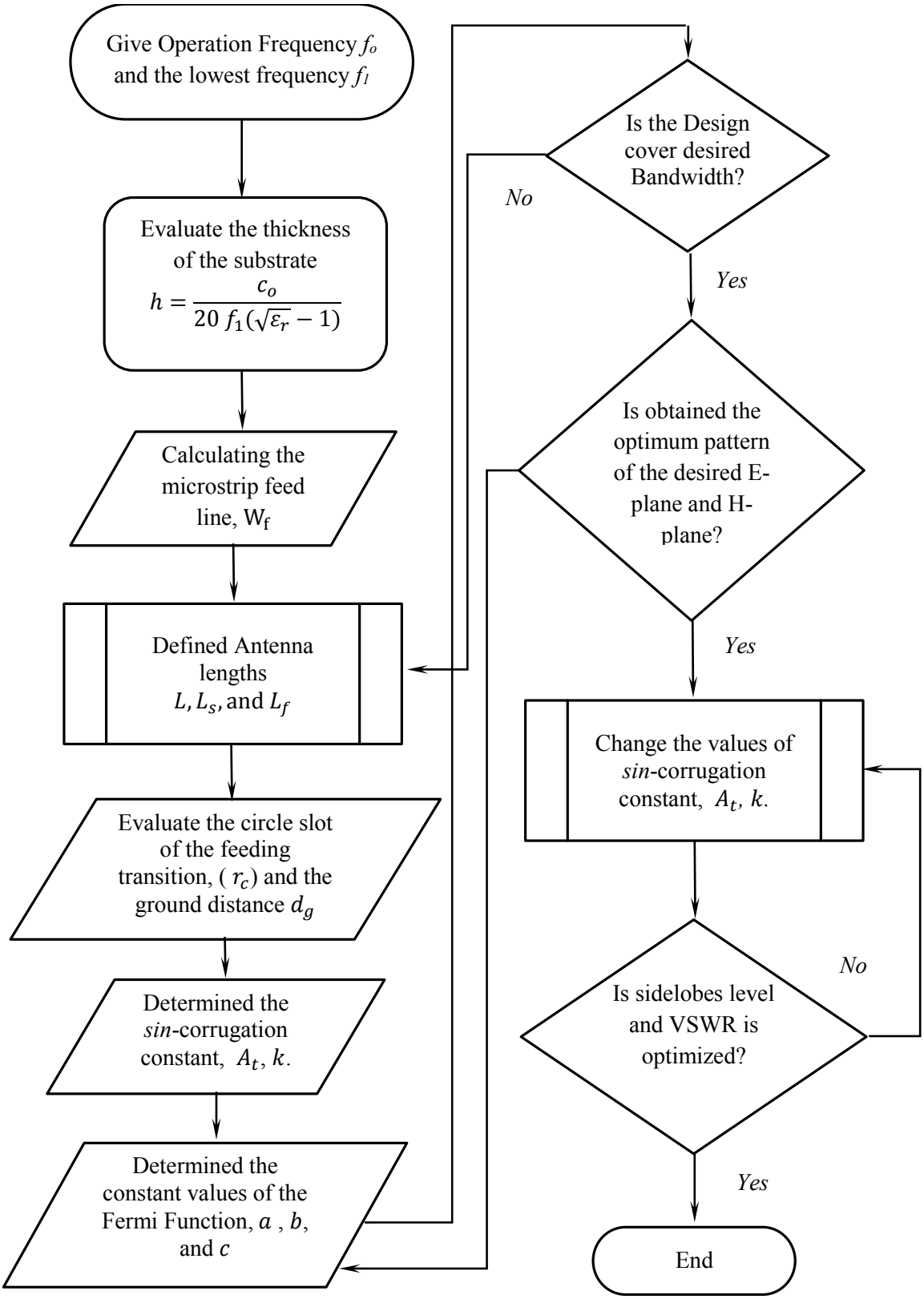

Figure 3.5 The flowchart of FTSA-SC design procedure.

-er slot antenna (TSA).These features can be achieved using a single taper slot antenna (TSA). The TSA design can be implemented to reach a desired coverage band with high gain and endfire radiation pattern characteristics. Furthermore, this antenna can be designed on the PCB, which provide a lightweight alternative to the traditional horn array, and with this low profile structure, it can be implemented in a sufficiently compact size and low cost array architecture. In this thesis, the desired band operates from 57-64 GHz (ISM-band), where designing the single TSA element should exceed the ISM–band to compensate the bandwidth reduction caused when employed in an array structure.A wideband TSA design is performed with low loss when the receiver/transmitter system is individually attached to each antenna element [60], [99]. However, for the feeding network array structure, the reflection coefficient increases as a consequence of insertion loss leading to a reduction in array bandwidth. As a second important consideration, a feeding network is a critical design implementation to achieve a wide bandwidth.

$$\Delta R_z = \frac{c_o}{2B/\sqrt{\varepsilon_r}} \tag{3.34}$$

where ΔR_z is the range resolution important in case of imaging detection for the concealed objects. In other word, the range resolution is ability to distinguish between the ranges of the barrier and the target.

3.6.2 Losses

In the antenna array structure reduction of loss is important, as the receiver/transmitter of the imaging/detection system relies on a high signal to noise ratio for adequate performance. The antenna is the front-end part in the system, it receives and transmits the signal electromagnetically and any lack in total radiation efficiency leads to

decay in system performance. The total radiation efficiency loss in a PCB antenna array's architecture depends on dielectric loss, metallic loss, line discontinuity loss, and mutual coupling loss. These loss factors are important requirements to consider for designing a low loss antenna array structure.

3.6.3 Aperture distribution

In many applications of imaging/detection systems the spatial resolution depends on the HPBW of the mainbeam to detect the target, any signal detected from other lobes such as sidelobe causes image distortion, where a high sidelobe level could detect the unwanted signal out of the target spot. An aperture distribution tapering is used in order to suppress the sidelobe level and grading lobe level. Depending on the suppression level of the sidelobe and the shape of the mainlobe required in a certain application, an aperture distribution method will be selected. In imaging systems, the minimum sidelobe level required is defined as $\leq$ -13dB and $\leq$ -30dB in an active and a passive system, respectively. There are many methods that have the advantage of suppressing side lobe levels and grading lobes, which could be done digitally or by feeding line power distribution. In this thesis, the chosen method is Taylor *N-bar* distribution as an extension to the Villeneuve distribution, which is able to achieve a lower sidelobe level and the highest directivity [37].

3.6.4 Number of Elements

A beam shaping tapered distribution using a feeding line power distribution depends on the number of elements in an array. The spatial resolution parameter defining the performance of an imaging/detection system requires a high gain and a HPBW angle. Furthermore, a certain amount of amplitude taper is expected to suppress the sidelobes level and reduce the grating lobes - all require a certain number elements in an array.

Regarding the equation, $\alpha_{HPBW} \approx \frac{0.8858\lambda_0}{N_e d_x}$, the preferable spacing between the antenna elements is $d_x = 0.5\ \lambda_0$, and λ_0 is the wavelength at the center frequency of the desired band, yield is $\alpha_{HPBW} \approx 6.346°$ at $N_e = 16$. In order to obtain desired beam shaping tapered distribution that satisfies a sufficiently low sidelobe, a narrow beamwidth, and grading lobe in the case of $d_x > 0.5\ \lambda_0$, thus, 16- elements are chosen for the antenna array structure.

3.7 Software Tools

In general, millimeter wave antenna designs are very delicate to implement and verify antenna performance. To reduce unnecessary time, cost and design errors, it is important to simulate the MMW antenna design using software program to optimize it instead of experimenting before producing prototypes. There are several numerical techniques, which have a practical use in solving electromagnetic problems [100], such as Method of Moment (MoM), Transmission Line Matrix (TLM), Uniform Theory of Diffraction (UTD), Finite Difference Time Domain (FDTD), Finite Element Method (FEM) [103], Finite Integration Technique (FIT) [180], and Fast Multipole Method (FMM). These method

s are impeded in commercial CAD tools able to analyze a 3D structure to obtain a full-wave solution. As an example, the numerical translation into a time-stepping algorithm was introduced by MR. Kane Yee in 1966 [101], which utilized Maxwell's differential equations to solve the E-field and H-field at any 3D cell of the meshed structure - shown in the Fig. 3.6. In antenna design, the CAD tools assist in obtaining, for example, the radiation pattern in far field or near field, radiation efficiency, polarization, reflection coefficient, and surface field distribution results. Furthermore, simulation results are close enough to measured results, which makes the design optimization much easier than

experimentation. Therefore, the antenna can be intensively optimized to meet the desired requirement, then it will be prototyped, and the simulated results will be validated to the fabricated ones.

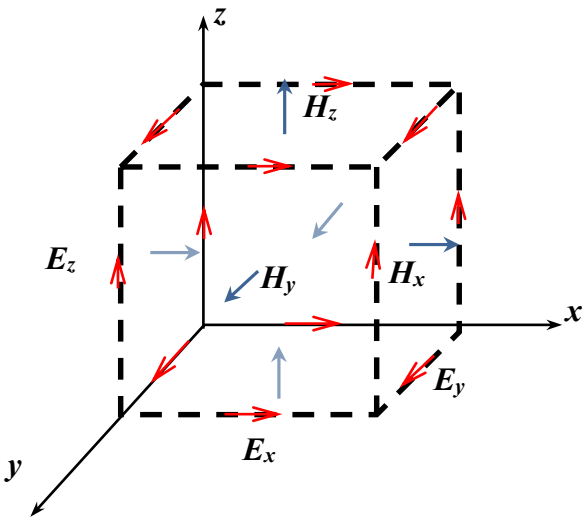

Figure 3.6 The Yee cell, illustrates the distribution of the E- and H-fields as used in discretizing the fields in FDTD simulators [101].

In this research, the antenna design simulations are carried out using two different commercial software packages. The first simulator is the Ansoft High Frequency Structure Simulator (HFSS) software [102]. HFSS is a 3D full-wave Finite Element Method (FEM) which is a frequency-domain numerical technique for solving Maxwell's equations. The common techniques for spatial discretization of partial differential equations is FEM. The solution of the partial differential equations is transformed and approximated by linear combinations of the basic functions on all elements. The FEM method is combined with modern mesh generation techniques to make an accurate solution of model design of partial differential equations on complex domains. Several meshing techniques are employed to minimize the errors caused by discretization of a design structure, such as tetrahedron, hexahedron, prism, and pyramid shapes, which are able to cover a complex structure. The

Finite Element Method for analyzing a design problem generally includes the following steps [103]: meshing the structure under test into a finite number of elements, deriving equations for each element, combining all elements in the solution region, employing the boundary conditions and solving the equations obtained.

The second simulator is the Computer Simulation Technology Microwave Studio (CST MWS) [104]. This simulator is a Finite Difference Time Domain (FDTD), which is based on the Finite Integration Technique (FIT), and thus it is able to use both a time-domain and frequency-domain numerical technique for solving Maxwell's equations. This method is able to provide electromagnetic solutions for large and complex structures as well as applicably utilizes a different type of discretization to reduce discretization error. [105]. Furthermore, the advantage of this method is its ability in handling some non-linearity distributions of arbitrary materials. However, in a complex and large structure, the solution region can be divided into a large number of mesh cells, which could necessitate a computer with a large memory, for solving algorithms, as well the solution time increases with large problems. In order to solve a problem using FIT, required step can be inquired [103], such as, discretizing a solution region to grid of nodes, at each a point node apply differential equation by a finite difference equivalent in relative approximation to solution of neighboring points, and then apply boundary conditions to solve these difference equations.

3.8 Summary

This chapter introduced the theoretical background and methodology needed for the MMW antenna design. It also introduced spherical design equations and a literature review for tapered slot antennas, design, a formula for the antipodal tapered slot antenna

(AFTSA), and the empirical equations for the sin-corrugation design. In addition, we presented the antenna array design requirements for the MMW imaging/detection system. Finally, a brief discussion about numerical techniques utilized by commercial simulation software tools was introduced.

Chapter 4: Millimeter-Wave antennas Design and Results

4.1 Introduction

This chapter presents several developed 60 GHz antenna sensors. A high gain 60 GHz circular patch-fed transparent lens in spherical shape antenna is introduced. Then, a low-cost 60 GHz printed Yagi antenna array with high radiation efficiency suitable for MMW-MMIC packaging is introduced. Four novel designs of antipodal Fermi tapered slot antennas are implemented especially for optimum performance to be employ in imaging/detection system applications. First, a high-gain single element antipodal Fermi TSA with new sin-corrugation which operates at the unlicensed 60-GHz ISM band is introduced. Second, a new design of dual-polarized antipodal Fermi tapered slot antenna is introduced. Third, a novel circular polarized AFTSA sine-shape corrugated with a single feed topology constructed in RHCP and in LHCP deliver high gain, high efficiency, low cost, and wide bandwith is intreduced. Finally, a new multi *sin*-corrugation (MSC) applied to increase the degree of optimization when the AFTSA antenna loaded with the grooved lens, and wide-scan three element array AFTSC-MSC fed grooved spherical lens antenna are introduced.

All proposed antenna sensors are designed to fulfill the requirements to be employed in imaging/detection systems. These requirements include a wide bandwidth matching impedance, directive main beam, high radiation efficiency, low sidelobe level, easy to fabricate, low profile, and stable radiation patterns and high gain over the ISM band. Furthermore, these proposed designs are fabricated and the experimental results are

validated with the simulated ones, and a good agreement is found between numerical and measured results.

4.2 60 GHz Circular Patch-Fed High Gain Transparent Lens Antenna

In the design presented in [J1], [C10], the proposed antenna consists of a full spherical dielectric lens, which is usually inexpensive and easier to manufacture than hyper hemispherical and elliptical lenses. The dielectric spherical lens is fed by a single element, a circular patch antenna, and supported by a cylindrical air cavity. The top side of the air cavity takes the shape of a convex lens, which is the key factor of the proposed antenna. This convex shape collimates the beam in order to obtain a more concentrated radiation of waves from the patch antenna compared to those from an extended hemispherical lens with or without an air cavity [106]. Thus, the proposed design with a cylindrical air cavity increases the pencil beam directivity, enhances the antenna radiation characteristic, and improves antenna efficiency.

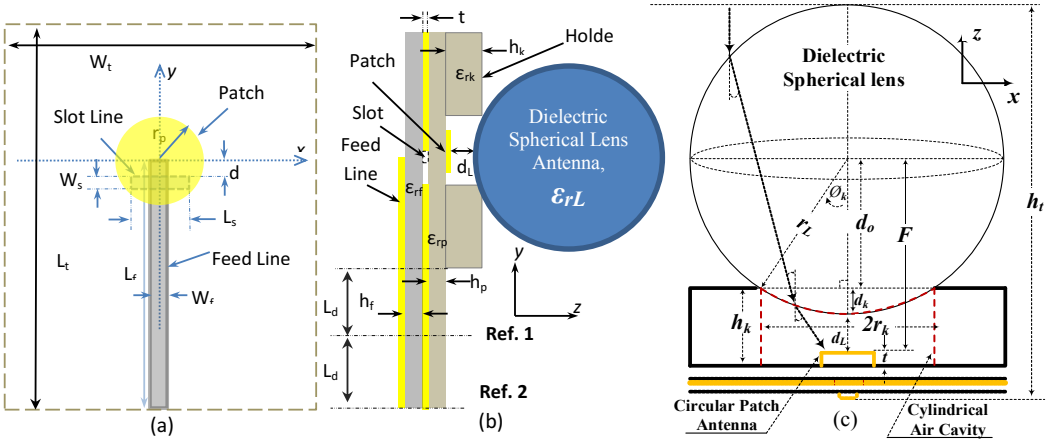

Figure 4.1 Antenna geometry; (a) top view, (b), side view, and (c) side view of the proposed antenna.

This proposed design is considers as a high gain, low cost and easy to fabricate millimeter-wave (MMW) antenna is presented in this section. To focus the radiation into a

very thin main beam, a concept based on employing a cylindrical air cavity with a convex front-end linking a microstrip patch radiator and a transparent dielectric lens is introduced. This principle is applied to enhance the coupling between the patch antenna and dielectric lens at 60 GHz. The design shows very directive and stable radiation patterns in both the E and H-planes. The proposed antenna exhibits a measured gain of 20 dB over the ISM-band, as well as high radiation efficiency (greater than 90%) based on calculated directivity over measured gain method [181]. The performance of the proposed antenna makes it a promising solution for various MMW applications, including short distance wireless communications and MMW imaging.

The proposed geometry consists of three components: a lens, the air-cavity, and a microstrip patch antenna, as illustrated in Fig. 4.1. The spherical dielectric lens antenna is fed by a circular microstrip patch with radius r_p= 0.78 mm. The patch is etched on a thin Rogers RT Duroid 5880 (h_p = 0.254mm, $\varepsilon_{rL} \approx 2.2$, $tan\delta \approx 0.0009$) substrate. It is aperture-coupled by a resonant slot with length L_s=0.835mm and × width W_s=0.1524mm. This rectangular radiating slot has an approximate length of $\lambda_g/4$, where λ_g is the guided wavelength at 60 GHz. The slot was drilled with offset from the center of the patch by d = 0.3 mm; this distance can be tuned to ensure that the optimum energy of TM_{010} excitation mode is passed through the feed line to the circular patch antenna. The microstrip feed line sits on the back side of the second thin layer composed of Rogers RT Duroid 6010 (h_f = 0.254-mm, $\varepsilon_{rf} \approx 10.2$, $tan\delta \approx 0.0023$), which excites the patch via a resonant slotted ground plane. The microstrip patch, feed line and ground plane are simulated as glossy copper sheets of thickness t = 0.035 mm with a conductivity of $\sigma = 5.80 \times 10^7$ S/m.

Fig. 4.1 (c) shows the dielectric lens model. The spherical lenses have the advantage of a multi-beam option, which gives them the ability to simultaneously collect signals from all directions. Another advantage is their ability to be manufactured with inexpensive dielectric materials and without the need for active elements. The spherical lens is a homogeneous dielectric sphere [107], which, for dielectric constants in the range $1 \leq \varepsilon_{rL} \leq 4$, focuses paraxial rays to a focal point (the radiated element) outside the sphere. The distance F of the focal point from the centre of a lens with radius r_L, and dielectric constant ε_{rL}, is approximately determined by geometrical optics (GO) and is given by

$$F = \frac{r_L\sqrt{\varepsilon_{rL}}}{2(\sqrt{\varepsilon_{rL}}-1)} \tag{4.1}$$

The lens was selected with same characteristics as those of RO5880. The optimum diameter of the dielectric spherical lens antenna was chosen to be $D_L = 2 \times r_L = 20$ mm $= 4 \times \lambda o$ (λ_o is the wavelength in free space) at the central frequency, 60 GHz.

The cylindrical hole of the proposed air cavity is drilled on a Rogers RT Duroid 5880 (h_k=1.575mm, $\varepsilon_{rL} \approx 2.2$, $tan\delta \approx 0.0009$) substrate with a size $W_k \times L_k = 10.5 \times 9.872$ mm^2. ×The starting design point for the radius (r_k) and height (h_k) of the cylindrical air cavity depends on the focal point distance (F) and the space between the lens end surface and the patch antenna, d_L. In Fig. 4.1 (c) the aperture angle to the air-cavity edge is $\emptyset_k = sin^{-1}(r_k/r_L)$. The distance from the center of the lens to the edge of the cavity is described by $d_o = \sqrt{{r_L}^2 - {r_k}^2}$. This leads to determining the lens inset distance into the air-cavity, $d_k = r_L - d_o$, and $d_L = h_k - d_k - t$, where the copper thickness t is taken into account in particular at MMW frequencies. Thus, the focal point is determined as $F = r_L + d_L$ by

substituting F in (1). d_L is expressed by Eq. (4.2), which considers the theoretical GO value as the initial value to determine the approximate focal point at the patch antenna level:

$$d_L = \frac{r_L\sqrt{\varepsilon_{rL}}}{2(\sqrt{\varepsilon_{rL}}-1)} - r_L \tag{4.2}$$

The proposed antenna was studied numerically using the commercial electromagnetic simulator CST Microwave Studio® (CST-MWS). The model was simulated to investigate the effect of different design parameters and their performance at operating frequencies from 55 GHz to 65 GHz.

A standard milling machine with low-cost PCB processes was used to fabricate the two layers slot-coupled patch antenna as well the third layer cavity and the lens holder. The copper thickness of the substrate is 35µm with a conductivity σ = 5.80 × 10^7 S/m. A Photograph of the fabricated prototype is shown in Fig. 4.2. The antenna layers are manually attached using a thin film of bonding material and are correctly aligned to ensure that the feed line, the aperture slot, and the patch are in their positions.

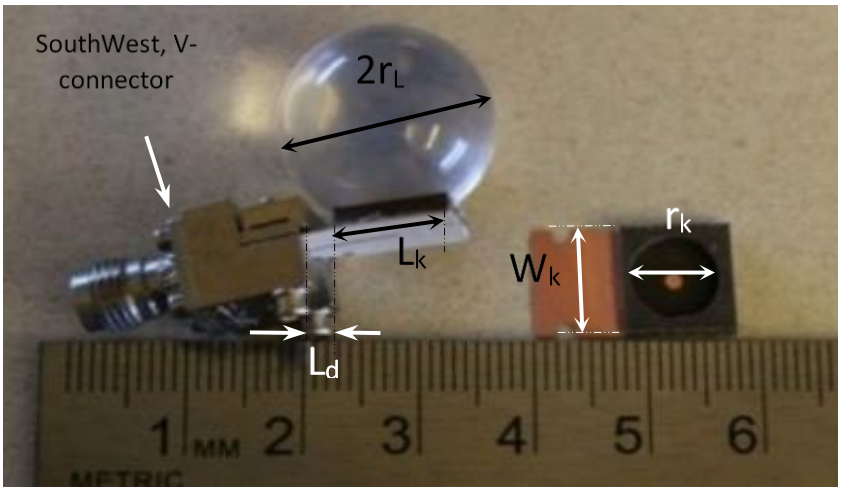

Figure 4.2 Photographs of the lens antenna with the circular microstrip patch, fed with the holder substrate.

As shown in Fig. 4.1 additional length from Ref1 to Ref2 was necessary to create a large enough ground plane for the SouthWest V- connector (1.85 mm connector). In addition and as shown on the right side of Fig. 4.2, a circular shaped gap was drilled through the first layer to insert the screws of the V- connector. The 12.7 mm radius spherical dielectric lens is made of polymethyl methacrylate PMMA (Acrylic) material, a lightweight transparent thermoplastic with $\varepsilon_{rL} \approx 2.57$, $tan\delta \approx 0.0032$ at 24 GHz, and $\varepsilon_{rL} \approx 2.61$, $tan\delta \approx 0.002$ at 71 GHz [108]. According to the dielectric constant of the lens material given in [108], the interpolated value of the dielectric constant at 60 GHz is $\varepsilon_{rL} \approx 2.6$, $tan\delta \approx 0.0026$.

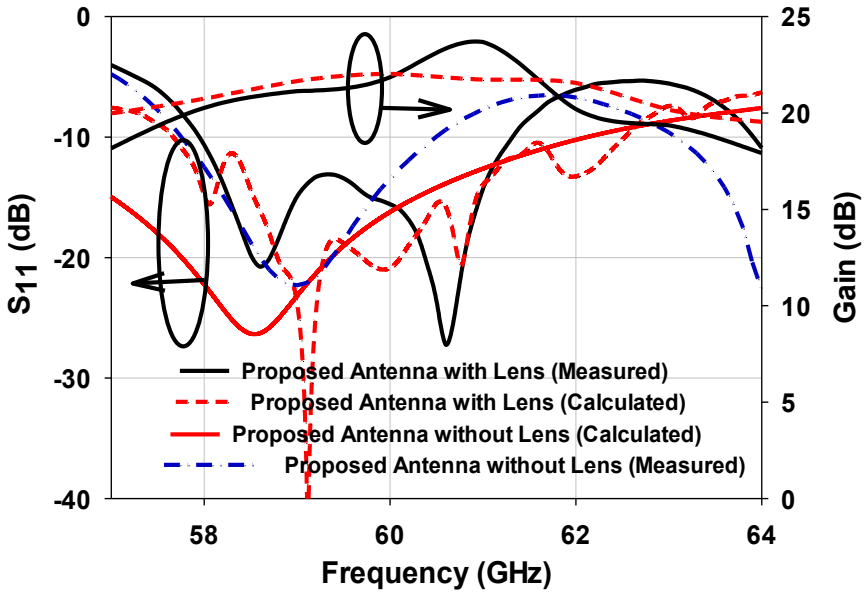

Figure 4.3 Measured and calculated reflection coefficient of the proposed antenna.

The measurements of the reflection coefficient (S_{11}) for the proposed antenna are done using Anritsu 37397C Vector Network Analyzer and Anritsu 3680V 60 GHz Universal Test Fixture. The reflection coefficient measurements were performed with the Through-Reflect-Line (TRL) calibration kit, instead of the standard coaxial line

calibration. The TRL calibration technique is a more accurate way to determine precise values for the reflection coefficient, especially for the MMW band, where any inaccurate connection during the measurements could cause inaccurate results for measured antenna parameters [109].

Fig. 4.3 compares the measured reflection coefficient and antenna gain with CST results for two antenna configurations of the radiated element with and without the lens. The measured impedance bandwidth (≤ -10 dB) is 3.5 GHz corresponds to 5.84% at 60 GHz. In the measured result of $|S_{11}|$, there is a shift in resonant frequency compared with CST results – this may be caused by inaccuracy in the substrate material properties at 60 GHz and/or by the effects of etching and alignment tolerances in the fabrication process. The material used in the simulation for the microstrip feed line is RO6010, and the patch's substrate is RO5880. Dielectric constants of both substrates are slightly different at 60 GHz, from those specified by the manufacture at 10 GHz.

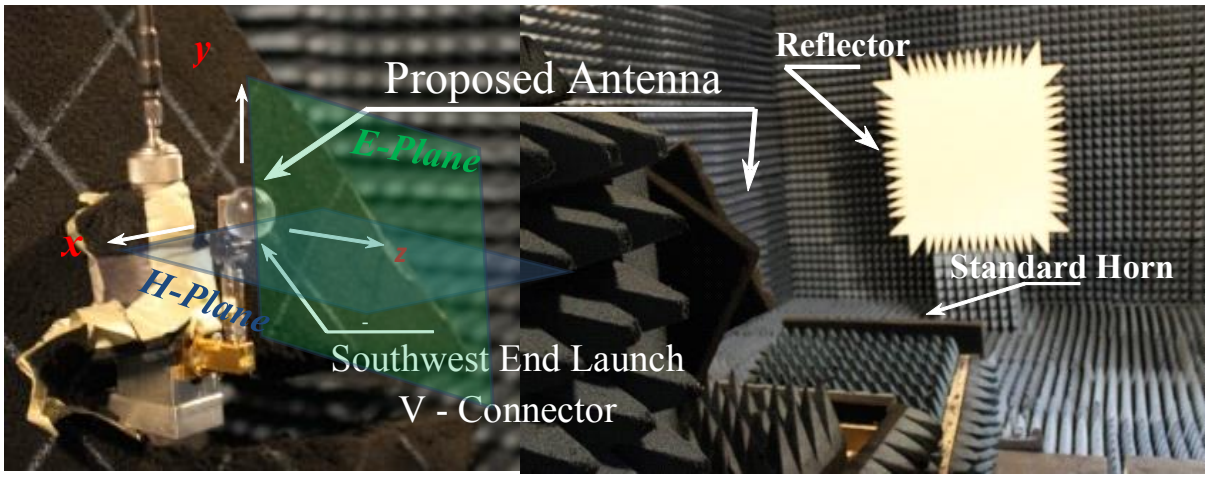

Figure 4.4 Setup for radiation pattern measurements shows the antenna mounted in a vertical position.

The radiation patterns within the bandwidth range (from 58 GHz to 61GHz) are measured in an anechoic chamber. As shown in Fig. 4.4, the E-plane is the *yz*-plane, and the H-plane is *xy*-plane. Two prototypes are measured: the first is the radiating element (a circular patch with cavity), and the second is the proposed antenna (a lens mounted on the radiating element). In both cases, the radiation pattern is measured with the antennas directly mounted by a 1.85 mm South-West Microwave connector.

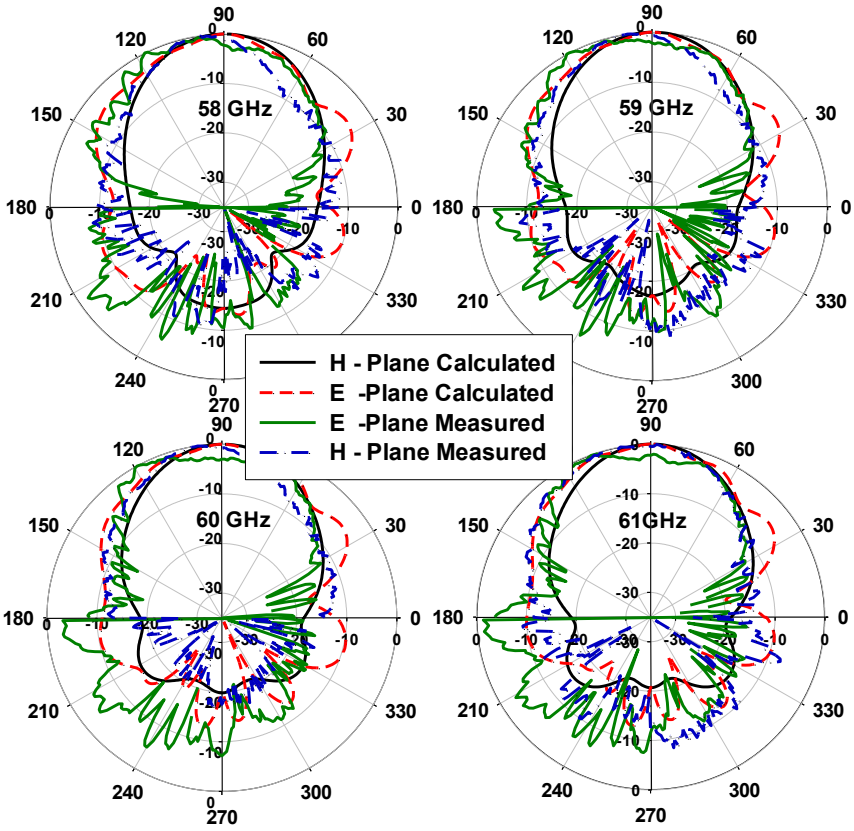

Figure 4.5 The normalized E- and H- plane co-pol patterns of the circular patch with holder for 58 GHz -61 GHz.

The measured and calculated E and H planes radiation patterns for the patch antenna with the holder only (no lens) within the ISM frequency band at 58 GHz to 61 GHz are shown in Fig. 4.5. Both the CST and measured results agree well within the main lobe and HPBW range. In the results, the back lobe radiation of both the E and H planes was

higher than expected due to the small ground plane and strong resonance occur at the cavity . Furthermore, a higher side lobe level (SLL) within an angle range of 150° to 270°, the side of the setup and the antenna's connector, was observed for the measured E-plane pattern.

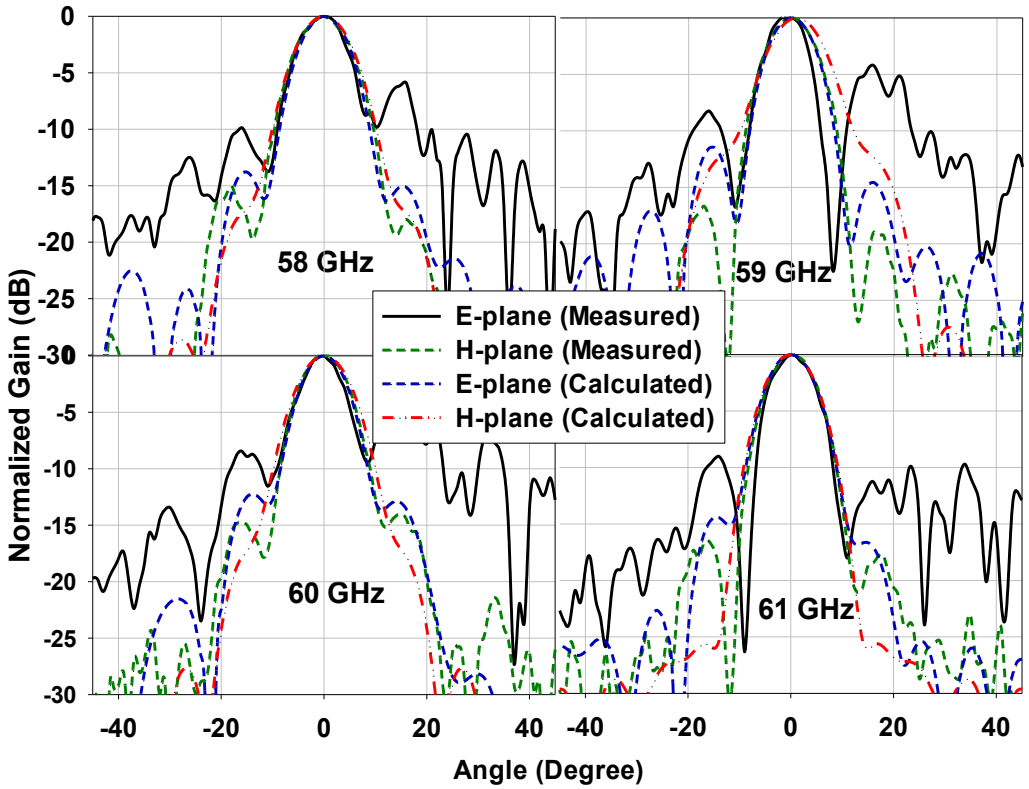

Figure 4.6 Normalized E- and H- plane patterns of the proposed antenna at 58 GHz -61 GHZ.

In Fig. 4.6, the measured and the calculated results of the far-field patterns are presented for both the E and H- planes of the proposed antenna, at 58 GHz to 61 GHz. The HPBW of the measured results agreed with the CST results for the entire ISM band. Moreover, the measured results of the H-plane agree quite well with the calculated results. However, the SLL in the measured results of the E-plane is higher than expected, due to the effect the antenna's setup and the reflection from cable and connectors. The high

reflection is caused by the Southwest connector, which is perpendicular to E-plane radiation pattern, as seen in Fig 4.4. A large reflection is also shown at the side lobe in Fig. 4.6, especially from the feed line side. Meanwhile, the radiation pattern at the H-plane is far from the connectors, and thus the measured results of the radiation pattern agree well with CST results.

4.3 High-Efficiency 60 GHz Printed Yagi Antenna Array

The aim of this study is to design a low-cost antenna with high radiation efficiency suitable for MMW-MMIC packaging used in wireless communications and imaging systems. Moreover, the design presented in [J4], [C11], and this study focuses on investigating the influence of the parasitic printed Yagi array substrate thickness and the size of the Yagi array patches on the antenna performance. The proposed double layer compact Yagi array antenna operating at 60 GHz is based on the general concept of the printed microstrip Yagi antenna array [110]-[115]. The arrangement of the parasitic elements above the feeding patch antenna elements is widely considered to be an effective technique for improving the radiation efficiency, as examined in [112], [113], [116]-[120]. The stacked design is commonly used in MMIC structures due to its efficiency in width size reduction. A multi-stacked parasitic antenna, however, can problematically increase the structure's height [112]. The design introduced in [113] with six stacked layers achieved 4.2% bandwidth at 60 GHz but adds more complexity to the fabrication process. Instead of such a multi-stacked structure, the proposed antenna shown in Fig. 4.7 introduces only one stacked layer for size and weight reduction while enhancing the antenna performance, and achieves 7.2% in bandwidth at 60 GHz. Parasitic elements in the second (top) layer are designed with the same design principle as the printed Yagi antenna

in the first layer. The coupling between these layers provides an additional increase in the radiated power of the antenna and its radiation efficiency compared to a single-layer structure. Moreover, the parasitic structure of the second layer creates multi-frequency resonance that improves the bandwidth while maintaining the same radiation characteristics of the first layer Yagi array. Simulated results show that the proposed two-layer structure has an 8.5 GHz impedance bandwidth - compared to a 5.3 GHz bandwidth for a single layer structure. In addition, the parasitic layer increases radiation efficiency and reduces backlobe radiation.

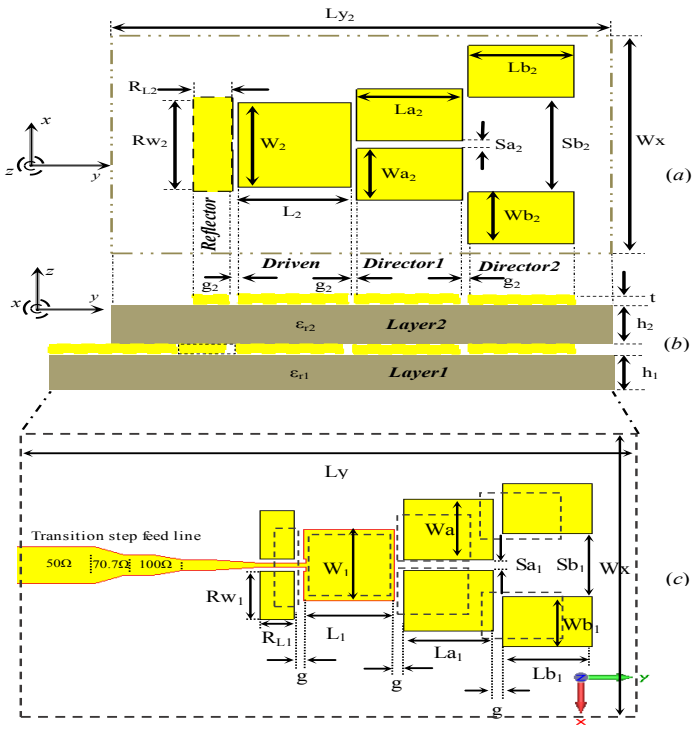

Figure 4.7 Geometry of the proposed antenna: (a) top view of the parasitic layer, (b) side view of both layers, and (c) is the top view of the first layer.

The configuration of the proposed antenna is illustrated in Fig. 4.7. The antenna is composed of two layers. The first layer consists of a 2-element split reflector patch and two pairs of directors. The position of each element is optimized to achieve better impedance

matching and to maximize the antenna directivity. The second printed Yagi array, which is mounted on top of the first layer, contains the reflector, the parasitic driven elements, and an additional pair of two director elements. This technique improves the radiation efficiency when the parasitic elements are positioned above the feeding Yagi array of the first layer.

Fig. 4.7 (b) shows a side view of the antenna, where the substrate thicknesses of layer1 and layer2 are $h_1 = 0.254$ mm and $h_2 = 0.508$ mm, respectively. Both layers have the same dielectric constant of Rogers 5880 substrate ($\varepsilon_{r1} = \varepsilon_{r2} = 2.2$, $tan\delta = 0.0009$ at 10 GHz). Fig. 4.7 (c) shows the top view of the first layer, where the proposed Yagi array elements are designed to operate at 60 GHz ($\lambda_o = 5$ mm). The printed Yagi array, shown in Fig. 4.7 (c), has the optimized parameters: $W_x = 1.603\lambda o$, $L_{y1} = 2.1374\lambda_o$, $R_{L1} = 0.1068\lambda o$, $R_{w1} = 0.2157\lambda_o$, $L_1 = 0.273\lambda_o$, $W_1 = 0.32\lambda_o$, $W_{a1} = 0.27\lambda_o$, $L_{a1} = L_{b1} = 0.28\lambda_o$ and $W_{b1} = 0.224\lambda_o$. The gap between the elements is $g_1 = 0.028\lambda_o$. Furthermore, the spaces between director1 and director2 elements are $S_{a1} = 0.048\lambda_o$ and $S_{b1} = L_{a1}$, thereby influencing the effective aperture of the antenna. The separation between director elements improves the directivity of the antenna. The 50Ω feed-line characteristic impedance is matched to the first patch using three feed-line impedance transitions: 70.4 Ω, 100 Ω and 144 Ω. Quarter-wave transformers improve the input impedance matching and chamfering edges minimize the feed-line edge radiation.

The dimensions of the parasitic Yagi array shown in Fig. 4.7 (a) are: $W_x = 1.603\lambda_o$, $L_{y2} = 1.781\lambda_o$, R_{w2} $0.3626\lambda_o$, R_{L2} $0.0902\lambda_o$, L_2 $0.2306\lambda_o$, $W_2 = 0.2704\lambda_o$, $L_{a2} = 0.2366\lambda_o$, $Wa2 = 0.228\lambda_o$, $L_{b2} = L_{a2}$, and $W_{b2} = 0.1892\lambda_o$. The gap between the elements is $g_2 = 0.0236\lambda_o$. The distances between the director1 and director2 elements are $S_{a2} = 0.0406\lambda_o$ and $S_{b2} = L_{a2}$.

In a printed Yagi antenna, the dielectric constant governs the guided wavelength, patch size, separation distance, and the gaps between patches. The antenna elements are coupled both through space and by a surface wave in the substrate. As a result, to enhance the constructive mutual coupling for the Yagi radiating elements, the dielectric constant and the thickness of the substrate are carefully chosen to improve the antenna's performance. Simulated results show that the proposed double-layer structure increases the 10dB matched impedance bandwidth by more than 3 GHz and improves the radiation efficiency over the ISM-band, as shown in Fig. 4.8.

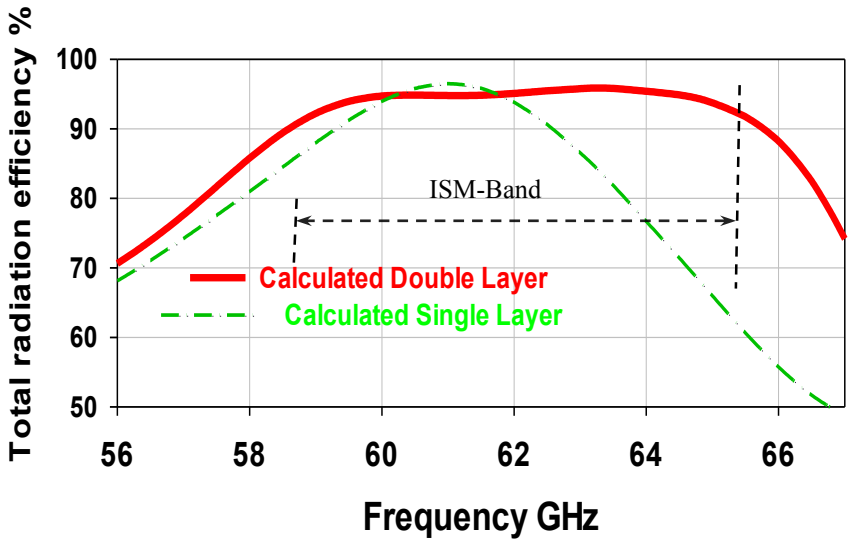

Figure 4.8 Calculated total radiation efficiency of the single and double layer.

Fig. 4.10 shows the measured and calculated reflection coefficient of the single- and double-layer configurations. The reflection coefficient was measured with the TRL-kit for a more accurate calibration of the two configuration models. The measured impedance bandwidth (<-10 dB) covers frequencies from 60.7 to 65 GHz with 7.2% at 60 GHz. Furthermore, about 5 GHz can be achieved using the two close resonances of the driven and parasitic elements. Notably, the resonant frequency is shifted up due to possible

variations in the material properties at 60 GHz and the effects of fabrication tolerance. The material used in the simulation is RO5880. It has $\varepsilon_r = 2.2$ measured at 10 GHz with a loss tangent of $tan\delta = 0.0009$. These parameters are typically frequency-dependent and may be different at 60 GHz. Moreover, based on the measured results of the reflection coefficient for several prototypes, we observed that the material permittivity of the RO5880 substrate is found to be slightly smaller than $\varepsilon_r = 2.2$. In Fig. 12, the $|S_{11}|$ of the single and double layer cases are calculated using the dielectric constant $\varepsilon_p = 2.18$ taking into account potential variation with frequency. A photograph of the prototype antenna is illustrated in Fig. 4.9. Fig. 4.9 (a) shows the first-layer of the proposed Yagi array antenna and Fig. 4.9 (b) shows its second layer.

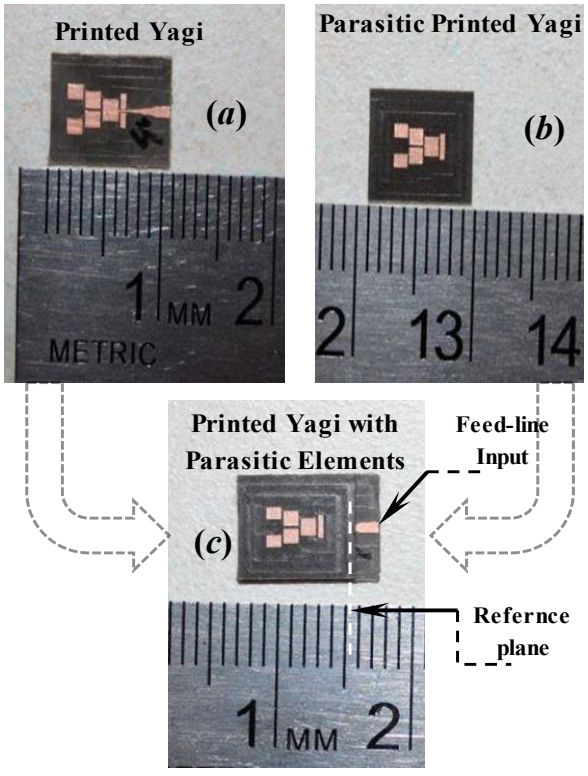

Figure 4.9 Photograph of fabricated prototype: (a) first layer of Yagi array, (b) parasitic array, (c) combined layers.

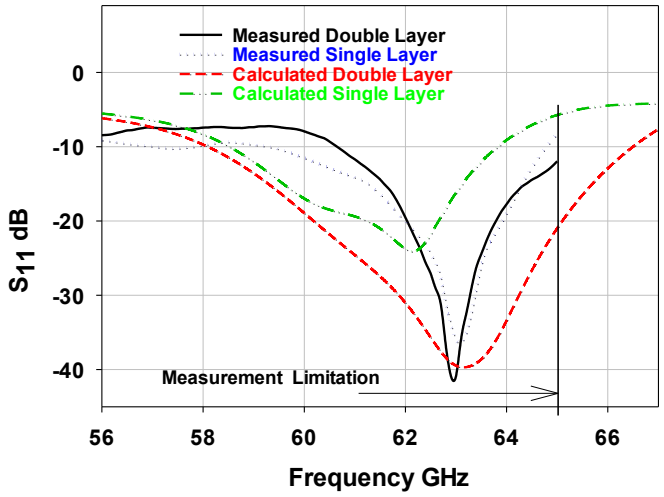

Figure 4.10 Measured and calculated reflection coefficient of the single and double layer.

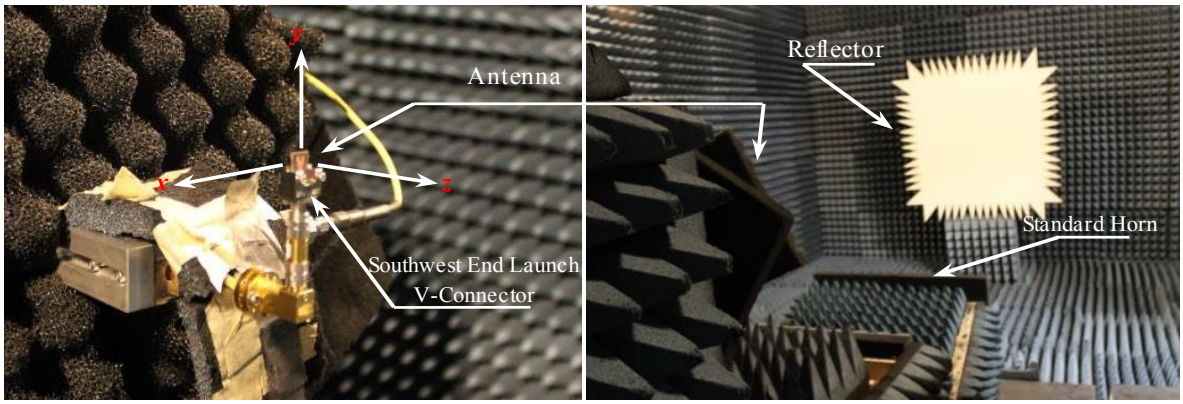

Figure 4.11 Illustration of the anechoic chamber up to 110 GHz, showing the antenna mounted on a SouthWest End Launch V-connector and the setup for measuring the radiation pattern.

The Yagi array radiation pattern is measured in an anechoic chamber, as shown in Fig. 4.11. The co-polarized radiation patterns in the E-plane (*yz*-plane) and H-plane (*xy*-plane) are measured over the ISM-band, at 59- 64 GHz, as illustrated in Fig. 4.11. The 3 dB beamwidth of both the H-plane and E-plane are about 25°-40° and the antenna achieves a radiation efficiency greater than 94% at 60 GHz. The F/B ratio at 60 GHz in the simulated results achieves 29 dB for the double layer while it is 23 dB for the single layer. The

measured absolute gain of the proposed prototype is 10 dB with an E-plane F/B ratio of more than 18 dB.

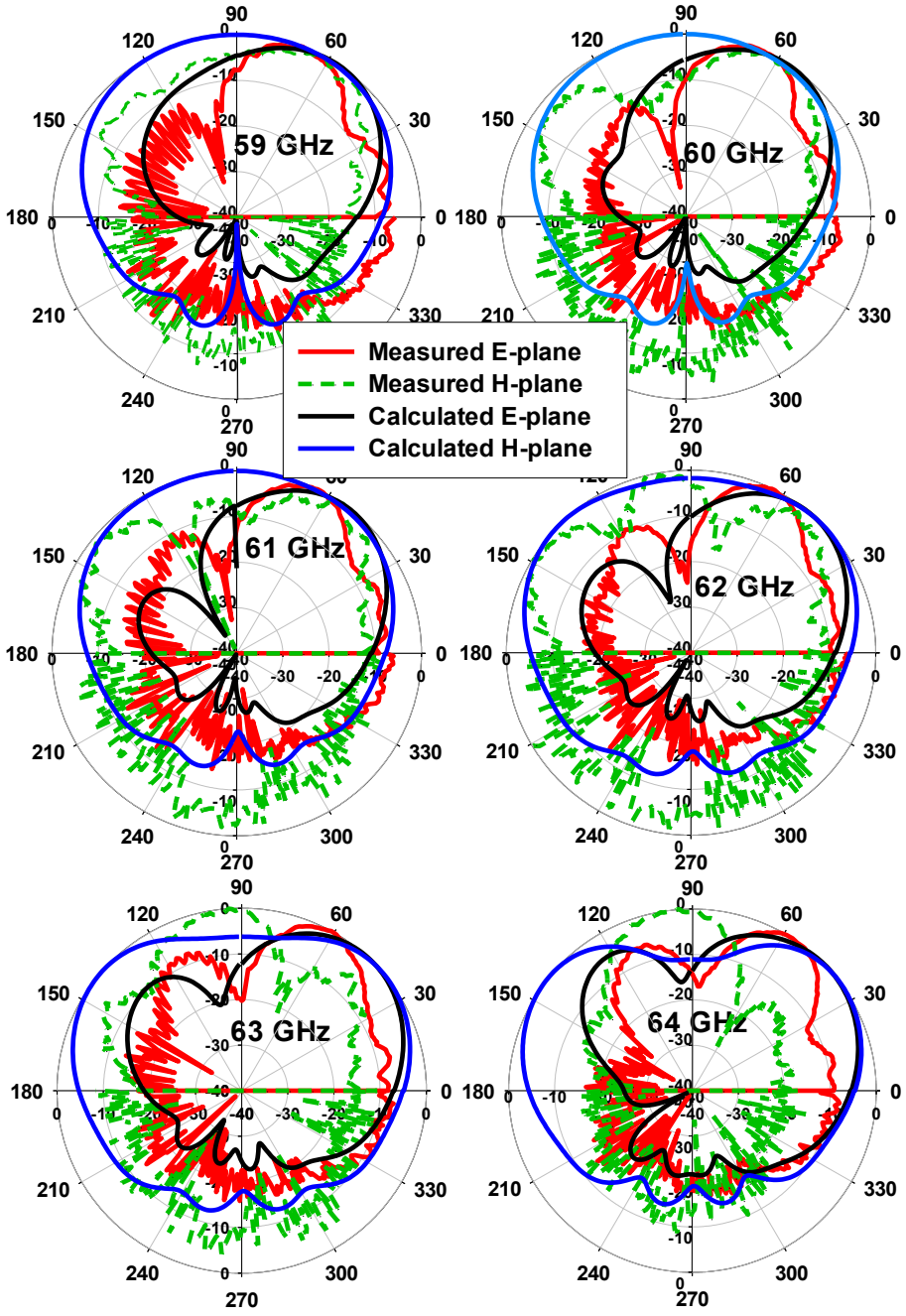

Figure 4.12 The measured and calculated radiation pattern results of the ISM-band, from 59 to 64 GHz.

The radiation behaviour of a printed Yagi array is very sensitive to various array parameters. The peak of the main beam is tilted by $25^{o} – 45^{o}$ from the broadside direction towards the direction of the director patches. This kind of behaviour occurs due to the strong coupling between the driven and parasitic patches. The measured radiation pattern results in Fig. 4.12 show that the main beam is tilted by 20^{o} to 40^{o} over the ISM-band with a slight difference from calculated results. This difference is potentially caused by several factors, such as fabrication tolerances, variation of the substrate dielectric constant within the V band, and the effect of connectors during radiation pattern measurements. Simulated results show that the tilted beam angle depends on the substrate thickness, dielectric constant, gap distance, patch separation and the size of the parasitic patches. These parameters show a high degree of interrelation on the main beam tilted angle direction. Thus, for the E-plane radiation pattern, the minor deviation angle increases with the frequency, as shown in Fig. 4.12.

The backside radiation is associated with the size of the ground plane. A large ground plane reduces the backlobe and sidelobes caused by the fringing field in the far edges between the radiating elements and ground plane. The backlobe is partially reduced by optimizing the reflector elements of the printed Yagi antenna.

4.4 A 60 GHz Antipodal Fermi Tapered Slot Antenna with *Sin*-Corrugation

In proposed design introduced in [J2], [C8], presents a sinusoidal corrugation for a high-gain single element antipodal Fermi TSA which operates at the unlicensed 60-GHz ISM band. This model provides the flexibility to control the surface waves that flow on the side edges of the substrate. In addition, the smooth curved shape of the sine wave reduces the radiation from the sharp edges. Such features provide an improved performance

compared to conventional corrugation-type antennas [74]–[77], resulting in a broader operating bandwidth and a low sidelobe level. As shown in Fig. 4.13, a broadband match covering the entire ISM band and a high gain value of 18.75 dB at 60 GHz were experimentally obtained for this antenna.

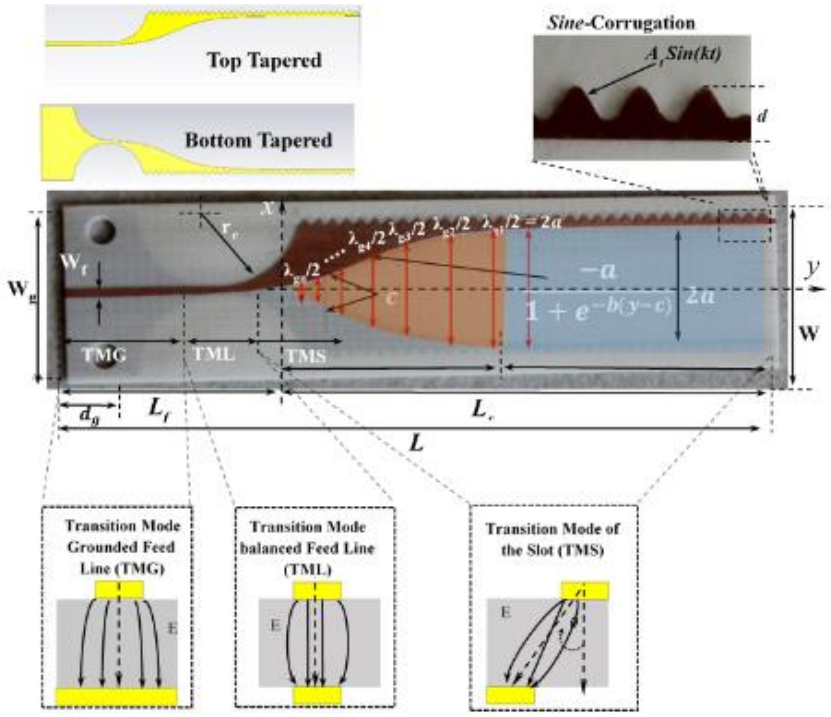

Figure 4.13 Antipodal Fermi tapered slot antenna configuration with sine-shaped corrugation.

The antipodal tapered slot radiator is constructed with two conducting tapered slots positioned symmetrically on opposite sides of the substrate, as shown in Fig. 4.13. The antenna is fed gradually via a circular slot r_c , ($r_c \cong a + d + W_f$) , and it is symmetric to the back side of the grounded tapered slot. This circular slot is the key to achieving a broad impedance matching. The feed line is optimized to satisfy the 50 Ω input impedance with width W_f, and it is grounded with a width of W_g. The feed line and the circular slot structures are essentially a broadband balun. The antenna's gain is in direct proportion to the length

of the tapered slot, L_s. This antenna model has its E-plane in the *xy*-plane ($\theta = 90^o$), and its H-plane in the *yz*-plane ($\phi = 90^o$).

Table 4.1 Antenna Parameters

Symbol	***dg***	L_f	L_s	***W***	W_f	W_g	***k***
Value (mm)	5.42	18	35	13	0.58	12	6
Symbol	***d***	***a***	***b***	***c***	r_c	A_t	r_h
Value (mm)	0.915	4.8	0.35	4	6	0.27	1.98

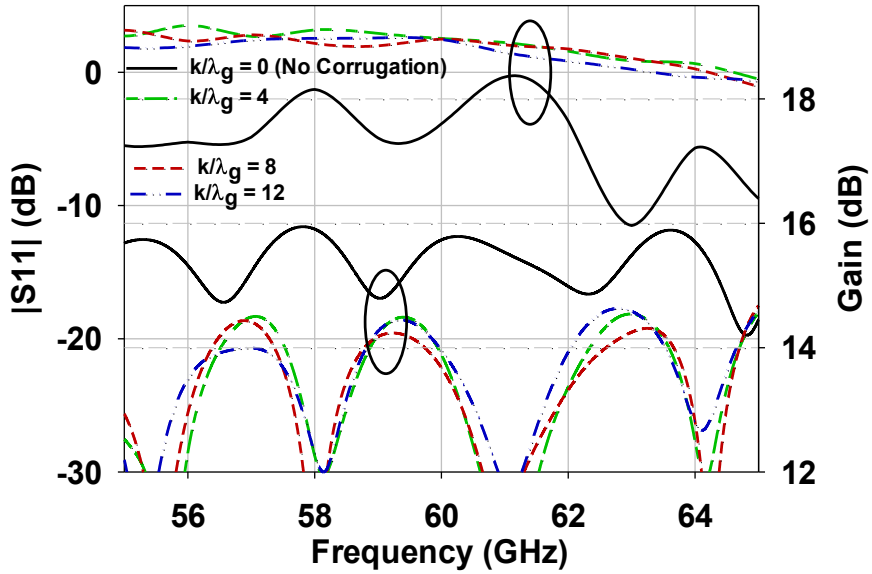

Figure 4.14 The effect of varying the period constant of the sine-corrugation (k) on S_{11} and on antenna gain.

The initiate a starting point for designing this antenna model, Eq. (4.4) identifies the desired operating band [121].

$$0.005 \leq h = \frac{c_o}{f_1(\sqrt{\varepsilon_r}-1)} \leq 0.03 \tag{4.4}$$

where c_o is the speed of light and ε_r is the dielectric constant of the substrate. Basically, Eq. (4.4) is an empirical approach to determine the thickness of the substrate (h), which is

associated with an operated wavelength. In Eq (4.4), the optimized range of 0.005 to 0.03 was experimentally determined by Yngvesson et al [121]. However, to operate an AFTSA-SC at 60 GHz we found this optimized formula for h defines the lowest operating frequency f_1 of the desired band. The frequency f_1 represents the first resonance frequency, which is responsible for 20% of the overall antenna bandwidth. The optimized parameters are presented in Table 4.1.

The edges of the AFTSA consist of periodic sine wave shaped corrugations. The corrugation is a new flexible profile described as $A_t \sin kt$. The effect of the sine corrugation was studied for two parameters: the period k and the amplitude A_t. Figures 4.14, 4.15, 4.16, and 4.17 depict the impact of the sine wave corrugation on the input impedance, on the antenna gain, and side lobe level for E- and H-plane by varying the period and the amplitude, respectively. Basically, when k increases, the sine wave shrinks. As shown in Fig. 4.14, when *k=0* the antenna is considered to be without corrugation and the antenna has a poor S_{11} response and lower gain. An increase in k varies the distance between each ripple of the sine-corrugation, changing the capacitor coupling between them and hence enhancing the S_{11} response and the antenna gain. Moreover, the constant k influences the characteristic of the radiation pattern of the E- and H-plane, and can be adjusted to optimize the sidelobe level, as shown in Fig. 4.15. Variation of the constant A_t leads to a change in the coupling area between each period.

In Fig. 4.16, the sine-shaped amplitude constant A_t is represented by A_t/λ_g (10^{-2}), which is varied from 9.4 to 18.9. This A_t constant has a strong influence on the antenna gain, and is used to optimize the maximum gain at $A_t = 0.132/\lambda_g$. On the other hand, as shown in Fig. 4.16, A_t has a limited effect on the S_{11} response. The two

parameters, A_t and k, decrease the reflection coefficient towards the feed line, which in turn guides the propagating wave in the desired direction, thereby increasing the antenna gain. The radiation pattern is affected by these changes as well. Based on iterative simulation, we found that A_t and k have empirical guideline ranges of $\lambda_g/3 \geq A_t \geq \lambda_g/10$ and $k \geq 1.5\lambda_g$. These ranges which establish the starting point for optimizing the reflection coefficient and antenna gain, as well as reducing sidelobe level, as showing in Fig. 4.17.

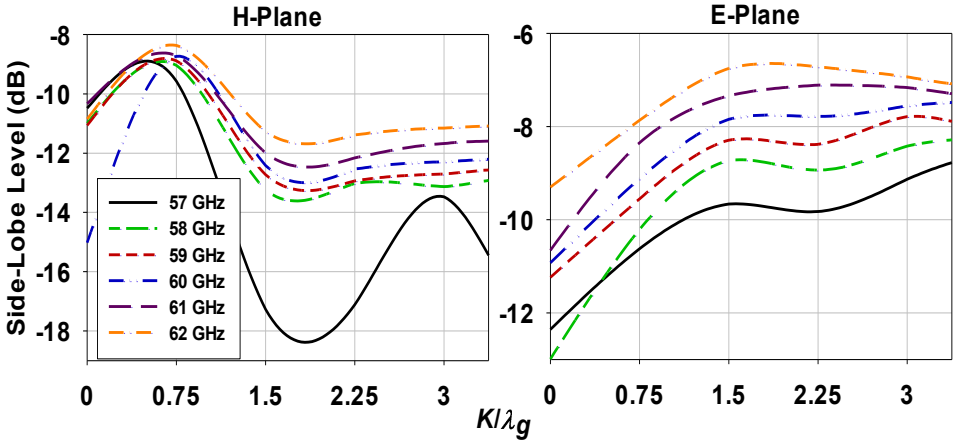

Figure 4.15 The impact of varying the period constant k on the sidelobe level.

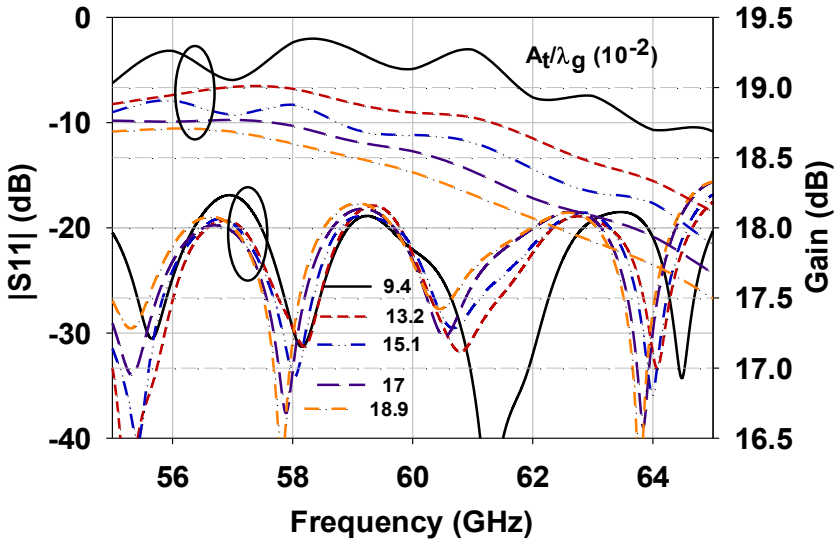

Figure 4.16 The effect of varying the amplitude constant of the sine-corrugation (At) on S11 and antenna gain.

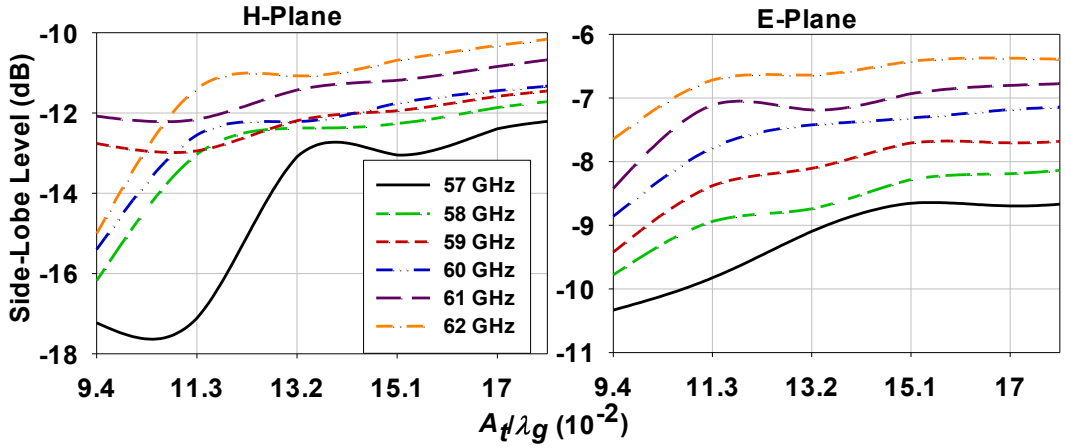

Figure 4.17 The impact of varying the amplitude of sine-wave and A_t on the sidelobe level.

The proposed AFTSA-SC antenna is compared to two other AFTSA antennas, as shown in Fig. 4.18. The dimensions of the AFTSA rectangular corrugation (RC) are length $l_c = 0.134\lambda_o$, width $w_c = 0.1\lambda_o$, and pitch $p = 2w_c$. The length of the antenna is L=5. 3 cm, and the substrate width is W=13 mm.

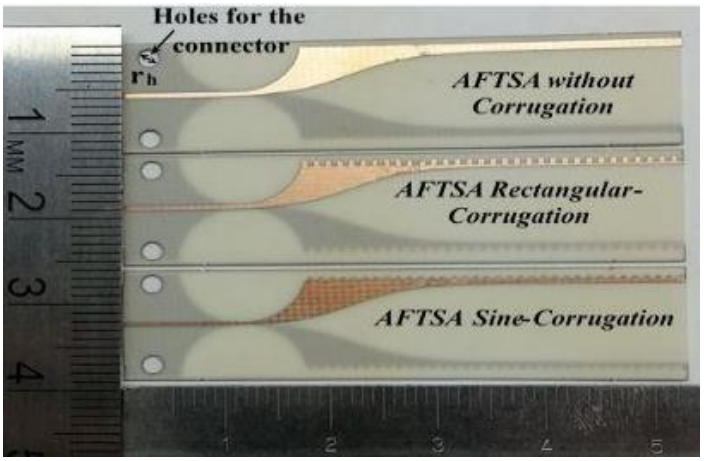

Figure 4.18 Photographs of three antenna configurations of the antipodal Fermi tapered slot: with sine-shaped corrugation, with rectangular corrugation, and without corrugation.

Fig. 4.19 illustrates the comparison of the return losses $|S_{11}|$ and the gain of three antenna configurations, including the measured results of the $|S_{11}|$ for the three antenna configurations and the measured gain of the AFTSA-SC. It can be observed that the

impedance matching responses are improved by the corrugations, as was expected. In addition, the $|S_{11}|$ response of the AFTSA-SC antenna is less than -18 dB and more stable over the band of 55-65 GHz. Meanwhile, the measured results of the S_{11} and the gain agree well with the simulated results of the AFTSA-SC. Therefore, the proposed antenna successfully achieves considerable improvement for the return loss and gain, compared to the other two antenna configurations over the entire selected frequency band.

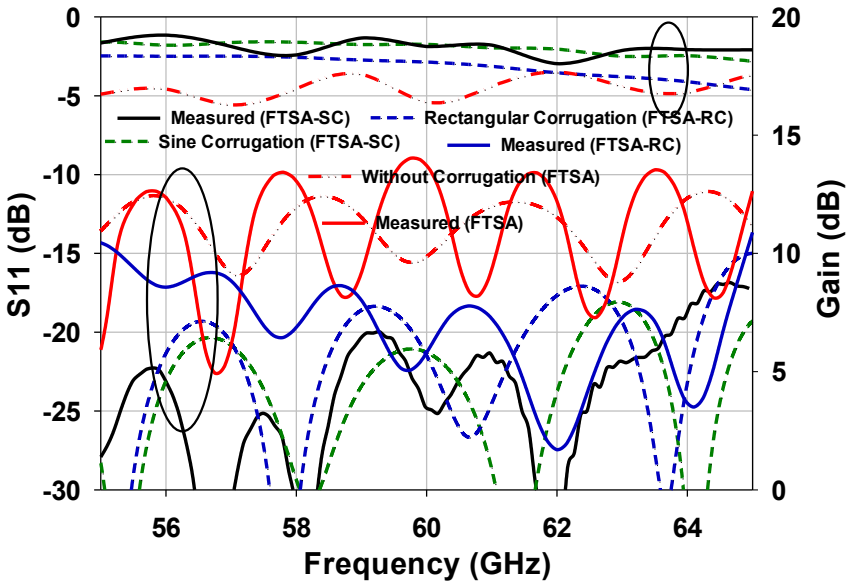

Figure 4.19 Measured and simulated results comparison of the proposed antipodal FTSA-SC and two other FTSA antennas.

In Fig. 4.20, the measured and simulated radiation pattern of the AFTSA-SC is compared to the other two antenna results at 59 to 61 GHz for the E- and H-planes. The observed radiation patterns at 58 to 61 GHz show a good agreement between the experimental results and the CST-MWS simulated results. The gain has been improved and low sidelobe levels are obtained for both the E- and H-planes using the sine corrugation structure.

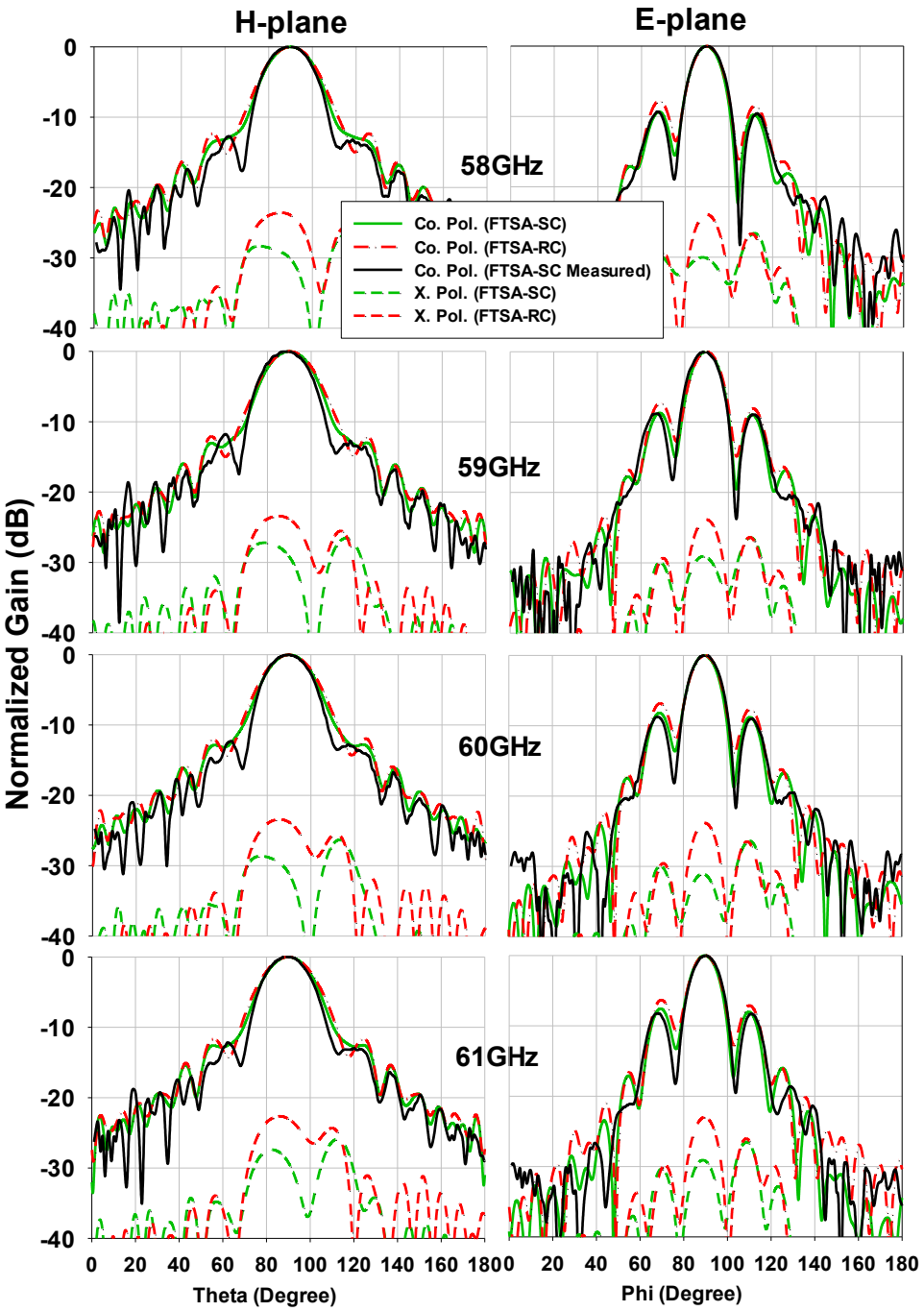

Figure 4.20 Measured and simulated radiation pattern at 58-61 GHz for the E- and H-planes.

It can be observed that the proposed antenna exhibits endfire radiation characteristics. The experimental results show that modifying the sine wave corrugation leads to control of the shape of radiation patterns in the E- and H-planes. The proposed

antenna thus presents stable radiation characteristics within the ISM band. As a result, the antenna with sine-shaped corrugation achieves a better return loss of <-20 dB compared with <-15 dB for the rectangular-shaped corrugation (RC) case and a 2 dB higher gain on average over the ISM band. The AFTSA-SC obtained 2 to 5 dB less side lobe levels with about 7 dB reduction in the cross-polarization over the operating band compared with AFTSA-RC.

4.5 Dual and Circular Polarized AFTS-SC

This section presents two antennas with different polarization. The first is a dual linearly polarized antenna, and the second is a circularly polarized antenna. The proposed antennas are mainly designed for millimeter-wave imaging detection system applications. In wireless communication systems, dual polarized antennas typically have two separate ports to distinguish between different information and/or increase channel capacity, etc. However, for imaging detection applications, we are not interested in separation of information, but rather, information recognition for the target image. The single-feed dual-polarized antenna is based on a combination of horizontal and vertical polarized antennas that increase the target's image intensity contrast. This polarization diversity makes it possible to obtain additional information about the surface shape and material. As well, the polarization diversity evenly increases the target image resolution's pixel intensity based on the imaging detection systems [122] - [124].

4.5.1 Dual-Polarized AFTSA-SC

A novel model of the antipodal Fermi-Tapered slot antenna is the creation of a dual-polarized antenna. This dual-polarized is a pair of linearly polarized antennas; it consists of two layers of AFTSA-SC aligned orthogonal to each other in a cross-shape. The

horizontal layer contains a microstrip feed line - this layer consists of the top radiation element which can easily be converted to a microstrip line, and the radiation element on the other side of the substrate that can be shaped into the ground plane of a microstrip line. The designed antenna produced two co-polarizations in the elevation and azimuth planes, and the cross polarization in the diagonal plane (± 45°).

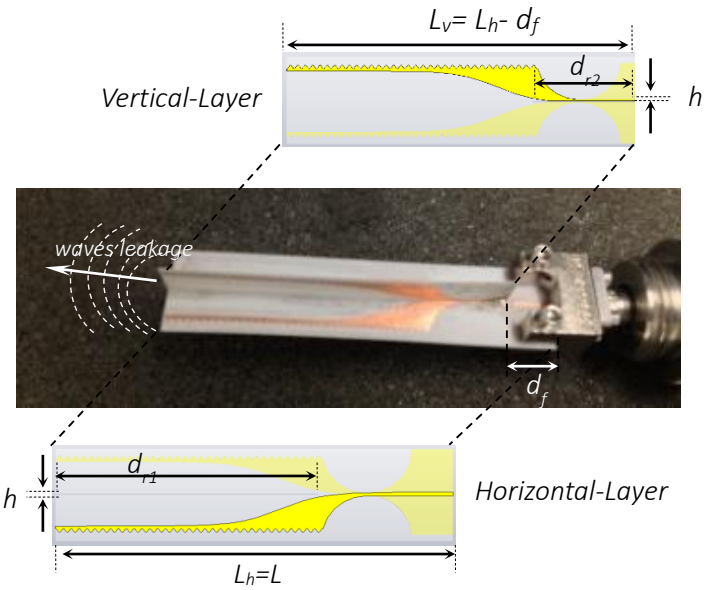

Figure 4.21 Geometry configuration of Fabricated Dual-Polarized antipodal Fermi tapered slot with sin-corrugation

Consequently, as illustrated in Fig. 4.21, the radiating elements of the vertical and horizontal layers of the dual-polarized antenna are faing each other perpendicularly. The single element of the proposed antenna exhibits the same design as in Fig. 4.13, therefore, the optimized parameter is presented in Table 4.1. Meanwhile, Fig. 4.21 shows the horizontal-layer (H-layer) has a groove, dr1= 35 mm, and with a width, h = 12 mil, is to make enough space to slide the vertical-layer (V-layer) which has a smaller groove, dr2= 12 mm, and the same width (h), in order to insert it inside the horizontal-layer. The length of the vertical-layer is shorter by *df* = 6 mm from the horizontal feed line side. Furthermore,

the feeding line is excited horizontal element while the vertical element is attached at the beginning of the horizontal-slot. The excitation mechanism of the V-layer is excited by horizontal-feed line, this feed line is responsible for splitting the current field distribution in parallel to both the H and V-layer. Therefore, the dual - shape of Fermi TSA-SC is a dual polarized maintaining the same received power whether the transmitter antenna is aligned vertically or horizontally.

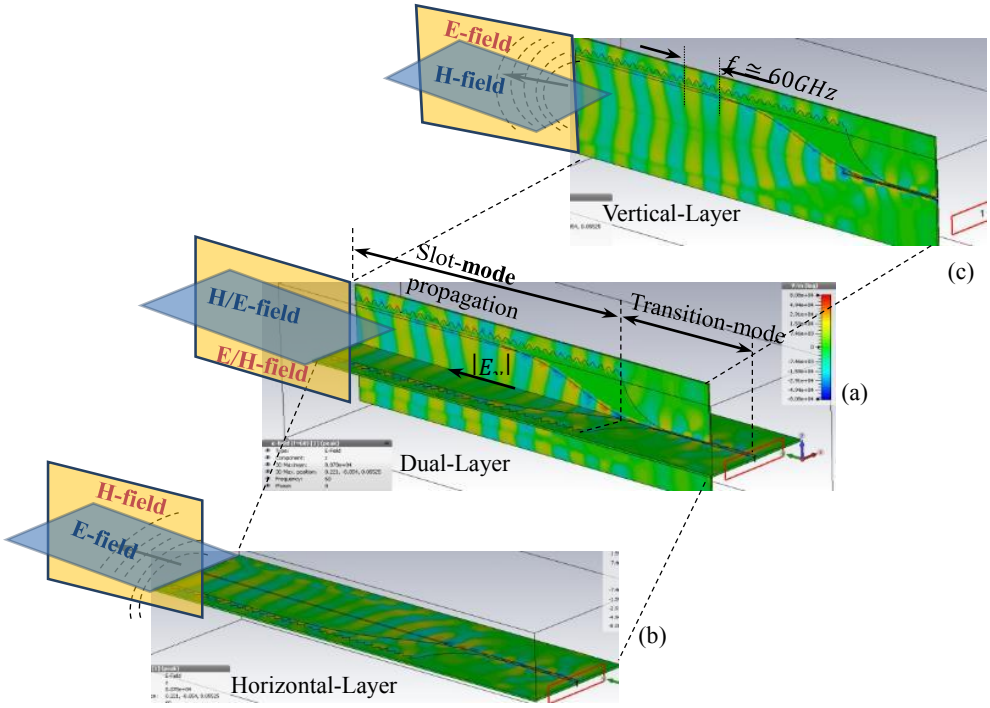

Figure 4.22 Electric field current distribution at 60 GHz: (a) V-layer and H-layer are both visible, (b) V-layer is hidden and H-layer is visible, and (c) V-layer is visible and H-layer is hidden.

The current distribution formally gives the physical behaviour of the antenna. In the CST-MWS simulator, the dual-polarized AFTSA-SC is investigated at 60 GHz. The antipodal structure contains two radiation elements: the top tapered slot element is fed-element radiators, while the bottom tapered slot is considered a ground-radiating element. Fig. 4.22 illustrates the visualization of the electric field current distribution at 60 GHz

supporting our argument for dual-polarized for the cross-shaped AFTSA-SC geometry with current distribution. As you can see, the propagation of the waves is in the direction of the excitation feed-line; in other words, the propagation behaviour is considered surface-wave leakage antenna. The single-feed is exciting both perpendicular slot-elements as a feed-merge for both H and E-layer. In addition, Fig. 4.22 (a) shows the E-plane current distribution which is presented as instantaneously linearly-polarized antenna, meaning the vertical and horizontal-polarized were both propagated from the V- and H-layers, respectively. The electric field current distribution concentrates on the slot-mode along the flared edges of the antenna and on the corrugated edges.

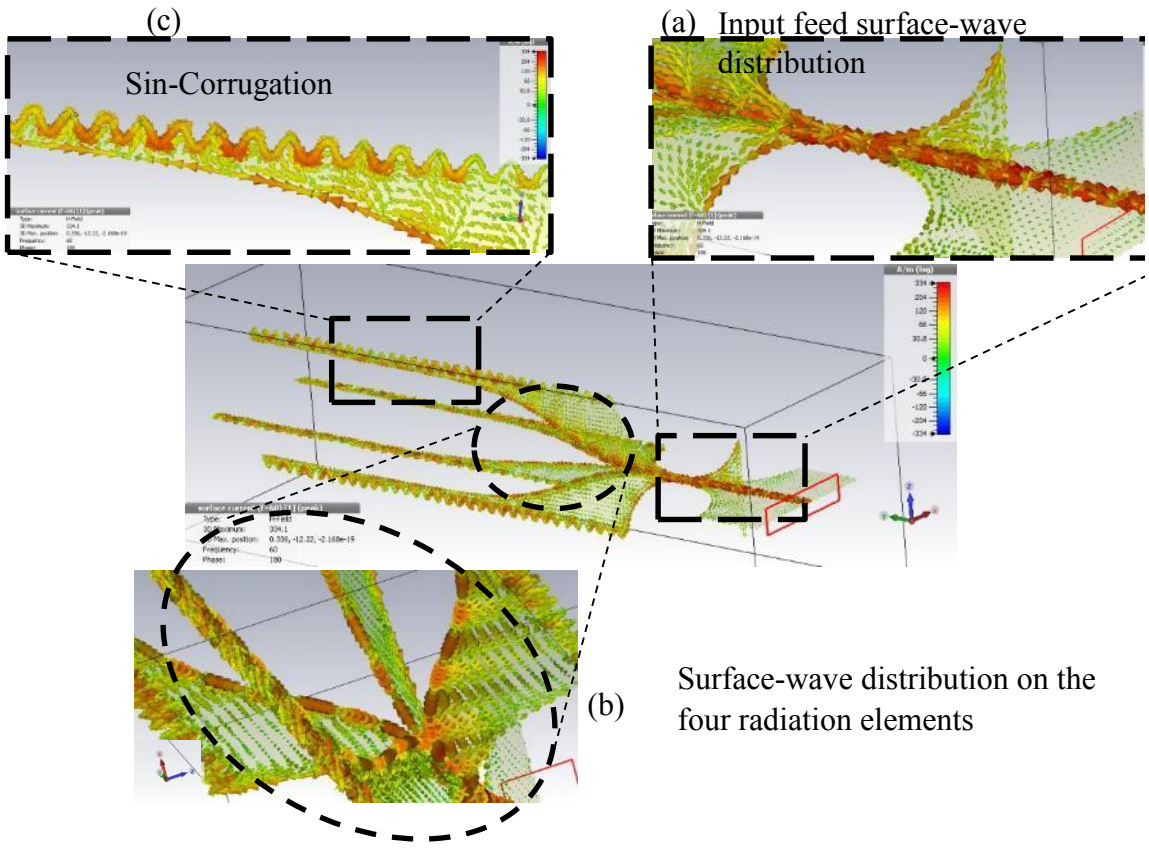

Figure 4.23 Surface-wave distribution at: (a) Sin-Corrugation, (b) Input feed and (c) four radiation elements.

The continuity of propagating wave behaviours along the tapered slot improves radiation directivity, and enhances matching impedance performance over a broad frequency range. Since the wavelength at 60 GHz is about 5 mm and the length of the AFTSA metal-radiator is about 40 mm, the leakage-wave behaviour can be figured out along the propagated current distribution; approximately 8-wave-cycles that include both positive and negative phase cycles are clearly observed among the flared edges. Furthermore, increasing the length of the antenna increases the number of traveling-waves, which are directly proportional to the antenna gain.

The current distribution that comes from the feed line splits into two pairs in the beginning of the antenna slot. One pair is horizontal pear-waves, as illustrated in Fig. 4.22 (b) - which presents the E-plane that propagates on the *xy*-plane. Meanwhile, the current distribution behaviours show that there is less effect of vertical layer and groove on the H-layer. Likewise, as is observed with the H-layer, the E-plane that propagates on the *zy*-plane has less effect on the current distribution that comes from the V-layer, as illustrated in Fig. 4.22 (c). As a result, the antenna proves that the horizontal and vertical field have a pair of linear-polarization components: both components have equal magnitude and no time-phase difference between them; they are also perpendicular to each other.

In order to further understand the AFTSA structure, its surface current distribution has been studied at 60 GHz, with the help of the simulator CST-MWS. The results are shown in Fig. 4.23. However, the surface current is distributed in the metal parts and the dielectric is not represented. Therefore, surface current distribution to find the propagation-wave mode of the antenna, which is screened as a frequency-independent that shows quasi-TEM mode is launched at the end of diverging tapered slots guiding each conductor pair

that forms the radiating sections. The current is distributed on the feed-line, as shown in Fig. 4.23 (a). The surface current is distributed on the four-element conductors - as observed, the intensity of the current density is equally distributed on the four flared slot edges of the model; this is illustrated in Fig. 4.23 (b). Meanwhile, the sine-shaped corrugation reduces the effect of current disruption on the sharp angled edges. In addition, the natural *sin*-corrugation shape creates smooth surface current distribution behaviour, as shown in Fig. 4.23 (c).

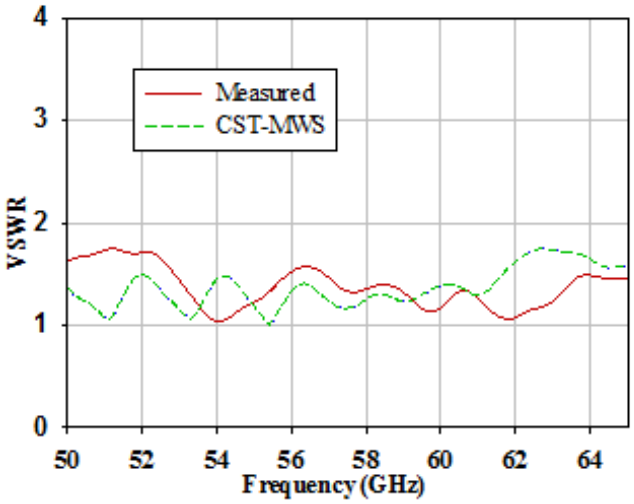

Figure 4.24 Measured and CST simulated VSWR, for the AFTSA-SC.

The simulated and measured results investigate the effect of different design parameters on the performance of the proposed Dual-polarized antipodal FTSA-SC. Fig. 4.24 illustrates the simulated and measured comparison of matching impedance presented with VSWR. The results exhibit good agreement, since both are below 2-VSWR over a band of 50-65 GHz.

The measured and simulated radiation patterns of Dual-polarized AFTSA-SC have been compared for the vertical and horizontal polarizations at 60 and 61 GHz, as presented in Fig. 4.25. The radiation pattern exhibits equal amplitude for vertical and horizontal

polarizations in measured and simulated results; in addition, the simulated results for both vertical and horizontal exhibit good agreement with measured results. Notably, at 60 GHz and 61 GHz, the HPBW in horizontal -polarization responses are less than those of HPBW in vertical -polarization responses. Meanwhile, in the experimental results, the radiation pattern for the H-plane exhibits asymmetrical behaviour to the E - plane. In summary, the radiation pattern of this structure model proves the antenna is linearly dual-polarized.

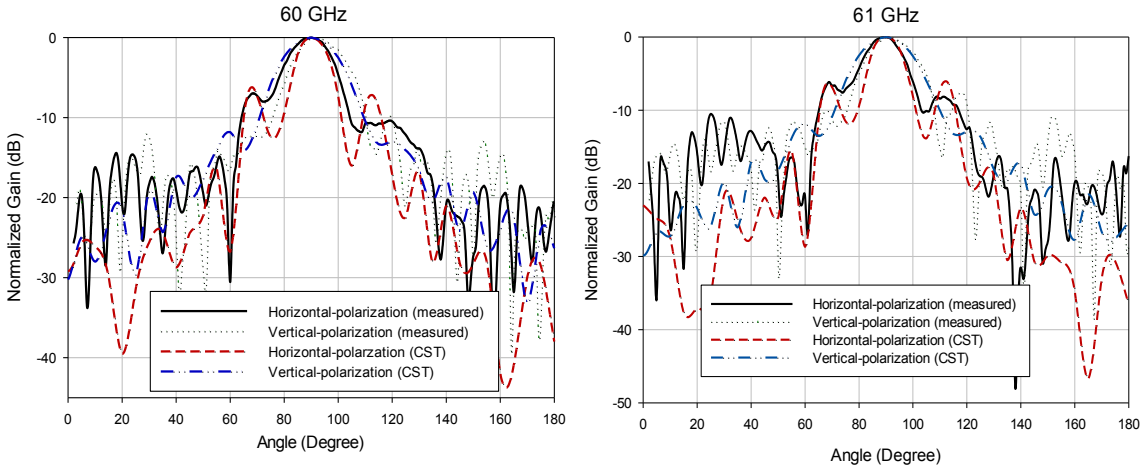

Figure 4.25 Measured and Simulated Radiation pattern results for AFTSA-SC.

4.5.1.1 Dual Polarized antenna detecting vertical and horizontal polarization signals

A point-to-point communication is conducted to demonstrate the capability of dual polarized antenna. Transmission coefficient measurements are carried out between dual-polarized AFTSA-SC and linear polarized AFTSA-SC antennas. Fig. 4.26 (a) shows both antennas in a line of sight alignment with 14 cm separation. Fig. 4.26 (b) shows the transmission and reflection coefficients' measurements. The maximum transmission coefficient between the two antennas appears when the linear polarized antenna is aligned, either vertically or horizontally polarized, as shown in Fig. 4.25 (c), and (d), which indicate co-polarization for both antennas. However, cross-polarization occurs at the minimum

transmission coefficient, as illustrated in Fig. 4.25 (f). This is occurred when either of the antennas is rotated by ± 45° off the co-polarization alignment.

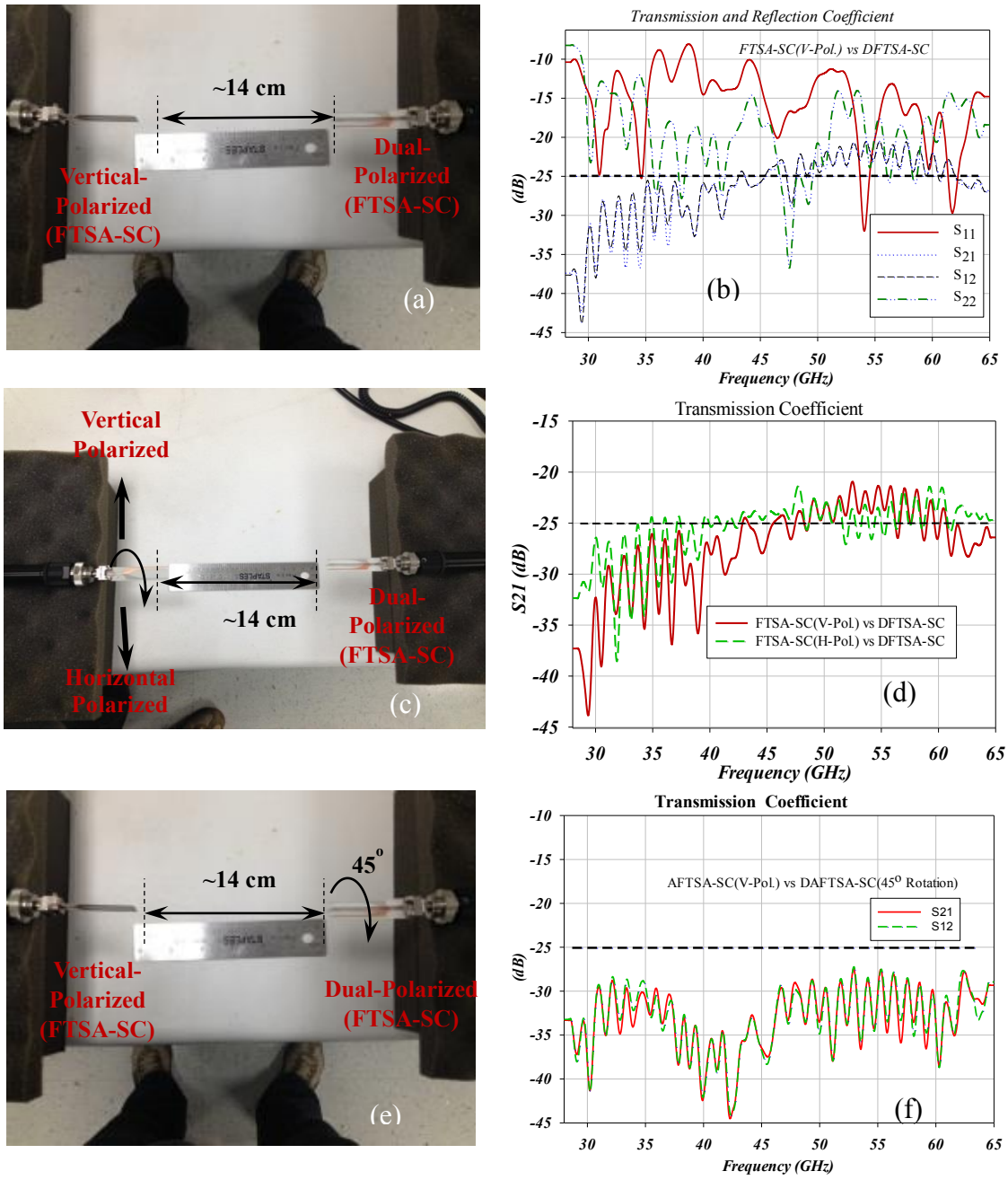

Figure 4.25 Point-to-point communications between Dual polarized AFTSA-SC and linear polarized, (a) photograph of both antennas in co-polarization alignment, (b) the transmission and reflection coefficient results, (c) photograph of prototypes, (d) measured results of the transmission coefficient, (e) either antenna is rotated by ±45° and (f) the corresponding results of case (e).

4.5.2 A 60 GHz Circularly Polarized AFTS-SC

PCB - TSAs are forms of traveling wave antennas, in which the tapering structure topology creates only a linear polarization, or dual polarization achieved with single or dual feed. The circular polarization can be achieved with a dual TSA, one oriented horizontally and the other vertically, with a 90 degree phase shift required between the feeding ports. Single feed circular polarized TSAs were not reported anywhere to the best of the authors' knowledge. This work presents a novel circularly polarized AFTSA-SC with single feed topology implemented design that is easy to fabricate. Furthermore, the CP-AFTSA-SC design can be constructed in RHCP and in LHCP, and the antenna is easy to be optimized to the desired characteristics.

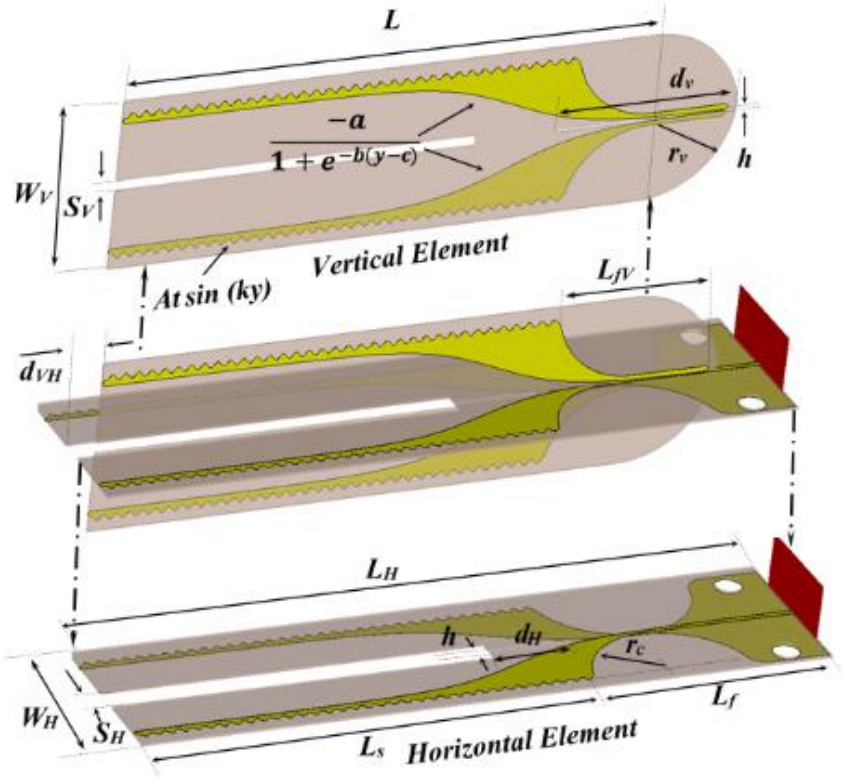

Figure 4.27 Geometry of the antipodal circularly polarized AFTSA-SC antenna.

Fig. 4.27 shows a 60 GHz circularly polarized antipodal Fermi tapered slot antenna with sin-corrugation (PC-AFTSA-SC) [C2]. This PC AFTSA-SC is designed in order to obtain the RHCP with dimensions to achieve high gain and high efficiency. In Fig. 4.27, the PC AFTSA-SC consists of a pair of AFTSA-SC elements orthogonally aligned to each other. Both the vertical and horizontal elements are fed by a single microstrip line with a 50 Ω input impedance. The single feed excites both elements simultaneously to obtain equal power distribution. The circular polarization is achieved by creating a 90° phase delay between the vertical and horizontal element. This delay is obtained from the slotted cutouts in the center of each element's substrate, to satisfy the 90° phase delay between the vertical and horizontal elements.

Table 4.2 The RHCP-AFTSA-SC optimized parameters

Parameter	L_H	L_f	L_s	W_H	W_V	S_H	S_V	r_c	r_v	a
Value (mm)	*51.5*	*17.7*	*34*	*13*	*13*	*2*	*0.8*	*6*	*7*	*4.8*
Parameter	d_H	d_v	d_{VH}	h	L_{fV}	At	k	b	c	
Value (mm)	*6.07*	*13.7*	*1.7*	*0.2*	*11.7*	*0.2*	*6.5*	*0.35*	*4*	

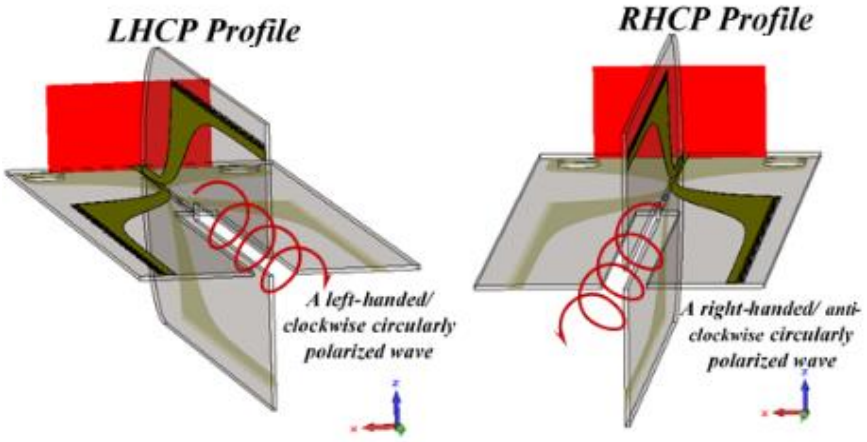

Figure 4.28 The architecture of RHCP and LHCP for the AFTSA-SC antenna.

The CP AFTSA-SC is simulated using a Rogers RT/Duroid 4003 substrate where $\varepsilon_r = 3.55$, tan $\delta = 0.0027$@ 10 GHz, and thickness = 0.2 mm. The overall antenna size is 51.5 mm × 13 mm. The optimized RHCP-AFTSA-SC parameter is presented in Table 4.2. Also, this antenna can be modeled to obtain a LHCP, as shown in Fig. 4.28. The direction of the circular polarization wave depends on the horizontal and vertical elements' feed line taper slot positions. When replacing both feed tapered slots on the right side of the aperture, the antenna generates a RHCP; if both feed tapered slots are replaced on the left side of the aperture, the antenna generates a LHCP, as shown in Fig. 4.28.

Fig. 4.29 shows the simulated RHCP axial-ratio (AR) of the CP-FTSA-SC antenna and the realized gain results of the RHCP and LHCP. In Fig. 4.29 (a), a wide circular polarization bandwidth of 3.8 GHz for an AR of less than 3dB is maintained across a band of 59.1-62.9 GHz. Furthermore, Fig. 4.29 (b) shows the results of the RHCP and LHCP realized gain, illustrating that the CP antenna is RHCP dominant than LHCP with 9 dB in a different range of gain.

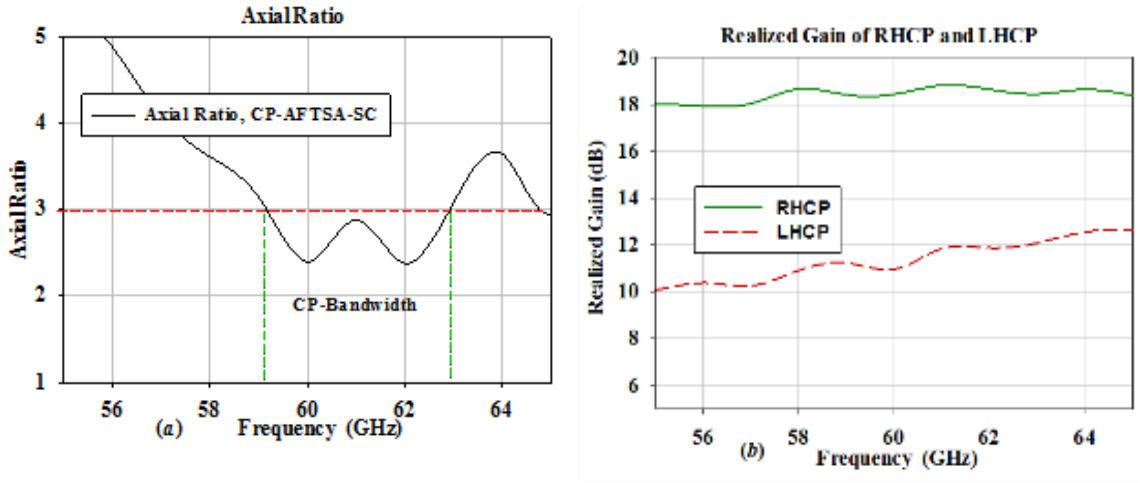

Figure 4.29 (*a*) Simulated axial ratio of RHCP and (*b*) realized gain at RHCP and LHCP of the CP-FTSA-SC antenna.

The CP-AFTSA-SC prototypes are fabricated using an LPKF etching laser machine. The Photographs of the CP-AFTSA-SC RHCP design prototypes are shown in Fig 4.30, which also shows a top and bottom view of both the horizontal and vertical elements. The laser machine cuts slots through the substrate, where the vertical element is cross aligned, and it is slid through the grooved slot of the horizontal elements, then the feed line of the vertical element is soldered to the horizontal element feed line.

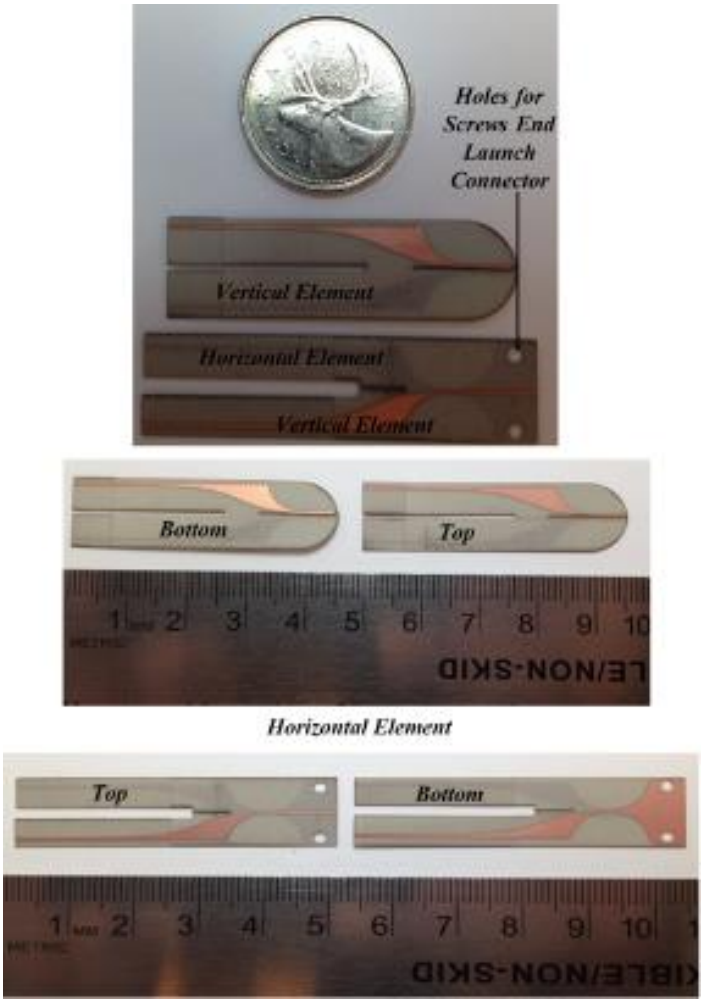

Figure 4. 30 Photographs of the CP-AFTSA-SC prototypes, horizontal and vertical elements RHCP design.

Fig. 4.31 shows the setup of the reflection coefficient measurement for the prototype, the simulated and measured reflection coefficient S_{11} results of the CP-AFTSA-

SC, and the linear polarization for AFTSA-SC elements. The reflection coefficient measurement conducted using an Agilent network analyzer PNA (N5227A) at a band of 55-67 GHz, and the antenna is connected using Anritsu Test Fixture (3680V). The vertical antenna element is inserted and soldered at the feed line connection to the horizontal elements, and a piece of foam is attached to the antenna, as indicated in the Fig. 4.31 (a), to maintain alignment of the vertical and horizontal elements.

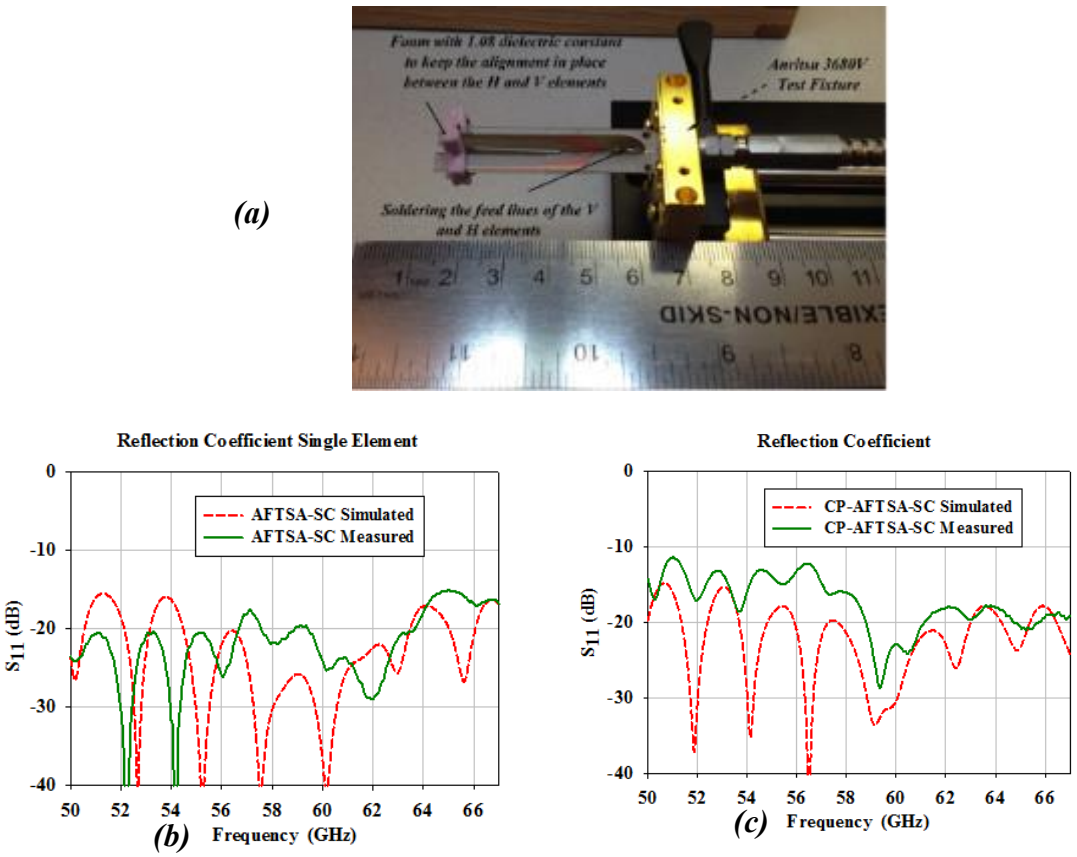

Figure 4.31 Illustrated: (a) the reflection coefficient measurement of the prototype setup, the simulated and measured reflection coefficient S_{11} results of (b) the CP-AFTSA-SC and (c) linear polarization for AFTSA-SC elements.

Fig. 4.31 (b) shows the reflection coefficient of the single elements of the AFTSA-SC. The antenna bandwidth defined as S_{11} < - 10 dB covers the entire band of 55 - 67 GHz. There is a good agreement between simulated and measured results. Fig. 4.31 (c)

shows a comparison between the measured and simulated reflection coefficients S_{11} for the CP-AFTSA-SC design. The simulated and measured results show the CP-AFTSA-SC exhibits an impedance bandwidth for S_{11} < - 10 dB over the entire band of 55 - 67 GHz. In addition, some fabrication imperfections, including misalignment between elements and soldering, might cause a discrepancy between simulated and measured prototypes.

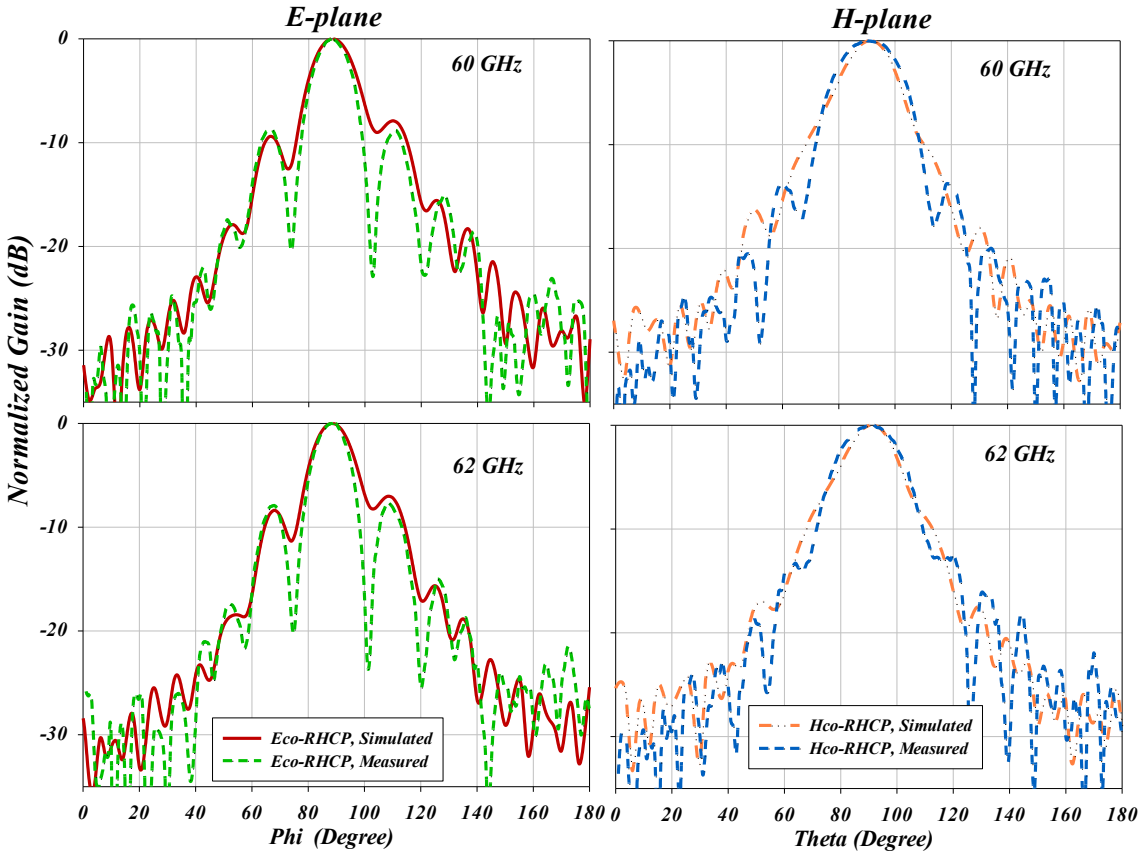

Figure 4.32 Measured and simulated radiation patterns of the PC AFTSA-SC at 60 and 62 GHz.

Fig. 4.32 shows the radiation patterns of the PC AFTSA-SC at 60 and 62 GHz. The radiation patterns at the selected frequencies show a good agreement between the measured and simulated results Furthermore, a low sidelobe level of about -16.3 dB and -7.9 dB in the H- and E-plane, respectively, at 60GHz. The pattern has a symmetry radiation

pattern until about -15 dB. The AFTSA-SC exhibits endfire directive patterns with a HPBW of 18.7° and 15.4° in the H- and E-plane, respectively. Finally, the proposed antenna shows a stability and good radiation pattern for the whole range of the impedance bandwidth.

4.6 Multi Sin-Corrugation Antipodal Fermi Tapered Slot Antenna Loaded with a Spherical Lens

The AFTSA model presented in this section has a newly implemented corrugation design for antennas operating in the 60 GHz unlicensed band as in [C1]. A new multi *sin*-corrugation (MSC) is applied to increase the degree of optimization when the AFTSA antenna is loaded with a lens. Furthermore, the different patterns in the *sin*-corrugation enhance the radiation characteristic of the antenna. Thus, this model is able to enhance antenna directivity and matching, and reduces the sidelobe and backlobe levels.

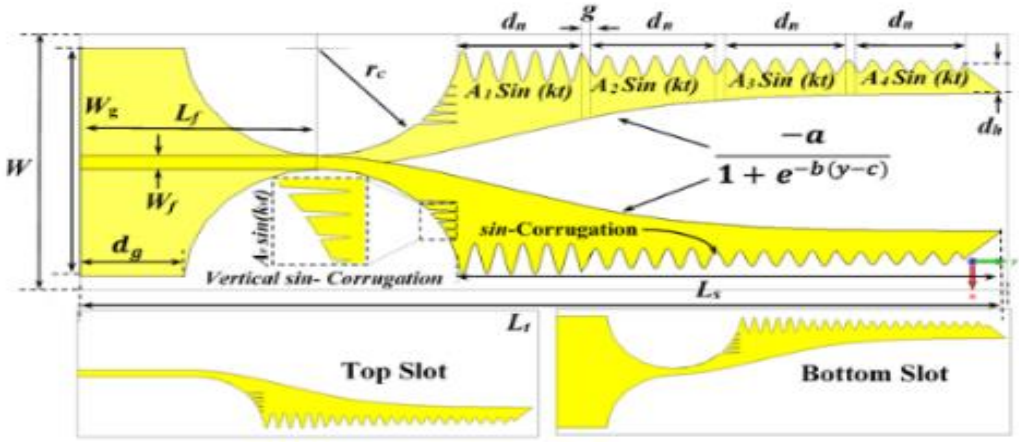

Figure 4.33 Proposed feeding element of AFTSA with multi sin-corrugation patterns.

A new grooved spherical lens (GS-Lens) is implemented and placed in the AFTSA-MSC antenna. A hemispherical lens (HS-Lens) is also used and compared with the proposed GS-lens. Moreover, the lenses are molded with polymethyl methacrylate (PMMA), a lightweight transparent thermoplastic with a relatively low dielectric constant. The length

of the antenna with a GS-lens is 8 λ_o (λ_o = 5mm at 60 GHz), which is relatively the same length as with HS-lens. The design of the GS-lens helps to deflect the propagating waves in the end fire pattern much better than the HS-Lens with a 5dB gain enhancement.

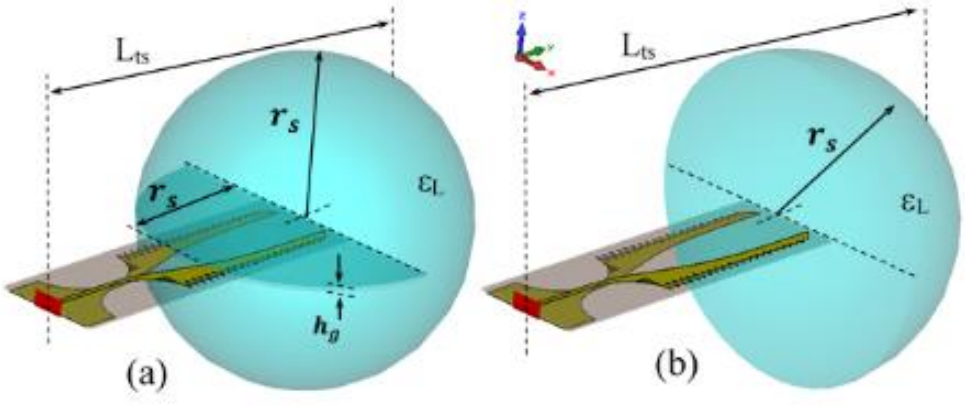

Figure 4.34 MC-AFTSA loaded with: (a) grooved spherical lens, (b) hemispherical lens.

Table 4.3 Optimized dimensions of the antenna.

Symbol	***dg***	L_f	L_s	W	W_f	W_g	***kv***	***A3***	d_n
Value (*mm*)	3	7	16	9	0.46	8	20	0.33	3.66
Symbol	d_h	***a***	***b***	***c***	r_c	***g***	r_h	***A4***	***Lts2***
Value (*mm*)	1	3	0.4	4.5	4	0.27	1.98	0.27	44.2
Symbol	***Av***	L_t	L_{ts}	h_g	r_s	A_1	A_2	***k***	
Value (*mm*)	1.5	27	39.7	0.36	12.7	0.67	0.45	9	

The configuration of the proposed antipodal Fermi tapered slot antenna is shown in Fig. 4.33. The AFTSA-MSC is designed on a thin 20 mm RO4003 (ε_r = 3.55, $tan\delta$ = 0.0027) substrate. A 50Ω microstrip feed line with a width of W_f, and a grounded width of W_g, is gradually fed to the circular slot r_c (= a + d_h), that is a partially corrugated sine wave shape defined by $A_v sin\ (k_v t)$ - where A_v is the amplitude, k_v is the period, and t is the fraction of the variable x-axis. This slotted circle feeding is used as a balun for impedance matching. The corrugated edges along the y-axis are formed in four sine wave patterns of $A_n sin(kt)$

with different amplitudes (A_1, A_2, A_3 and A_4) and a period (k). $f(y) = \frac{-a}{1+e^{-b(y-c)}}$ is the Fermi-Dirac function, where a is an asymptotic value of the half tapered aperture, and b is the gradient at inflection point c.

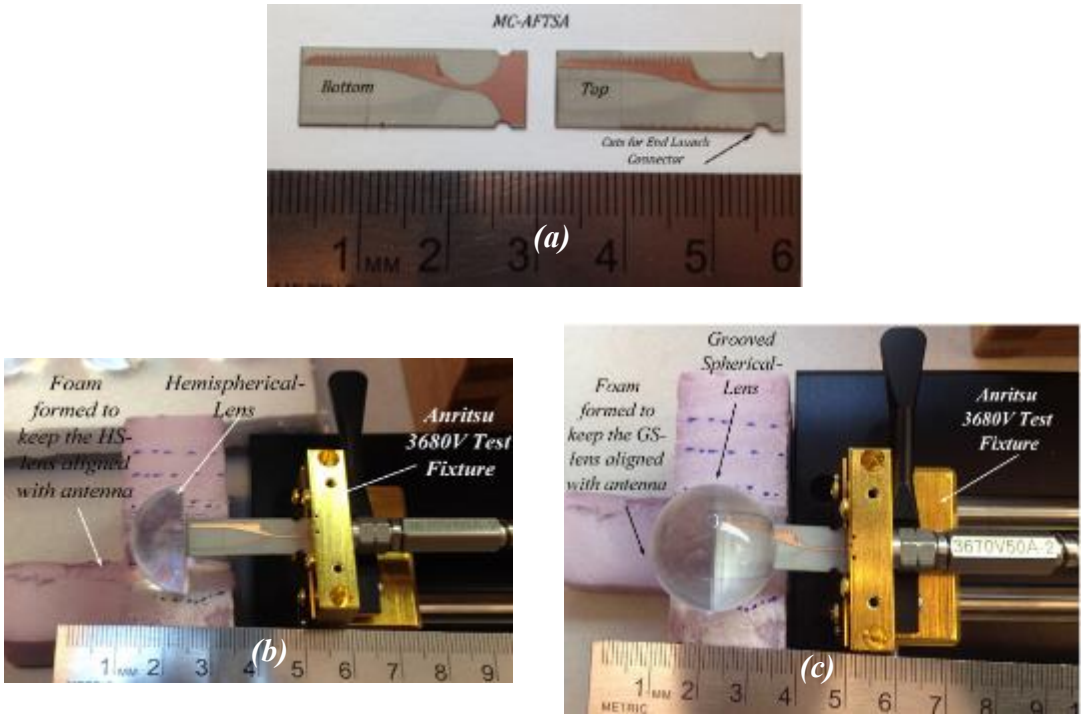

Figure 4.35 (*a*)**:** Top and bottom layer photographs of the proposed AFTSA-MSC design, and measurement setup when (*b*): AFTSA-MSC is loaded with a hemispherical lens and (*c*): AFTSA-MSC is loaded with a grooved spherical lens.

The proposed grooved lens and the comparable conventional hemispherical lens are shown in Fig. 4.34. Both lenses are simulated incorporating PMMA material with a dielectric constant of $\varepsilon_L \approx 2.6$, and a loss factor of $tan\delta \approx 0.0026$ at 60 GHz. In addition, the radius (r_s) is the same for the GS- and HS-lenses. The AFTSA-MSC antenna is placed at the center of the HS-lens' flat end, as shown in Fig. 4.34 (b). Meanwhile, as seen in Fig. 4.34 (a), the AFTSA-MSC antenna is inserted in the groove up to the center of the GS-lens. Both antenna feeds are modeled to excite the TE mode wave at the rear end port, as shown in Fig 4.39. The optimized dimensions of the antenna are listed in Table 4.3.

The AFTSA-MSC design is fabricated by a LPKF ProtoLaser. Photographs of the proposed AFTSA-MSC design are shown in Fig. 4.35. Views of the top and bottom layers are shown in Fig. 4.35. (*a*). The reflection coefficient measurement setups when AFTSA-MSC is loaded with a hemispherical lens and when AFTSA-MSC is loaded with a grooved spherical lens are illustrated in Fig. 4.35, (b) and (c), respectively.

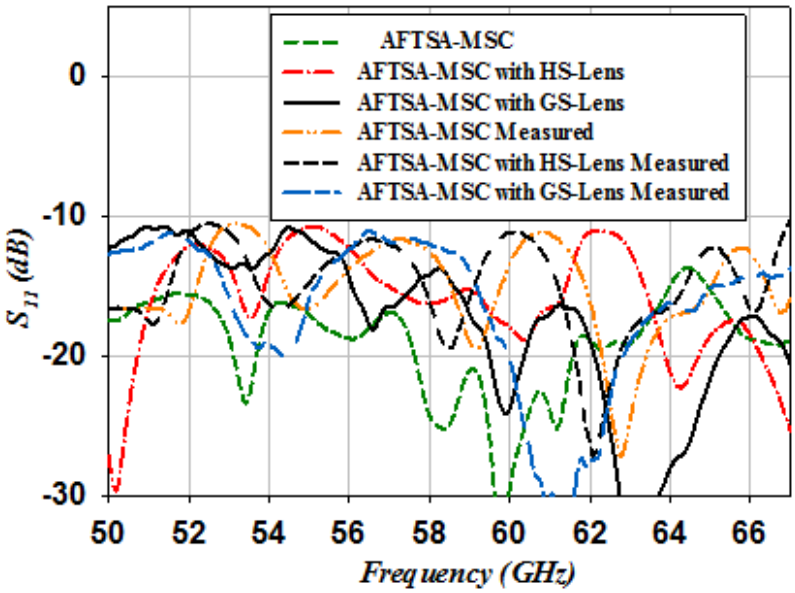

Figure 4.36 Illustrated: a comparison of the measured and calculated reflection coefficients for: AFTSA-MSC, AFTSA-MSC with HS- lens, and AFTSA-MSC with GS-lens.

The results for the AFTSA-MSC loaded with a hemispherical (HS) lens, and the AFTSA-MSC loaded with a grooved spherical (GS) lens are compared. A full wave analysis is carried out and performed within the time-domain solver of the CST Microwave Studio 2014. The return loss (S_{11}) of measured and simulated results for the three antenna types are presented in Fig. 4.36. The S_{11} for all responses is <-10 dB indicating a wide bandwidth covers the band from 55 - 67 GHz. A reflection coefficient loss deterioration is observed

when the antenna is loaded with the hemispherical lens. On the other hand, there is a better matching response when the antenna is loaded with the grooved spherical lens.

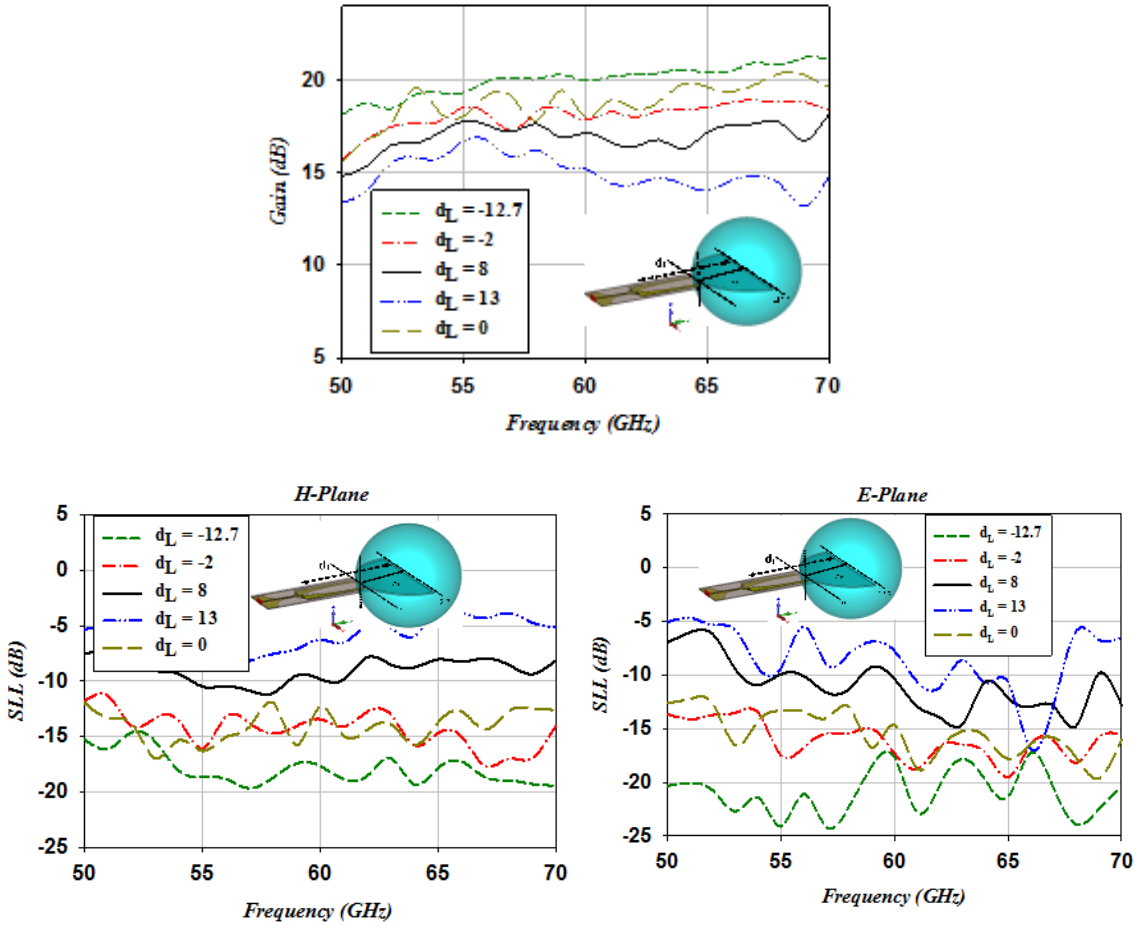

Figure 4.37 The impact of varying the inserting distance through the grooved spherical lens.

The proposed design of the AFTSA-MSC with a GS-lens achieves a high normalized gain of 20dB at 60 GHz, which is 5dB higher than the two other antennas. The scattered field is very high for the antenna loaded with an HS-lens, since the antenna radiation fields are facing a flat end side of the HS-lens. Meanwhile, inserting the antenna in the groove absorbs the scattered field in the end fire antenna direction. This makes the proposed antenna loaded with a grooved spherical lens capable of increasing the antenna gain and

decreasing the return loss. Extensive parametric studies of corrugation amplitudes $A1$, A_2, A_3 A_4, A_v, and periods, k, and k_v, are carried out using CST-MWS to investigate the effect of multi-corrugation on the grooved-lens antenna. The optimized dimensions of the proposed grooved lens antenna prototype are presented in Table 4.3. These multi-corrugation variables provide a further scale in optimizing the antenna when insert to a grooved lens in order to obtain a low sidelobe in the E- and H-plane, better matching impedance, and high gain performance.

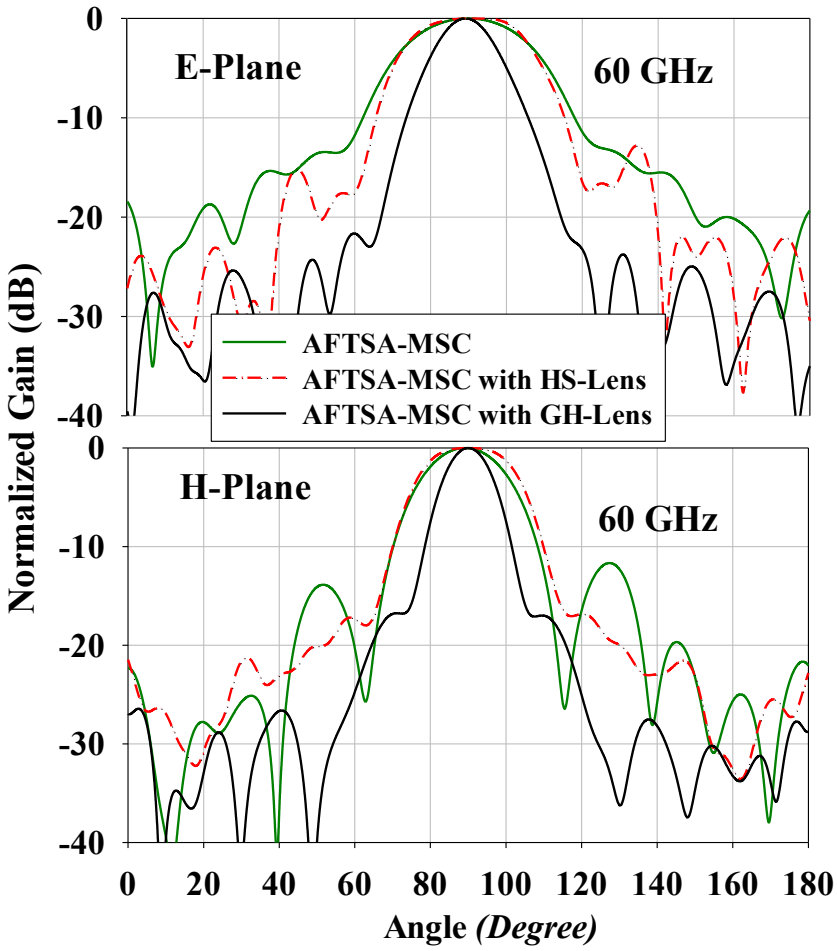

Figure 4.38 E – and H –plane radiation patterns comparison between the AFTSA-MSC without a lens, with an HS-lens, and with a GS-lens, at 60 GHz.

In further investigation of antenna parameters, d_L represents the inserting distance. Where $d_L = 0$, the AFTSA-MSC was placed on the edge of the lens, and where $d_L = -12.7$, the antenna was inserted into the center of the grooved spherical lens. The insertion position of the antenna is an important parameter. In order to understand the impact of d_L on the sidelobe level in the E- and H-planes, and antenna gain, d_L is varied from -12.7 to 0, and the results of this study are illustrated in Fig. 4.37. As a conclusion, the optimum inserting distance is at $d_L = -12.7$, which makes the design help deflect propagating waves in the end fire pattern.

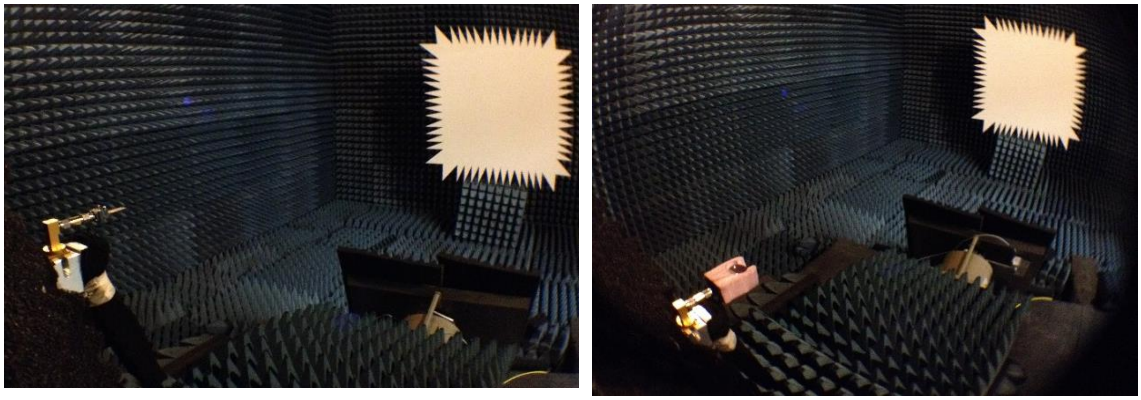

Figure 4.39 The photographs of the measurement setup of MC-AFTSA design, and MC-AFTSA is loaded with a grooved spherical lens and fixtured with a foam.

The radiation patterns at 60 GHz for the three antennas in the E–and H–plane are presented in Fig. 4.38. As shown, the groove in the GS–lens narrows the H–plane field. The HPBW reaches 18.5° and 13° in the H–plane and E–plane, respectively. Moreover, the sidelobe levels are below -20dB in both the E– and H–plane. It is noted that when the AFTS–SC is loaded with the HS–lens, it exhibits a similar track to each other. In the E-plane, the curve is almost symmetrical. The HPBW for the AFTS–SC with an HS–lens is 35° in the H–plane and 27° in the E–plane. Fig. 4.39 shows the photographs of the

measurement setup of MC-AFTSA design, and the setup of MC-AFTSA when loaded with a grooved spherical lens and fixtured with a foam. The measured E and H-plane radiation pattern at 60 GHz comparison between a MC-AFTSA and MC-AFTSA with GS-Lens shown in Fig. 4.40. The antennas exhibits pattern stability over the impedance bandwidth. The patterns shows an endfire directive in both E-plane and H-plane, the simulated results and the measurement results demonstrated a good agreement.

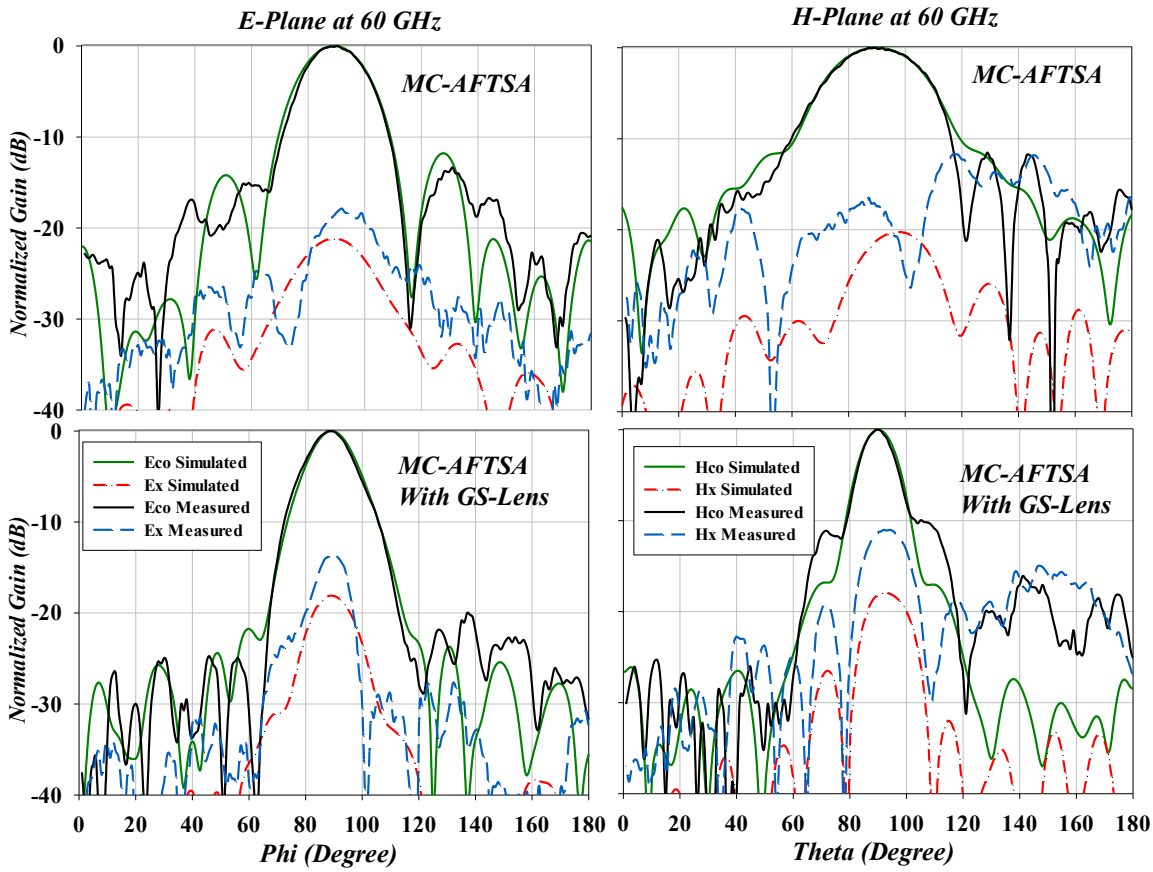

Figure 4.40 Measured and Simulated of the E – and H –plane radiation patterns comparison between the AFTSA-MSC without a lens and with a GS-lens, at 60 GHz.

4.7 Summary

In this chapter, multiple 60 GHz antenna sensors have been presented. A circular patch slot-fed antenna was loaded with a dielectric lens, and optimized for operation at 60 GHz; the prototype achieves a high measured gain of ~ 20 dB along the ISM band. The antenna impedance bandwidth is 3.5 GHz within the ISM unlicensed band and it is considered a low cost sensor with a simple structure and a small size of 12.412 × 10.5 × 27.553 mm^3. Then, A 60 GHz double-layer printed Yagi array antenna was proposed, and the measured impedance bandwidth was more than 5 GHz with a gain of 10 dB measured at 60 GHz. This Yagi antenna, implemented to obtain wide radiation efficiency, is potentially useful for MMW-MMIC packaging circuits, short range wireless communications, and imaging applications. High gain novel designs of antipodal Fermi tapered slot antennas have been implemented to fulfill optimum performance requirements for imaging/detection systems. First, a single element antipodal Fermi TSA with a sin-corrugated shape was implemented, with its corrugation reduces the discontinuity in tapered edges, leading to reducing the sidelobe lever and enhancing radiation characteristic. This design presents a broad bandwidth that covers the entire ISM band, along with a stable directive gain of 18.75 dB at 60 GHz. It is fabricated on a single layer with a low-cost PCB process. Second, a new design for a dual-polarized antipodal Fermi tapered slot antenna has been presented. This design employs a single feed for dual-polarized, horizontal, and vertical polarization, providing diverse polarity, which enhances image contrast in the imaging/detection system. Third, a novel single feed circular polarized AFTSA sine-shape corrugated antenna has been introduced. This CP design exhibits an experimental impedance bandwidth which covers the entire band of 55 - 67 GHz, and a wide circular polarization bandwidth of 3.8 GHz for an AR less than 3dB. Finally, a new

multi *sin*-corrugation AFTSA antenna has been introduced - the implemented design introduces a high level of optimization when the antenna is loaded with a grooved lens. The proposed design of the AFTSA-MSC with a GS-lens achieves a high normalized gain of 20 dB at 60 GHz, the sidelobe levels are below -20 dB in both the E– and H–plane, and a wide measured bandwidth covers the band from 55 - 67 GHz. The weight and size for these proposed 60 GHz antennas are small compared with traditional horn antennas - which can be integrated in a compact structure and impeded in low profile array to obtain a desired gain. Thus, with these characteristics, these antenna prototypes could be employed as a 60 GHz scanning probes for imaging / detection applications.

Chapter 5: A 60 GHz Switched beam Antenna Array

5.1 Introduction

In recent technologies, such as imaging detection systems, wireless communication, and radar systems, wideband MMW systems, able to steer beams to cover a desired area or to scan a target, are more in demand. Therefore, phased array antennas are essential for satellite radiometric applications, real time active or passive MMW imaging detection systems [125]-[129], MIMO applications [130], and radar anti-collision systems. A low cost phase shifter technique developed by Kim and Chang [43], [44], [46], [91], [131] introduced the piezoelectric transducer (PET) controlled phase shifter. This phased array offers a functional alternative to conventional phased arrays requiring more design complexity and fabrication expense. This technique is capable of generating a true time-delay phase shifter array over a wide frequency range with the advantage of simplicity and low cost even though the overall scanning range is at slow speed depending on the PET perturber.

This chapter introduces a 57-64 GHz, 1 × 16-element beam steering antenna array with a low-cost piezoelectric transducer (PET) controlled phase shifter. The first, an alternative power divider with a triangular-shaped feed which reduces the discontinuity caused by the feed line corners, is presented. The new concept presented splits the power in unequal division and enhances the distribution of the electric field with a high level of control at each feed line. The second, a 1 × 16-element beam steering phased array designed with a 60 GHz AFTSA-SC, and a single antenna designed to achieve a symmetric E-plane and H-plane radiation pattern, is then presented. The feed network design is surrounded by

electromagnetic band-gap (EBG) structures to reduce the surface waves and coupling between the feed lines. The third, a design of a circularly polarized 1 × 16-element beam steering phased array with and without EBG structures, was further investigated. These analytical results aid toward the development of new 60 GHz arrays for MMW applications which provide significant enhancements on system performance.

5.2 60 GHz Power Divider

A wide bandwidth array system requiring a wideband feeding network that distributes the power equally/unequally is a critical task in the MMW band design. The frequently used microstrip power dividers are Wilkinson, Rat-race, and T- or Y-junction power dividers. The Wilkinson is well known for a good isolation due to the resistor between the output ports, which allows three matched ports at the designed frequency [132], [133]. However, the quarter-wavelength branches at high frequencies are difficult to achieve as the wavelength decreases. The lag in performance caused by the resistor due to its parasitic effect in terms of equivalence in inductance and capacitance increases with increasing frequencies leading to increasing the losses and mismatch between the ports. The Rat-race (180° hybrid) with four-port structure has good isolation between output terminals as well, however, the drawbacks are the discontinuity causes radiation losses, and the long race line causes ohmic and dielectric losses, which are higher than the losses of the T- or Y-junction splitter. Furthermore, with the resistor at the fourth-port in the Rat-race and the one between output ports in the Wilkinson, there are not only losses, but it is also difficult to mount the resistor on transmission line at higher frequencies leading to expensive fabrication [134]. The planar T- and Y-junction power divider provides a simple three-port design structure, and it is easy to achieve equal or unequal power division [135],

[50]. The T- and Y-junction does not require high frequency resistors; although, the drawback is this power divider provides a low isolation between the output ports [132].

5.2.1 T-Junction and Y-Junction Power Divider Comparison

The discontinuity at the junction and at the bends of the microstrip line creates higher order modes and fringing fields, and that makes a stored energy accounted as a lumped susceptance. The T-junction and Y-junction power divider structures are shown in Fig. 5.1. The T-junction design has a high discontinuity at the junction and at the bends which leads to a mismatch between the ports and reduces the impedance bandwidth, however, with right angle chamfering such as V-shape at the junction and at bends there is a reduction in discontinuity [136]. In order to minimize discontinuity, the Y-junction design causes lower reflection at the junction and lower effect at the bends than the T-junction model, which achieves a wide impedance bandwidth and low insertion loss [137].

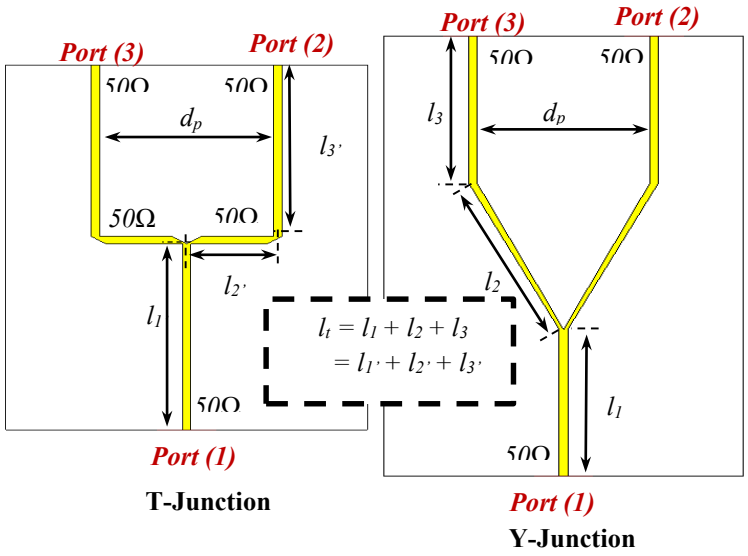

Figure 5.1 The T-Junction and Y-Junction power divider.

In Fig. 5.1 shows the optimized design at a 60 GHz center frequency for the T-Junction and Y-Junction power dividers. Both structures are designed on RO4003 (ε_r =

3.55, $tan\delta = 0.0027$@ 10GHz) which is 0.2mm in thickness, the distance between the output ports is $d_p = 2.14\lambda$ (wavelength $\lambda = 5mm$ @ 60 GHz), and the overall length of the microstrip line path is $l_t = 6.27\lambda$. The characteristic impedance of the input and the output ports are 50 Ω. The S-parameter results of the power dividers are shown in Fig. 5.2. The Y-junction yielded a reflection coefficient S_{11} of less than -15dB for even beyond the selected band (55 - 65 GHz), and the return loss S_{12} (or S_{13}) is approximately -3.7dB. Meanwhile, the T-junction yielded a S_{11} of less than -15dB for only the band of 58 - 64 GHz, and the S_{12} (or S_{13}) is about -4.3dB. These results indicate the Y-junction power divider achieved less return loss and a wider impedance bandwidth than the T-junction.

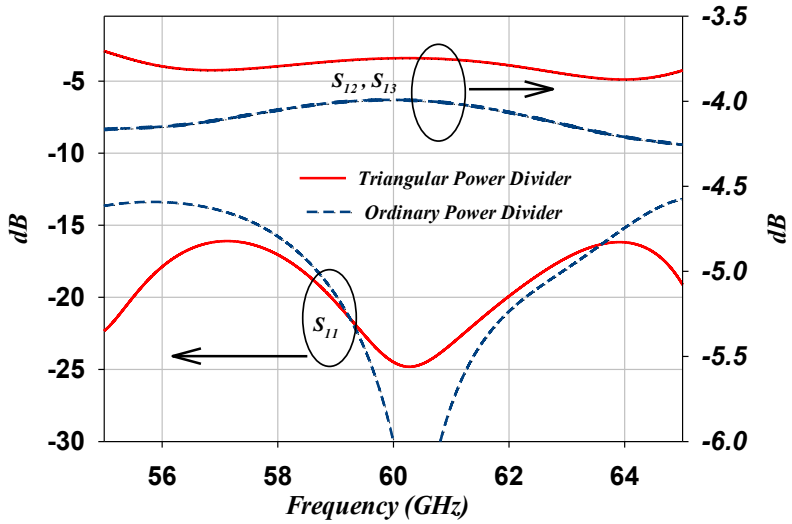

Figure 5.2 The S-parameter results of the T-Junction and Y-Junction power dividers.

In order to understand the behaviour of the T-Junction and Y-Junction power divider structures, the surface current distribution was calculated using CST-MS, as presented in Fig.5.3. The figure shows three different phases are monitored at 0°, 45°, and 90°, and the field distribution from the input port is divided into the two output ports. The time snapshots of the electric field clearly show the stronger reflection of the current field

caused by the splitting junction of the T-type; on the other hand, the reflected field is monitored lower at the Y-junction indicating low surface wave and low loss. This discontinuity of the T-junction type caused by the sharp angle at the junction and at the bends creates a form of wave propagation creating a surface current distribution that affects the feeding network performance, especially at MMW band. In addition, the surface wave between the output ports is lower with the Y-junction than with the T-junction, which is important for minimizing mutual coupling between elements. Therefore, this thesis proposes a Y-junction power dividor design with an insignificant loss as a practical choice to employ in a in a 1 × 16 -element MMW band, for its high performance compared to the T-junction model.

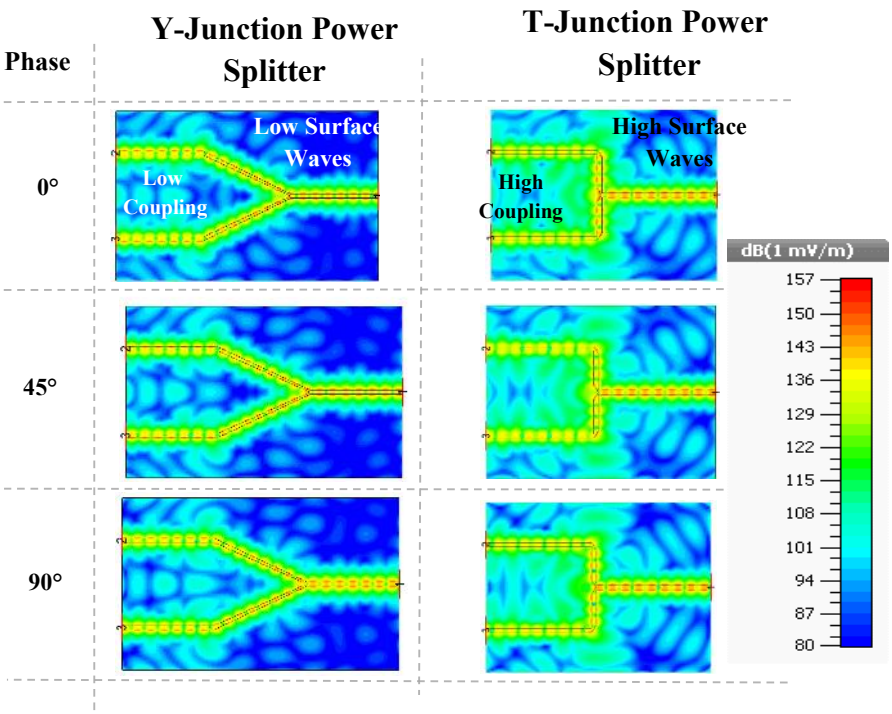

Figure 5.3 A time snapshot of the electric field for the T-Junction and Y-Junction power dividers in three cases, at 0^{o}, 45^{o}, and 90^{o}.

5.2.2 Unequal Y-Junction Power Divider

The Y-Junction power divider can be made with unequal power splits; a transmission line model of unequal loss that is less at the Y-junction is illustrated in Fig. 5.4. The triangular tapered line from the input line port to the output line port is applied in the Y-junction design splitter. The input port line Z_0 splits the tapered slot into two lines: Z_1 and Z_2. These Z_1 and Z_2 lines gradually merge into the output line Z_0 of port 2 and port 3, respectively.

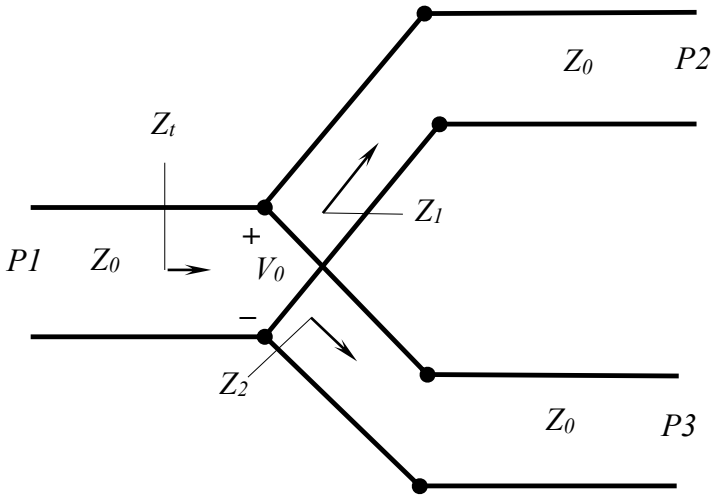

Figure 5.4 Transmission line model of unequal lossless Y-junction power divider.

Assuming V_0 is the voltage at the junction as shown in Fig. 5.4, then to calculate the input power to the matched divider:

$$P_{in} = P_1 = \frac{V_o^2}{2(Z_0)} \tag{5.1}$$

The distributed power at each output port is expressed as

$$P_2 = \frac{V_o^2}{2(Z_1)} \quad , \qquad and \quad P_3 = \frac{V_o^2}{2(Z_2)} \tag{5.2}$$

The total power of the ideal (lossless) design at the output ports (P_{out}) is equal to the input power (P_{in}) as represented in

$$P_{out} = P_2 + P_3 = P_{in} \tag{5.3}$$

Consequently, to determine an unequal power distribution for each output port is

$$P_2 = KP_{in}$$

$$P_3 = (1-K)P_{in} \ , \qquad 0 < K < 1 \tag{5.4}$$

The output ports power yields the Z_2 and Z_3 impedance by combining Eq.s 5.1 and 5.2 into 5.4 as follows

$$Z_2 = \frac{Z_0}{K} \tag{5.5}$$

$$Z_3 = \frac{Z_0}{(1-K)}$$

Therefore, the total impedance at junction $Z_t = Z_2 /\!/ Z_3$ while maintaining matching conditions is equal to the input impedance Z_0 .

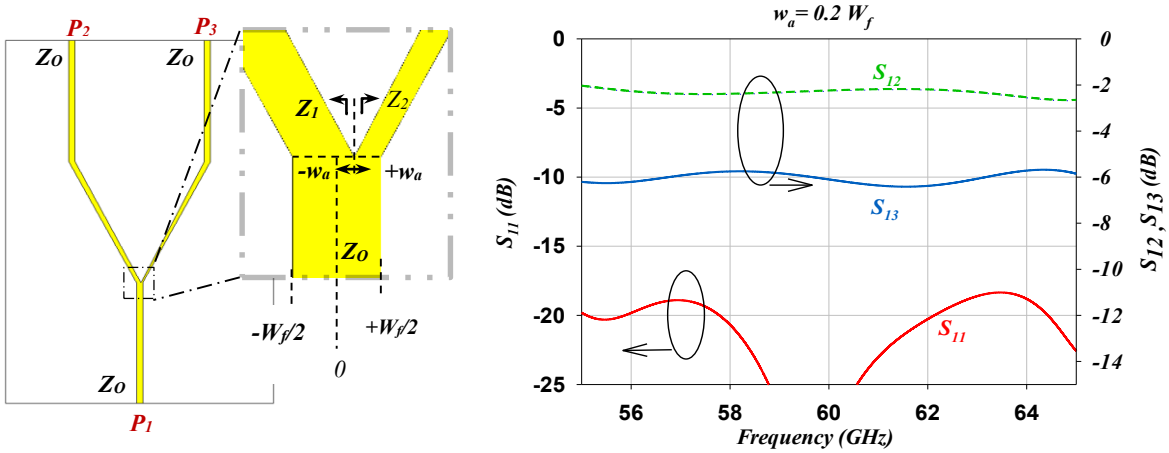

Figure 5.5 Microstrip model of the unequal Y-junction power divider, on the left, and the S-parameters results, on the right.

Fig. 5.5 shows a microstrip model of the unequal Y-junction power divider and the S-parameters results designed to operate at 60 GHz. The structure is designed on RO4003 (εr = 3.55, tanδ = 0.0027@ 10GHz) and is 0.2mm in thickness, the distance between the output ports is 2.14λ, and characteristic impedance of the input and the output ports are 50 *Ω*. The dimensions of the Y-junction power divider length are kept, as in Fig. 5.1; however, the input port line Z_0 splits into two unequal lines Z_1 and Z_2 in the tapered slot. Practically, the output power of the Y-junction is not lossless, and $P_{out} = P_{in} - P_{loss,}$ where P_{loss} is the sum of dielectric, radiation, and ohmic losses. The value of impedances Z_1 and Z_2 control the power distributed in each output port by the value of $\pm w_a$, when the chosen value is $+w_a$ the current flow is higher in the Z_1 line (Port2) and lower at Z_2 (Port3). Consequently, as the S-parameters show in Fig. 5.5, when the $w_a = 0.2\ W_f$, where W_f is the microstrip feed line width, as estimated the insertion loss of S_{13} is higher than S_{12}.

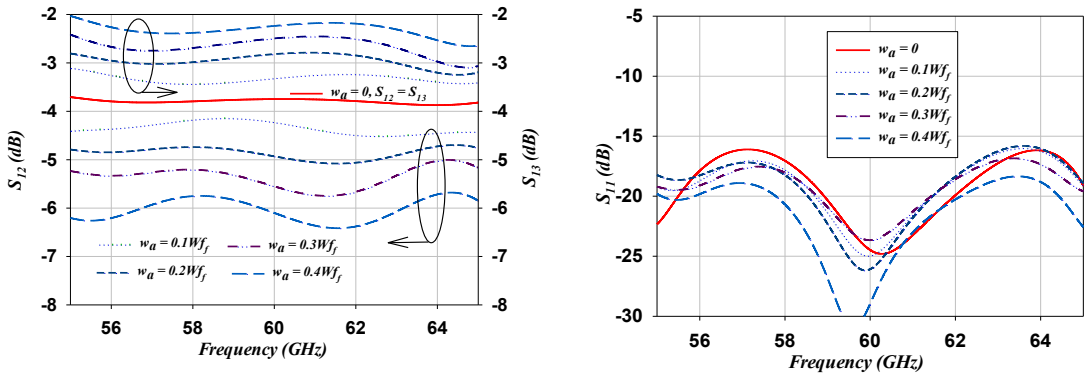

Figure 5.6 The effect in varying the power distribution controller w_a on the S-parameters.

In further investigation, the power distribution controller w_a is varied from 0 to $0.4W_f$. This effect is presented in the results of the insertion loss for each port and reflection coefficient, as shown in the Fig. 5.6. When $w_a = 0$ presents the equal feed in the Y-junction, in this case the S12=S31, also as seen in the figure when the w_a increases this makes the

difference of the power distribute between the output ports increase. While there is a minor effect on the reflection coefficient S_{11} with stable impedance bandwidth with a range of ± $w_a \leq \pm W_f$. Therefore, this type of unequal Y-junction power divider is suitable for controling the distribution of power with efficient optimization.

5.3 A 60 GHz 16-way Y-junction with Unequal Power Distributor

A phased array employs an equal power feeding network, which leads to increasing the sidelobe level ratio (SLR) rapidly, and as the value of the phase taper increases, an unequal power divider is necessary to reduce SLR. The unequal power distribution employs different methods to synthesize amplitude array weights that yield a desired sidelobe level. The commonly used methods to suppress the side lobe level are the Dolph-Chebyshev and Taylor taper. The Dolph-Chebyshev taper distribution design yields for the smallest possible SLR for a given first null beamwidth; meanwhile, the Taylor tapering yields a distribution that is an optimum trade-off between beamwidth and side lobe level. The Taylor $\bar{n}$ distribution method gives the highest directivity for a particular SLR [138] - this method is broadly utilized [139], [140]. The expression of aperture distribution is formed as a finite Fourier series by Hansen [139] as

$$g(p) = 1 + 2\sum_{n=1}^{\bar{n}-1} F(n, A, \bar{n}) \cos n\pi p \tag{5.6}$$

where p is defined as a finite range from $-\pi$ *to* $+\pi$, A is a single parameter related to an SLR, presents the number of the ports or the array elements, and $\bar{n}$ is a constant chosen at a certain digit to optimize the design. The coefficient is expressed in [139] as

$$F(n, A, \bar{n}) = \frac{[(\bar{n}-1)!]^2}{(\bar{n}-1+n)!\,(\bar{n}-1-n)!} \sum_{m=1}^{\bar{n}-1} (1 - n^2/z_m^2) \tag{5.7}$$

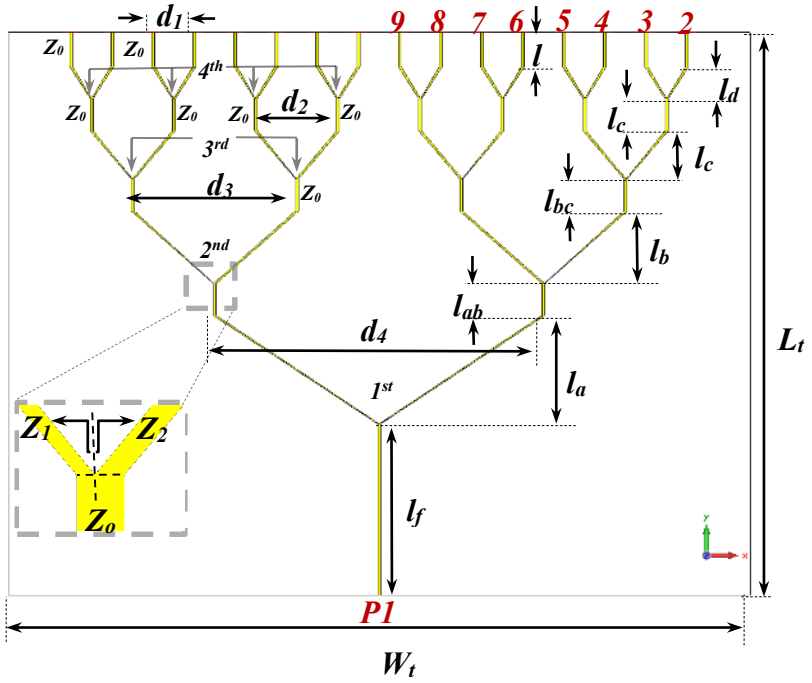

Figure 5.7 The structure of 16-way unequal Y-junction power divider.

Table 5.1 Optimized dimensions of the 16-way unequal power divider

Parameter	l_f	l_a	l_{ab}	l_b	l_{bc}	l_c	l_{cd}
Value(mm)	*25*	*15.8*	*4.7*	*10.6*	*4.7*	*7.1*	*4.7*
Parameter	l_p	d_1	d_2	d_3	d_4	W_t	L_t
Value(mm)	*5*	*6*	*12*	*24*	*48*	*108*	*82*

For applications, such as imaging detection and radars, it is desirable to keep the target detected through the main lobe, otherwise a minor lobe might detect a signal as a false target. In order to suppress the SLR and reduce system noise level, The Taylor $\bar{n}$

distribution method is used in the 16-way Y-junction with unequal power distributor to optimize the design and obtain a lower SLR.

Table 5.2 Calculated Coefficients of a 16-Element Array with *N*-bar = 6 and SLR=30 dB.

Port No.	Coefficients	Normalized Coefficients
2	0.417778	0.326350109
3	0.50464	0.355965128
4	0.689013	0.428035494
5	0.921505	0.540069426
6	1.138886	0.671207631
7	1.324878	0.808411666
8	1.465739	0.930694942
9	1.537562	1

The 16-way unequal power divider, designed with CST-MS to operate at ISM 60 GHz band, is shown in Fig. 5.7. The structure, designed on a 0.2mm RO4003 (ε_r = 3.55, $tan\delta$ = 0.0027@ 10GHz) with copper cladding is 35μm in thickness. The distanced between output ports is d_1 = 1.2λ (λ @ 60 GHz) to decrease the mutual coupling effect, and the characteristic impedance of the input and the output ports are 50 Ω. The optimized dimensions are listed in Table 5.1. In Fig. 5.7, the narrowest line width at the junction is 47.8μm, which is within accessible fabrication margins.

The fabrication limitation regarding the tapered line for unequal splitting is taken into account, in that sense the Tayler *N*-bar distribution parameters, particularly the SLR, are chosen at reasonable value to meet both the array requirements and the fabrication machines. In order to reach a sidelobe level of -30 dB, a Taylor *N*-bar distribution obtained with sidelobe ratio (SLR) =30dB, and *N*-bar = 6 and is chosen as the amplitude taper at the first 8-port normalized weight, as seen in Table 5.2 which shows calculations obtained using Matlab [141]. The normalized output power ratios at 58, 60 and 62 GHz of the

simulation results with and without EBG structure are compared with the ideal calculated results, regarding ideal values the unequal impedances at the power divider junctions are optimized. The desired pattern is symmetrical with respect to the center of the array; therefore, 16 elements are such that the 8 elements of the first-half mirror the 8 elements of the second-half.

Table 5.3 Simulated *K* values for the second to fourth stages.

Stage	***K* values**			
2nd	0.5651			
3rd	0.2528		0.2528	
4th	0.2511	0.2758	0.2416	0.2162

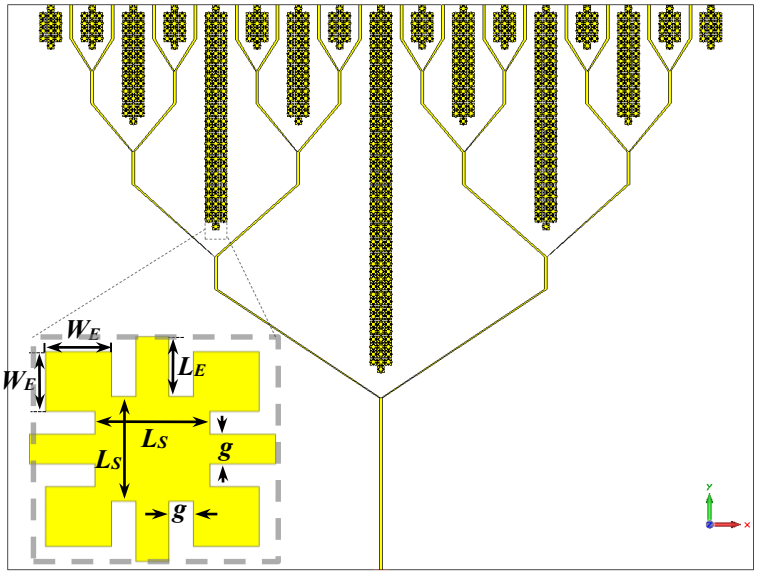

Figure 5.8 The 16-way unequal Y-junction power divider 16-Way with EBG.

In the 16-way unequal power splitter in Fig. 5.7, the first stage divided impedances are equal, then the values from the second to fourth stages correspond to displacement from the center of the junction (w_a), listed in terms of *K* value in Table 5.3, which presents the impedances transformed after each branch. The impedances at each branch can be calculated by the power ratio using Eq. (5.5). Accordingly, the characteristic impedances

at junction start from right to the left on the second stage are 115Ω, and 88Ω, the third stage ones are 150Ω, 75Ω, 198Ω, and 67Ω, and then the fourth stages ones are 231Ω, 64Ω, 207Ω, 66Ω, 181Ω, 69Ω, 199Ω, and 67Ω. The characteristic impedances at the junction are optimized to reduce the sidelobe levels to margins within fabrication limitation.

Table 5.4 The Optimized dimensions of EBG unit cell.

Parameter	***g***	L_S	L_E	W_E
Value (*mm*)	0.146	0.511	0.292	0.292

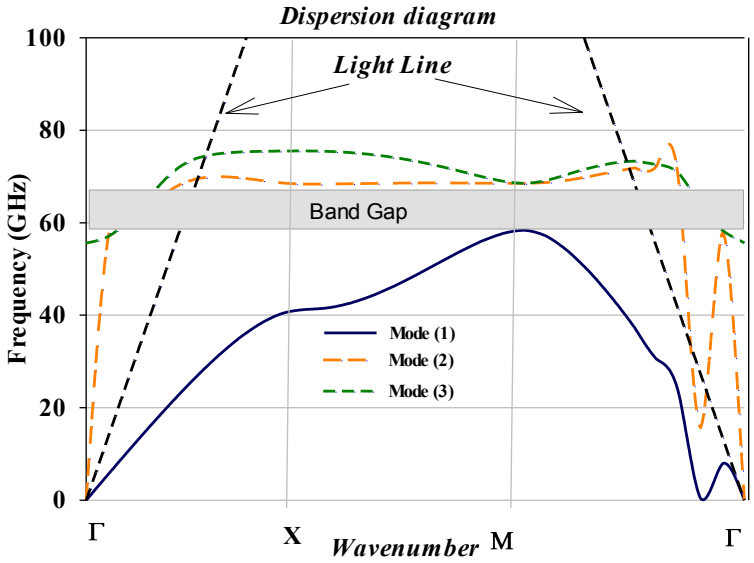

Figure 5.9 2D uniplanar EBG unit cell dispersion diagram.

Fig. 5.8 shows the same model of the 16-way unequal feeding network modified with the electromagnetic band gap structure (EBG), 2D uniplanar model. The EBG structure is implemented to surround microstrip feeding lines in order to reduce the potential radiation caused by the discontinuity at the bend lines and suppress the surface waves [142]. Furthermore, The EBG creates an electromagnetic gap at designing band that increases the isolation between the output ports leading to a reduction in the mutual coupling [142]. [143], [144].

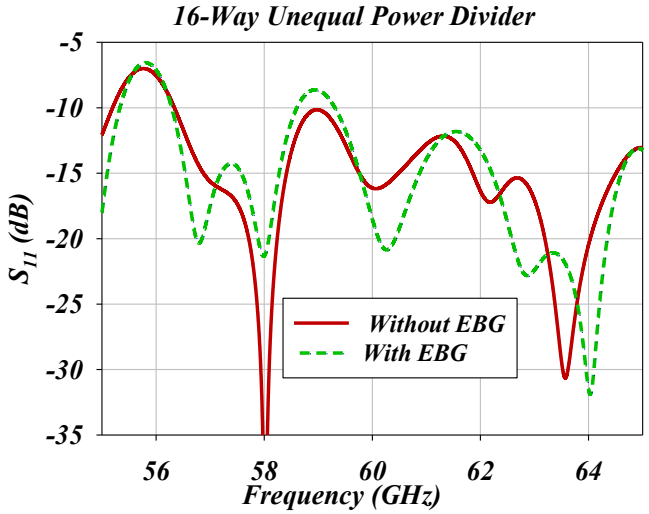

Figure 5.10 Reflection coefficient of 16-way unequal Y-junction power divider with and without 2D uniplanar EBG.

The 2D uniplanar EBG structure is designed on a RO4003 substrate which is 0.2mm thick and optimized to obtain a band gap (bandstop) around 60 GHz, as shown in the Fig. 5.8; it is distributed in a planar structure around the microstrip feed lines. The finalized dimensions of the unit cell are listed in Table 5.4. The dispersion diagram of the uniplanar 2D EBG unit cell is illustrated in Fig. 5.9. It shows a 9 GHz band-gap between the first and second propagation modes around 60 GHz covering the ISM band.

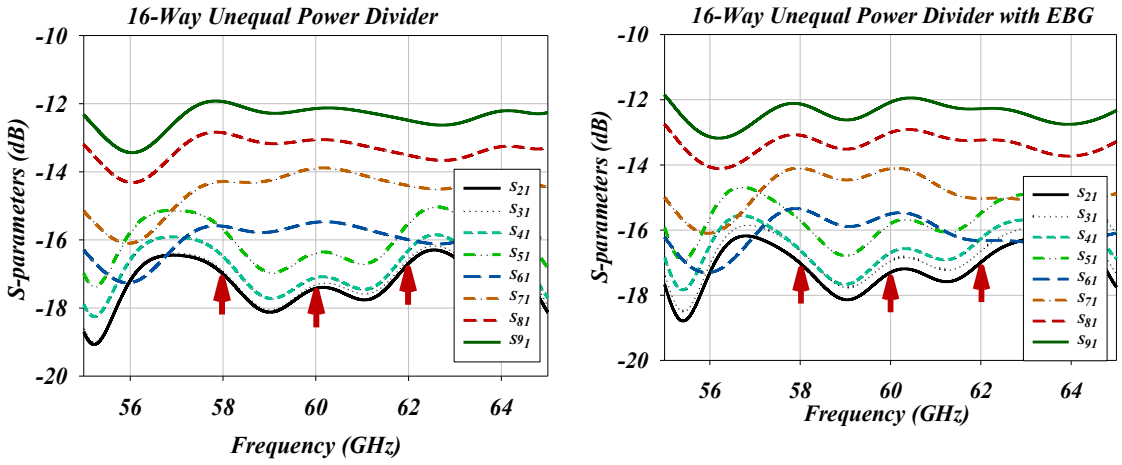

Figure 5.11 S-parameters, insertion loss of 16-way unequal Y-junction power divider with and without 2D uniplanar EBG.

Fig. 5.10 shows the reflection coefficient of the Y-junction power divider with and without an EBG structure. The 16-way Y-junction power divider design has wide bandwidth covering a band of ≤ -10dB (S_{11}) from 56.2 GHz to beyond 65 GHz. The EGB unit cells around the power divider have no effect on return loss, in fact it enhances the operating bandwidth.

The 16-way Y-junction power divider results of the insertion loss for the first 8-terminals at each output port are presented in Fig. 5.11. The transmission coefficient is distributed higher at port 9 (S_{91}) and gradually declines to port 2 (S_{21}), appearing with and without EBG structure. In the simulation design, transmission coefficient responses of the edge ports, from port 2 to 4 are difficult to optimize because of line limitation with respect to the fabrication margin, as seen in the case without EBG, the responses of S_{21}, S_{31}, and S_{41} are close to each other. However, the transmission coefficient responses with EBG unit cells present a controllable gap between the edge ports that can be optimized by the power division to approach the designing values of Taylor N-bar distribution. Therefore, 16-way Y-junction power divider results present an efficient unequal division reducing the sidelobe level for ease of fabrication - it is practical to employ for antenna array.

5.4 The 1 × 16 Phased Antenna Array Design Based On the Piezoelectric Transducer Controlled Delay Line Technique

Phased antenna arrays (PAAs) with high gain, wide bandwidth, low sidelobes, low cost, and compact design are in demand for many military and commercial applications [36], [50], [147]-[150]. Numerous applications at millimeter wave band require a high gain and wide bandwidth, for the use of true time-delay-based PAAs as an alternative to the phase-shifter for eliminating beam squinting. A wide bandwidth and high gain antenna is

the complement to operate with PAAs in many system applications. In [50], a good performer of 18–40 GHz, the 1 × 16 beam shaping and 1×8 beam steering PAA used a low-cost true time PET as a controller phase shifter, however, the drawback is in high sidelobe level and mutual coupling between antenna elements caused by discontinuity at the amplitude taper of the power divider that reduces the total radiation efficiency. In [151], a planar feeding technique using a phase-and amplitude-corrected SIW horn to feed 1×8 antipodal linear TSA arrays. However, beam bifurcation occurs at the E-plane when a single-difference-beam antenna is applied.

The tapered slot antenna featured with high gain, wide bandwidth, and with a stable end fire radiation pattern making it suitable for imaging detection systems and broader radar applications [152]-[156]. As introduced in [157], a 16-element Vivaldi subarray is used with a real-time ultra-wideband see-through-wall imaging radar system. In [158], 64 tapered-slot antenna elements with low voltage standing wave ratios, array scanning capabilities up to 45° are presented to utilize in next-generation radio telescope of the Square Kilometer Array (SKA). The 8- element TSA phased antenna array system used nonlinear delay line (NDL) technology [159], and the 144 element dual-polarized endfire tapered-slot phased arrays exanimated the phase of the mutual coupling coefficients [160]. In this work, PAA uses Fermi tapered slot antenna with sin-corrugation design, as proposed in [J2], [C5], [C8], [C9]. Also, this work has designed a new AFTSA-SC able to provide small spacing between antennas and symmetrical E-plane and H-plane radiation pattern, with high gain and wide bandwidth to fulfil the requirement to operate in the 60 GHz array structure.

In order to enhance the array performance in reducing the side lobe level, a Tayler N-bar unequal power distribution implementing a Y-junction splitter is introduced in this PAA design. The phase shifter proposed in 1×16 PAA is controlled by a low cost piezoelectric transducer (PET), which was developed by Kim and Chang [91], [161]; this provides a simple mechanism with low cost able to cover a wide frequency, and achieving a true time-delay phase shifter [50].

In this section two forms of 1 × 16 PAAs with PET controller are presented. The first is with 16 of AFTSA-SC antenna with EBG surrounding the feeding network and the second is the circularly polarized AFTSA-SC antenna with EBG, the antenna as single elements is designed for both arrays as symmetric E- plane and H-plane.

5.4.1 A 60 GHz 1 × 16 E-Plane Beam Steering Phased Array AFTSA-SC Antenna Symmetric E- plane and H-plane

In this section, we will present a 60 GHz, 1 × 16 E-plane beam steering phased array. First, the AFTSA-SC antenna is designed to be in a symmetric E- and H-plane pattern - the design details, results, and discussion will be presented. Then, we will present a 60 GHz, 1 × 16 E-plane beam steering phased array AFTSA-SC antenna with symmetric E- plane and H-plane, the design details, results, and discussion are included.

5.4.1.1 A 60 GHz AFTSA-SC Antenna Symmetric E- plane and H-plane

The 60 GHz AFTSA-SC is designed specifically to employ in PAA structure, with radiation patterns able to remain symmetric in E- plane and H-plane for a wide bandwidth. The schematic of the AFTSA-SC is presented in Fig. 5.12. The AFTSA-SC is simulated on a Rogers RT/Duriod 4003 substrate with $\varepsilon_r = 3.55$, $\tan \delta = 0.0027$@ 10 GHz, thickness

= 0.2 mm. The overall antenna size is relatively small with 37 *mm* in length and 6.5mm in width. Furthermore, the optimized antenna parameter is presented in Table 5.5.

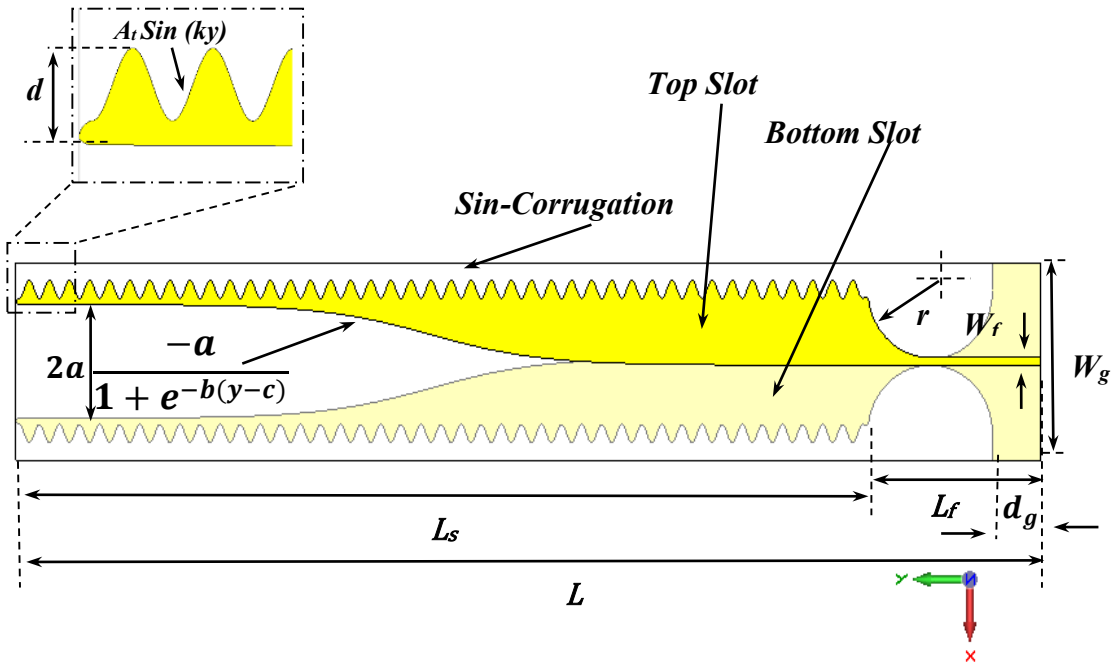

Figure 5.12 Geometry of AFTSA-SC antenna symmetric E- plane and H-plane.

Table 5.5 The AFTSA-SC, one element optimized parameters.

Parameter	***Wf***	***rc***	***Wg***	***Lf***	***Ls***	***L***	
Value(mm)	*0.25*	*2.25*	*6.5*	*6.25*	*30.75*	*37*	
Parameter	***dg***	***At***	***k***	***d***	***a***	***b***	***c***
Value(mm)	*1.75*	*0.3*	*8.67*	*0.5*	*2*	*0.5*	*20*

Fig. 5.13 shows the simulated bandwidth of AFTSA-SC antenna defined as S_{11} < -10 dB covering the entire band of 55 - 65 GHz. Also, for the selected band, the gain is stable and about 15dB at 60 GHz. Furthermore, the total radiation efficiency is about 88% on average for the band of 55 - 65 GHz. The radiation patterns of AFTSA-SC at 59, 60, 61, and 62 GHz are presented in Fig. 5.14. The mainbeam of E- and H-plane are in symmetry over the whole band. The radiation patterns of the selected frequencies show

stable endfire over the entire range and low sidelobe level indicated in the E-plane and the H-plane, with about -13 dB of SLR on average for the selected band.

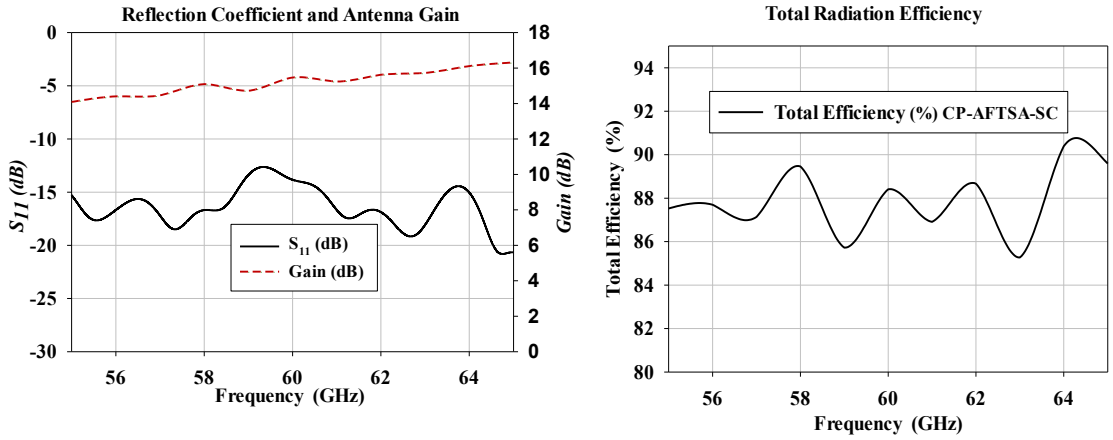

Figure 5.13 AFTSA-SC antenna simulated gain, return loss S11, and total radiation efficiency.

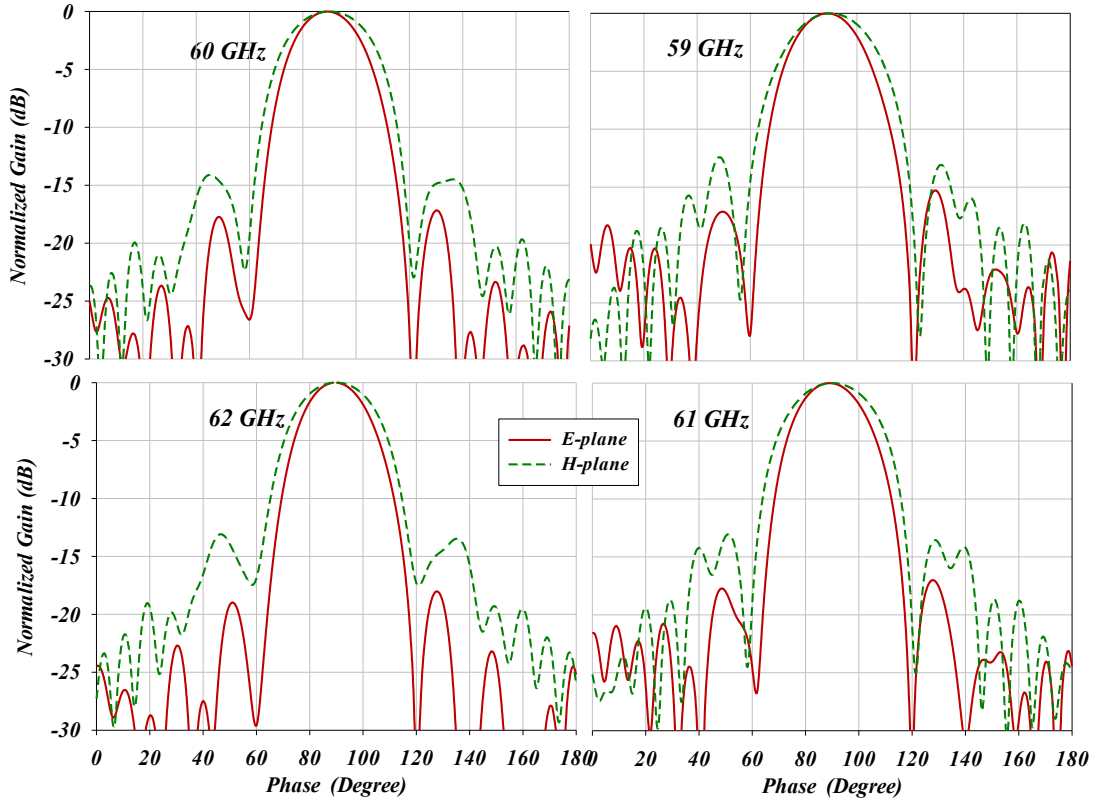

Figure 514 Simulated radiation patterns of symmetric E- plane and H-plane AFTSA-SC at 59–62 GHz.

5.4.1.2 The 1 × 16 E-Plane Beam Steering Phased Arrays AFTSA-SC with EBG Structure

Fig. 5.15 shows the schematic of the PAA system which contains 16-element of the AFTSA-SC antenna, phase shifter, and power feeding network. The feed network is a Y-junction 16-way unequal designed according to Taylor N-bar distribution power divider, where N= 6 and SLR = -30 dB. This Tayler distribution is used in order to minimize the sidelobe level with a center to center spacing between antenna elements of 1.2 λ_0 (λ_0 =5mm @ 60 GHz). The 2D uniplanar EBG structure is a sounded feeding network, and it is modelled on a RO4003 substrate with 0.2mm in thickness. The EBG structure is optimized to obtain a band gap to cover the entire ISM band, as shown in Fig. 5.8. Further, the dimensions of the 2D EBG unit cell are listed in Table 5.4. Moreover, the dimensions of the1 × 16 PAA structure are: length = 174.3mm, height = 6.83mm, and width = 108.2mm.

The phase shifter uses PET to perturb a right triangle shaped substrate with a 0.2mm thick RO4003. The perturber is mounted on the microstrip feeding network lines, and the perturber triangle shape creates different propagation delay from line to another. Practically, at a certain DC bias line voltage, the PET is perturbed at a certain height Δ_L which causes a phase shift that steers the beam. The perturber triangle substrate is mounted on 15 microstrip lines, the 16th microstrip line is kept with no perturber on top, as a reference, i.e., with no delay line effect. The length of the perturber is 10 mm at the center and 0 mm at the edge.

Fig 5.16 presents the simulated reflection coefficient of the 1 × 16 AFTAS beam steering phased array results for four different structures. The simulated bandwidth for S_{11} < -10 dB covers 56.5- 65 GHz. Fig 5.16 shows the slightest impact on reflection

coefficients when the PAA is under maximum perturbation (Δ_L = 0mm) and no perturbation as with EBG. Thus, the PAA is established broadband characteristics and no effect on the reflection coefficient under PET perturbation.

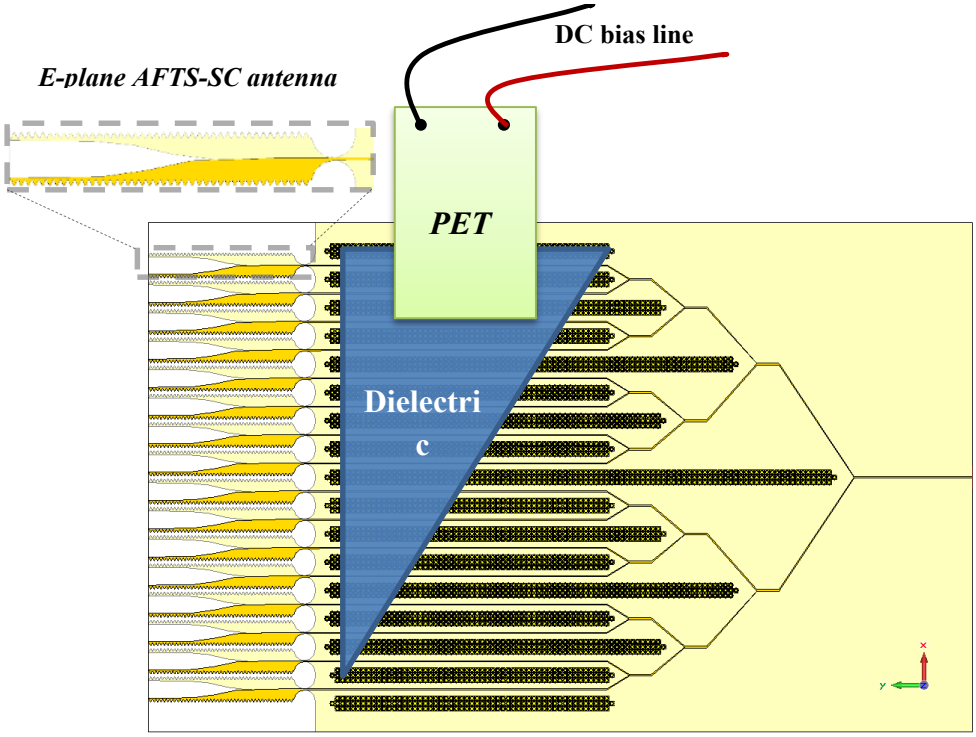

Figure 5.15 1 × 16 E-plane beam-steering phased array with AFTS-SC Antenna and EBG structure.

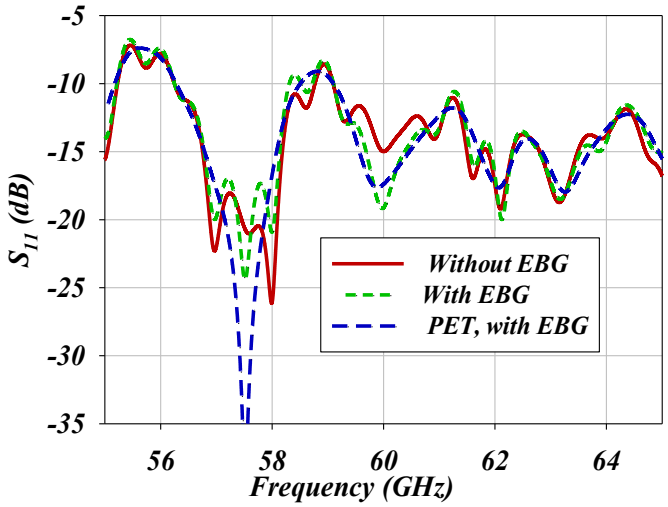

Figure 5.16 The reflection coefficient of 1 × 16 AFTAS beam steering phased array results with EBG, without EBG, and PET with EBG.

The simulated E-plane beam steering radiation patterns when varied Δ_L = 0 to 0.25mm at 57, 60 GHz, and 64 GHz is illustrated in Fig.5.17. The maximum beam steering angle occurs at Δ_L = 0mm, steered by 6, 6.5°, and 6° at 57, 60, and 64 GHz, respectively. At Δ_L = 0.25mm, corresponding to no delay line and no steering effect, the highest SLRs -10, -14.5, and -13.5 dB at 57, 60, and 64 GHz, respectively, and HPBW is stable around 2.9° at E-plane and 31° at H-plane . In all perturbations (*Δ_L = 0 to 0.25mm),* the SLR is kept lower, which indicates stable performance over the 60 GHz ISM band.

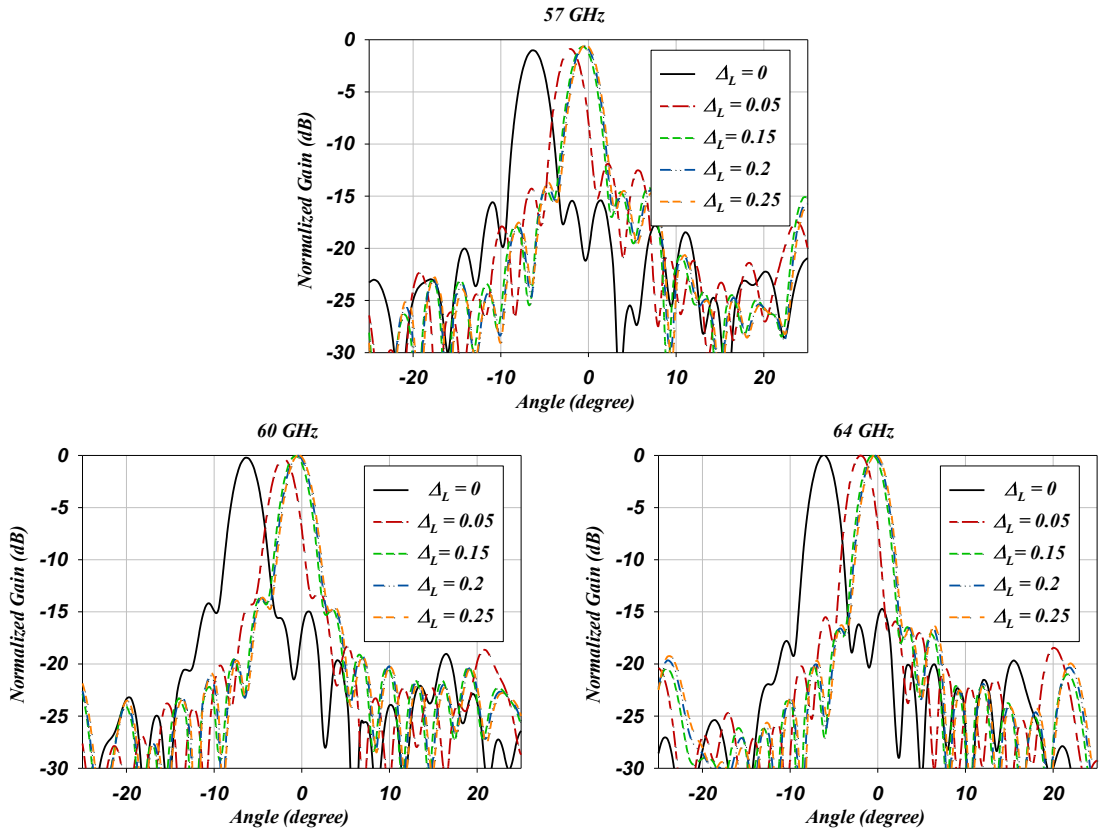

Figure 5.17 Simulated E-plane beam steering radiation patterns with *Δ_L = 0 to 0.25mm* perturbations at 57, 60, and 64 GHz.

Fig. 14, shows the fabricated prototype for the proposed 1 × 16 E-plane phased antenna array with EBG structure mounted on the test fixture in the anechoic chamber. The

test fixture is made of 0.5 in thick aluminum sheeting designed specifically to amount the array PCB, End-Launch V-band connector, and PET system. This design made it easy to mount the thin substrate and align it at the testing scanning arm in the anechoic chamber, performing radiation pattern measurements. The E-plane is presented in xy-plane, which aligned horizontally with test fixture and the PET system that affect the radiation patterns .Furthermore, during the integration process of the PET, the flatness and position of perturber substrate top of the microstrip lines might be changed slightly.

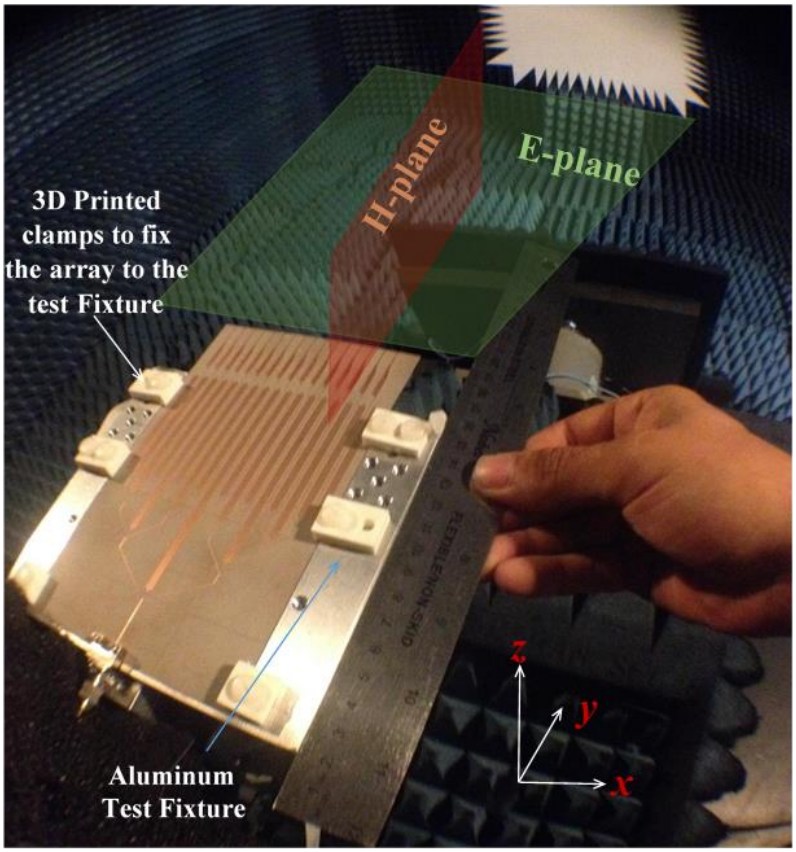

Figure 5.18 The prototype photograph of the 1 × 16 E-plane AFTSA-SC phased array with EBG at anechoic chamber.

Fig. 5.19 shows the measured and simulated S11 results in case when PET is at maximum perturbation and without PET, where S11 measurement is conducted by PNA A5227N. The measured results shows a wide bandwidth impedance S11 <-10 dB covers

band of 55 - 65 GHz for both cases with or without PET. Notably, the measured S11 indicates a similar trace to the calculated ones. Nevertheless, the fabrication tolerance may cause a slight shift, and the tolerance in the substrate's dielectric constant. However, the measured results elaborates wideband characteristics and with no effect on the return losses under these two conditions, which is essential advantage of this technique [50].

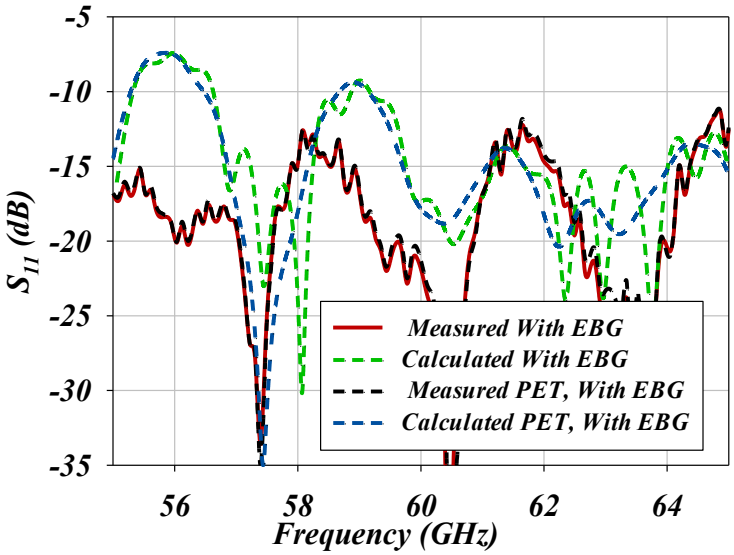

Figure 5.19 The measured and calculated results of reflection coefficient for 1 × 16 E-plane AFTSA phased array results with EBG in case with and without PET.

Fig. 5.20 shows the steered beam of E-plane patterns when 100 DC-volts are applied to the PET, causing maximum perturbation at right/left scan. The measured E-plane radiation patterns at 57 GHz (a), 60 GHz (a), and 62 GHz (c) exhibit a beam scanning range of approximately 1.1° - 2°. At 57 GHz, the - 3 dB beamwidth is approximately 2°, which is the requirement for imaging/detection systems. The high side lobe level ratio at high frequencies is attributed to increase in the mutual coupling between antenna elements, and beam broadening appears. The system with EBG, the sidelobe level is relatively suppressed, as shown in Fig. 21.

The measured and radiation patterns of E-plane with EBG beam steering at maximum perturbations for 57, 60, 62 GHz are illustrated in Fig. 21 (a), (b), and (c). In the same figure, the simulated radiation pattern of the array without perturbation is presented at each frequency. The HPBW (- 3 dB) is approximately 2° at 57 GHz. Furthermore, it shows a beam scanning ranges of 1.6° - 2.9°, which by employing EBGs increases relatively the scanning range from 0.5° to 0.9° than ones performed without EBGs as in Fig. 5.20.

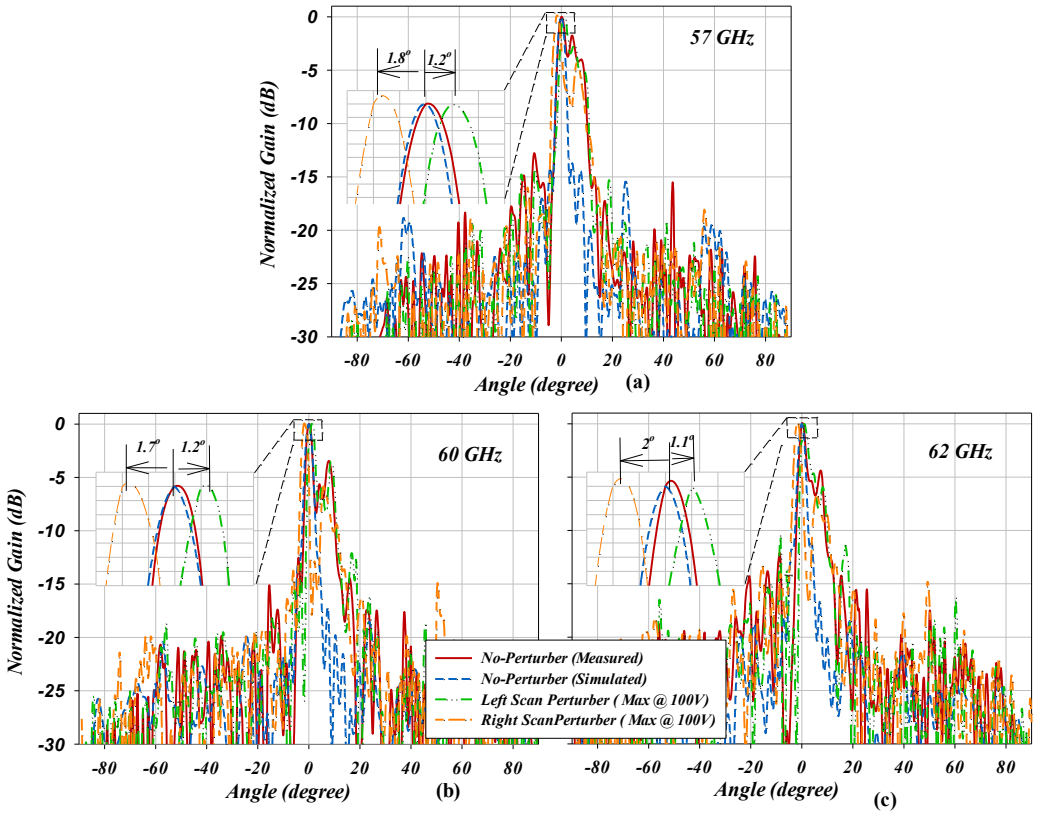

Figure 5.20 Measured radiation pattern of E-plane without EBG beam steering with maximum perturbations at 57, 60, and 62 GHz.

The radiation patterns of the EBG structure that surrounded the feeding network suppressed the surface waves and reduced the mutual coupling between antenna elements, leading to maintaining the sidelobe level lower and main beam more directive than the

array without EBG. The measured results elaborate the effectiveness of EBG's employment in the feeding network at ISM – band of 57 - 64 GHZ. It makes the proposed design operate efficiently in ultra-wideband MMW phased antenna array applications.

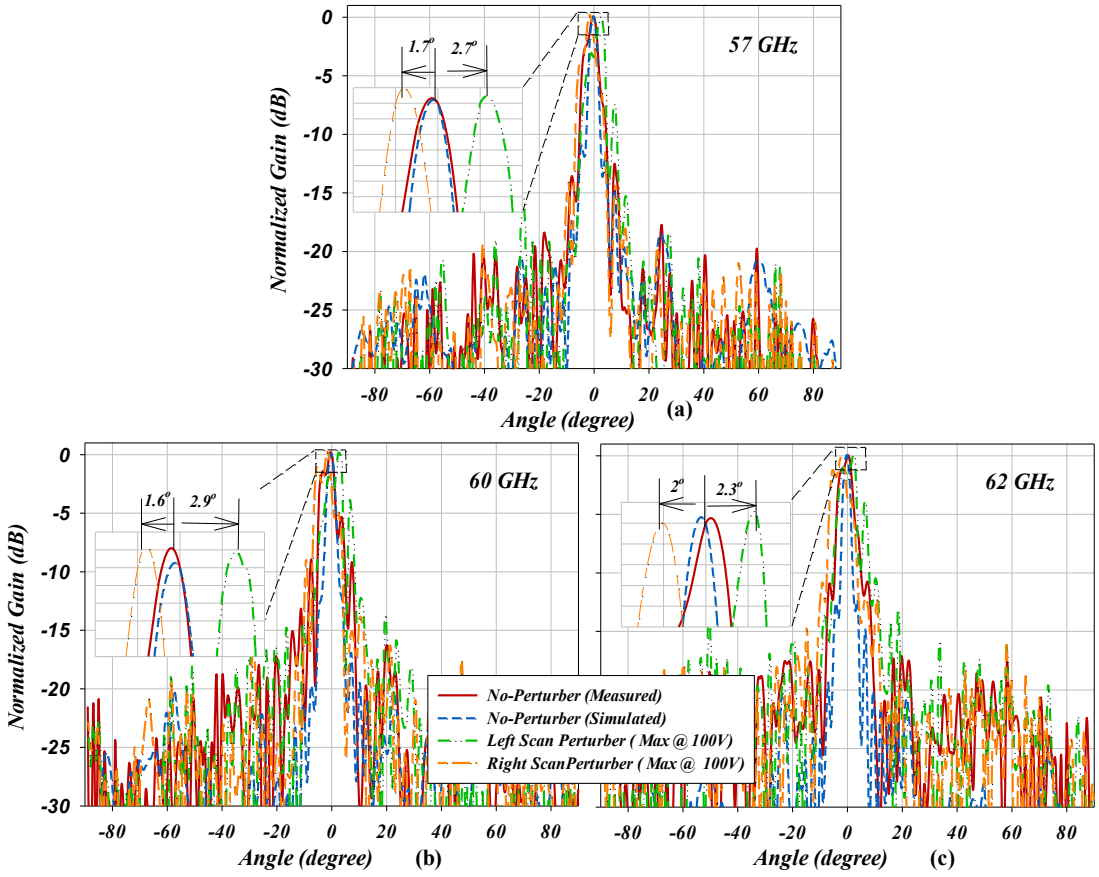

Figure 5.21 Measured radiation patterns of E-plane with EBG beam steering with maximum perturbations at 57, 60, and 62 GHz.

5.4.2 Circular Polarized 1 × 16 Beam Steering Phased Array

This section will present a novel structure circular polarized 1 × 16 beam steering phased array. First, it will present the design details, results, and discussion of the circularly polarized single element of the PAA system. Then, it will present the circular polarized 1 × 16 PAA including design details, results, and discussion.

5.4.2.1 A 60 GHz Symmetric E- plane and H-plane and PC AFTSA-SC

A 60 GHz circularly polarized antipodal Fermi tapered slot antenna with sin-corrugation (PC AFTSA-SC) is presented in Fig. 5.22. This PC AFTSA-SC is designed to employ in array structure, with radiation patterns capable of maintaining a symmetric E-plane and H-plane for a wide bandwidth. As in Fig, 5.22, the circularly-polarized antenna element consists of a pair of AFTSA-SC elements. These two elements are aligned orthogonally to each other. Both the horizontal and vertical elements are fed by a single microstrip line with a 50 Ω input impedance. This design is a single feed exciting horizontal and vertical elements, where the circular polarization is achieved by the slotted cutouts in the center of each substrate to satisfy the 90° phase delay between the horizontal and vertical elements.

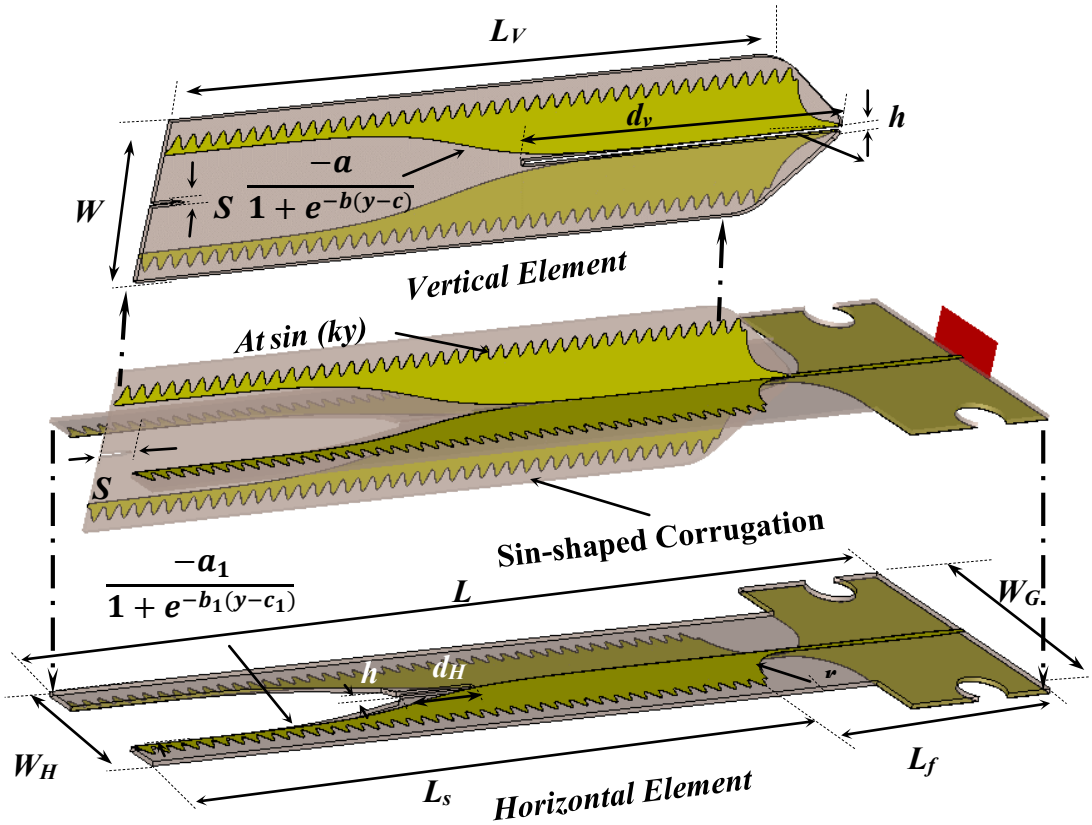

Figure 5.22 Geometry of the antipodal circularly polarized AFTSA-SC antenna.

Table 5.6 The CP-AFTSA-SC optimized parameters.

Parameter	L_H	L_f	L_s	W_H	W_V	W_G	S_{Vd}	S_V	r_c	b	a
Value(mm)	*42*	*9*	*33*	*6.5*	*6.8*	*10.9*	*1.5*	*0.15*	*2.25*	*0.5*	*2*
Parameter	d_H	d_v	h	L_v	At	k	a_1	b_1	c_1	c	
Value(mm)	*3.57*	*15.5*	*0.2*	*28.4*	*0.3*	*8.7*	*2*	*0.5*	*2.25*	*20.25*	

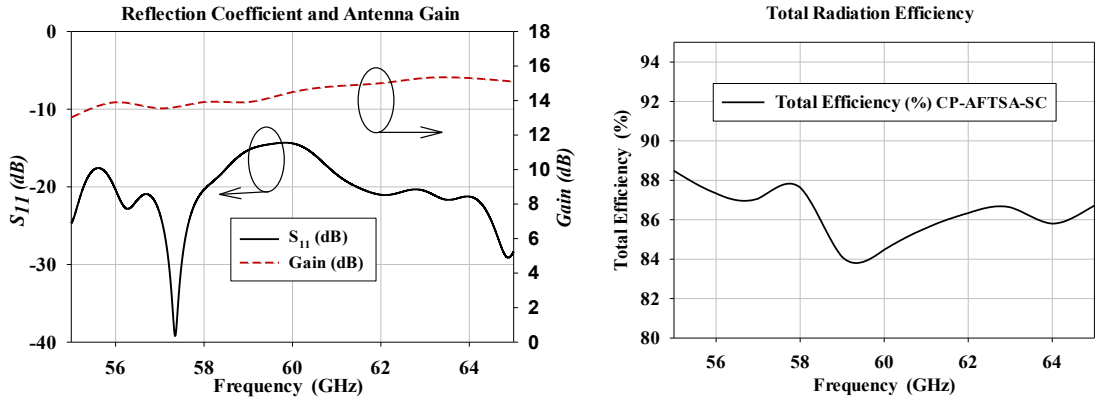

Figure 5.23 CP-AFTSA-SC antenna symmetric E- plane and H-plane results: gain, return loss S_{11}, and total radiation efficiency.

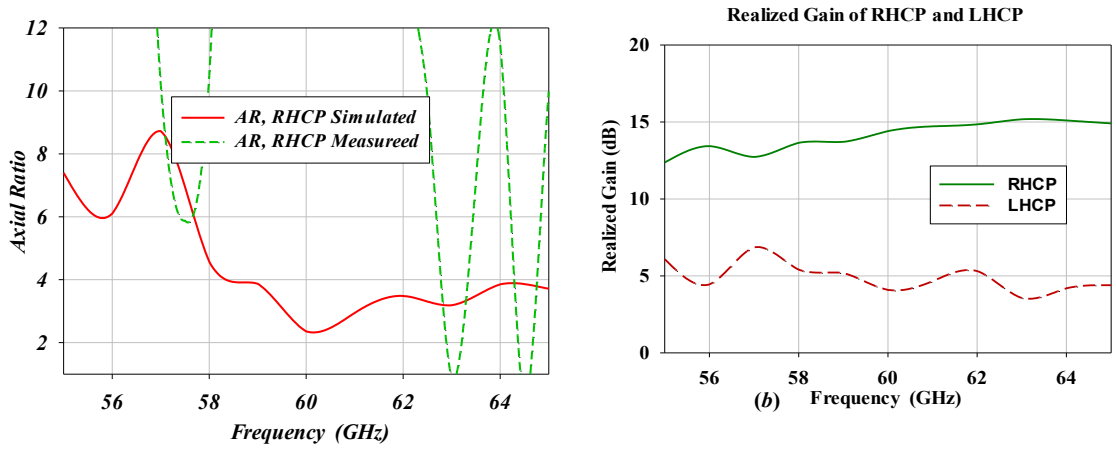

Figure 5.24 (*a*) Measured and simulated axial ratio of RHCP and (*b*) realized gain at RHCP and LHCP of CP-FTSA-SC antenna.

The circularly polarized AFTSA-SC is simulated on Rogers RT/Duriod 4003 substrate with $\varepsilon_r = 3.55$, $\tan\delta = 0.0027$@ 10 GHz, thickness = 0.2 mm. The overall antenna size is 51.5 *mm* × 13 *mm*. Furthermore, the AFTSA-SC is modelled to radiate in the right-

hand circularly polarized antenna (RHCP) wave. The optimized antenna parameter is presented in Table 5.6.

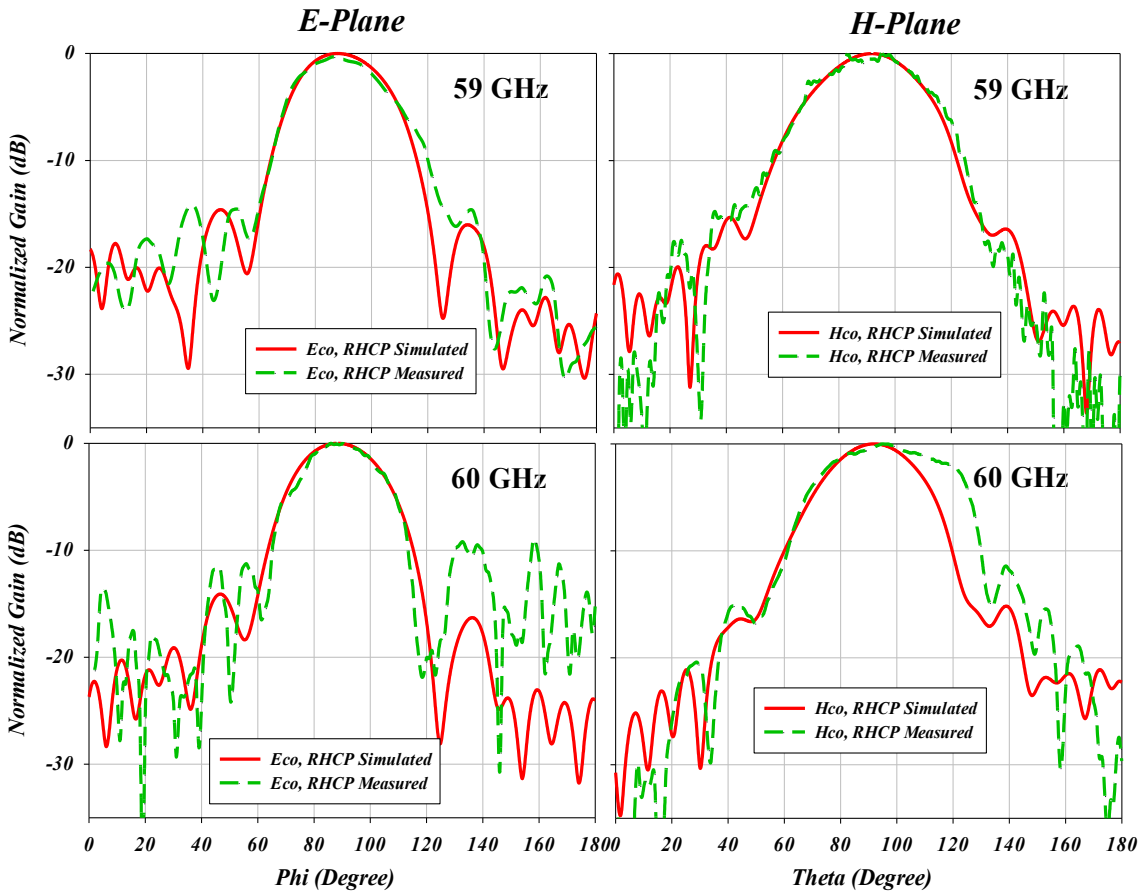

Figure 5.25 Measured and simulated radiation patterns of the symmetric E- plane and H-plane PC AFTSA-SC at 59 and 60 GHz.

The bandwidth for the CP-AFTSA-SC antenna is defined as S_{11} < - 10 dB and covers the entire band of 55 - 65 GHz, as shown in Fig. 5.23. Furthermore, the gain is stable for the selected band, and is about 15dB at 60 GHz. The total radiation efficiency is about 86% on average for the band of 55 - 65 GHz. Fig. 5.24 (a), shows the measured and simulated RHCP axial-ratio (AR) of the FTSA-SC antenna, less than 3dB is maintained across the band of 59.5-61 GHz, at the simulated result about 1.5 GHz circular polarized bandwidth with minimum AR is about 2.3dB at 60 GHz. The measured AR result indicates

a circular polarized around 63.5 GHz and 64.5 GHz. This discrepancy between the measured and the simulated results may cause by the fabrication tolerances and imperfection in soldering the vertical into the horizontal element. Fig. 5.24 (b), shows the results of the RHCP and LHCP realized gain, which indicates the CP antenna is RHCP dominant to LHCP with a 10dB difference in gain range.

Fig. 5.25 shows the radiation patterns of PC AFTSA-SC at 59, and 60 GHz. The radiation pattern of the selected frequencies shows stable endfire over the whole range, and there are a good agreement between the measured and simulated results. The E- and H-plane have a symmetry radiation pattern until about -15 dB.

5.4.2.2 The 1 X 16 Beam Steering Phased Antenna Arrays with Circular Polarized AFTS Antenna with EBG Structure

In Fig. 5.26, the schematic of the PAA system contains a 16-element circular polarized AFTS antenna, phase shifter, and power feeding network. The Y-junction 16-way unequal feed network used a Taylor *N*-bar distribution power divider, where *N*= 6 and SLR = -30 dB, and it is designed on RO4003, 0.2 mm in thickness. This Tayler distribution is adapted to suppress the sidelobe level and reduce the grading lobe, where the center to center spacing is 1.2 λ_0 (λ_0 =5mm @ 60 GHz). The feeding network is sounded with a 2D uniplanar EBG structure, and it is designed on a RO4003 substrate with 0.2mm in thickness and optimized to obtain a band gap around 60 GHz to cover the ISM band, as shown in the Fig. 5.8. The optimized dimensions of the 2D EBG unit cell are listed in Table 5.4. The overall dimensions of the1 × 16 E-plane beam-steering phased array are 174.3mm in length, height is 6.83mm, and width is 108.2mm.

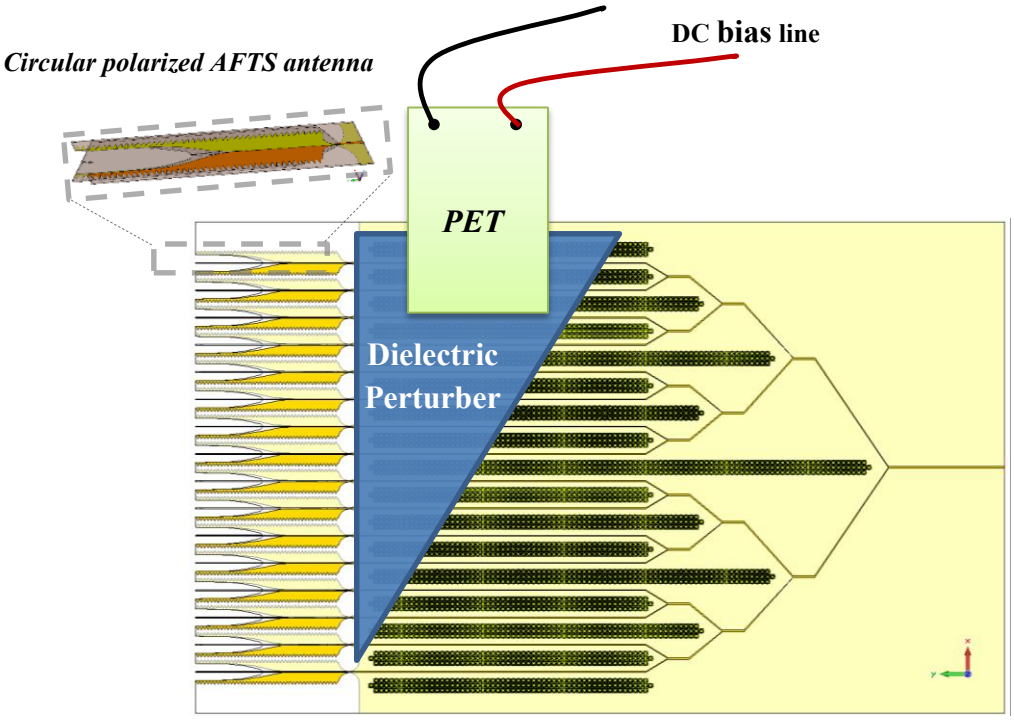

Figure 5.26 1 × 16 E-plane beam-steering phased array with circularly polarized AFTS-SC antenna and EBG structure.

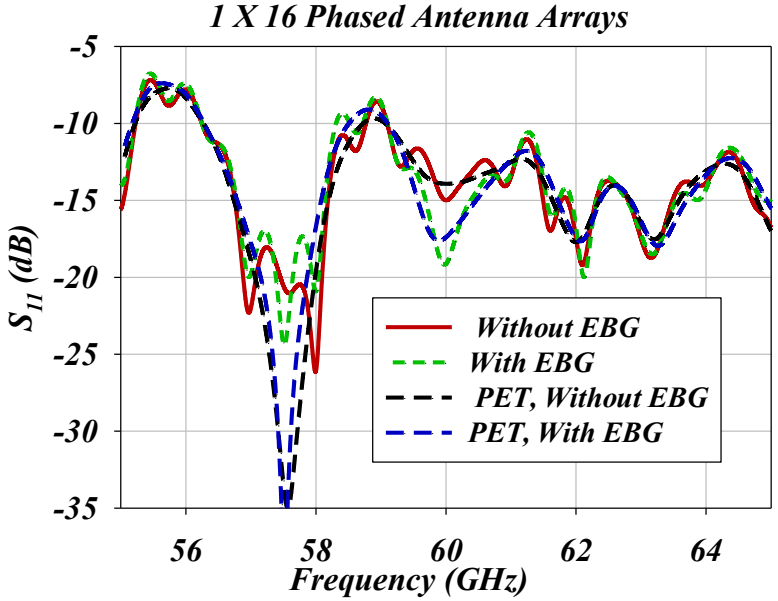

Figure 5.27 The reflection coefficient of 1 × 16 CP AFTS beam steering phased array results with EBG, without EBG, with PET and EBG, and PET without EBG.

The reflection coefficient from the 1 × 16 CP AFTS beam steering phased array results simulated at four different structures is shown in Fig 5.27. The simulated bandwidth

for S_{11} < -10 dB covers 56.2-65 GHz. There is an insignificant impact on S_{11} for the PAA under maximum perturbation ($\Delta_L = 0mm$) and no perturbation as with EBG or without EBG through the entire bandwidth. This establishes broadband characteristics and there is an insignificant effect on the reflection coefficient under these four conditions, which is a major advantage of this approach.

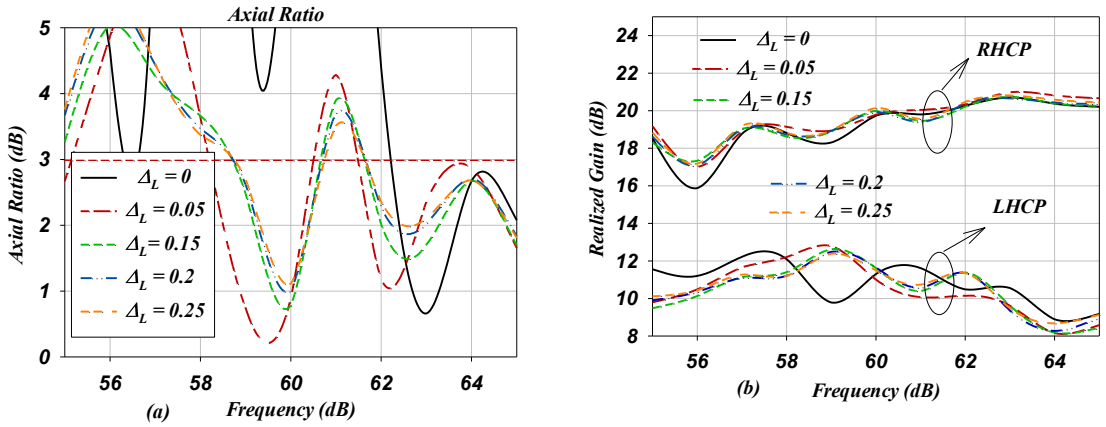

Figure 5.28 The impact of perturbations between values of 0 - 0.25mm on (*a*) the axial ratio, and (*b*) RHCP and LHCP realized gain.

The PET perturbes the triangle shaped substrates when voltage DC is applied in practical employment; the perturber change of Δ_L can be simulated with CST-MS to investigate its impact on overall PAA characteristics. Furthermore, the impact of varying Δ_L from 0 - 0.25mm perturbations on the axial ratio, and RHCP and LHCP realized gain is shown in Fig. 5.28. The simulated RHCP axial-ratio of the PAA system, with Δ_L from 0.05 - 0.25mm, at an AR of less than 3dB maintained across two bands of about 58.5-60.5 GHz and 61.5.5-65 GHz, is indicated in Fig. 5.28 (*a*). The minimum AR is about 0.2dB at 59.5GHz, when $\Delta_L = 0.05mm$. However, when the perturber substrate is in contact with the microstrip line, which is at $\Delta_L = 0$ *mm*, the AR (< 3dB) shifts to a higher frequency band to cover 62.5-65 GHz. This indicates high EM coupling between the microstrip lines occurring at direct contact of the perturber, which can be eliminated by Δ_L just above zero

value if avoiding perturber to be in direct contact as when $\Delta_L = 0.05mm$. Meanwhile, there is the insignificant impact of perturbations when Δ_L is varied from 0.05 - 0.25mm on RHCP and LHCP realized gain. This is seen in the results of the RHCP and LHCP realized gain, which indicate that the CP of the PAA system is RHCP dominant to LHCP, and which also show 10dB in gain range difference for most values of Δ_L.

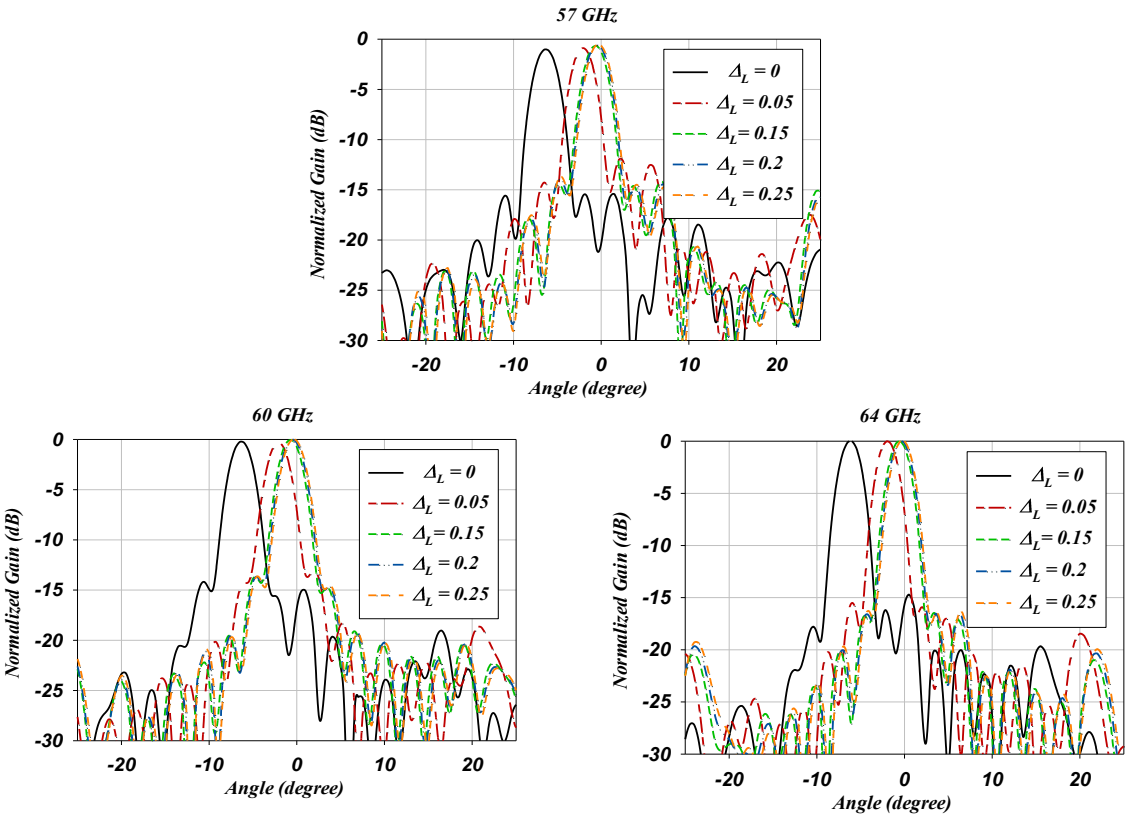

Figure 5.29 Simulated CP beam steering radiation patterns with Δ_L = 0 to 0.25mm perturbations at 57, 60, and 64 GHz.

Fig. 5.29 shows the simulated E-plane beam steering radiation patterns when varied Δ_L = 0 to 0.25mm at 57, 60 GHz, and 64 GHz. At Δ_L = 0.25mm, corresponding to no delay line and no steering effect, the highest SLRs are -14, -14.5, and -17 dB at 57, 60, and 64 GHz, respectively. Furthermore, the maximum beam steering angle occurs at Δ_L = 0mm, steered by 6.3°, 6.29°, and 6.1° at 57, 60, and 64 GHz, respectively, where the HPBW is stable about 2.8° at E-plane and 31.5° at H-plane. The SLR is kept lower at all perturbations

(Δ_L = *0 to 0.25mm)*, which indicates stable performance over the 60 GHz ISM band. In addition, the PAA system approaches excellent circular polarization with a wideband about 2 GHz around 60 GHz.

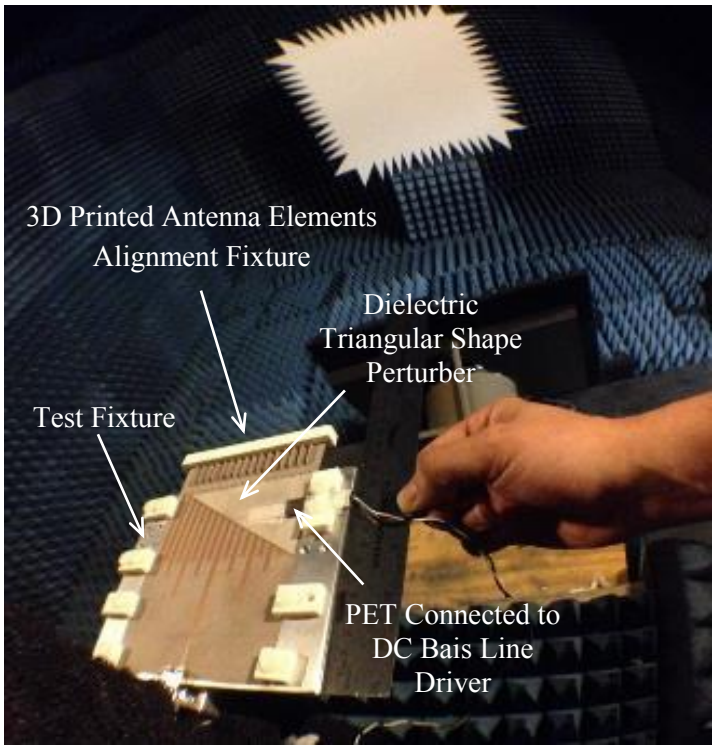

Figure 5.30 The prototype photograph of the 1 × 16 CP AFTSA PET phased array mounted on test fixture at anechoic chamber.

The fabricated prototype of the proposed The 1 X 16 phased antenna array with circular polarized with EBG structure is presented in Fig. 5.30. A triangular shaped dielectric perturber attached to the PET moves vertically on the microstrip lines with the DC bias voltage provided by driven circuit provides DC 0-100volts. The prototype was fabricated using a LPKF ProtoLaser machine. Fig. 5.31 shows the measured and simulated S_{11} results in case when PET is at maximum perturber and without PET, where the S_{11} measured by PNA A5227N.

The measured S11 <-10 dB covers the entire bandwidth from 55 - 65 GHz for both cases without and with maximum PET perturbation. It demonstrates under these two conditions, the return losses do not change significantly, which is an important advantage of use PET technique [50]. The measurement results are in good agreement with the calculated results. The measurement results show similar three resonances trace to the calculated. However, a slight shift may be caused by fabrication tolerance, and the tolerance in the substrate's dielectric constant.

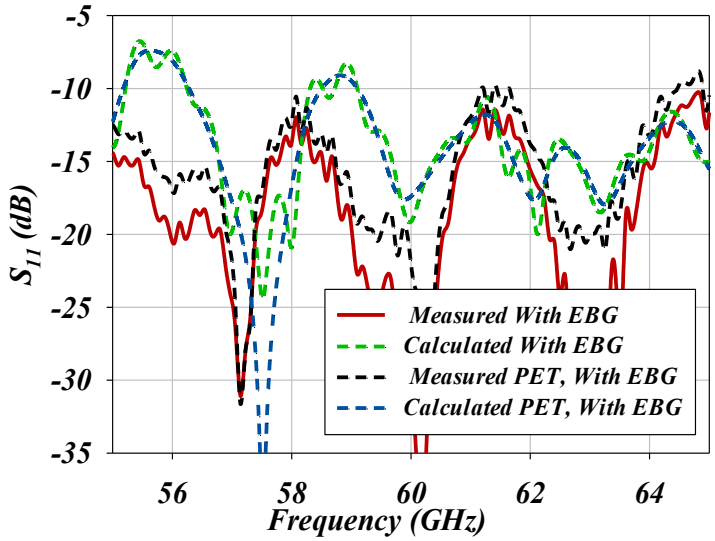

Figure 5.31 the measured and calculated results of reflection coefficient for 1 × 16 CP AFTSA phased array results with EBG in case with and without PET.

Fig. 32 shows the measured and simulated RHCP axial-ratio of the PAA system, with no perturber and with maximum perturbation when PET in the right side and when PET in the left side. The measured AR at maximum perturbations are alternated similarly to the calculated results when $\Delta_L = 0$ (maximum perturbation). Both results agrees for an AR of less than 3dB after 62 GHz to 65 GHz. Fig. 5.33 shows the measured radiation patterns of E-plane in case without EBG at 57, 60, and 62 GHz. This radiation measurement is done with two triangular dielectrics perturber tested individually. In order

to steer the beam to the left, The PET is performed with the right side triangular perturber, and replaced to the left side triangular perturber to steer the beam to the right. Fig. 5.33 shows the E-plane beam steering when 100 DC-volt is applied to the PET caused a maximum perturbation when PET performed with the right side triangular perturber and when performed with left side triangular perturber to steer the beam to the right. The high SLR at these frequencies is attributed to increases in the mutual coupling between antenna elements and beam broadening appears caused an increase in sidelobe levels.

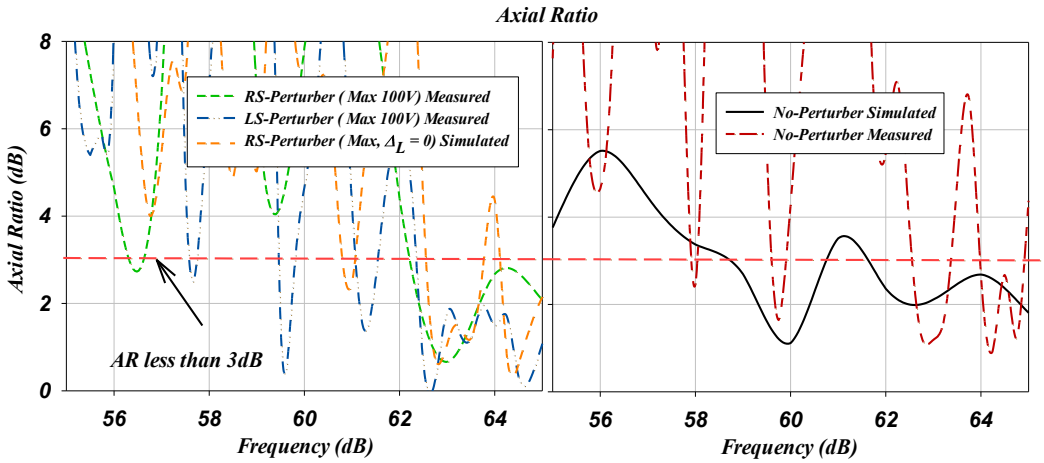

Figure 5.32 The measured and calculated axial ratio for 1 × 16 CP AFTSA phased array results without EBG in case without and with PET mounted on right side (RS) and when mounted on left side

Fig. 34 shows the measured AR results of a circular polarized of 1 × 16 CP AFTSA phased array with EBG, AR ≤ 3 dB are around 59.75 GHz and from 62.75 GHz to 65 GHz. The measured AR for RS-perturber and LS- perturber results appeared to be relatively similar and in a good agreement to the calculated one. However, there are some discrepancy between the measured results caused mainly by three facts. First, the tolerances of the measurement setup and equipment errors, where the AR depends on the ratio of the E and H, which is more likely at any small error will reflect clearly on the axial

ration results. Second, is the fabrication tolerance, and third is imperfection in soldering that proceed to attach the 16-vertical-element into the horizontal element

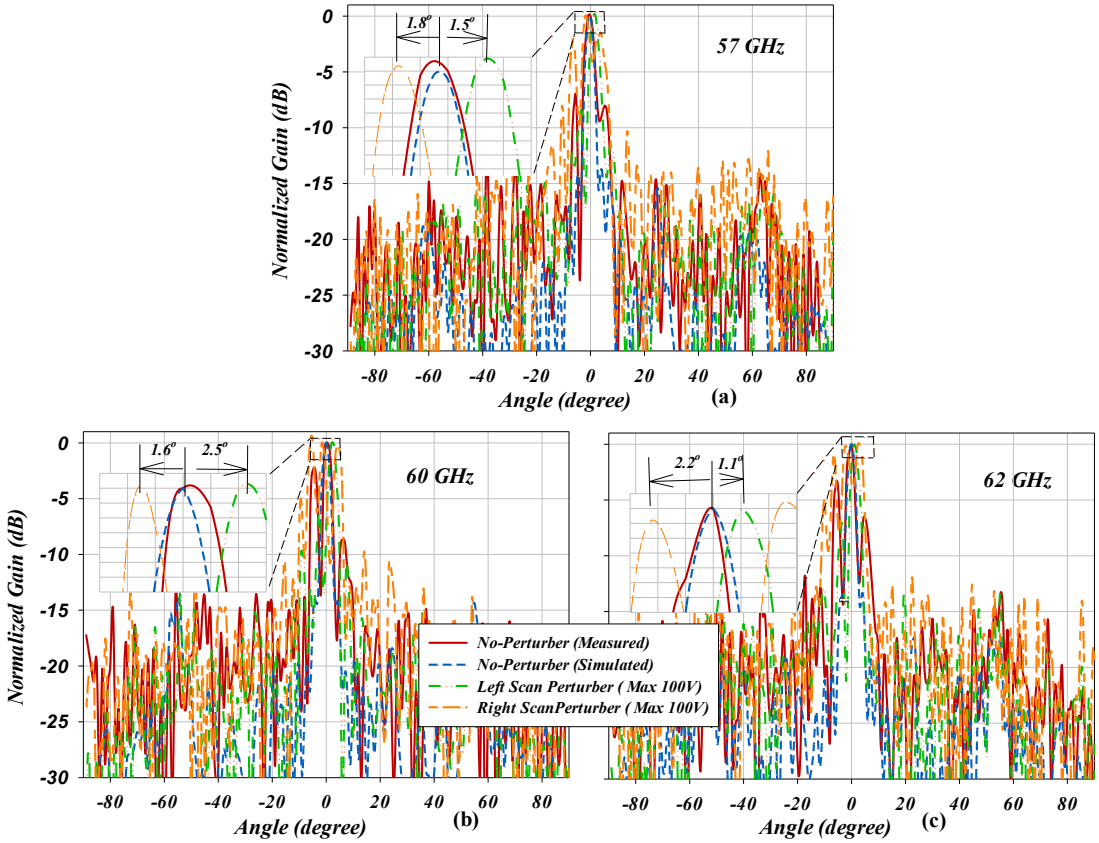

Figure 5.33 Measured E-plane beam steering radiation patterns of CP 1 × 16 AFTSA-SC array without EBG, maximum perturbations at 57, 60, and 62 GHz.

Fig. 35 shows the measured radiation patterns 1 × 16 CP AFTSA phased array results in case with EBG. As shown, the sidelobe level is supressed and the mainlobe directive in the presence of EBG. The feeding network is surrounded by EBG structure that reduced the surface waves and supressed the mutual coupling between the antenna elements and maintain the sidelobe level lower compared with the array without EBG as shown in Fig. 5.35. The measured E-plane radiation patterns at 57, 60, 62 GHz are exhibits beam scanning range approximately 2.5°-3.1°. At 57-64 GHz, the - 3 dB beamwidth are

varied approximately from 2°-2.7°, which is the requirement for imaging/ detection systems.

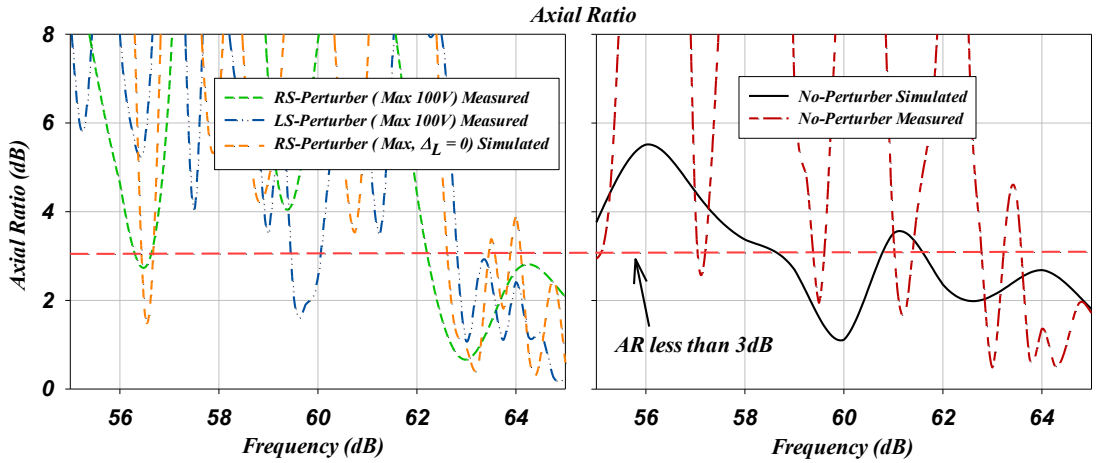

Figure 5.34 The measured and calculated axial ratio for 1 × 16 CP AFTSA phased array results with EBG in case without and with PET mounted on right side (RS) and when mounted on left side.

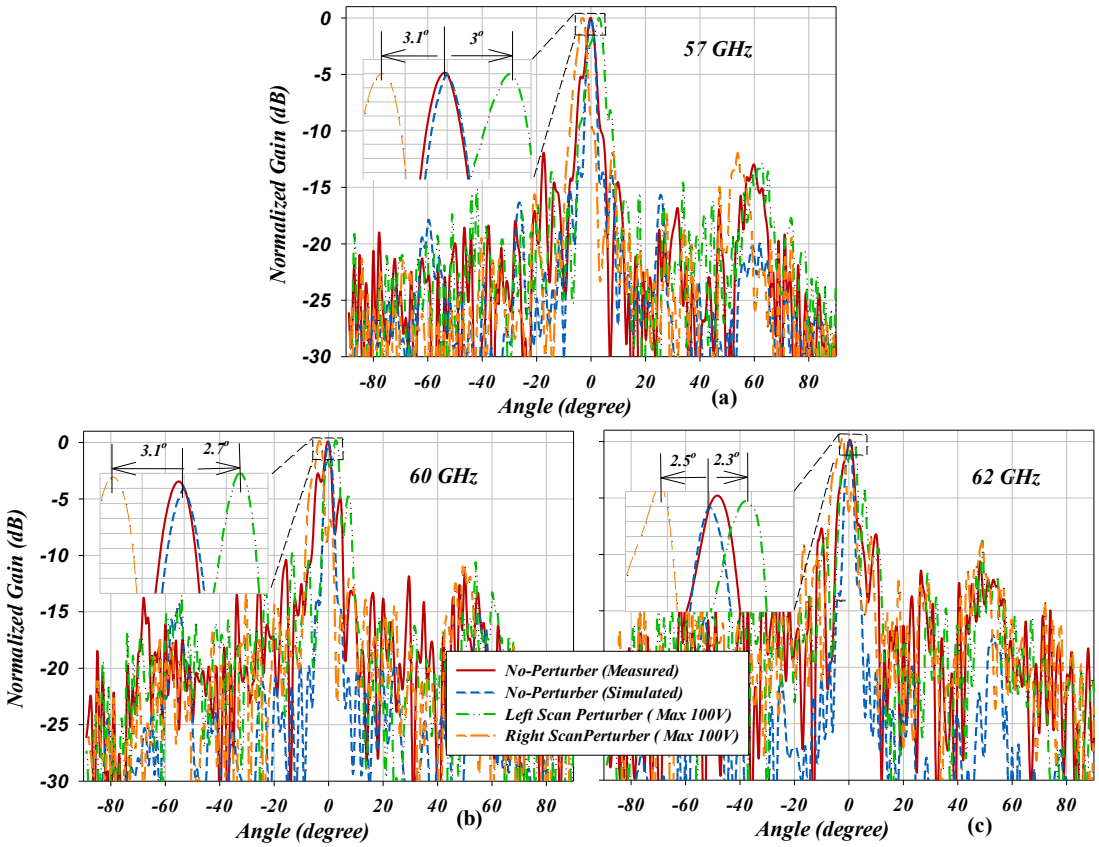

Figure 5.35 Measured E-plane beam steering radiation patterns of CP 1 × 16 AFTSA-SC array with EBG, maximum perturbations at 57, 60, and 62 GHz.

5.5 Wide-Scan AFTSC-MSC Array Fed with Grooved Spherical Lens Antenna

A new profile for a three-element switched-beam AFTSC-MSC array loaded with a grooved homogeneous PMMA spherical lens is presented. Fig. 5.36 shows the three elements of the AFTSC-MSC array profile, as well as the array profile loaded with a grooved spherical lens. The angular spacing for three AFTSC-MSC elements is 30° along the *x-y* axis, and the three elements are designed on a thin 20 mm RO4003 (ε_r = 3. 55, $tan\delta$ = 0.0027) substrate. Each single element is designed to cover the ISM-band, and the optimized dimensions are listed in Table 4.3 (chapter 4). The angular spacing φ = 30° can be utilized to cover a 60° radiation angle.

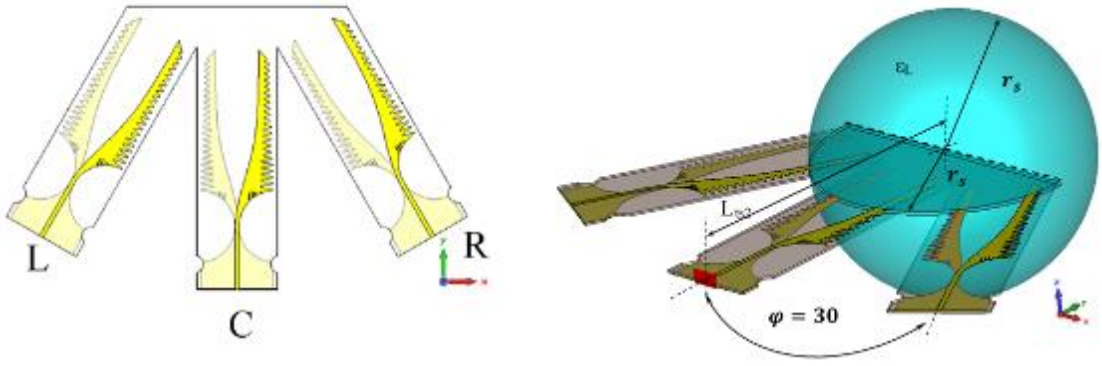

Figure 5.36 Three-element AFTSC-MSC array profile on the left, and on the right, the array loaded with a grooved spherical lens.

The calculated gain responses of the proposed antenna with and without a GS-lens are presented individually at each excitation feed for the antenna's C, R, and L elements, as shown in Fig. 5.37. The gain of the three-element AFTSC-MSC array profile without a GS-lens is relatively similar, although, the gain for the C- element is slightly higher than for the other two side-elements, which is expected, since the substrate extension at the front end of the C-element increases the gain. For the three-element AFTSC-MSC array loaded with a GS-lens, the gain increases by 2.5 dB to 5 dB, and the gain is almost stable over the

entire frequency band. Also, because the C-element is positioned at the center, the gain is higher by 1-2 dB compared to the side elements.

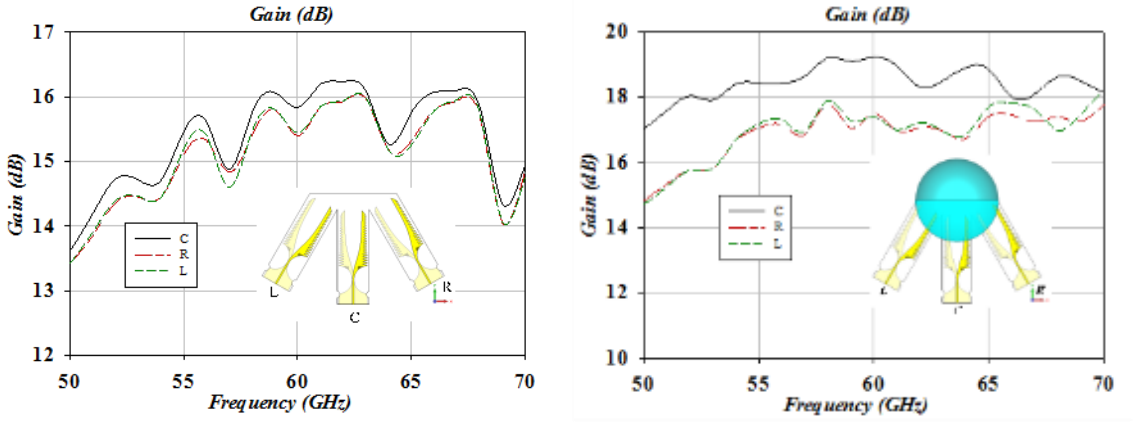

Figure 5.37 The gain comparison between the three-element AFTSC-MSC array profile on the left; and on the right, the array loaded with a grooved spherical lens.

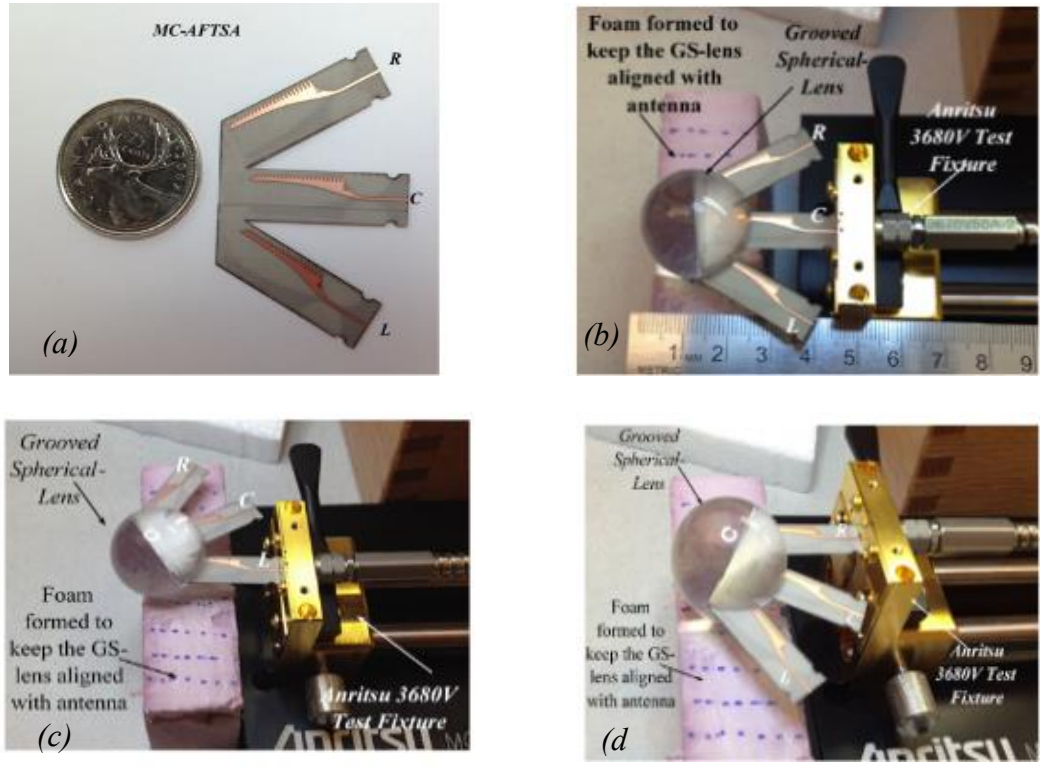

Figure 5.38 (*a*)**:** Photograph of the proposed AFTSA-MSC array design and the S11 measurement setup of the antenna with a grooved spherical lens when (*b*) element- C is connected, (*c*) element- L is connected, and (*d*) element- R is connected.

The fabricated prototypes of the proposed AFTSA-MSC array, and the S_{11} measurement setup for the antenna with a grooved spherical lens at three feeding stages, is illustrated in Fig. 5.38. The prototypes were fabricated using a LPKF ProtoLaser machine. The S_{11} of three AFTSA-MSC array is measured by PNA A5227N, and the proposed antennas are connected to Anritsu 3680V test fixture able to measure up to 67 GHz.

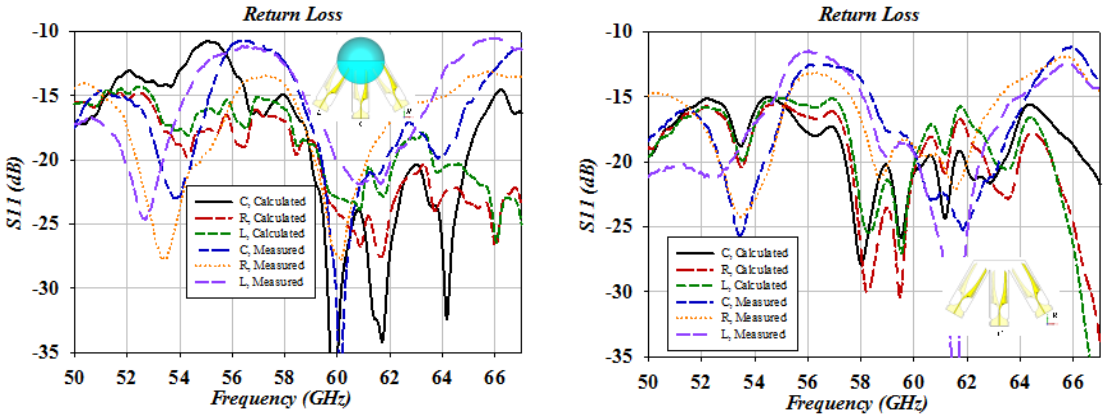

Figure 5.39 Measured and simulated return loss comparison between the three-element AFTSC-MSC array profile, on the right, and the array loaded with a grooved spherical lens, on the left.

Fig 5.39 shows the measured and simulated S11 results in a comparison between the three-element AFTSC-MSC array profile, on the right, and the array loaded with a grooved spherical lens, on the left. The S11 <-10 dB covers the selected band from 50 - 67 GHz for both arrays with or without a GS-lens. There is no physical contact of the conductive layers (copper) between the three antennas, and the input ports are separated by 30 degrees angle to achieve a very low coupling. Therefore, at the measurement of each antenna port, no need for 50 Ohm terminals for other two antennas, similar technique was used by [41]. The measurement results show an adequate trace to the calculated ones; however, a slight shift may be caused by fabrication tolerance, and the tolerance in the

substrate's dielectric constant. Consequently, the measurement results are in good agreement with the calculated results.

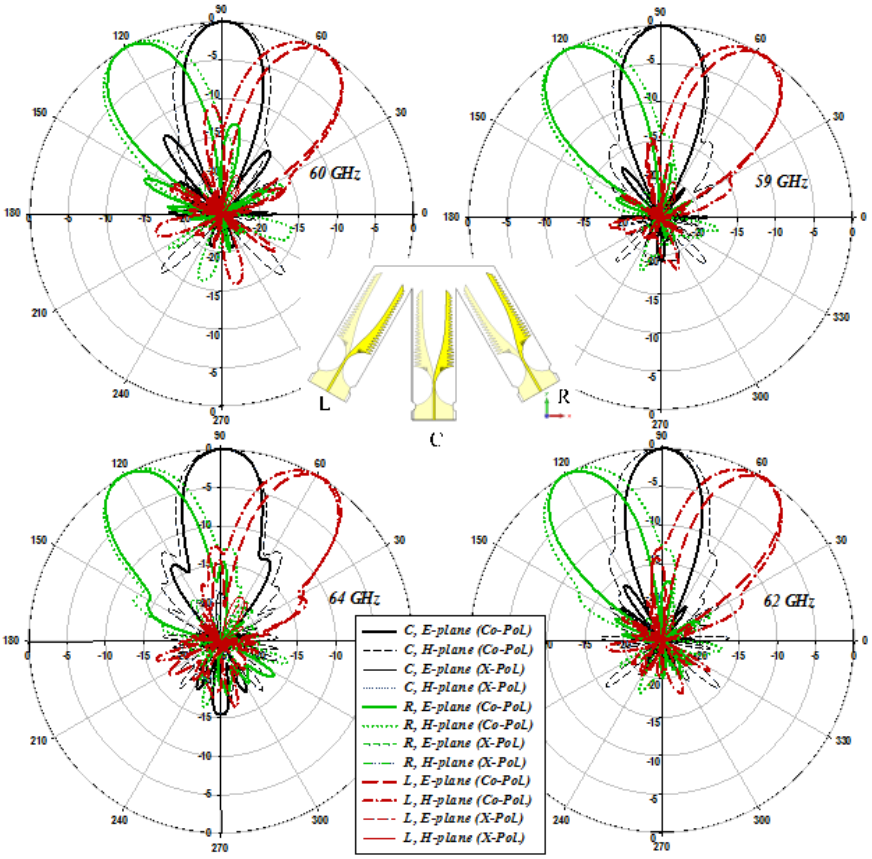

Figure 5.40 Radiation patterns simulated at 59, 60, 62, and 64 GHz for the three-element array.

In order to increase the data rate, a three-element AFTSC-MSC array with a GS-lens loaded operating as a single-pole three-throw switch can be used to alternate between the three beams. This proposed three-array can also be used as independent transceivers connected to each element, which leads to increasing the data rate of communications. Fig. 5.40 shows the simulated radiation patterns of the three-element array, and Fig. 5.41 shows the measured and simulated radiation patterns of the three-element array loaded with a grooved spherical lens. The radiation patterns are presented in the co-polarization and cross-polarization of both the E- and H-plane. The beam peak of the C-element is pointed

at 90°, the L-element at 60°, and the R-element at 120° in array of total radiation angle coverage of 60°. As seen in Fig. 5.40, radiation patterns are in the endfire direction with relatively similar patterns in the E-plane and H-plane and very low sidelobes. Fig. 5.41 shows the measured and simulated E-plane patterns that when the proposed grooved spherical lens is loaded to the three-element array at frequencies of 59, 60, and 62 GHz. The array is beamformed the radiation patterns, where the beamwidth of the E-plane is wider than the H-plane and there is coverage of a wider angle area and an increase in antenna gain while keeping the sidelobe level low. Therefore, this proposed antenna profile delivers a high performance in beam switching with wide angle coverage, a low profile, and a low mutual coupling design.

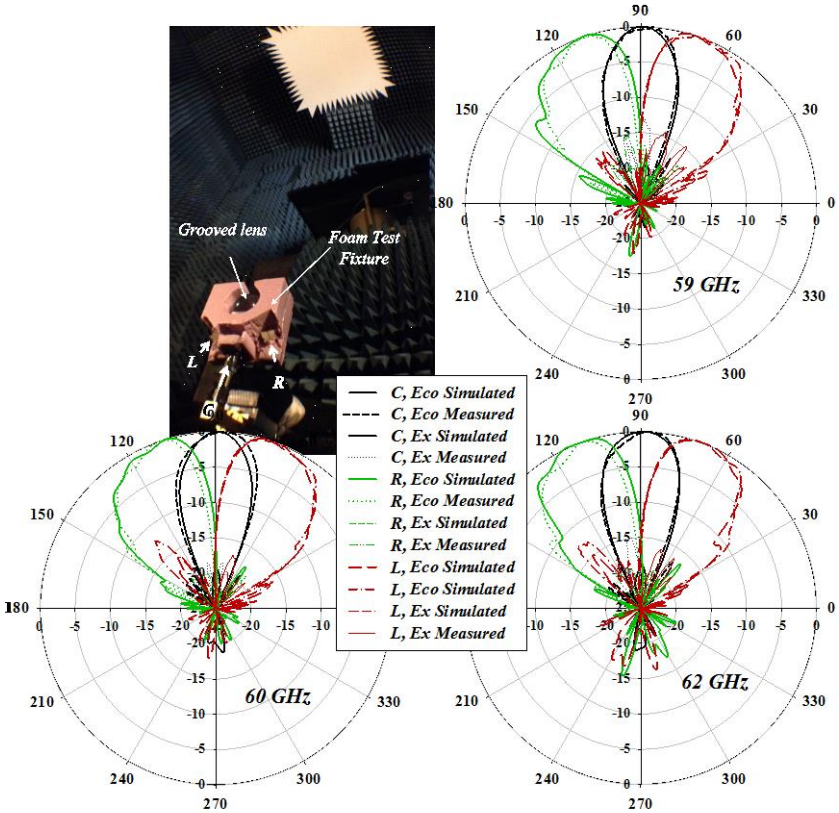

Figure 5.41 Measured and simulated radiation patterns at 59, 60, and 62, for the three-element array loaded with a grooved spherical lens.

5.6 Summary

In this chapter, different 1 × 16-element beam steering antenna arrays with low-cost piezoelectric transducer (PET) controlled phase shifters were presented. First, a Y-junction power divider with an alternative feed network reducing the discontinuity caused by the feed line bends was introduced. The new unequal division is used with Taylor N-bar in order to reduce the SLR and grading lobes. Second, the 1 × 16-element beam steering phased array designed with a 60 GHz AFTSA-SC achieves a gain around 20dB, with a feed network surrounded by EBG structures to reduce the coupling between feed lines and surface waves. Finally, the design of a circularly polarized 1 × 16-element beam steering phased array with and without EBG structures shows a wideband impedance band which covers the entire ISM band, and a circular polarization bandwidth of 2 GHz is achieved. Finally, a wide-scan array AFTSC-MSC fed grooved spherical lens antenna has also been presented. AFTSC-MSC array introduces a high level of optimization when the antenna is loaded with a grooved lens. These 60 GHz phased array designs achieve a high performance in such a wide bandwidth; they have high gain, low feeding network loss, low cost, and low profile. Thus, with these features, the PAA fulfills the requirement to operate in MMW imaging/detection systems as a scanning sensor.

Chapter 6: 60GHz Imaging Detection Applications of Concealed Objects

6.1 Introduction

This chapter is divided into two main sections. Section 6.2 introduces the background materials for imaging / detection of a target, and then compares the performance of two different scanning probes: a V-band standard gain horn (SGH) and an improved 60 GHz AFTSA -based antenna. While, the second section presents the experimental imaging /detection results for various types of concealed weapons and liquids underneath different materials including clothes, plywood, and plastics. The proposed 60 GHz scanning system setup is described showing its flexibility and reliability.

6.2 60GHz ISM-Band Imaging/Detection

An active monostatic 60GHz ISM-band imaging system for detecting a target will be presented in this section. The image is established by linear planar scanning, through a set of points arranged to form a rectangular contour plot. This technique uses a short pulse in the 60GHz ISM-band frequencies, provided by a network analyzer (N5227A PNA) after the calibration over the desired frequency band [59]. This signal pulse is reflected back from the object under test (OUT) presented in the time domain and transformed to the Inverse Fast Fourier Transform (IFFT) [162].

6.2.1 60 GHz ISM-band Monostatic Imaging/Detection System Configuration

Fig. 6.1 shows the proposed 60 GHz ISM-band detection /imaging system. The system consists of a linear mechanical scanning platform, generating XY movement with a 300*mm* × 300*mm* scanning range of the object field of view, and oriented perpendicular with respect to the lens-focused beam. The overall platform is 66 × 43 × 13 cm^3 and is

surrounded by microwave absorbers to prevent any reflections from the 2D scanner structure. The absorber is framed with a lightweight foam panel and this structure is mounted on a linear actuator plate. The target is replaced at the center of the platform, and behind the target is 270 × 205 × 1 mm^3 of natural animal leather (to simulate human skin) supported by ≈ 2mm in thickness of reinforced paper. The millimeter wave antenna probe is located at the optical lens focal plane position, and a microwave absorber is placed behind the antenna to prevent any back reflections. The convex lens aperture is 114.3mm in diameter and made of Polymethylpentene (TPX, ε_r =2.13).

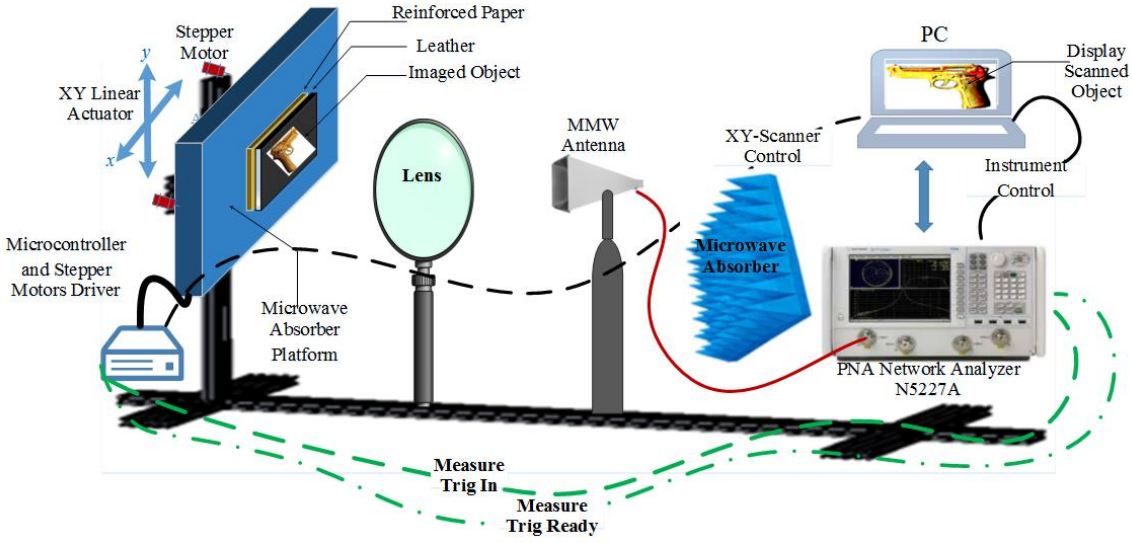

Figure 6.1 Monostatic MMW imaging/detection system setup.

A V-band coaxial cable line feeding the probe is connected, after prior calibration at ISM-band, 57GHz to 64GHz, to Agilent network analyzer PNA (N5227A). The calibration is done using the N4694A Electronic Calibration Module (ECal), 1.85 *mm* connector. After calibration, the obtained S_{11} data in frequency domain are considered as representation for the target reflections. The S_{11} data is then transformed into time domain using the Inverse Fast Fourier Transform (IFFT) embedded code in the PNA. The probe transmits a pulse and receives a reflected signal from the object. This reflection effect

appears in a certain peak of the IFFT curve, which is expressed as a change in the amplitude of the S_{11} at a certain time domain slot.

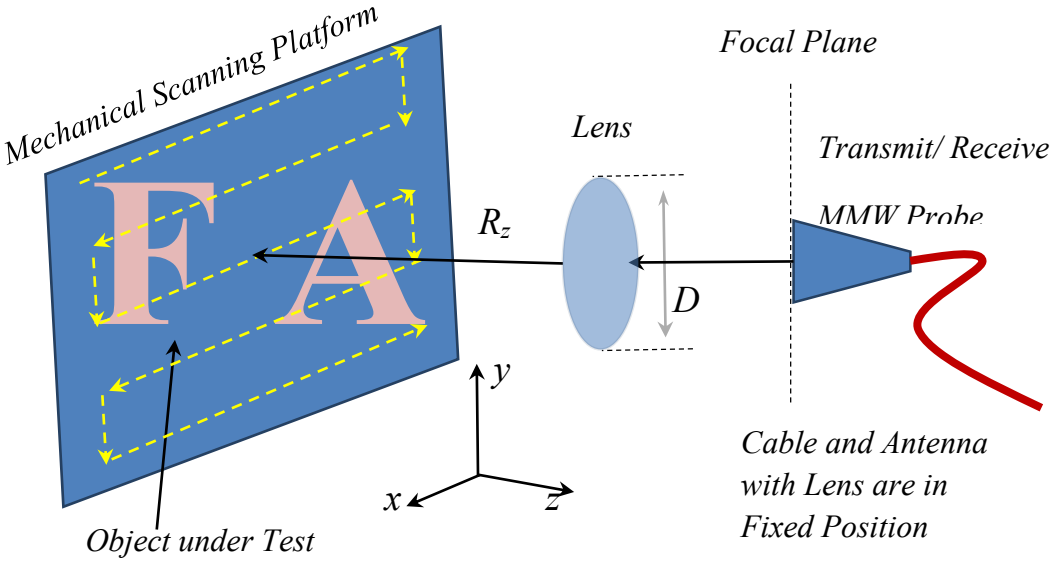

Figure 6.2 The scanning mechanism for monostatic imaging detection. The yellow dash lines illustrate the path for mechanical scanning of the platform with the object.

The system is controlled by the PC embedded in the PNA (N5227A) that sends and receives command signals from the microcontroller. Furthermore, the microcontroller is designed to drive two stepper motors that move the platform with the object in a 2D motion, as shown in Fig. 6.2's yellow dash path. The PC controls the step motion at X and Y locations and likewise for the image resolution steps, which can achieve a minimum of 1mm for each XY step of 300 × 300 pixels. At each specific step, the microcontroller sends a trigger pulse to the PNA to read and record the measured data of the S_{11} amplitude peak values, which are marked at the specified time domain slot. When the measured data is recorded and inserted into a real time 2D plot, the PNA sends a signal as a ready trigger

back to the microcontroller with the command to move to the next step, until the scanning of the 2D frame is completed.

6.2.1.1 Signal Pre-Processing

The reflection coefficient measurement S_{11} is based on Monostatic system type as stepped frequency continuous wave (SFCW) mode has been conducted using network analyzer PNA (N5227A). After calibrating the PNA, the S_{11} is measured at N = 201 frequency points. The PNA measures both the amplitude and phase of the received signal at each frequency point (f_n) with respect to the transmitted signal has been illustrated in [163], [164]. The transmitting continuous wave signal at the antenna at f_n is

$$E_t(f_n) = E_o e^{j2\pi f_n t} \tag{6.1}$$

The receiver signal from the object under test of a complex scattering coefficient $s(z)$ at a distance z from the antenna with respect to transmitted signal is expressed by

$$S(f_n) = \frac{E_r(f_n)}{E_t(f_n)} = \frac{1}{z_o}\int_0^{z_o} s(z)\, e^{-j2\pi f_n\left(\frac{2z}{c}\right)}\ dz \tag{6.2}$$

$$z_o = \frac{c_o}{2\Delta f} \tag{6.3}$$

$$\Delta f = \frac{BW}{(N-1)} \tag{6.4}$$

where z_o is the unambiguous range of the radar, c_o is the velocity of the signal, Δf is frequency step size of the network analyzer full spectrum, and BW is antenna bandwidth. Transforming the data from frequency domain to time domain is obtained using Inverse Fast Fourier Transform (IFFT), as given by

$$s(z) = \sum_{n=1}^{N-1} S(f_n)\, e^{j2\pi f_n\left(\frac{2z}{c}\right)} \quad dz \tag{6.5}$$

The received signal contains a scattered reflection from the target and unwanted scattered signals caused by the coaxial cable, connectors, and the antenna. These unwanted signals may add some delay to the received signal. In [165], this delay is subtracted in order to obtain the exact target distance through elimination of the unwanted signal effect by

$$s(z) = \sum_{n=1}^{N-1} S(f_n)\, e^{j2\pi f_n\left(z - z_{ref}\right)\frac{2}{c}} \quad dz \tag{6.6}$$

where z_{ref} is the distance measured from the target to the antenna. The Hamming window function may also be applied to eliminate any background clutter reflections and surface reflections.

6.2.1.2 Experiment Scanning Methodology

The movements of the platform are in an x-y plane trace motion as shown in Fig. 6.2's yellow dash line. The target is placed on the platform that mechanically scans in 2D movements, while the lens, antenna, and the cable connected to PNA is stationary, as demonstrated in Fig. 6.2.

The scanning method with a single antenna element measurement is similar to that utilized for a synthetic aperture array of $L_x \times L_y$ in the *x-y* (lateral dimensions), which is referred to as the overall step $i{+}p_x$ taking to scan in x-direction, and $i{+}p_y$ for y-direction; *PX* and *pay* indicate the final step values. Additionally, the synthetic element aperture is

$\Delta L_x \times \Delta L_y$ as illustrated in Fig. 6.3. The antenna range resolution ΔR_z and the cross range resolution ΔL_x are defined by

$$\Delta R_z = \frac{c_o}{2N\Delta f} \tag{6.7}$$

$$\Delta L_x = \frac{\lambda_c R_z}{2D} \tag{6.8}$$

where λ_c is the wavelength at the center of the bandwidth, R_z is the distance from the antenna to the target, and D is the geometric length of the antenna. The experiment scanning methodology of the MMW imaging/detection system is presented in the flow chart in Fig. 6.4.

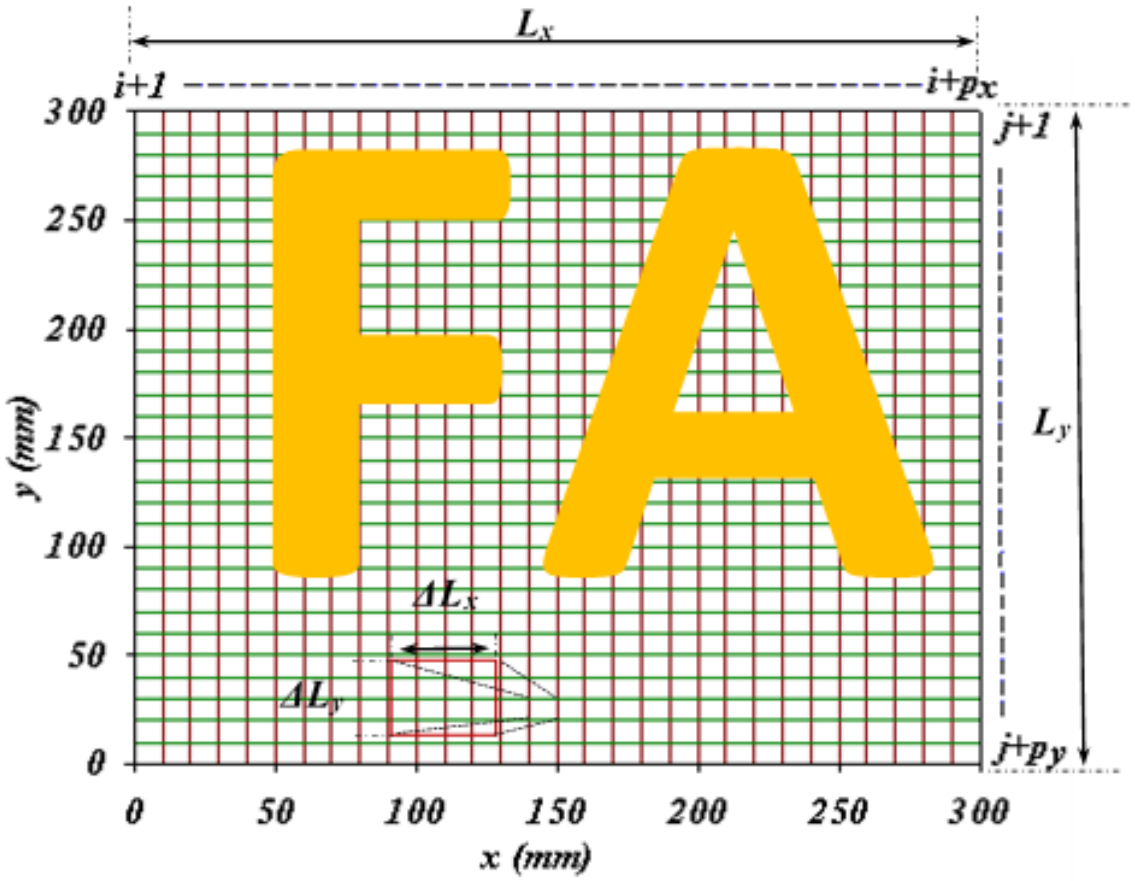

Figure 6.3 The platform scanned area of the synthetic aperture.

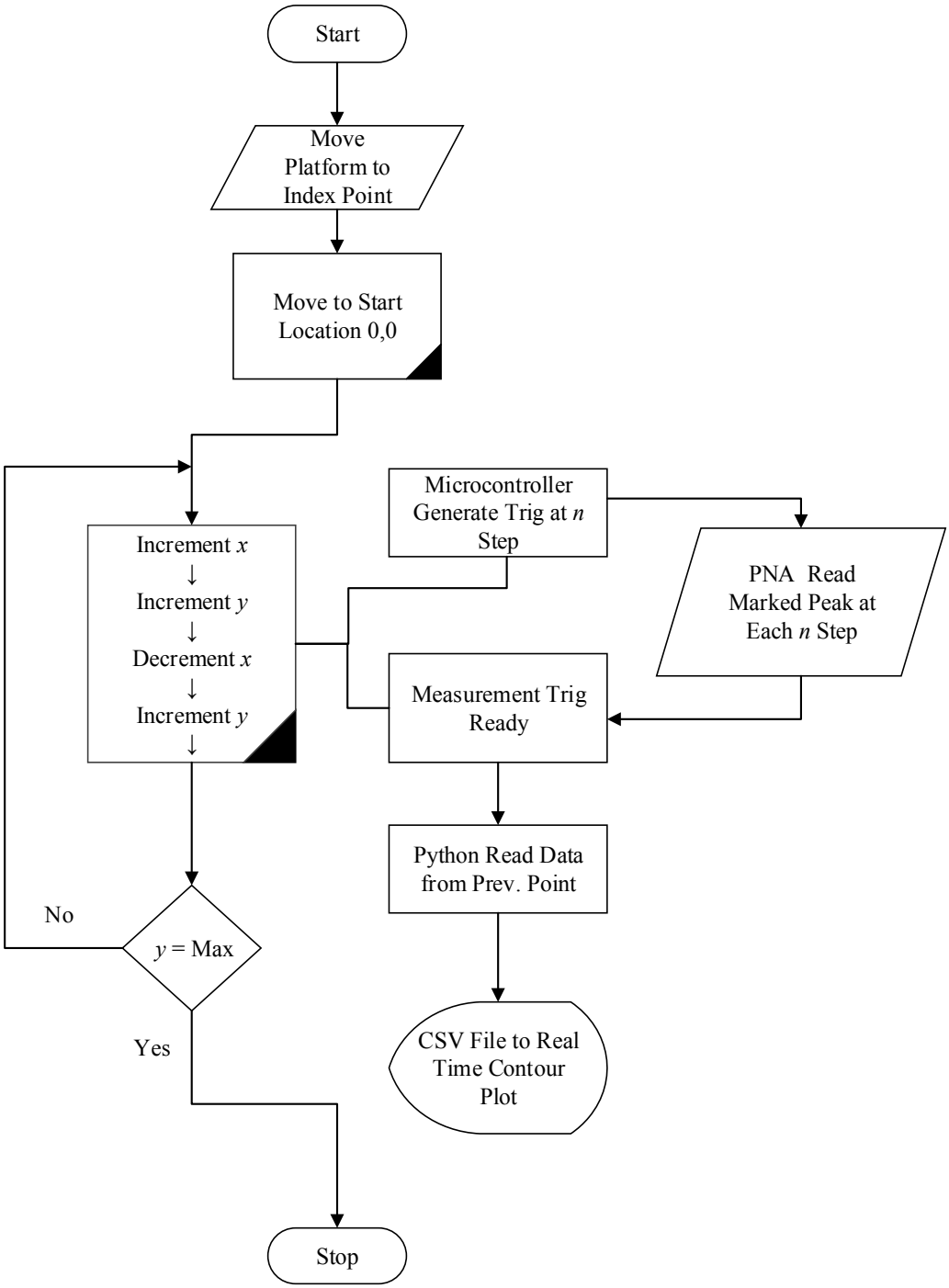

Figure 6.4 MMW imaging / detection system algorithm.

6.2.2 System Operation and Primary Results Using a V-Band SGH Antenna

The system performance and proposed antennas capabilities to operate at 60GHz imaging / detection system, initial experiment test is performed using a standard gain horn

(SGH) antenna as in system setup as shown in Fig. 6.5. The V-band pyramidal horn antenna (SGH-15-RP000 A16789) is connected to a coaxial to W15 waveguide transition (NCA-15-VRF00 A16789), which is connected to the network analyzer PNA through V-band coaxial cable (Megaphase, TM67-V1V1-36, DC to 67 GHz, 0.85mm). The SGH antenna is operated in a monostatic mode for transmitting and receiving EM waves. The calibration bandwidth of the PNA for the scanning system is selected to operate at an ISM V - band with a range 57 to 64 GHz. Fig. 6.6 shows the measured reflection coefficient of the SGH antenna.

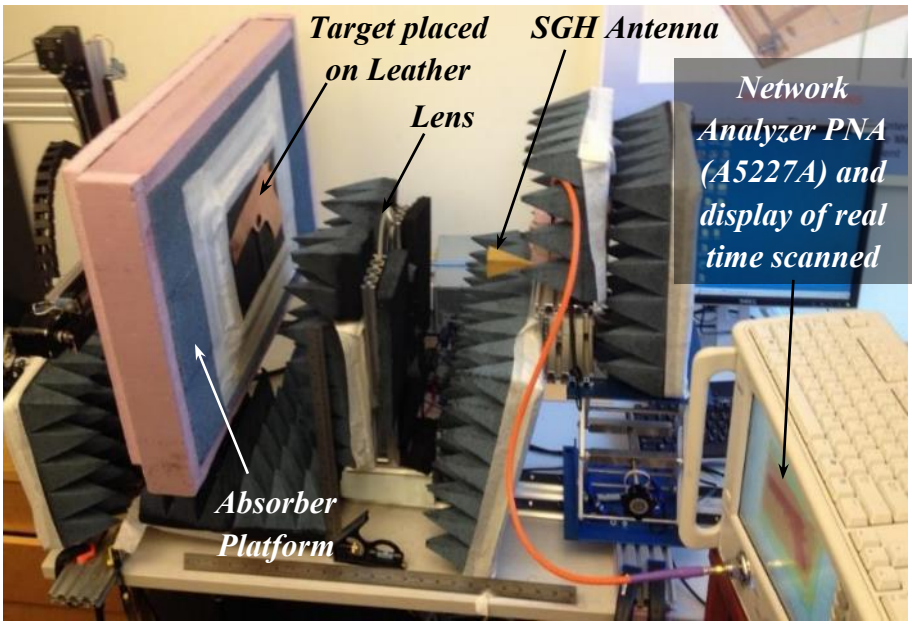

Figure 6.5 Imaging/ detection system setup using the SGH antenna.

Fig. 6.7 illustrates the result of the reflection coefficient S_{11} measurement in the time domain obtained by the SGH antenna at a single position, when the microwave absorber is in front of the antenna. Three main peaks are monitored: at 0.15 *ns*, 0.55 *ns*, and 1.2 *ns*. The first peak is due to the coaxial line, the second due to the transition from coaxial to W15 waveguide, and the third is due to the waveguide to pyramidal horn transition.

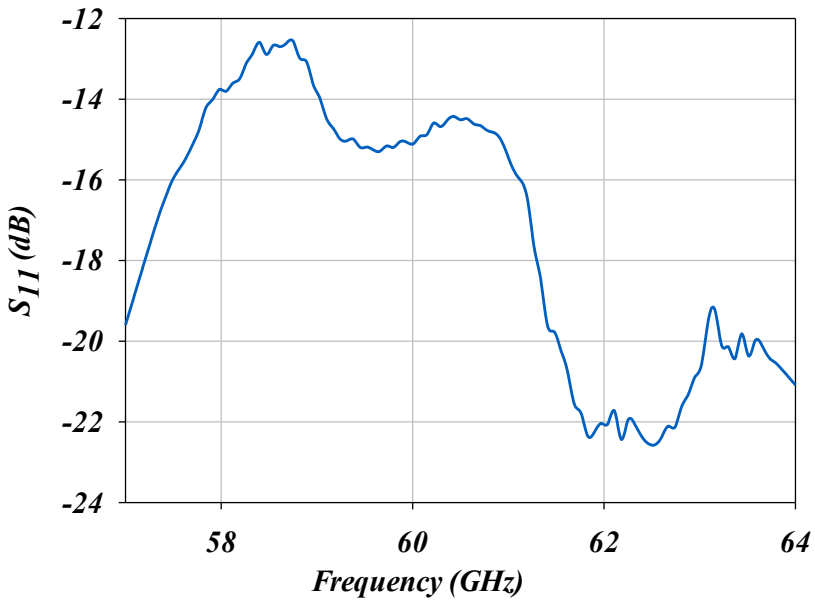

Figure 6.6 Reflection coefficient S_{11} of the SGH antenna.

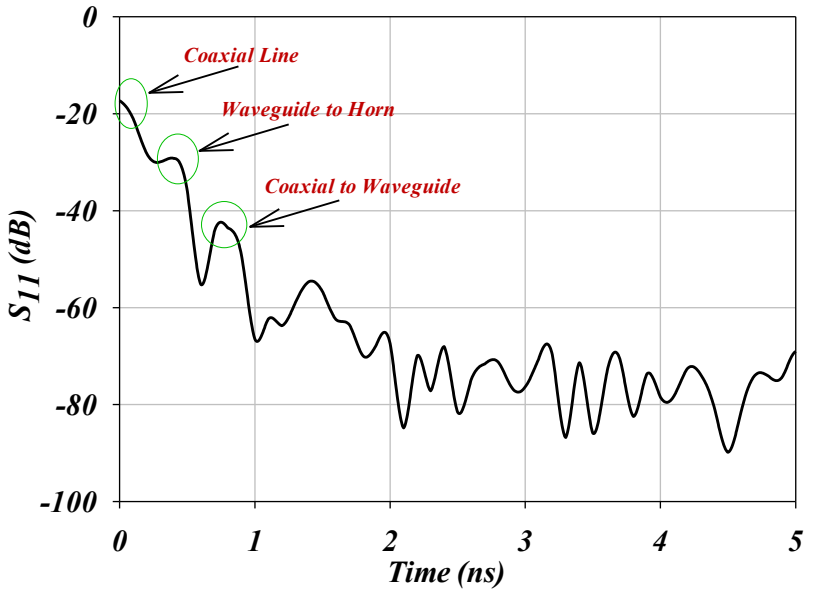

Figure 6.7 Reflection coefficient S_{11} vs time domain results of SGH antenna in front of an absorber.

The effect of the target presence in front of the scanning SGH antenna is monitored in the reflection coefficient S_{11} vs time domain results, as shown in Fig. 6.8. The peak at 2.7ns represents the reflection effected by the lens and the peak around 3.55 ns presents the effect of the targets. The effect of body model to be scanned is replicated using about

a 1mm layer of natural animal leather supported by a 2 mm thick layer of reinforced paper. Also, a 0.13 mm thick copper sheet is placed in the scanning system, and Fig. 6.8 shows a clear, high, difference between the reflection due to the leather, and the copper is about 15dB in amplitude value of S_{11} at 3.55 ns time slot.

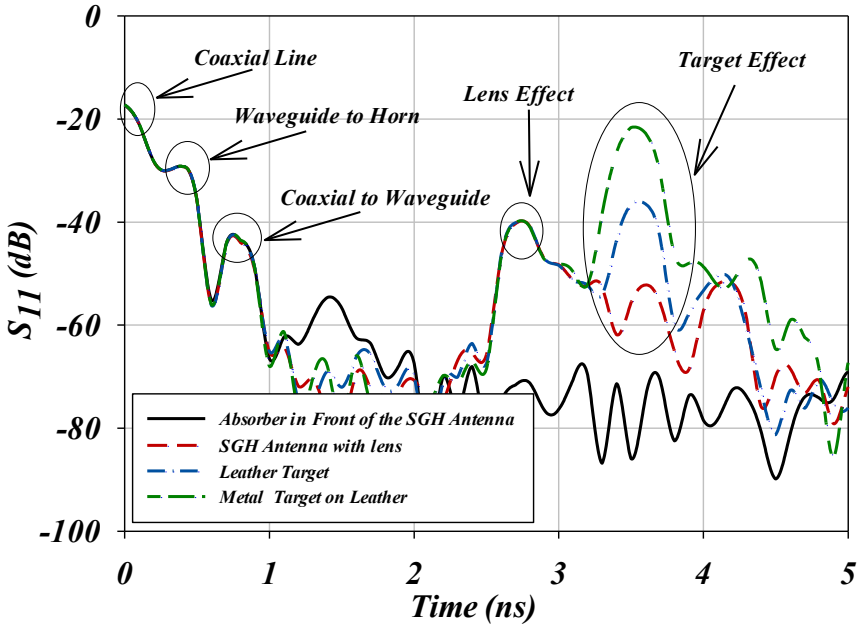

Figure 6.8 SGH Antenna responses in different stages; illustrates the target effect compared to SGH antenna in front of an absorber.

The initial scanning system used two test object charts (TOC) to experiment with detection of target shapes and orientations, as shown in Fig. 6.9. The test chart in Fig. 6.9 (*a*) is $70.5\times12.7\times0.13mm^3$ strip-lines supported with a 2 mm thick layer of reinforced paper. The spacing starts from 1.12*mm* to 25*mm*, and the strip lines are oriented horizontally, vertically, and by 45° angle. In Fig. 6.9 (*b*), a 0.13mm thick copper sheet is supported by a 2 mm thick layer of reinforced paper; the copper has had several holes cut out with different diameters starting from 1.68mm to 35mm. These two object charts are placed on a 1mm layer of natural animal leather supported by a 2 mm thick layer of

reinforced paper, all mounted individually in the center of the mechanical scanner platform (microwave absorber).

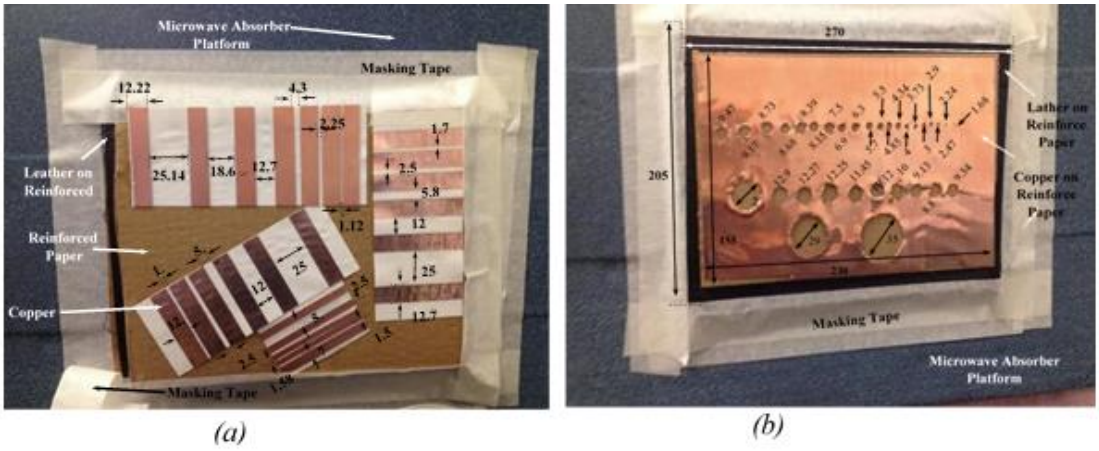

Figure 6.9 Photographs of the test object charts used in the imaging/ detection experiment, (*a*): copper strip-lines in different spacing orientations (*b*): copper sheet with circular holes of different diameters. All Dimensions are in millimeter.

The experimental results of the 60GHz imaging detection system are performed on two test object charts as shown in Fig. 6.9 and the corresponding results are shown in Fig. 6.10. The image resolution in the *x*-plane and *y*-plane are $\delta_x = \delta_y = 3mm$, and the field of view is $300 \times 300mm^2$ in the *x*-*y* plane. The 2D -image is obtained with real time contour reconstruction corresponding to target peak reflection after signal pre-processing. Figs. 6.10 (*a1*) and (*a2*) show, respectively, the image with and without natural leather in background of copper strip-lines in different spacing orientation. The illumination of the strip-lines dominates the illumination that comes from the leather layer, and the spacing between the slots is very clear for larger distances, however, the smallest gaps are slightly detected. Figs. 6.10, (*b1*) and (*b2*) show the images with and without natural leather in background of copper sheet with circular cutout holes. The majority of holes are detected, however, the holes $\leq$ 2.9mm in diameter are not. The illumination of the leather layer comes

through the holes in different intensity and the results show reliable reconstructed target image dimensions.

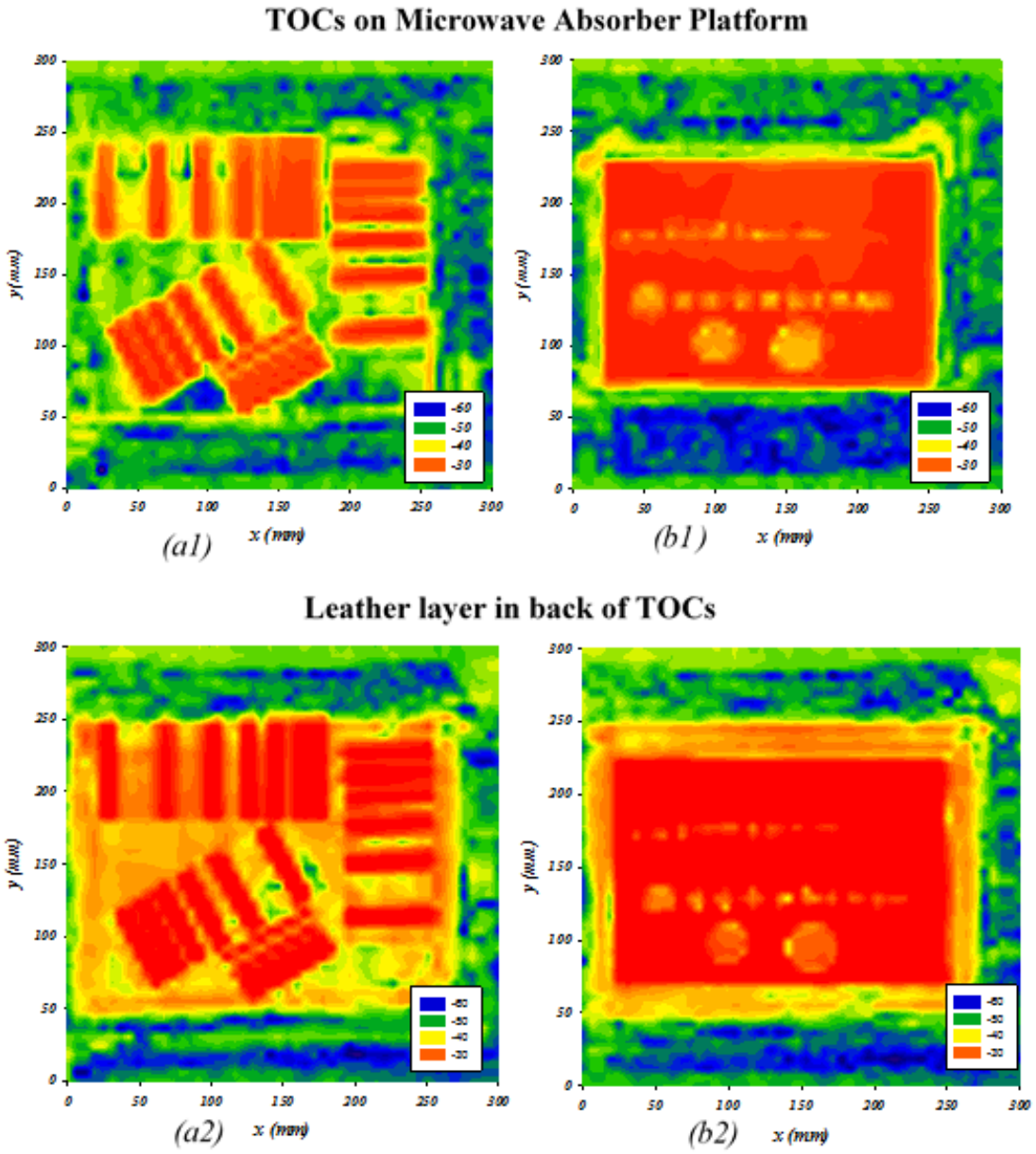

Figure 6.10 Measured 60 GHz image detection results on the x–y plane of the test object chart using SGH antenna; (*a1*): image of copper strip-lines, (*a2*): image of copper strip-lines in different spacing orientations with natural leather in the background (*b1*): image of copper sheet with circular holes, (*b2*): image of copper sheet with circular holes with natural leather in the background. Magnitude is in dB.

6.2.3 MMW Imaging Using Proposed Probes of Antipodal Fermi Tapered Slot Antennas

In this section, four proposed antennas presented in chapter 4 are utilized as a single element 60GHz probe for imaging/detection system. The multi sin-corrugations AFTSA antenna loaded with grooved spherical lens is experimentally tested in the monastic MMW image system as a probe. Then, a Dual polarized AFTSA-SC antenna probe is tested with regard to diversity in dual polarization effects on image resolution. Finally, a circularly polarized AFTSA-SC antenna MMW imaging probe is presented. The Reflection coefficient S_{11} vs time domain results are presented for each antenna. The probes are tested to reconstruct a MMW image for the same test object charts and two targets shown in Fig. 6.9.

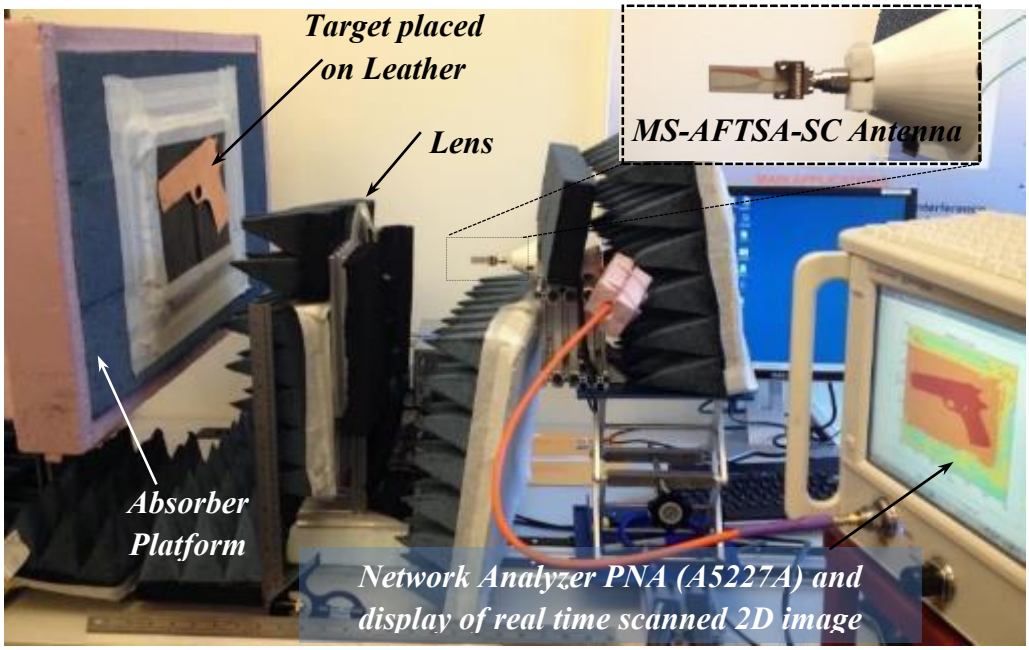

Figure 6.11 Imaging/ detection system setup using proposed AFTSA antenna probe.

Fig. 6.11 presents the photograph of the system setup, which corresponds to the detailed graph in Fig. 6.1. The proposed probe is placed in the lens focal plane at 140mm from the lens plane. An optical lens that is 114.3 mm in diameter is used, and the target

placed at about 125mm from lens aperture to measure a near-field MMW image. The antenna operates in a monostatic mode for transmitting and receiving EM waves generated by network analyzer PNA (Agilent, N5227A), which is connected through a V-band coaxial cable (TM67-V1V1-36, DC to 67 GHz, 0.85mm) from Megaphase. The calibration bandwidth of the PNA is selected to range from 57 to 64 GHz for all proposed probes.

6.2.3.1 60 GHz Multi *Sin*-Corrugations AFTSA Antenna MMW Image Probe

The characteristics of the multi *sin*-corrugations AFTSA antenna are described in section 4.6. Fig. 6.12 illustrates the measurement result for reflection coefficient S_{11} obtained in the time domain by the proposed probe. Four main peaks are detected, at 0.2 *ns*, at 0.6 *ns*, at 2.3 *ns* and at 3.1 *ns*. The first peak is due to the coaxial line, and a low reflection in the second peak indicates a good transition from coaxial to microstrip line of the antenna. The third peak is due to the reflection from the lens-air boundary. The fourth peak is the dominant one and presents the reflection caused by the target placed on the mechanical scanner platform. Furthermore, at 3.1 ns time slot, the difference in amplitude between the reflection caused by the leather and the copper is about 12dB, and that is enough in MMW image contrast.

MMW image results using the MC AFTSA-SC probe are shown in Fig. 6.13. The size of each image is 100 × 100 pixels, and the step size resolution is $\delta x = \delta y$ = 3mm. The reconstructed 2D -image is obtained corresponding to the target peak reflection (S_{11}). The MMW images presented in Fig 6.13 (a) and (b) correspond to the visual image of the test object chart shown in Fig. 6.9. The MMW image of strip-lines shows a clear illumination, and the smallest gaps between the lines are low intensity contract, as shown in Fig 6.13 (a). The MMW image of circular holes has distinctly lower intensity, as shown in Fig 6.13(b).

The quality of the MMW images' performance with the MC AFTSA-SC probe is very similar to those are scanned using SGH antenna. Therefore, the MC AFTSA-SC probe with low profile, light weight, high gain, broadband, and low sidelobe achieves a good standard MMW image.

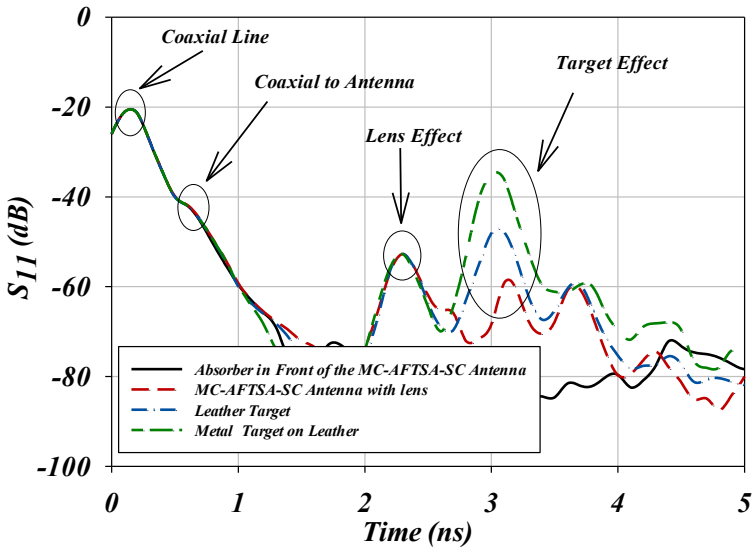

Figure 6.12 Reflection coefficient S_{11} vs time domain results of the MS-AFTSA-SC antenna probe in different stages; illustrating the target effect compared to probe in front of an absorber.

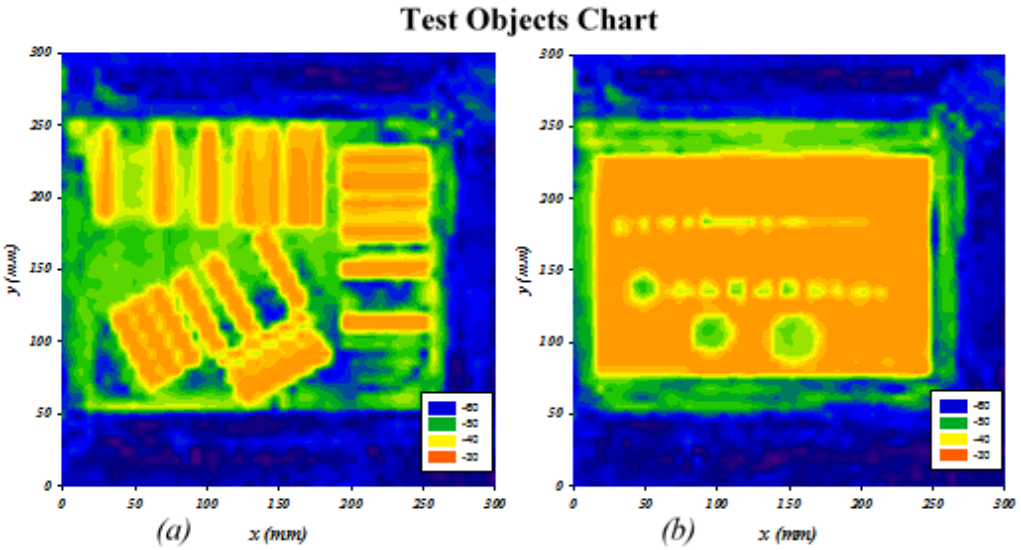

Figure 6.13 Measured 60 GHz image detection results on the x–y plane of the test object chart using MC-AFTSA-SC antenna probe; (*a*): image of copper strip-lines, (*b*): image of copper sheet with circular holes cutout. In all targets, natural leather is present in the background. Magnitude is in dB.

6.2.3.2 60 GHz Multi Sin-Corrugations AFTSA Antenna Loaded with a Spherical Lens MMW Probe

The multi *sin*-corrugations AFTSA antenna that is loaded with a grooved spherical lens is described in section 4.6. The grooved spherical lens is designed to enhance the E-plane and H-plane radiation pattern and reduce the sidelobe level. The probe response of the reflection coefficient S_{11} vs the time domain is shown in Fig. 6.14. The initial reflection at 0.2 *ns* is due to the coaxial line, the second peak at 1.2 *ns* is due to an interior reflection on the intersection between the coaxial to the grooved spherical lens antenna. The reflected waves at 2.32 ns are due to the optical lens of the system. The target peaks presented at 3.2 ns show about a 15dB difference in amplitude between the waves reflected from the leather and copper sheets.

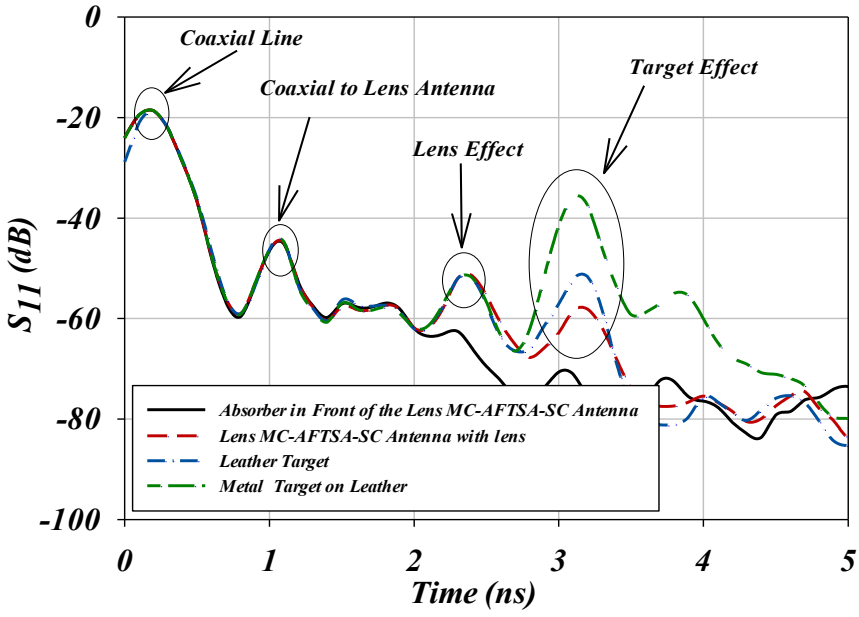

Figure 6.14 Reflection coefficient S_{11} vs time domain results of the lens MS-AFTSA-SC antenna probe in different stages; illustrating the target effect compared to probe in front of an absorber.

Fig. 6.15 shows the MMW images scanned by the MC AFTSA SC when loaded with a spherical lens. The MMW image resolution is kept 3mm for each pixel at x-y plane and the image size is 300 × 300mm^2. After signal pre-processing, a 2D -image is reconstructed with a real time contour corresponding to target peak reflection S_{11} vs time domain. All targets are placed on a background of natural leather to simulate the human body effect [172], [173], [174]. The differences between the MMW images shown in Fig. 6.15 compared with the ones presented with the probe in Fig. 6.13 is that the groove lens increases the antenna gain leading to an increase in the contrast in the image. However, the images' recognition of target shape overall is detectable and very similar in both cases.

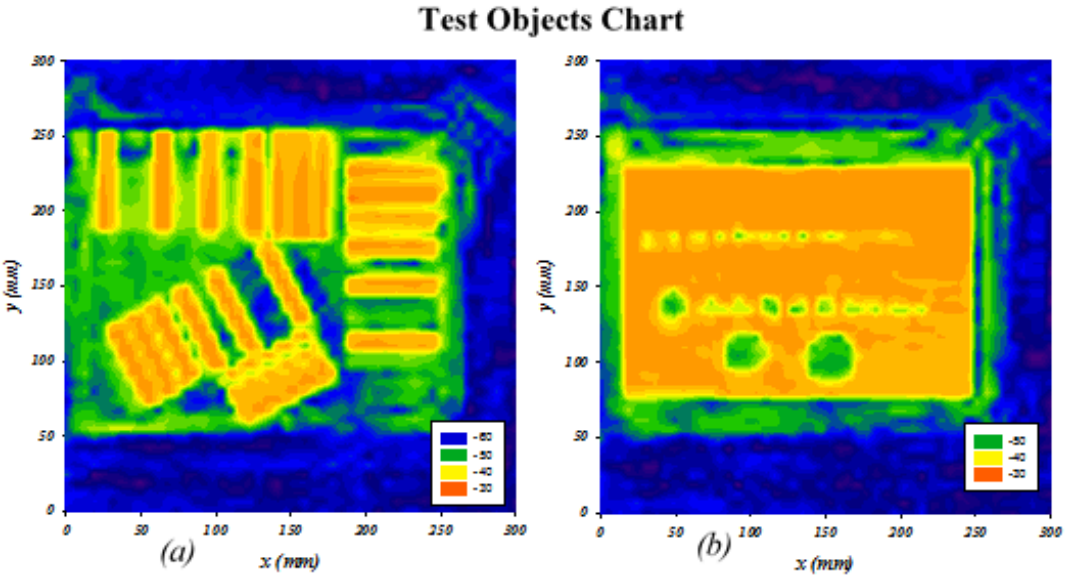

Figure 6.15 Measured 60 GHz image detection results on the x–y plane of the test object chart using Lens MC-AFTSA-SC antenna probe; (*a*): image of copper strip-lines, (*b*): image of copper sheet with circular holes cutout. In all targets, natural leather is present in the background. Magnitude is in dB.

6.2.3.3 A 60 GHz Dual polarized AFTSA-SC antenna probe

A single-feed dual- polarized AFTSA-SC antenna is presented to operate as a probe in active MMW imaging/detection system. The dual polarized probe improves the

capability of target recognition based on the combination of vertical and horizontal polarized elements that increase the intensity contrast from the target. The details of this antenna are given in Section 4.5.1. Furthermore, this polarization diversity allows obtaining two sets of reflected EM wave that are meant to provide additional variation about the surface shape of the target. Fig. 6.16 shows the reflection coefficient measurement in the time domain obtained by the proposed probe. The target presents peaks at 3.55 ns, and shows about 10dB difference in amplitude between the waves reflected from the metal target and leather target.

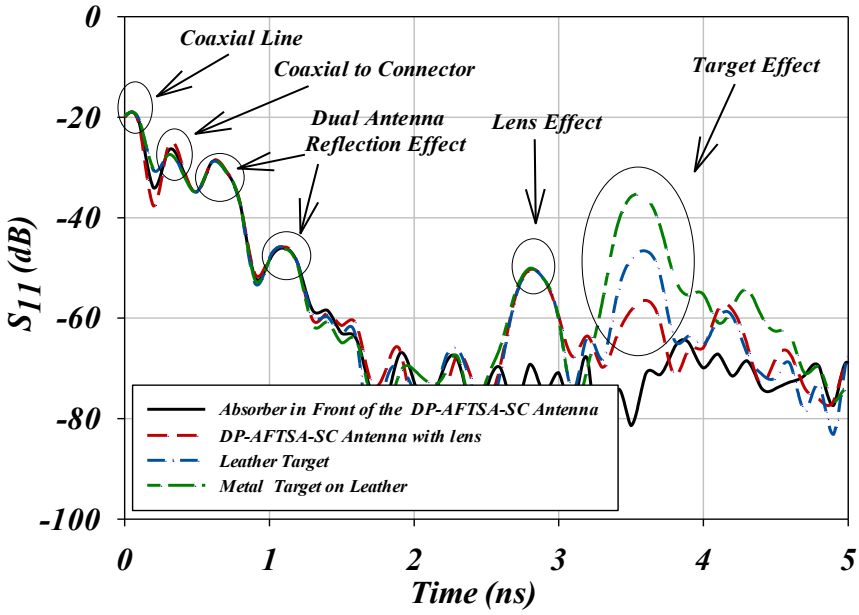

Figure 6.16 Reflection coefficient S_{11} vs time domain results of the DP-AFTSA-SC antenna probe in different stages; illustrates the target effect compared to probe in front of an absorber.

The results of the MMW imaging/detection system using the DP AFTSA-SC probe are presented in Fig. 6.17. The scanned visual images of the test object chart from Fig. 6.9 are presented in Fig. 6.17's (*a*), and (*b*), respectively. The MMW images show a clear

contrast between the conducted target and the natural leather compared with the images' performance with SGH antenna.

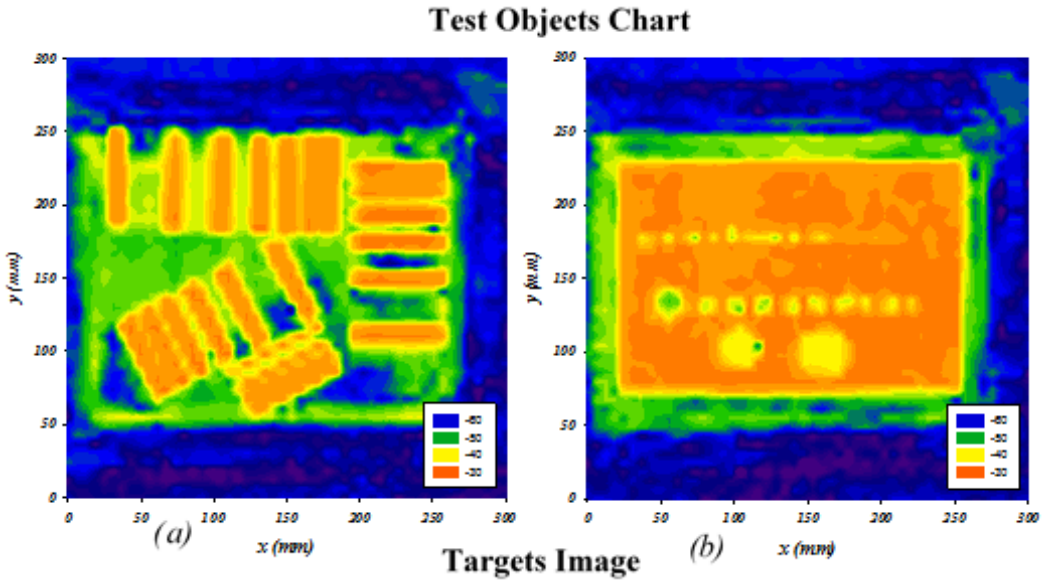

Figure 6.17 Measured 60 GHz image detection results on the x–y plane of the test object chart using DP-AFTSA-SC antenna probe; (*a*): image of copper strip-lines, (*b*): image of copper sheet with circular holes cutout. In all targets natural leather is present in the background. Magnitude is in dB.

6.2.3.4 A 60 GHz Circular polarized AFTSA-SC antenna probe

A single feed circular polarized (CP) AFTSA-SC antenna is utilized as a probe in MMW imaging/detection system, presented in Section 4.5.2. The CP AFTSA-SC is modeled to radiate in the right-hand circularly polarized antenna (RHCP), with an HPBW that reaches 15.4° and 18.7° in the H–plane and E–plane, respectively. An axial ratio bandwidth of < 3dB is maintained from 59 to 63 GHz. Fig. 6.18 shows the measured reflection coefficient in the time domain. The target presents a peak at 3.6 ns with a 15dB difference in amplitude between the waves reflected from the metal target and the leather target. The reflected peaks are relatively low compared with performance responses with linearly polarized probes. Seeing as the probe generates RHCP wave fields, the reflected

back waves from the target are dominantly left hand circularly polarized (LHCP) [169], which leads to reduction in receiving waves.

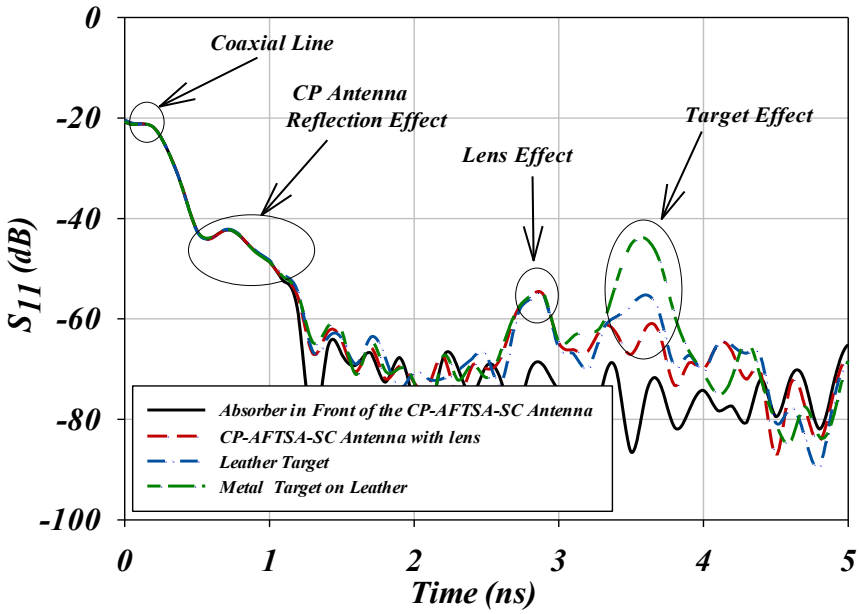

Figure 6.18 Reflection coefficient S_{11} vs time domain results of the CP-AFTSA-SC antenna probe in different stages; illustrated is the target effect compared to probe in front of an absorber.

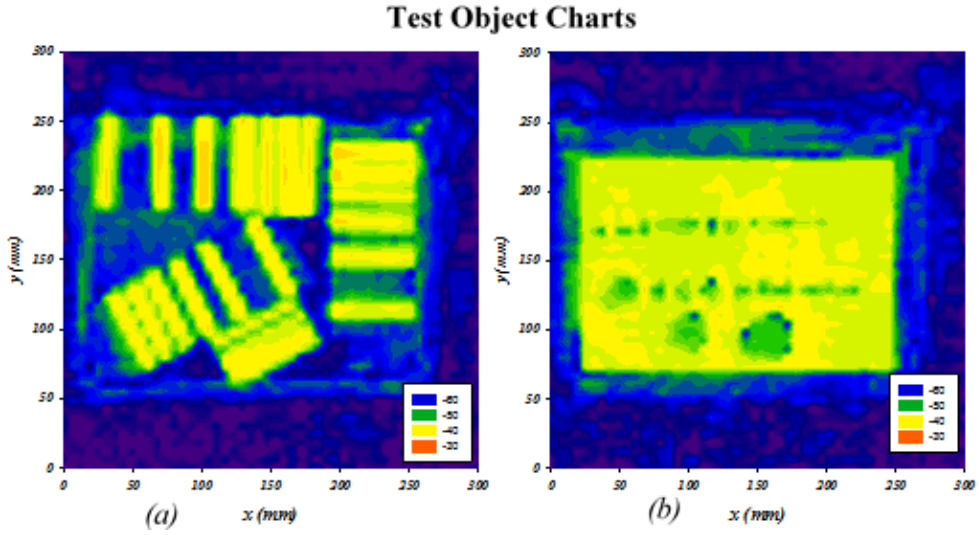

Figure 6.19 Measured 60 GHz image detection results on the x–y plane of the test object chart using CP -AFTSA-SC antenna probe; (*a*): image of copper strip-lines, (*b*): image of copper sheet with circular holes cutout. In all targets natural leather is present in the background. Magnitude is in dB.

Fig. 6.19 shows the results of MMW images using performance by CP AFTSA-SC probe detecting two test object charts, strip-lines shaped in the letters “F” and “A”, and the metal model image of a handgun. The step size is equal in the x-plane and y-plane; $\delta x = \delta y = 3mm$, with a $300 \times 300mm^2$ field of view. The corresponding target peak reflection S_{11} is reconstructed into a 2D -image obtained with the real time contour plot. As expected, in Fig. 6.19, the contrast of the MMW images is relatively low, where it is proportional to reflect waves polarity caused by the target surface shape.

In the case of the propagated waves of RHCP antenna pointed toward a flat surface, the reflected wave changes the polarity to LHCP [169], which is the case in this experiment in monostatic MMW image using CP-AFTSA-SC. Consequently, increasing the probe sensitivity is possible by applying two probes in different polarity, for example, a transmitter as LHCP probe and a receiver as RHCP probe. In this case, the transmitted waves of the LHCP probe that illuminate the target are reflected back dominated by RHCP waves that match the receiver polarity of RHCP probe. Despite the back scattering from the target that is indifferent polarity with the probe, the MMW images are inadequate contrast using CP AFTSA-SC probe, as shown in Fig. 6.19.

6.3 60 GHz Imaging for Concealed Target Detection

In this section, detections of hidden weapons using a single element MC-AFTSA-SC probe to reconstruct 60 GHz images are presented. Three scenarios are employed to conceal a weapon; inside clothing, behind a plywood sheet, and behind plastic sheet materials. Furthermore, the 60 GHz imaging system is tested to detect liquid materials such as water, salt water, oil, and alcohol, concealed with the materials in the three scenarios mentioned above.

6.3.1 MMW Imaging/Detection System Setup

The photograph of the system setup using MC-AFTSA-SC probe is presented in Fig. 6.11, which corresponds to the detailed diagram in Fig. 6.1. The probe (MC-AFTSA-SC described in section 4.6) is operating in a monostatic mode via transceiver EM waves generated by the network analyzer. The PNA (Agilent, N5227A) is connected to the probe through a V-band coaxial cable (TM67-V1V1-36, DC to 67 GHz, 0.85mm).

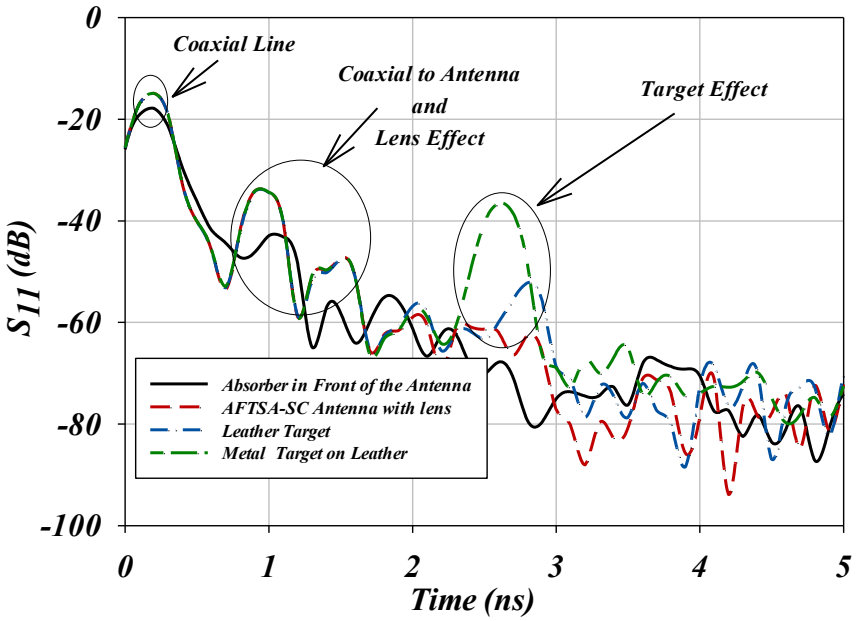

Figure 6.20 Reflection coefficient S_{11} vs time domain results of the MS-AFTSA-SC antenna probe in different stages; illustrates the target effect compared to probe in front of an absorber

The MC-AFTSA-SC probe is operated in ISM-band frequency range 57 to 64 GHz used in the calibration bandwidth of the PNA, and with 0dBm ($1mW$) transmitted power chosen as the reference value for all scanning scenarios in this experiment. The frequency point is N = 201, frequency step size is Δf = 35 MHz, the wavelength at the center of the bandwidth is λ_c = 4.96 mm (at 60.5 GHz), the calculated range resolution is ΔR_z = 21.3 *mm*, and the calculated cross range resolution is ΔL_x = 4.88 *mm,* when the R_z =*12.5 cm* and lens diameter D = *12.7cm.* The probe is placed at the focal plane 14 *cm* from the lens, and

an absorber is mounted behind the antenna to prevent any undesired background clutter reflections. Behind the target is 270mm × 205mm of natural animal leather (≈ 1mm in thickness) supported by ≈ 2mm in thickness of reinforced paper and placed in the center of the platform.

The PC controls the step motion at the X and Y locations of the platform and the image resolution step is $\delta_x = \delta_y = 3mm$, and field of view is 300 × 300mm^2 at x-y plane, this corresponded to 100 × 100 pixels in one image. The reconstructed 2D MMW image is obtained with a contour plot corresponding to target peak reflection after signal pre-processing. In Fig. 6.20, the reflection coefficient S_{11} vs time domain results of the MS-AFTSA-SC indicate the target effect in different stages compared to probe in front of an absorber. Several reflected peaks are detected: the peak at 0.2 is due to the coaxial line, the peaks at a period of 0.8 *ns to* 1.5 *ns* are due to the transition from coaxial to microstrip line of the antenna and the reflection from the lens, the peaks at a period of 2.5 *ns to* 2.9 *ns* are due to reflection caused by the metal sheet target and the leather on the mechanical scanner platform.

6.3.2 A 60GHz Imaging for Concealed Weapon Detection

A 60 GHz imaging experiment is performed to evaluate MC-AFTSA-SC as a probe to detect various targets with diverse barrier materials. Three different conventional weapons, a handgun, scissors and a knife, are placed with different materials to test the reflection contrast of each item. The handgun is wrapped with aluminum tape in order to increase surface reflectivity and to simulate the real gun. A knife made of ceramic blade and plastic handle is commonly undetectable by metal detectors at security checkpoints. The third target is the scissors made of stainless steel with plastic handles. The three

weapons are placed on 1mm thick natural leather with 2mm thick reinforced paper and mounted in the center of the 2D scanner platform. The leather that is in the background of these weapons provides similar millimeter-wave reflective properties as the human skin. In this section, the MMW images of three situations of concealed weapons - inside clothing, behind a plywood sheet, and behind plastic sheet material - are employed in different scenarios to test the reflectivity and penetration that correspond to the scanned images.

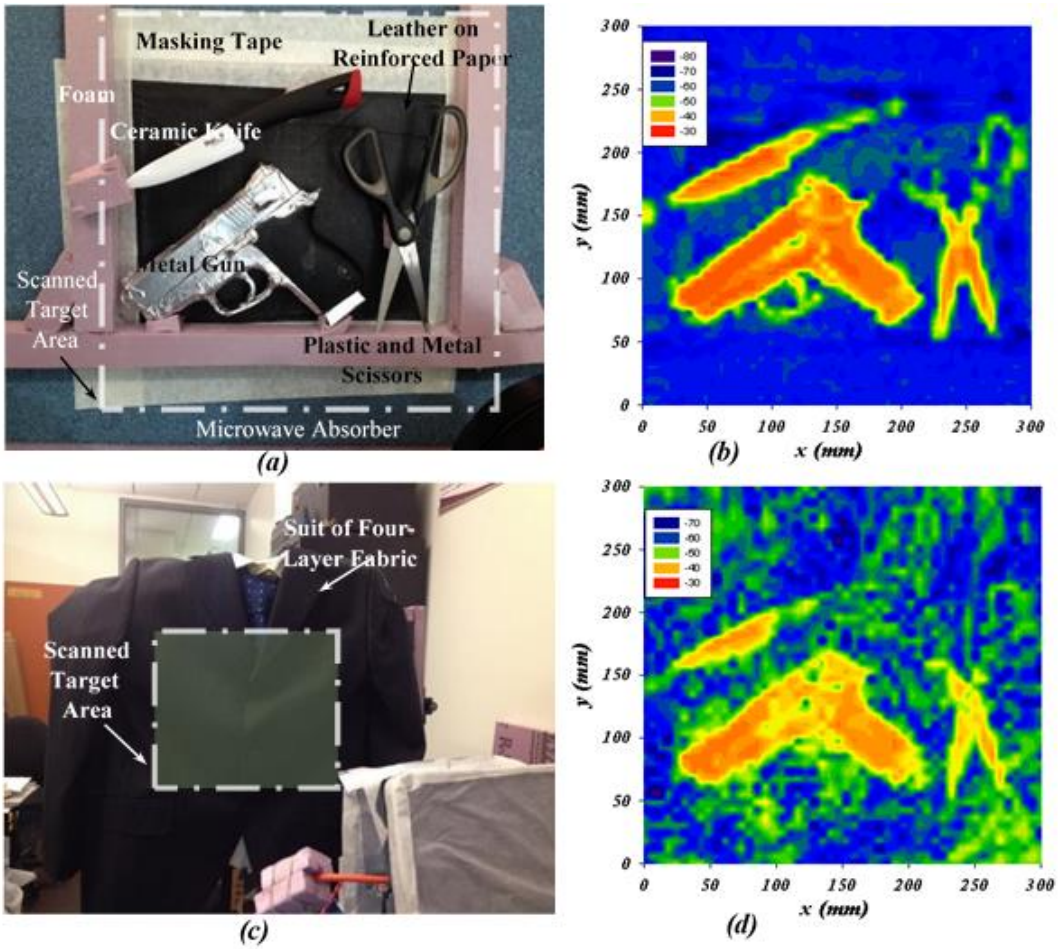

Figure 6.21 (*a*) The optical image of the metal gun model, metallic scissors, and ceramic knife with their MMW image in (*b*). (*c*) The target is concealed inside a four layer suit jacket and its MMW image in (d).

Fig. 6.21 shows, in (*a*), the optical image of the metal gun model, metallic scissors, and ceramic knife at the test platform, fixed on a layer of natural leather to simulate weapons on the human body. The corresponding MMW image is shown in Fig. 6.21 (*b*) with an aperture of 30 × 30 cm. It shows the contrast of each item - less illumination appears on the plastic handles. This MMW image is obtained without any clothing barrier or obscuration in front of the weapons, as shown in Fig. 6.21 (*a*) and (*b*) for reference. The experiment primarily demonstrates MMW imaging/detection of the target hidden behind clothing, in Fig. 6.21 (*c*), the weapons are concealed inside four layers of fabric; two layers of cotton, and two layers of polyester that represent a suit jacket, a shirt, a tie, and a T-shirt. The MMW image reveals the weapons beneath the clothing are very well, as shown in Fig. 6.21 (*d*).

6.3.2.1 MMW Imaging for Concealed Weapon Detection behind Clothing

The initial experiment is to investigate the detection of concealed weapons behind clothing. This experiment demonstrates the ability of a 60 GHz imaging detection system to recognize the hidden weapons concealed behind different layers of the most commonly worn fabric (cotton) [170]. Fig. 6.22 shows the reflection coefficient S_{11} vs time when the target is concealed with different layers of cotton towels - two layers, five layers, seven layers - and a suit jacket which has four layers. These different layers are to simulate several clothing scenarios to conceal weapons. The reflection of the target is slightly affected when it is concealed by different layers of fabric, as shown in Fig. 6.22 - there is a small variation in the reflected peak. This approves the ability of millimeter-waves to penetrate through clothing.

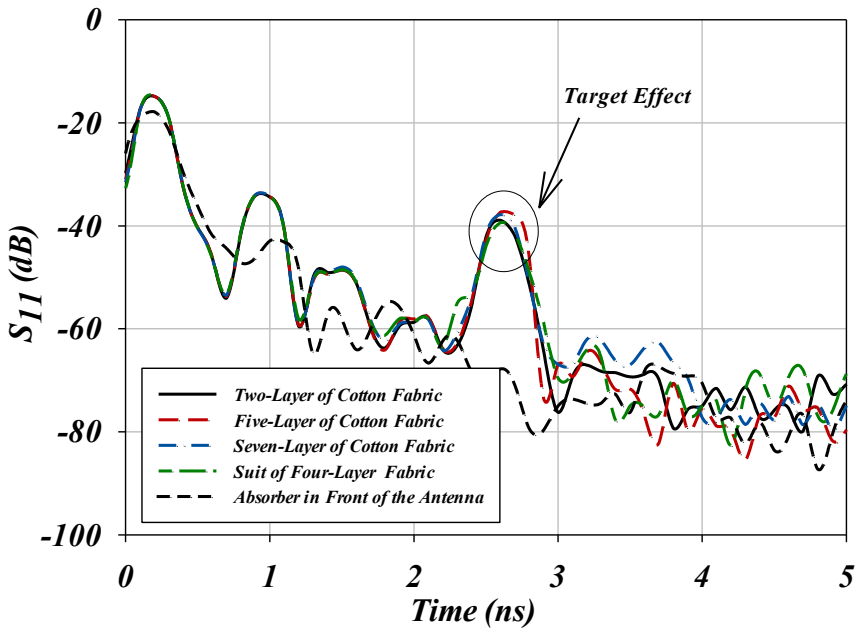

Figure 6.22 The effect of layers of cotton fabric on a concealed target.

Fig. 6.23 shows the optical image of three scenarios of concealed weapons involving cotton fabric, presented on the left side of the figure. The right side of the figure shows the detected MMW images. Fig. 6.23 (*a*) shows the weapons concealed behind one layer of cotton fabric and the corresponding MMW image. Fig. 6.23 (*b*) shows the weapons concealed behind five layers of cotton fabric and the corresponding MMW image. Seven layers of cotton fabric concealing the target and the matching MMW image are shown in Fig. 6.23 (*c*). The shape of the handgun, knife, and scissors are clearly detected by the MMW imaging system. Therefore, the resolution of the image quality effectively reveals the shapes of the metallic and dielectric items.

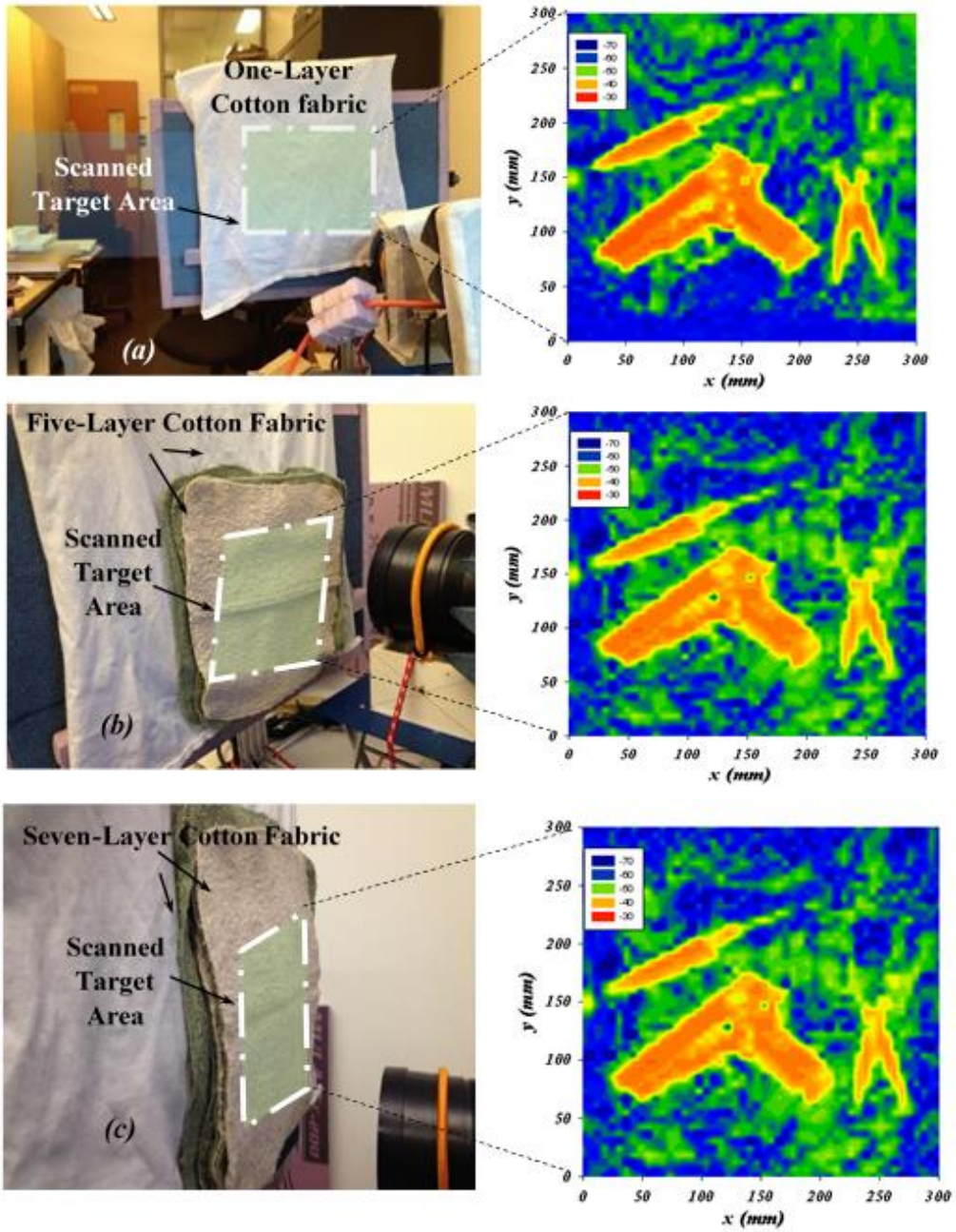

Figure 6.23 (*a*) The target concealed behind one layer of cotton fabric and its MMW image. (*b*) When it is concealed behind five layers of cotton fabric, and its MMW image. (*c*) Seven layers of cotton fabric are concealing the target, and its MMW image on the right side.

6.3.2.2 MMW Imaging for Weapon Detection behind Plywood Sheet

The MMW imaging system employed 60GHz MC-AFTSA-SC as a probe to experiment the ability to detect weapons behind different barriers. For example, a wooden

box is a common container for shipping goods or personal items, and its panels are usually made of plywood. Several scenarios are tested by using plywood sheets as a barrier to hide weapons. Fig. 6.24 shows the reflection coefficient S_{11} vs time domain responses when the target is behind different thicknesses of plywood; 0.5 inch, 1 inch, 1.5 inch, and 2 inch. It is noted that when the thickness of the plywood is increased, the reflection peak value of the target decreases.

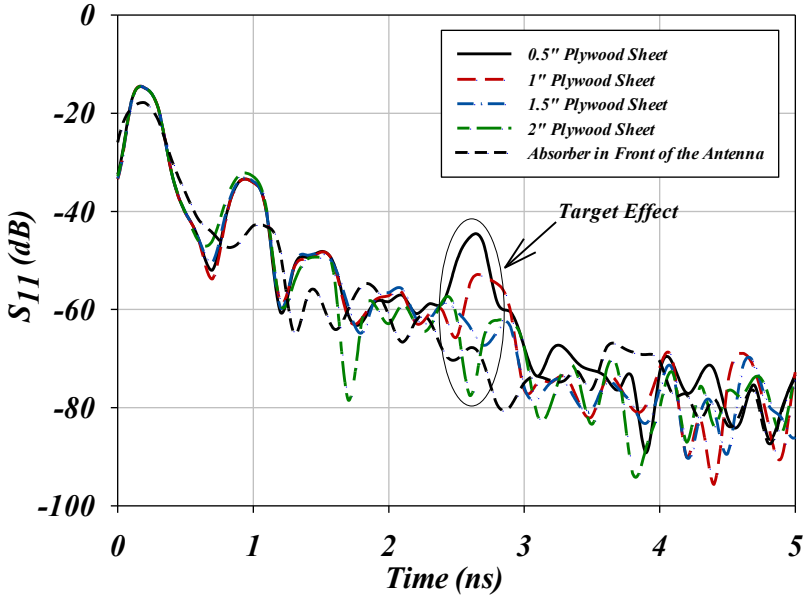

Figure 6.24 The effect of different thicknesses of plywood on a concealed target.

Fig. 6.25 shows the optical images and MMW images of the weapons behind sheets of plywood, in which the sheet areas are orthogonal with respect to the incident field of the probe. In Fig. 6.25 (*a*) and (*b*) show the mounted weapons hidden behind a 0.5″ plywood sheet, and its MMW image, respectively. Fig. 6.25 (*c*) and (*d*) are MMW images of the weapons hidden behind 1″ and 1.5″ of the plywood sheet, respectively. Fig. 6.25 (*e*) and (*f*) shows the weapons hidden behind a 2″ plywood, with the MMW image. The handgun, ceramic knife, and metal/plastic scissors are clearly identified in Fig. 6.25 (*b*) and (*c*), when the plywood barrier is 0.5 and 1″ in thickness, however, the barrier of 1.5″ in thickness shows very low reflection from the target, leading to a poor resolution MMW image, and

at 2″ in plywood thickness the MMW image of the target is undetectable. To increase the signal penetration, it is advisable to sense the target from many viewing angles while increasing the transmitted signal power of the PNA.

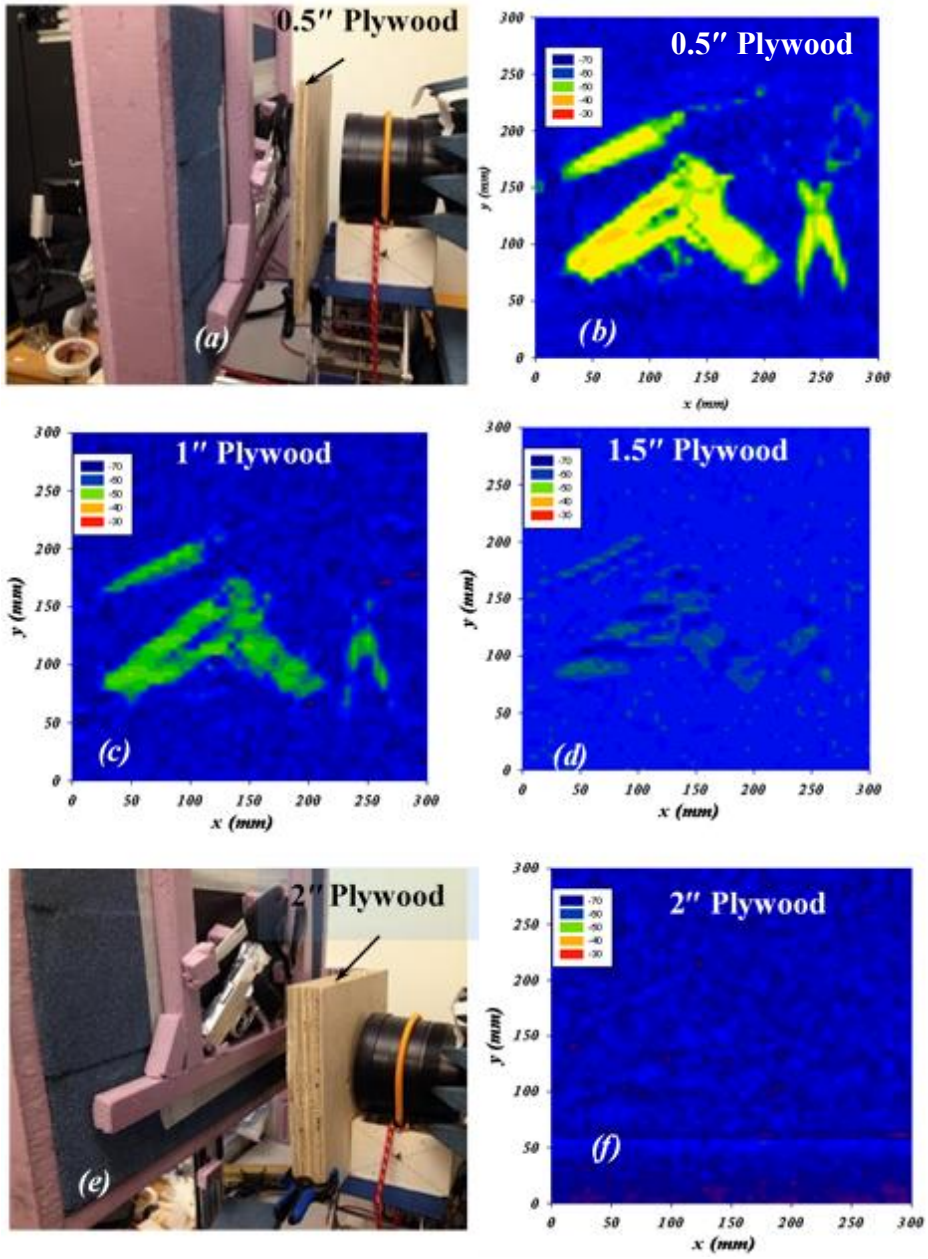

Figure 6.25 (*a*) The target is hidden behind a 0.5″ plywood sheet and (*b*) its MMW image. Both (*c*) and (*d*) are MMW images of when the target is hidden behind 1″ and 1.5″ of plywood. In (e) the target is hidden behind a 2″ plywood and (*f*) its MMW image is shown.

6.3.2.3 MMW Imaging for Weapon Detection behind Plastic Sheet

In this experiment, the MMW imaging system is tested to detect through plastic materials, such as a Plexiglas, to examine the quality of image contrast in hidden objects. This scenario is employed in the case of detecting objects behind windows, doors, buildings, or even through luggage, which are often made of plastic materials. Fig. 6.26 shows the reflection coefficient S_{11} vs time domain responses when the target is behind different thicknesses of plastic sheeting; 4.4 mm polycarbonate (PoC.), 2 × 4.4 mm PoC., 3 × 4.4 mm PoC. , and a 5.2 mm Acrylic sheet attached to a 3 × 4.4 mm PoC. sheet. The effect of different plastic thicknesses and materials on a concealed target shows a small variation on the reflected peak.

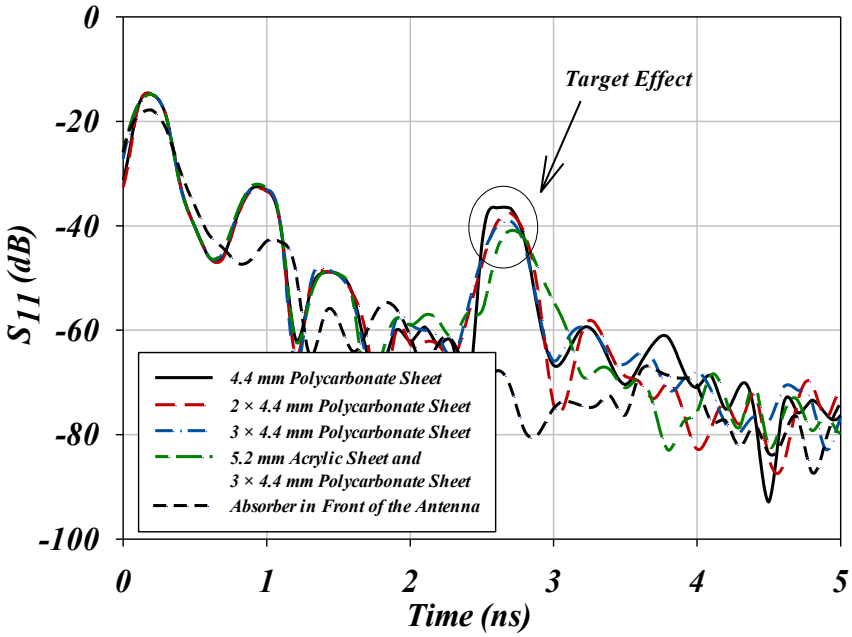

Figure 6.26 The effect of different plastic thicknesses and materials on a concealed target.

Fig. 6.27 (*a*) shows the optical image of the weapons behind the 4.4 mm PoC. and the MMW image on the right side. Fig. 6.27 (*b*) shows the target hidden behind 2 × 4.4 mm PoC, by the MMW image on the right side. Fig. 6.27 (*c*) shows a 3 × 4.4 mm PoC hiding the target, and the MMW image. In Fig. 6.28 (*a*) the weapons are hidden behind

three layers of 4.4 mm thickness PoC and 5.2 mm acrylic, and the MMW image is on the right. Fig. 6.28 (*b*) shows a 1" Teflon sheet hiding the weapons, and the MMW image. As demonstrated in these figures, the 60GHz images of the handgun, knife, and scissors are recognizable with clear resolution under coverage of different plastic materials.

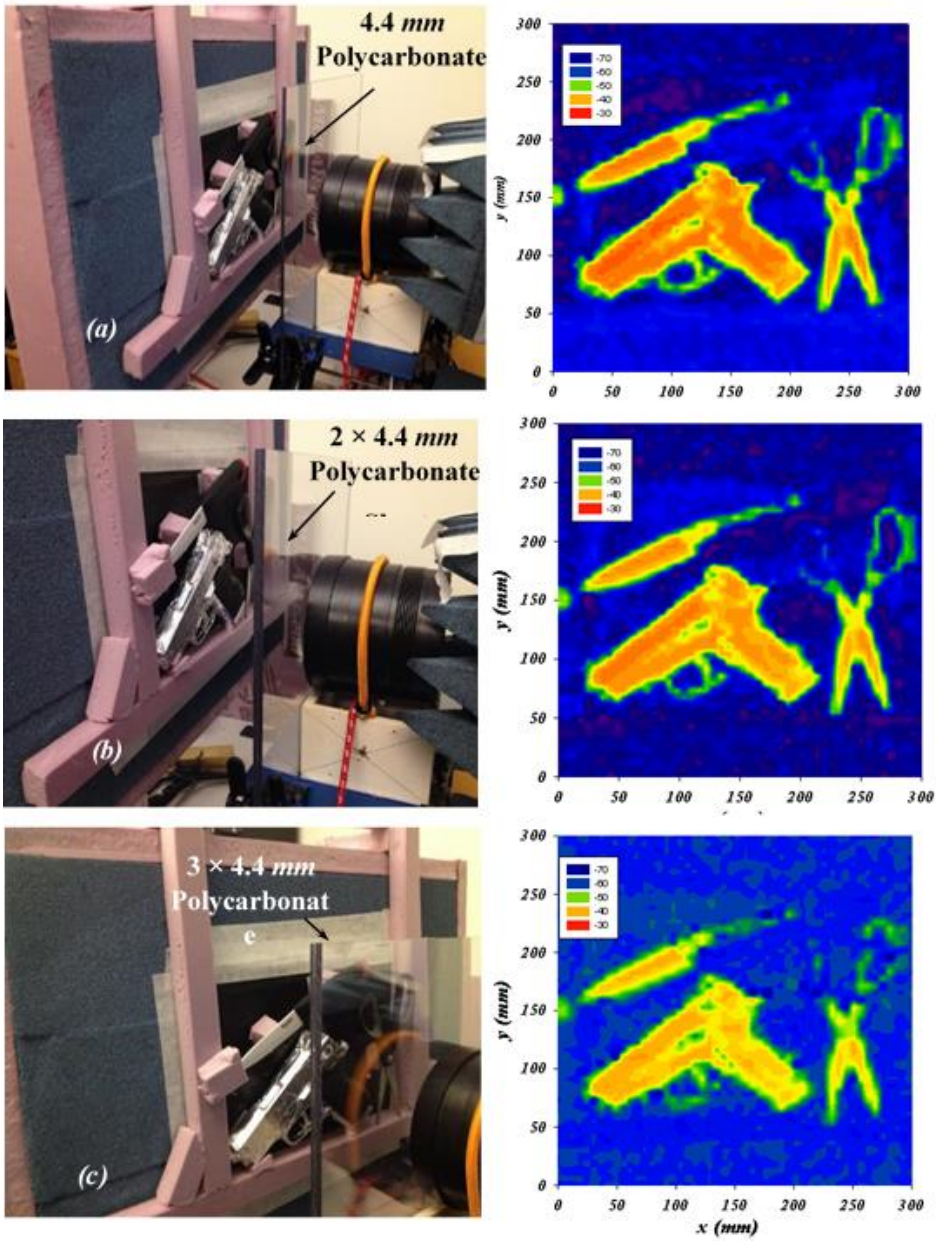

Figure 6.27 (*a*) The target behind one layer of polycarbonate, and its MMW image on the right side. (*b*). The target hidden behind two layers of polycarbonate, and its MMW image. (*c*) Three layers of polycarbonate hiding the target, and the MMW image.

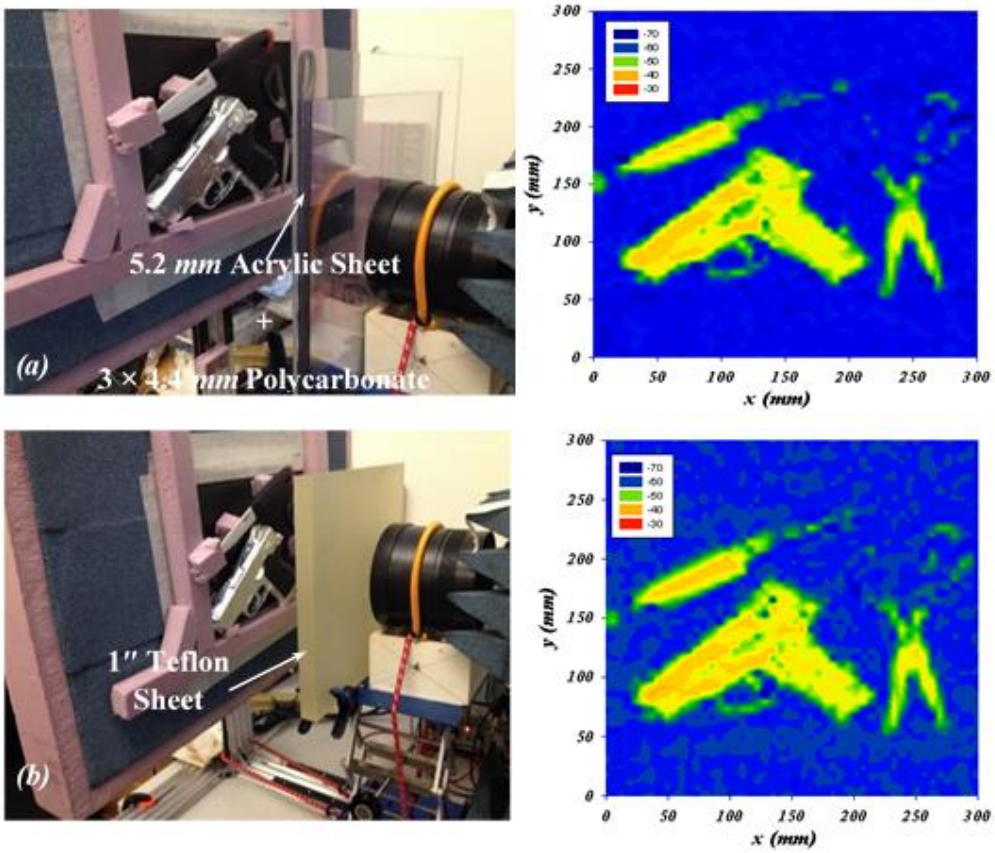

Figure 6.28 (*a*) The target hidden behind three layers of polycarbonate and one layer of acrylic, and the MMW image on the right side. (*b*) 1" Teflon sheet hiding the target, and the MMW image.

6.3.3 A 60GHz Imaging for Concealed Liquid Materials Detection

In this section, the 60 GHz imaging system is tested to detect different liquid materials: water, salt water, oil, and alcohol, and are concealed with the same materials in the three scenarios. This experiment is based on the fact that explosives and other prohibited dangerous chemicals have unique reflection contrast at the MMW frequency range depending on dielectric differences [171], which are simulated on those four different liquids. The dielectric properties of materials are known to be frequency dependent. The liquids are each in their own plastic bottle and are aligned close to one another with natural leather in the background; all are mounted on 2D scanner platform.

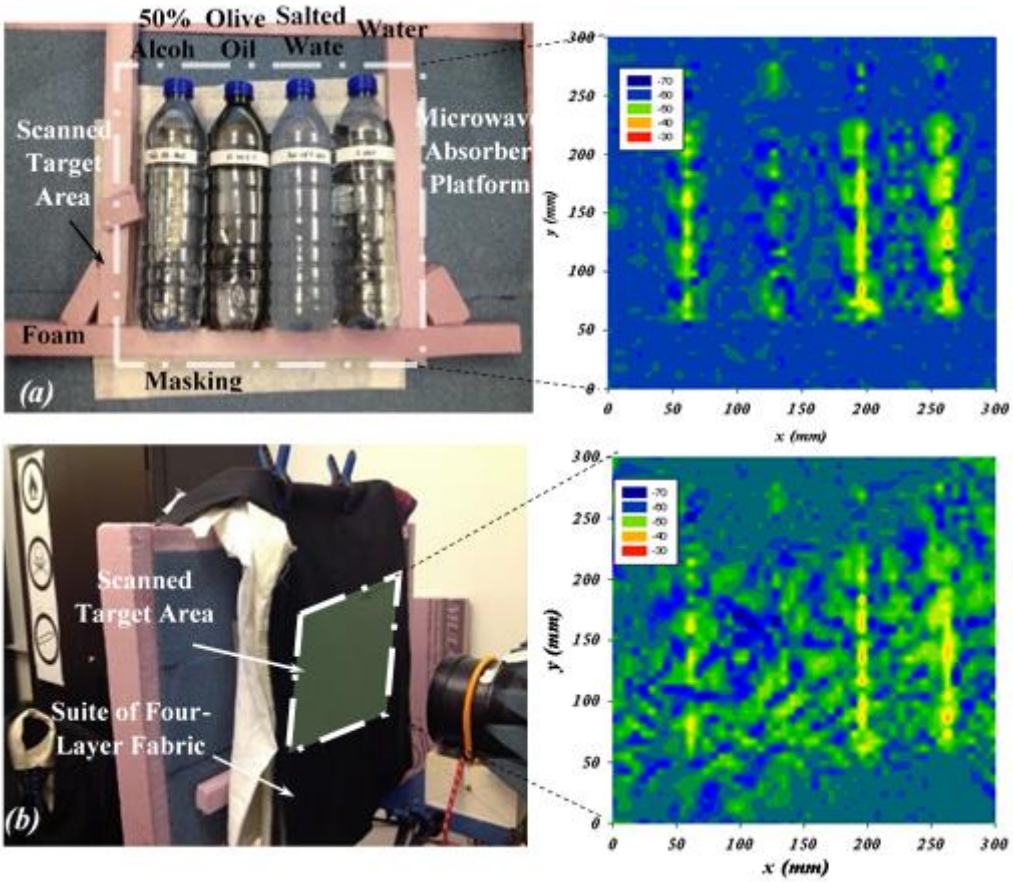

Figure 6.29 (*a*) The optical image of the four different liquids; water, salt water, olive oil, and 50% alcohol, and their MMW image on the right side. (b) The target of four different liquids is concealed inside a four layer suit and its MMW image.

The corresponding MMW image is shown in the right side of Fig. 6.29 (*a*) with an aperture resolution of 100 × 100 pixels - it shows the contrast of each liquid. This MMW image is obtained without a barrier or obscuration in front of the liquids, for reference. In order to demonstrate MMW imaging/detection of the liquids hidden behind clothing, in Fig. 6.29 (*b*), the bottles are concealed inside four layers of fabric, two layers of cotton, and two layers of polyester. The results reveal a contrast of MMW image associated with different liquid reflections for the four bottles beneath the clothing

6.3.3.1 MMW Imaging for Concealed Liquid Materials Detected behind Clothing

Fig. 6.30 shows MMW images of four scenarios of liquids concealed by several layers of cotton fabric. The image resolution is $\delta_x = \delta_y = 3mm$, and the field of view is 300 × $300mm^2$ at *x*-*y* plane. The 2D -image is obtained corresponding to the target peak reflection after signal pre-processing. The contrast of 60 GHz images depends on the object surface shape - the bottles are of cylinder-shape - while corresponding to this imaging setup most of the back reflections are from the orthogonal area of the bottles. From the four MMW images, it is clear that the most illumination appears from water and salt water, then it is followed by the contrast of alcohol, and then less contrast from oil.

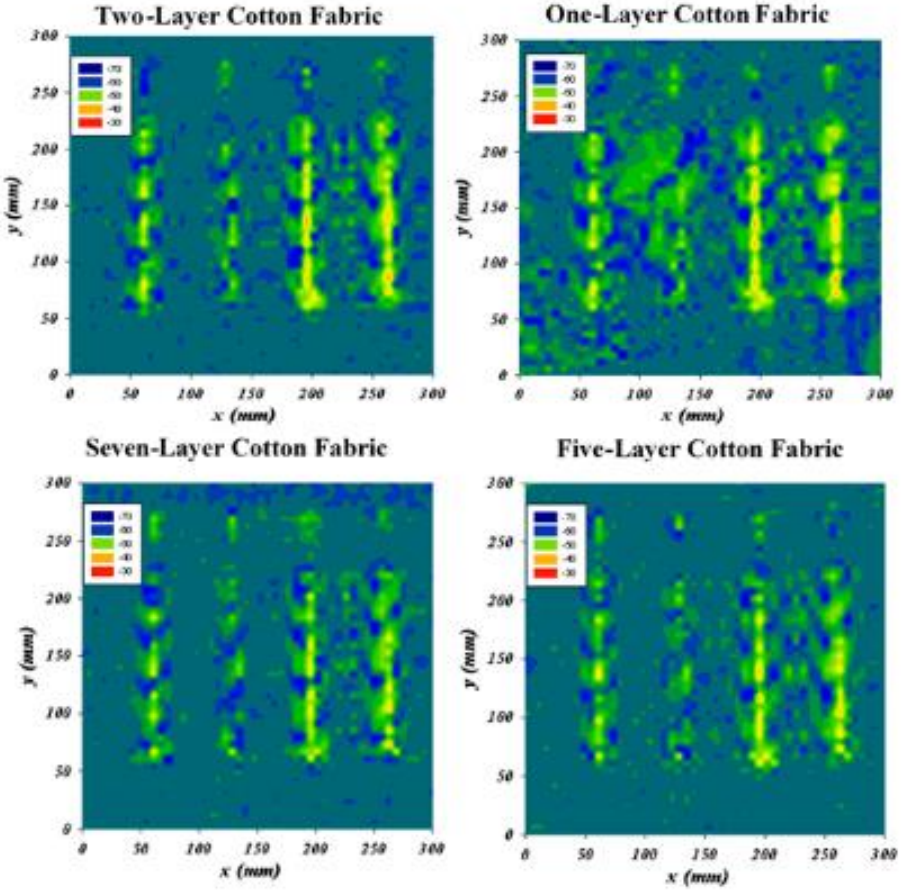

Figure 6.30 MMW images of different layers of cotton fabric concealing the target of four different liquids; one-layer at the top right, then two-layer to its left, then five-layer in the bottom left, then seven-layer in the bottom right.

6.3.3.2 MMW Imaging for Liquid Materials Detected Behind Plywood

Fig. 6.31 shows MMW images when plywood sheets of different thicknesses are placed in front of the four different liquids. The hidden liquids behind 0.5″ and 1″ thick plywood sheets are relatively detectable; however, the 1″ and 2″ thick plywood sheets are unrevealing of any target. Thus, to increase the reflected signal from the target, it is preferable to detect the object from a multi-viewing angle while increasing the transceiver signal power of the PNA.

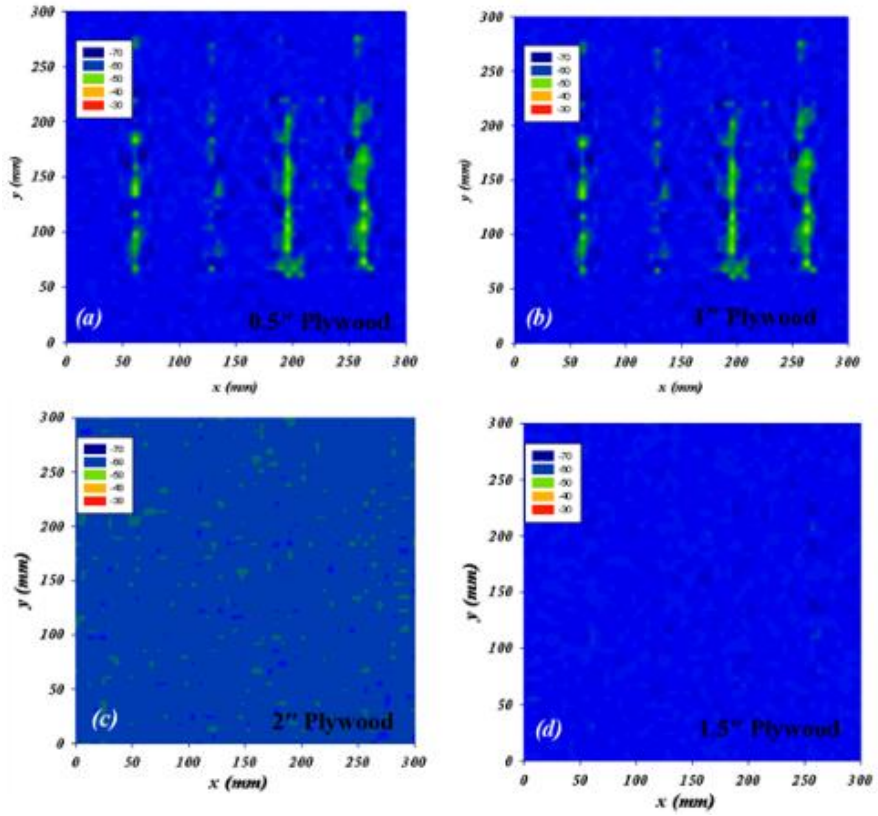

Figure 6.31 MMW images showing different thicknesses of plywood are in front of the target of the four different liquids.

6.3.3.3 MMW Imaging for Liquid Materials Detected behind Plastic

In further investigation, a MMW imaging system tested images through transparent plastic materials to examine the quality of MMW image contrast in detecting liquid objects. Fig. 6.32 (*a*) shows on the left side the optical image of the liquid bottles behind 4.4 mm

PoC with the matching MMW image shown on the right side. Fig. 6.32 (*b*) shows the liquids hidden behind 2 × 4.4 mm PoC and the corresponding MMW image is shown on the right side. Fig. 6.32 (*c*) shows a 3 × 4.4 mm PoC hiding the liquids, with the relevant MMW image shown on the right side.

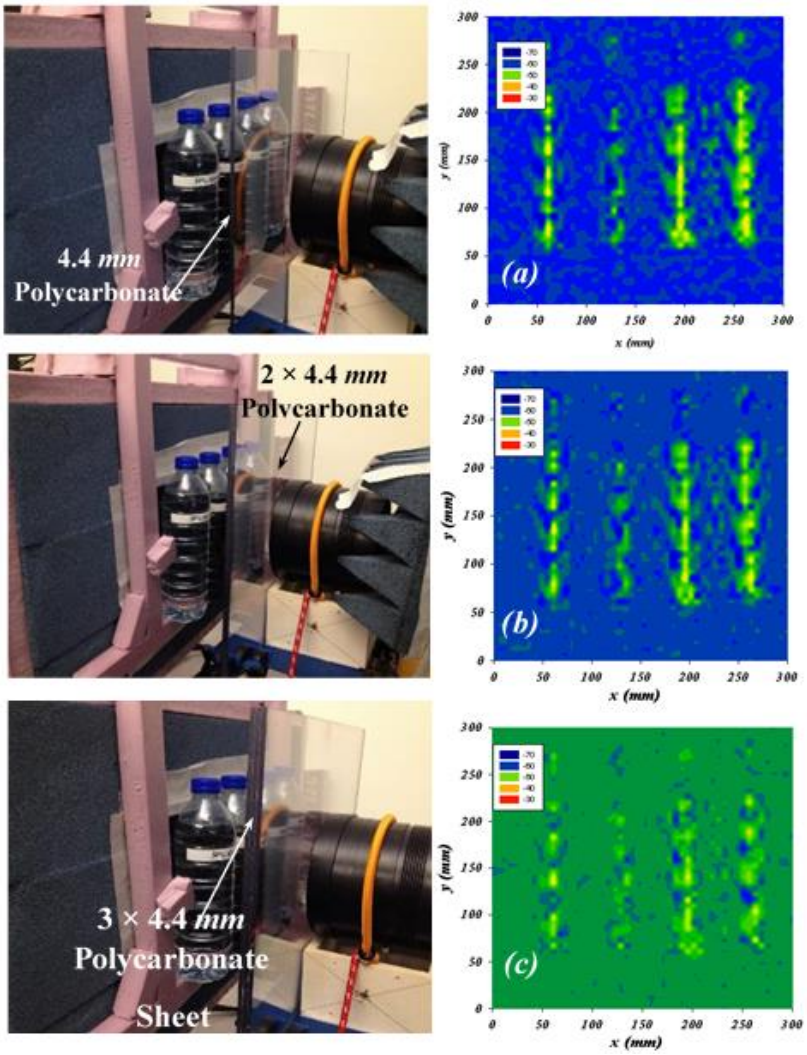

Figure 6.32 (*a*) The four different liquid targets behind one layer of polycarbonate, and the MMW image on the right side. (*b*) When the liquids are hidden behind two layers of polycarbonate, seen here in the MMW image. (*c*) Three layers of polycarbonate hide the target, and here is the MMW image.

In Fig. 6.33 (*a*), the liquids are hidden behind three layers of 4.4 mm PoC and 5.2 mm of acrylic, and the MMW image is on the right. Fig. 6.33 (*b*) shows a 1" Teflon sheet

hiding the liquids, and the MMW image. Overall, the 60GHz images of the four liquid bottles are relatively recognizable with equitable resolution under coverage of different plastic materials.

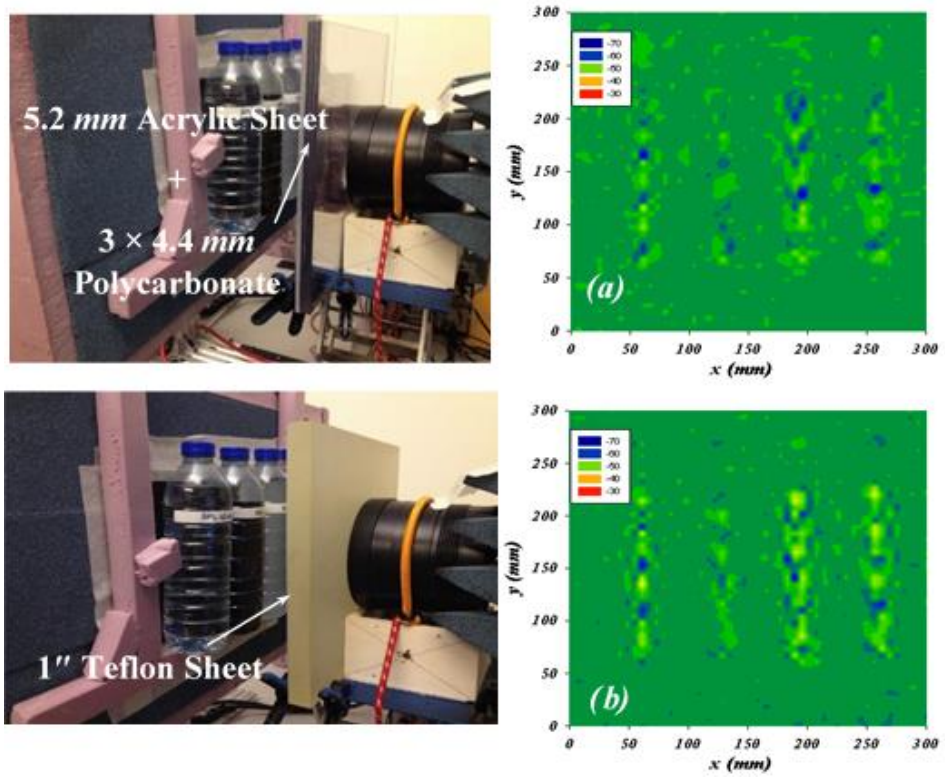

Figure 6.33 (*a*) The four different liquid targets behind three layers of polycarbonate and one layer of acrylic, with the MMW image on the right side. (*b*). 1" Teflon sheet hiding the target, and the corresponding MMW image.

6.4 Summary

In this chapter, imaging detection of a target utilizing a V-band standard gain horn (SGH) and proposed 60GHz antennas as probes are introduced. The MMW imaging system is designed to evaluate the proposed 60 GHz antenna probes on test object charts. The proposed MCAFTSA-SC probe is evaluated as an imaging / detection sensor, and scanned results for concealed weapons and liquids underneath clothing, behind plywood, and behind plastics are illustrated.

The MMW image is detected using a 2D linear scanning platform to generate XY movement with a $30cm \times 30cm$ mechanical range of the object field of view, and oriented perpendicular with respect to the lens focal plane. The mechanical setup is designed to test proposed probes, and this scanning method is utilized in a similar way to synthetic aperture array with a single antenna element measurement that is ideal to investigate the probe for MMW imaging. The 60 GHz imaging results of the V-band SGH antenna are compared with four proposed antennas presented in chapter 4 which are utilized as sensing probes. The imaging results using the proposed probes show a very similar contrast compared with those scanned using SGH antenna. Therefore, a low profile microstrip probe with lightweight, high gain, and broadband achieves a good standard MMW image.

Section 6.3 introduces experiments to detect different types of hidden weapons and liquids using the single element MC-AFTSA-SC probe to reconstruct 60 GHz images. Three scenarios are evaluated to detect each target when concealed by clothing, a plywood sheet, and plastic material. The low-power 60 GHz active monostatic transceiver proves that this system with the proposed probe is effective in detecting and identifying concealed conventional weapons, such as handguns, whether plastic or metal, ceramic knives, and explosives in liquids or plastics.

Chapter 7: Conclusions and Future Work

7.1 Conclusion

In this thesis, we have designed and implemented several 60 GHz antenna probes for potential use in imaging/detection systems for homeland security applications. The first part of the thesis discussed how the proposed antenna elements were optimized, fabricated, and tested. The second part presented design methodology and results for a 57-64 GHz 1 × 16-element beam steering antenna array with a low-cost piezoelectric transducer controlled phase shifter. Finally, a 57-64 GHz band mechanical scanner system was designed to test and evaluate antenna probes, utilizing the active monostatic transceivers principle. Different developed probe prototypes exhibit good performance in terms of excellent impedance matching over the ISM band (57-64 GHz), stable radiation patterns, low sidelobe levels, high realized gains, and high total radiation efficiency. The MMW imaging results for the 60 GHz probes show success for detecting/identifying hidden conventional weapons, such as handguns, ceramic knives, and explosives.

- **60 GHz Antenna Probes Design and Results**

As presented in chapter 4, several 60 GHz antenna probes were fabricated and experimentally investigated. The calculation and experimental results showed an antenna impedance bandwidth with a reflection coefficient less than -10 dB over the whole ISM band for most of the antennas. The antipodal Fermi tapered slot antenna with sine-shape corrugation was designed, with its corrugation intended to reduce discontinuity in tapered edges. This novel design led to reducing the sidelobe level and enhancing the radiation characteristic with a stable directive gain of 18.75 dB at 60 GHz. A new single feed for

dual-polarized antenna, providing a diverse polarity to enhance image contrast, is introduced. Then, a novel single feed circular polarized AFTSA sine-shape corrugated antenna is developed to generate a stable radiation characteristic and a RHCP bandwidth of 3.8 GHz for AR less than 3dB. Finally, a new multi *sine*-corrugation AFTSA antenna integrated with a grooved lens was introduced, optimized and implemented. The multi-corrugation design was considered an upgrade for enhancing the radiation characteristic in terms of reducing sidelobes as well as enhancing coupling when the grooved lens was loaded. The proposed design of AFTSA-MSC with GS-lens achieves a high normalized gain of 20 dB at 60 GHz, the sidelobe levels are below -20 dB in both E– and H–plane, and a wide measured bandwidth covered the band from 55 - 67 GHz. These proposed 60 GHz antennas' weight and size are small compared to conventional horn antennas, which can be impeded in a low profile array to obtain a desired gain and to be used as a good scanning probe for imaging / detection applications.

- **Beam Steering Phased Array Antenna Using a Piezoelectric Transducer Controlled Delay Line**

Chapter 5 introduced different 1 × 16-element beam steering antenna arrays with a low-cost piezoelectric transducer (PET) controlled phase shifter. A Y-junction power divider was presented as an alternative feed network reducing discontinuity from feed line bends. The single antenna element was designed to achieve symmetric E- and H-plane radiation patterns. The array gain was around 20dB, with low radiation loss due to the feeding network's low loss design. Furthermore, the feed network design is surrounded by EBG structures to reduce coupling between feed lines and surface waves. A circularly polarized 1 × 16-element beam steering phased array with and without EBG structures shows a wide impedance covering the ISM band with 2 GHz of circular polarization

bandwidth. Finally, multi *sin*-corrugation AFTSA wide-scan array antenna implemented design loaded with a grooved spherical lens achieved 30° beam scanning angle, with a high gain of 20 dB. These implemented 60 GHz phased array designs and beam switcher show high performance in terms of wide bandwidth coverage, high gain, low feeding network loss, low cost, and low profile. It is believed that these features will fulfill the requirements for MMW scanning sensors and enhance their performance.

- **60 GHz Imaging Detection of Concealed Objects Applications**

In this part, we demonstrated the use of MCAFTSA-SC probe as part of imaging / detection systems of weapons and liquids hidden by clothing, plywood and plastics materials. Different images were detected using a mechanical 2D MMW linear scanning platform. This work in the ISM-band (57GHz to 64GHz) was performed with *range* resolution $\Delta R_z = 125\ mm,$ and field resolution of $\Delta L_x = \delta_x = \delta_y =$ 3mm achieving a 100 × 100 pixels MMW image. The mechanical setup was designed to test the proposed probes. This scanning method, similar to synthetic aperture array, with a single antenna element measurement was ideal to investigate different probes for MMW imaging.

The 60 GHz imaging results of the V-band SGH antenna compared with those generated by different antenna probes presented in this thesis as sensing probes. The Multi sine-corrugations AFTSA antenna, as a probe, was experimentally tested in the monastic MMW image system. The quality of the MMW images were very similar in contrast with those scanned using the SGH antenna. In section 6.2, a single element MC-AFTSA-SC probe was used to experimentally detect hidden weapons and liquid materials to reconstruct 60 GHz images. The 60 GHz images revealed weapons beneath clothing. For other materials, such as plywood, handgun, ceramic knife and metal/ and/or plastic scissors,

images were clearly identified when 0.5″ and 1″ thick plywood were used. However, for a 1.5″ thick plywood cover the resolution was poor, caused by low reflection from the target. At 1 *mW* (0 *dBm*) transmitter PNA power and when the target was hidden by 2″ plywood, the target was undetectable. Increasing the transmitted signal power of the PNA to increase penetration through plywood is one solution to improve the detection level. It was also observed that gun, knife, and scissors were recognizable with clear resolution despite covering them by different plastics including 1″ thick Teflon. The 60 GHz imaging system was also tested to detect four bottles filled with liquid - water, salted water, oil, and alcohol - concealed by materials of the previous scenarios. When hidden behind the 0.5″ and 1″ plywood, the liquids were relatively detectable. However, the cases with 1.5″ and 2″ plywood covers were undetectable. When the liquids were covered by plastics, they were relatively recognizable with equitable resolution.

7.2 Contributions

This thesis' contributions can be divided into three components. The first includes the design of antenna probes, while the second is phased antenna array designs, and the third is experiments and development of the 60 GHz imaging/detection system.

7.2.1 Antenna Probe Designs

- Design and implementation of a 60 GHz circular patch-fed high gain dielectric lens antenna where measured results validated calculated results [J1], [C10].
- A low cost, 60 GHz printed Yagi antenna array was designed, optimized, fabricated and tested [J4], [C11].

- Several new models of the antipodal Fermi tapered slot antenna (AFTSA) with a novel sine corrugated (SC) shape were designed, and measured results were validated with simulated results [J2], [J3], [J5], [C3], [C4] [C6], [C7], [C8], [C9].
- Novel single feed dual-polarized and circularly polarized AFTSA-CS designs were developed and validated [C2], [C5].
- A high gain, low cost, 60 GHz Multi Sine-Corrugations AFTSA with grooved spherical lens, in a 3-element beam steering form, was designed & implemented [C1].

7.2.2 60 GHz Phased Antenna Array Designs

- A 1 × 16-element beam steering phased array was designed and implemented with a 60 GHz AFTSA-SC with PET-controlled phase shifter, and a new antenna achieving symmetric E- and H-plane radiation patterns was presented. Results of the feed network surrounded by EBG structures were presented [work to be submitted for publication [J6].
- A circularly polarized 1 × 16-element beam steering phased array design with and without EBG structures, with a PET-controlled phase shifter was investigated [work to be submitted for publication.

7.2.3 System Level Design

- A 2D linear mechanical scanning platform setup was designed to test the optimized probes [J7].
- Several experimental investigations were conducted to detect concealed items and liquids, when screening the human body for a hidden explosive, or other threatening material, using the single element MC-AFTSA-SC probe to reconstruct 60 GHz

images. Three scenarios were used to detect targets concealed by clothing, plywood, and plastic.

7.3 Future Work

Recommendations and suggestions for future work can be summarized as follows:

- The design for the wideband circularly polarized 16 × 16 beam steering phased array with a 60 GHz AFTSA-SC with PET-controlled phase shifter integrated with a feed network EBG-surrounded design can be developed for wideband 2D scanning.
- For a fast mechanical scanner using one antenna element as a probe, it is suggested that the probe is attached to the focal point of the scanner reflector, the movements of the reflector can form a 2D FOV as one pixel scanning technique.
- Development of a large scale mechanical scanner to scan a full human body for a hidden target for further investigation in 60 GHz.
- Development of a fast switcher between the antenna array elements in order to obtain an efficient electronic scanning system.

References

[1] IEEE Standard Letter Designations for Radar-Frequency Bands, *IEEE Std* 521-2002 (Revision of IEEE Std 521-1984).

[2] Yujiri, L., Shoucri, M. and Moffa, P., "Passive millimeter-wave imaging," *IEEE Microwave Magazine*, September (2003).

[3] N. Skou and D. L. Vine, "Microwave Radiometer Systems," *Second Edition, Artech House, Inc*, 2006.

[4] R. Appleby, "Passive millimeter wave imaging and how it differs from terahertz imaging," *Phil. Trans. R. Soc. Lond. A*, vol. 362, pp. 379–394, 2004.

[5] E. Seok, C. Cao, D. Shim, D. J. Arenas, D. B. Tanner, and C. Hung, "A 410GHz CMOS push-push oscillator with an on-chip patch antenna," *In Solid-State Circuits Conf., 2008. ISSCC 2008. Digest of Tech. Papers. IEEE Intern.*, pp. 472-629, 2008.

[6] S. M. Aguilar, M. Al-Joumayly, M. J. Burfeindt, N.r Behdad, and S. C. Hagness, "Multiband miniaturized patch antennas for a compact shielded microwave breast imaging array," *Antennas and Propag., IEEE Trans.* vol. 62, no. 3, pp. 1221-1231, 2014.

[7] D. M Sheen, D. L. McMakin, and T. E. Hall, "Three-dimensional millimeter-wave imaging for concealed weapon detection," *Microwave Theory and Tech., IEEE Trans.*, vol. 49, no. 9 pp. 1581-1592, 2001.

[8] S. S. Ahmed, A. Schiessl, and L. Schmidt, "A novel fully electronic active real-time imager based on a planar multistatic sparse array," *Microwave Theory and Tech., IEEE Trans. vol.* 59, no. 12, pp. 3567-3576, 2011.

[9] B. Luo, L. C. Ong, and M. F. Karim, "Development of a 94GHz passive millimeter wave imaging system for target detection in haze and smoke," *In Microwave Workshop Series on RF and Wireless Technologies for Biomedical and Healthcare Applications (IMWS-BIO), 2013 IEEE MTT-S Intern.*, pp. 1-3. IEEE, 2013.

[10] L. Yujiri, "Passive millimeter wave imaging," *In Microwave Symposium Digest, IEEE MTT-S Intern., pp. 98-101. IEEE*, 2006.

[11] T. Nozokido, M. Noto, and T. Murai. "Passive millimeter-wave microscopy," *Microwave and Wireless Components Lett., IEEE* 19, no. 10 pp. 638-640, 2009.

[12] M. Shoucri, R. Davidheiser, Bruce Hauss, Paul Lee, Michael Mussetto, Steve Young, and Larry Yujiri, "A passive millimeter wave camera for aircraft landing in low visibility conditions," *Aerospace and Electronic Systems Magazine, IEEE 10*, no. 5, 37-42, 1995.

[13] M. Koulai, A. Nishikata, T. Sakai, and S. Watanabe, "Characterization of 60GHz Millimeter-Wave Focusing Beam for Living-Body Exposure Experiments," *EMC, Kyoto*, 2009.

[14] N. Alexander, C. Callejero, F. Fiore, I. Gomez, R. Gonzalo, A. E. de Luna, I. Ederra, and I. Palacios, "Mm-wave stand-off screening and detection," *IEEE, ICEAA'09, Intern. Conf.*, pp. 1038 – 1041, 2009.

[15] http://www.sds.l-3com.com/advancedimaging/provision-2.htm, 2nd June, 2015.

[16] http://www.arrowmid.com/Products/pdf/BIS-DS_GEN2_Cut_Sheet.pdf, 2nd June, 2015.

[17] Watabe, Ken-ichi, Koji Shimizu, Masahide Yoneyama, and Koji Mizuno. "Millimeter-wave active imaging using neural networks for signal processing," *Microwave Theory and Tech., IEEE Trans.*, vol. 51, no. 5 pp. 1512-1516, 2003.

[18] B. G. Valdes, G. Allan, Y. R.-Vaqueiro, Y. Alvarez, S. Mantzavinos, M.Nickerson, and et al, "Sparse array optimization using simulated annealing and compressed sensing for near-field millimeter wave imaging*." Antennas and Propag., IEEE Trans.*, vol.62, no. 4, pp. 1716-1722, 2014.

[19] M. T. Ghasr, S. Kharkovsky, R. Bohnert, B. Hirst, and R. Zoughi, "30 GHz linear high-resolution and rapid millimeter wave imaging system for NDE," *Antennas and Propag., IEEE Trans.,* vol 61, no. 9 (): pp. 4733-4740, 2013.

[20] W. L. Stewart, "Passive millimeter wave imaging considerations for tactical aircraft," *In Digital Avionics Systems, 2001. DASC. 20th Conf.,* vol. 1, pp. 2B2-1. IEEE, 2001.

[21] K. Gruner, W. Keydel, and Helmut Suss, "Application Possibilities of Passive Remote-Sensing Systems in the Millimeter-Wave Region," *Geoscience and Remote Sensing, IEEE Trans*. vol. 3, pp. 376-382, .

[22] A. Tang, Q. J. Gu, and M.-C. F. Chang, "CMOS receivers for active and passive mm-wave imaging," *IEEE Communications Magazine,* vol.49, no. 10, pp.190-198, 2011.

[23] A. Doghri, A. Ghiotto, T. Djerafi, and K. Wu. "Early demonstration of a passive millimeter-wave imaging system using substrate integrated waveguide technology," *In Mediterranean Microwave Symposium (MMS), 2011 11th*, pp. 215-218. *IEEE*, 2011.

[24] S. Liao, , N. Gopalsami, T. W. Elmer, E. R. Koehl, A. Heifetz, K. Avers, E. Dieckman, and A. C. Raptis, "Passive millimeter-wave dual-polarization imagers," *Instrumentation and Measurement, IEEE Trans.* vol. 61, no. 7, pp. 2042-2050, 2012.

[25] A. Schiessl, A. Genghammer, S. S. Ahmed, and L. Schmidt. "Hardware realization of a 2 m × 1 m fully electronic real-time mm-wave imaging system," In *Synthetic Aperture Radar, 2012. EUSAR. 9th European Conf. on*, pp. 40-43. VDE, 2012.

[26] S. S Ahmed, A. Schiessl, F. Gumbmann, M. Tiebout, S. Methfessel, and L. Schmidt. "Advanced microwave imaging," *Microwave Magazine, IEEE*, vol. 13, No. 6, pp. 26-43, 2012.

[27] S. Methfessel, and L. Schmidt, "Design of a balanced-fed patch-excited horn antenna at millimeter-wave frequencies," *In Antennas and Propag. (EuCAP), 2010 Proceedings of the Fourth European Conf*. on, pp. 1-4. IEEE, 2010.

[28] S. Methfessel, and L. Schmidt, "Size-reduction and suppression of cavity-resona419nces in hybrid mm-wave antennas for polarimetric measurements." *In Radar Conf. (EuRAD), 2013 European*, *IEEE,* pp. 427-430, 2013.

[29] W. Fang, P. Fei, and F. Nian, "Millimetre-wave end-fired antenna array for active 3D holographic imaging system," *Electronics Lett.* 50, no. 5 (2014): 341-343.

[30] H. Kamoda, T. Iwasaki, J. Tsumochi, T. Kuki, and O. Hashimoto, "60-GHz electronically reconfigurable large reflectarray using single-bit phase shifters," *Antennas and Propag., IEEE Trans. on*59, no. 7 (2011): 2524-2531.

[31] R. B. Waterhouse, "Printed Antennas for Wireless Communications," *Technology & Engineering,* 2008.

[32] K. Mizuno, "Millimeter wave imaging technologies," *2001 Asia-Pacific Microwave Conf., pp*. 394-398, Taipei, 2001.

[33] K. C. Huang and Z. Wang, Millimeter Wave Communication Systems, by *Published By John Wiley & Sons*, Inc, 2011.

[34] E. E. Altshuler and R. A. Marr, "A comparison of experimental and theoretical values of atmospheric absorption at the longer millimeter wavelengths," *IEEE Trans. Antennas Propag*., vol. AP-36, no. 10, pp. 1471–1480, Oct. 1988.

[35] W. L. Stutzman and G. A. Thiele, "Antenna theory and design," 3rd edition, 2013, Chapter 10.

[36] R.C. Hansen, "Phased Array Antennas," *John Wiley & Sons, Inc, 1998*.

[37] A. T. Villeneuve, "Taylor Patterns for Discrete Arrays," *IEEE Trans. On Antenna and Propag.*, vol. AP-32, No. 10, pp. 1089-1093, Oct. 1984.

[38] J. B. L. Rao, D. P. Patel, and V. Krichevsky, "Voltage-controlled ferroelectric lens phased arrays," *IEEE Trans. Antennas Propag., vol. 47, pp*. 458–468, Mar. 1999.

[39] C. S. Lee and J. M. Tran, "Coplanar waveguide semiconductor phase shifter," *Microwave Opt. Tech. Lett., vol*. 10, no. 2, pp. 100–102, Oct. 1995.

[40] S. Lucyszyn and I. D. Robertson, "Synthesis techniques for high performance octave bandwidth 180 analog phase shifters," *IEEE Trans. Microwave Theory Tech*., vol. 40, pp. 731–740, Apr. 1992.

[41] J. G. Yang, and K. Yang, "Ka-band 5-bit MMIC phase shifter using InGaAs PIN switching diodes," *Microwave and Wireless Components Lett., IEEE,* vol. 21, no. 3, pp. 151-153, 2011.

[42] P. Romano, O. Araromi, S. Rosset, H. Shea, and J. Perruisseau-Carrier, "Tunable millimeter-wave phase shifter based on dielectric elastomer actuation," *Applied Physics Lett.*, vol.104, no. 2, pp. 024104, 2014.

[43] San-Gyu Kim, Tae-Yeoul Yun and Kai Chang, "Time-delay phase shifter controlled by Piezoelectric Transducer on coplanar waveguide," *IEEE Microwave and Wireless Components Lett.*, vol. 13, no.l, pp. 19-20, 1993.

[44] T. Yun, and K. Chang, "A Low-Loss Time-Delay Phase Shifter Controlled by Piezoelectric Transducer to Perturb Microstrip Line," *IEEE Microwave and Guided Wave Lett.*, vol. 10, no. 3, pp.96-98, March 2000.

[45] TY. Yun, "One-Dimensional Photonic Bandgap Structures and Piezoelectric Transducer Controlled Devices for Microwave Applications," *PhD Dissertation, Texas A&M University*, 2001.

[46] TY. Yun, and K. Chang, "A Low-Cost 8 to 26.5 GHz Phased Array Antenna Using a piezoelectric Transducer Controlled Phase Shifter," *IEEE Tran. Antenna and Propag.*, vol. 49, no. 9, pp. 1290-98, Step. 2001.

[47] TY. Yun, C. Wang P. Zepeda, C. T. Rodenbeck, M. R. Coutant, M-Y Li and K. Chang, "A 10-to 21-GHz. Low-Cost, Multifrequency, and Full-Duplex Phased-Array Antenna System," *IEEE Tran. On Antenna and Propag.*, vol. 50, no. 5, pp.641-49, May 2002.

[48] K. Chang, MY. Li and T.-Y. Yun, "Novel Low-Cost Beam-Steering Technologies," *IEEE Trans. Antennas and Propag.*, vol. 50, No. 5, pp.618-27, May 2002.

[49] TY. Yun, , and K. Chang, "Analysis and optimization of a phase shifter controlled by a piezoelectric transducer," Microwave Theory and Tech., *IEEE Trans. on 50*, no. 1 (2002): 105-111.

[50] L. Yang, Naoki Ito, C. W. Domier, N. C. Luhmann Jr, and A. Mase, "18–40-GHz beam-shaping/steering phased antenna array system using Fermi antenna," *Microwave Theory and Tech.*, *IEEE Trans*. on 56, no. 4, pp. 767-773, 2008.

[51] R. C. Buchanan, Ed., Ceramic Materials for Electronics. *New York: Marcel Dekker*, 1986.

[52] D.T. Emerson, "The work of Jagadis Chandra Bose: 100 years of millimeter-wave research," *Microwave Theory and Tech., IEEE Trans.*, vol. 45, no. 12, pp. 2267-2273, Dec 1997.

[53] S. Costanzo, I. Venneri, G.D. Massa, G. Amendola, "Hybrid array antenna for broadband millimeter-wave applications," *Progress In Electromagnetics Research,* vol. 83, pp. 173-183, 2008.

[54] S. Z. Ying, H. Wei, "A Millimeter-wave gain enhanced multi-beam antenna based on a coplanar cylindrical dielectric lens," *Antennas and Propag., IEEE Trans.*, vol. 60, no. 7, pp. 3485-3488, July 2012.

[55] C. A. Balanis, "Antenna Theory: Analysis and Design," *3rd Edition, Hoboken, NJ: Wiley-Interscience*.

[56] H. Sato, and K. Sawaya, "Broadband Active Imaging method Using Auto-Correlation Pulse Response," *Intern. Symposium on Antennas and Propag.*, vol. 4, pp. 901-904, Singapore, 2006.

[57] R. Alhalabi, Y-C. Chiou, and G. M. Rebeiz, "Self-shielded high-efficiency Yagi-Uda antennas for 60 GHz communications," *Antennas and Propag., IEEE Trans*. on, vol. 59, no. 3, pp. 742-750, March 2011.

[58] O. Kramer, T. Djerafi, and Ke Wu, "Very small footprint 60 GHz stacked Yagi antenna array," *Antennas and Propag.*, *IEEE Trans.*, vol. 59, no. 9, pp. 3204-3210, Sept. 2011.

[59] A. Elboushi, and A. Sebak, "MMW Sensor for Hidden Targets Detection and Warning Based on Reflection/Scattering Approach," *Antennas and Propag., IEEE Trans.*, Vol. 62, 2014.

[60] M. Sato, T. Hirose, T. Ohki, T. Takahashi, K. Makiyama, H. Kobayashi, K. Sawaya, and K. Mizuno, "Compact receiver module for a 94 GHz band passive millimetre-wave imager," *IET Microwaves, Antennas & Propag.,* vol.2, no. 8, pp. 848-853, 2008.

[61] A. Rashidian, D. M. Klymyshyn, M. T. Aligodarz, M. Boerner, J. Mohr, "Development of polymer-based dielectric resonator antennas for millimeter-wave applications," *Progress In Electromagnetics Research C*, vol. 13, pp. 203-216, 2010.

[62] M. Li, and K.-M. Luk, "A low-profile unidirectional printed antenna for millimeter-wave applications," *Antennas and Propag., IEEE Trans.*, vol. 62, no. 99, pp.1232-1237, Dec. 2013.

[63] W. Fang, P. Fei, and F. Nian. "Millimeter-wave end-fired antenna array for active 3D holographic imaging system," *Electronics Lett.*, vol.50, no. 5, pp. 341-343, 2014.

[64] J. L. Volakis, "Antenna Engineering Handbook," 4th Edition, *The McGraw-Hill Companies*, 2007.

[65] S-W. Qu, and K. B. Ng. "Wideband millimeter-wave cavity-backed bowtie antenna," *Progress In Electromagnetics Research*, vol.133 pp. 477-493, 2013.

[66] F. K. Schwering, "Millimeter Wave Antenna," *Proc. of the IEEE*, vol. 80, no.1, pp. 92-102, 1992.

[67] S. Beer, H. Gulan, C. Rusch, G. Adamiuk, and T. Zwick, "A double-dipole antenna with parasitic elements for 122 GHz system-in-package radar sensors," *In Antennas and Propag. (EUCAP), Proceedings of the 5th European Conf.*, pp. 1903-1906. IEEE, 2011.

[68] C. A. Balanis, "Antenna Theory Analysis and Design," *Third edition, John Wiley& Sons, Inc., 2005.*

[69] T.-S. Horng and N. G. Alexopoulos, "Corporate feed design for microstrip arrays," *IEEE Trans. Antennas Propag*., vol. 41, no. 12, pp. 1615–1624, Dec. 1993.

[70] J. A. G. Malherbe, "Analysis of a linear antenna array including the effects of mutual coupling," *IEEE Trans. Educat*., vol. 32, no. 1, pp. 29–34, Feb. 1989.

[71] T. A. Milligan, "Modern Antenna Design," *Second Edition, 2005 John Wiley & Sons, Inc.*

[72] K.F. LEE, and W. CHEN, "Advances in Microstrip and Printed Antennas," *Wiley, New York, , 3rd edn*., Ch. 9, p. 884–892, 1992

[73] A.M. Abbosh, H.K. Kan, and M.E Bialkowski, "Effect of dielectric permittivity on infinite arrays of single-polarized Vivaldi antennas," *Microw. Opt. Technol. Lett.,* 48, (12), pp. 2448–2450, 2006.

[74] S. Sugawara, Y. Maita , K. Adachi, K. Mori, and K. Mizuno, "A mm-wave tapered slot antenna with improved radiation pattern," Proc. 1997 *IEEE MTT-S Digest*, pp. 959–962.

[75] S. Sugawara, Y. Maita , K. Adachi, K. Mori, and K. Mizuno, "Characteristics of a mm-wave tapered slot antenna with corrugated edges," *Proc. IEEE MTT-S Digest*, pp. 533–536, 1998.

[76] J.B. Rizk, and G.M. Rebeiz, "Millimeter-wave Fermi tapered slot antennas on micromachined silicon substrates," *IEEE Trans*. *Antennas Propag*., , 50, (3), pp. 379–387, 2002

[77] Y. Takagi, H. Sato, Y. Wagatsuma, K. Sawaya, and K. Mizuno, "Study of high gain and broadband antipodal Fermi antenna with corrugation," *Proc. Int. Symp. Antennas and Propag*., pp. 67–72, 2004.

[78] H. Sato, Y. Takagi, Y. Wagatsuma, K. Mizuno, and K. Sawaya, "Time domain characteristics of broadband antipodal Fermi antenna and its application to through-wall imaging," *Proc. Int. Symp. Antennas and Propag.,* pp. 387–390, 2005.

[79] W. Chen, Y. Yao, Z. Zhang, Z. Feng, Y. Chen, "Design of unsymmetrical anti-podal taper slot element for array antenna," *Proc. IEEE Int. Symp. Antennas and Propag*., session 532, p. 155, 2008.

[80] H. Oraizi, S. Jam, "Optimum design of tapered slot antenna profile," *IEEE Trans. Antennas Propag*., 51, (8), pp. 1987–1995, 2003.

[81] J. Kim, F.S. Barnes, "Dielectric slab rotman lens with tapered slot antenna array," *IEE Proc. Microw. Antennas Propag*., 2005, 152, (6), pp. 557–562

[82] R.N. Simons, R.Q. Lee, T.D. Perl, Tapered slot antenna using photonic band-gap structure to reduce substrate effects", *Electron. Lett*., 2005, 41, pp. 393–394

[83] I.K. Kim, N. Kidera, S. Pinel, J. Papapolymerou, J. Laskar, J.G. Yook, and M.M. Tentzeris, "Linear tapered cavity-backed slot antenna for MM-wave LTCC modules," *IEEE Antennas Wirel. Propag. Lett*., 2006, 5, pp. 175–178

[84] N.W. Chen, C.T. Chuang, And J.W. Shi, "A W-band linear tapered slot antenna on rectangular-grooved silicon substrate," *IEEE Antennas Wirel. Propag. Lett*., 2007, 6, pp. 90–92

[85] Y.J. Cheng, W. Hong, K. Wu, "Design of a monopulse antenna using a dual V-type linearly tapered slot antenna (DVLTSA)," *IEEE Trans. Antennas Propag*., 2008, 56, (9), pp. 2903–2909

[86] P. R. Acharya, H. Ekstrom, S. S. Gearhart, J. F. Johansson, S. Jacobson, G. M. Rebeiz, and E. L. Kollberg, "Tapered slotline antennas at 802 GHz," *IEEE Trans. Microwave Theory Tech.,* vol. 41, pp. 1715–1719, Oct. 1993.

[87] C. Hua, X. Wu, N. Yang, and W. Wu, "Air-Filled Parallel-Plate Cylindrical Modified Luneberg Lens Antenna for Multiple-Beam Scanning at Millimeter-Wave Frequencies," *IEEE Trans. Microwave Theory Tech.,* vol. 61, pp. 436–443, Jan. 2013.

[88] Kuo, L.-C., M.-C. Tsai, and H.-R. Chuang, "3-D FDTD design simulation and experimental measurement of a Ka-band planar antipodal linearly-tapered slot antenna (ALTSA)," *IEEE Guidedwave & Wireless Components Letter*, vol. 11, No. 9, 382– 384, Sep. 2001,

[89] M.C. Greenberg, K.L. Virga, And C.L. Hammond, "Performance characteristics of the dual exponentially tapered slot antenna (DETSA) for wireless communication applications," *IEEE Trans. Veh. Technol*., , 52, (2), pp. 305–312, 2003.

[90] J. Yoon, H. Kim, H.K. Yoon, Y.J. Yoon, Y.H. Kim, "Ultra-wideband tapered slot antenna with band cutoff characteristic," *Electron. Lett*., 41, pp. 629–630, 2005.

[91] C. T. Rodenbeck, S.-G. Kim, W.-H. Tu,M. R. Coutant, S. Hong, M. Li, and K. Chang, "Ultra-wideband low-cost phased-array radars," *IEEE Trans. Microw. Theory Tech.*, vol. 53, no. 12, pp. 3697–3703, Dec. 2005.

[92] N. Symeon, G.E. Ponchak, J. Papapolymerou, And M.M. Tentzeris, "Conformal double exponentially tapered slot antenna (DETSA) on LCP for UWB applications," *IEEE Trans. Antennas Propag*., 54, (6), pp. 1663–1669, 2006.

[93] G.E. Ponchak, J.L. Jordan, C.T. Chevalier, "Characteristics of double exponenttially tapered slot antenna (DETSA) conformed in the longitudinal direction around a cylinder," *IEEE Antennas Wirel. Propag. Lett*., 6, pp. 60–63, 2007

[94] K. Hettak, G.Y. Delisle, S. Tardif, G.A. Morin, And M.G. Stubbs, "A novel wideband Chebychev tapered slot antenna using broadband CPW to slotline transition," *Proc. IEEE Int. Symp. Antennas and Propag*., session 532, p. 155, 2008.

[95] E. Gazit, "Improved design of the Vivaldi antenna*," IEE Proc. Microw. Antennas Propag*., 135, (2), pp. 89–92, 1988.

[96] S. Kasturi, D.H. Schaubert, "Effect of dielectric permittivity on infinite arrays of single-polarized Vivaldi antennas," *IEEE Trans. Antennas Propag*., 54, (2), pp. 351–358, 2006.

[97] J. Y. Siddiqui, , Y. M. M. Antar, , A. P. Freundorfer, E. C. Smith, G. A. Morin, and T. Thayaparan,"Design of an Ultrawideband Antipodal Tapered Slot Antenna Using Elliptical Strip Conductors," *IEEE letter,* vol. 10, pp. 251-254, 2011.

[98] C. A. Balanis, "Advanced Engineering Electromagnetics," *Second edition, John Wiley& Sons, Inc., 2012.*

[99] D. M. Sheen, , D. L. McMakin, and T. E. Hall, "Near-field three dimensional radar imaging techniques and applications," *Applied Optics*, vol. 49, No. 19, E83–E93, 2010.

[100] R. Booton, "Computational Methods for Electromagnetics and Microwaves," USA: *John Wiley & sons Inc.,* 1992.

[101] D. M. Sullivan, "Electromagnetic Simulation Using the FDTD Method," *Second Edition, the Institute of Electrical and Electronics Engineers, Inc. Published 2013 by John Wiley & Sons, Inc.*

[102] ANSYS HFSS, v15, *ANSYS Corporation Software, Pittsburgh*, PA, USA.

[103] M. N. O. Sadiku, "Numerical Techniques in Electromagnetics," *Second Edition, CRC Press LLC,* 2001.

[104] CST Microwave Studio, Ver. 2014, *Computer Simulation Technology*, Framingham, MA, USA.

[105] I. Munteanu and T. Weiland, "RF & Microwave Simulation with the Finite Integration Technique- From Component to System Design," *in Scientific Computing in Electrical Engineering*, Springer, 2007.

[106] N.T. Nguyen, A.Rolland, A.V.Boriskin, G.Valerio, L. LeCoq, and R. Sauleau, "Size and weight reduction of integrated lens antennas using a cylindrical air cavity," *IEEE Trans. Antennas Propag.*, vol. 60, no. 12, pp. 5993–5998, Dec. 2012.

[107] J. J. Lee, "Lens antennas, Microwave passive and antenna components," in *Handbook of Microwave and Optical Components*, K. Chang, Ed. New York: Wiley, vol. 1, ch. 11.2, pp. 595–625, 1989.

[108] W. J. Lamb, "Miscellaneous data on materials for millimeter and submillimetre optics," *Int. J. Infrared Millimeter Waves*, vol. 17, no. 12, 1996.

[109] R. B. Marks, and D. F. Williams, "Characteristic impedance determination using propagations constant measurement," IEEE Microwave Guided Wave Let., vol. 1, pp. 141–143, June 1991.

[110] R. Waterhouse, "Printed antennas for wireless communications," Hoboken, NJ: Wiley, pp 69-100, 2007.

[111] J. Huang, "Planar microstrip Yagi array antenna," IEEE APS Intern. Symposium, vol. 2, pp. 894-897, June 1989.

[112] O. Kramer, T. Djerafi, K. Wu, "Very small foot print 60 GHz stacked Yagi antenna array," IEEE Trans .Antennas and Propag., Vol.59, pp.1879-1892, .July 2011.

[113] A. Nessel, A. Zaman, R. Q. Lee, and K. Lambert, "Demonstration of an X-band multilayer Yagi-like microstrip patch antenna with high directivity and large bandwidth," *in Proc. Antennas and Propag. Society Int. Symp., Washington, DC,* Jul. 3–8, vol. 1B, pp. 227–230, 2005.

[114] G. R. DeJean, and M. M. Tentzeris, "A new high-gain microstrip Yagi array antenna with a high front-to-back (F/B) ratio for WLAN and millimeter-wave applications," *IEEE Trans. on Antennas and Propa*g., vol.55, Issue: 2, pp. 298–304, Feb. 2007.

[115] J. Huang and A. Densmore, "Microstrip Yagi antenna for mobile satellite vehicle application," *IEEE Trans. Antennas Propag*., vol. 39, no. 7, pp. 1024–1030, Jul. 1991.

[116] H. Legay and L. Shafai, "A new stacked microstrip antenna with large bandwidth and high gain," *in Proc. IEEE AP-S Int. Symp*., pp. 948–951, Jul. 1993.

[117] F. Croq and D. M. Pozar, "Millimeter-Wave Design of Wide- Band Aperture-Coupled Stacked Microship Antennas," *IEEE Trans. on Antennas and Propag*., AP-39, pp. 1770-1776, 1991.

[118] S. D. Targonski, R. B. Waterhouse, and D. M. Pozar, "Design of wide band aperture-stacked patch microstrip antennas," *IEEE Trans. Antennas Propag*., vol. 46, no. 9, pp. 1245–1251, Sep. 1998.

[119] R. B. Waterhouse, "Stacked patches using high and low dielectric constant material combinations," *IEEE Trans. Antennas Propag*., vol. 47, no. 12, pp. 1767–1771, Dec. 1999.

[120] R. Li, G. Dejean, M. Maeng, K. Lim, S. Pinel, M. M. Tentzeris, and J. Laskar, "Design of compact stacked-patch antennas in LTCC multilayer packaging modules for wireless applications," *IEEE Trans. Adv. Packag*., vol. 27, no. 4, pp. 581–589, Nov. 2004.

[121] K. Yngvesson, T. L. Sigfrid, Y.S. Kim, Erik L. Kollberg, and J. F. Johansson, "The tapered slot antenna-a new integrated element for millimeter-wave applications," IEEE *Trans., Microwave Theory and Tech.*, vol. 37, no. 2 (1989): 365-374.

[122] W. Kim, N. Moon, H. Kim, and Y. Kim, "Linear Polarization Sum Imaging In Passive Millimeter-Wave Imaging System For Target Recognition," *Progress In Electroms. Research*, vol. 136, pp. 175-193, 2013

[123] A. Duric, A. Magun, A. Murk, C. Matzler, and N. Kampfer, "The fully polarimetric imaging radiometer SPIRA at 91GHz," IEEE Trans. on Geoscience and Remote Sensing, Vol. 46, 2323-2336, Aug. 2008.

[124] Stahli, O., C. Matzler, A. Murk, and N. Kampfer, "Sky measurements with the imaging polarimeter SPIRA at 91GHz," *Microwave Radiometry and Remote Sensing of the Environment* , 181-186, Mar. 2010

[125] P. F. Goldsmith, Hsieh, C.-T. G. R. Huguenin, J. Kapitzky, and E. L. Moore, "Focal plane imaging systems for millimeter wavelengths," *Microwave Theory and Tech., IEEE Trans. on* 41, no. 10, pp. 1664-1675, 1993.

[126] S. Masuyama, and H. Akira, "Walled LTSA array for rapid, high spatial resolution, and phase-sensitive imaging to visualize plastic landmines," *Geoscience and Remote Sensing, IEEE Trans. on* 45, no. 8 (2007): 2536-2543.

[127] S. Mustafa, B. Mohammed, and A. Abbosh, "Novel preprocessing techniques for accurate microwave imaging of human brain," *Antennas and Wireless Propag. Lett.s, IEEE* 12 (2013): 460-463.

[128] B. J. Mohammed, A. M. Abbosh, S. Mustafa, and D. Ireland, "Microwave system for head imaging," *Instrumentation and Measurement, IEEE Trans. on* 63, no. 1 (2014): 117-123.

[129] J. Richter, D. Notel, F. Kloppel, J. Huck, H. Essen, and L. Schmidt. "A multi-channel radiometer with focal plane array antenna for w-band passive millimeterwave imaging," In *Microwave Symposium Digest, 2006. IEEE MTT-S Intern.*, pp. 1592-1595. IEEE, 2006.

[130] X. Zhuge, and A. G. Yarovoy, "A sparse aperture MIMO-SAR-based UWB imaging system for concealed weapon detection," *Geoscience and Remote Sensing, IEEE Trans. on* 49, no. 1, pp 509-518, 2011.

[131] J. Wu, , J. Lou, M. Li, G. Yang, X. Yang, J. Adams, and N. X. Sun, "Compact, low-loss, wideband, and high-power handling phase shifters with piezoelectric transducer-controlled metallic perturber," *Microwave Theory and Tech., IEEE Trans. on* 60, no. 6, pp. 1587-1594, 2012.

[132] D. M. Pozar, "Microwave Engineering," *2nd Ed. New York: Wiley*, 1998, ch. 5 and 8.

[133] E. J. Wilkinson, "An N-way hybrid power divider," *IEEE Trans. Microw. Theory Tech.*, vol. MTT-8, no. 1, pp. 116–118, Jan. 1960.

[134] S. Horst, R. Bairavasubramanian, M. M. Tentzeris, and John Papapolymerou. "Modified Wilkinson power dividers for millimeter-wave integrated circuits," *Microwave Theory and Tech., IEEE Trans. on*55, no. 11, pp. 2439-2446, 2007.

[135] M. S. Barbetty, and M. Sanchez. "Design and implementation of a transceiver and a microstrip corporate feed for solid state x-band radar," *PhD Diss., University of Puerto Rico Mayagüez Campus*, 2005.

[136] Z. Hui, Z. Li, and J. Wang, "Research on the distributed circuit parameters of the chamfered bent microstrip line," In *Microwave and Millimeter Wave Technology (ICMMT), 2010 Intern. Conf. on*, *IEEE*, pp. 1294-1297, 2010.

[137] S. X. Ta, S. Kang, J.Han, and I. Park, "High-Efficiency, High-Gain, Broadband Quasi-Yagi Antenna and Its Array for 60-GHz Wireless Communications," *Journal of electromagnetic engineering and science* 13, no. 3 (2013): 178-185.

[138] T. T. Taylor, "Design of line-source antennas for narrow beamwidth and low side lobes," *Antennas and Propag., Trans. of the IRE Professional Group on* 3, no. 1, pp. 16-28, 1955.

[139] R. C. Hansen, "Array pattern control and synthesis," *Proceedings of the IEEE*80, no. 1, pp. 141-151, 1992

[140] R. J. Mailloux, "Phased array antenna handbook," *Boston: Artech House, 2005.*

[141] Matlab R2013a, using Taylor N-bar distribution function "w = taylorwin (n, N,SLR)"

[142] Y. Rahmat-Samii and Fan Yang, "Electromagnetic Band Gap Structures in Antenna Engineering," *Cambridge in microwave engineering series*, 2008.

[143] A. Elboushi, Z. Briqech, A. Sebak, "4-elements MMW array with EBG feeding network," *Antennas and Propag. Society Intern. Symposium (APSURSI), IEEE*, vol., no., pp.162-163, 7-13 July 2013.

[144] O. Haraz, A. Elboushi, S. Alshebeili, and A. Sebak, "Dense Dielectric Patch Array Antenna with Improved Radiation Characteristics Using EBG Ground Structure and Dielectric Superstrate for Future 5G Cellular Networks," *Access, IEEE* , Vol.2 , pp. 909 – 913, 2014.

[145] S. G. Kim and K. Chang, "A low cross-polarized antipodal Vivaldi antenna array for wide-band operation," *in Proc. IEEE Int. AP-S Symp., Monterey, CA*, pp. 2269–2272, Jun. 2004.

[146] C. Zhang,"Planar antipodal Vivaldi antenna array configuration for low cross-polarization and reduced mutual coupling performance," In *2007 IEEE Antennas and Propag. Society Intern. Symposium*, pp. 725-728. 2007.

[147] G. Cachier and F. Gautier, "Overview of Phased Arrays for Future Airborne Radars," Military Microwave Conf. Digest, pp.123-127, 1988.

[148] Aleksandar Nesic, Zoran Micic, Sinisa Jovanovic and Ivana Radnovic, "Millimeter wave printed antenna array with high side lobe suppression," IEEE Antenna Propagat. Society Int. Symp., pp. 3051-3054, June 2006.

[149] N. Fourikis, "Phases Array-Based Systems and Applications," *John Wiley & Sons, Inc*., 1997.

[150] G. M. Shaw and R. B. Dybdal, "Beam broadening for active aperture antennas," *IEEE Antenna Propagat. Society Int. Symp.,* vol.1, pp. 26-30, June 1989.

[151] L. Wang, , X. Yin, and H. Zhao, "A Planar Feeding Technology Using Phase-and-Amplitude-Corrected SIW Horn and Its pplication," *Antennas and Wireless Propag. Lett., IEEE,* vol.14, pp. 147-150, 2015.

[152] C.H. Liao, P. Hsu, and D.C. Chang, "Energy patterns of UWB antenna arrays with scan capability," *Antennas and Propag., IEEE Trans.* vol 59, no. 4, pp. 1140-1147, 2011

[153] Y. Yao, M. Liu, W. Chen, and Z. Feng, "Analysis and design of wideband widescan planar tapered slot antenna array," *IET microwaves, antennas & Propag.* Vol. 4, no.10, pp.1632-1638, 2010.

[154] R. W. Kindt, and W. R. Pickles, "Ultrawideband all-metal flared-notch array radiator," *Antennas and Propag., IEEE Trans.* vol 58, no. 11, pp. 3568-3575, 2010.

[155] R. W. Kindt, "Prototype Design of a Modular Ultrawideband Wavelength-Scaled Array of Flared Notches," *Antennas and Propag., IEEE Trans. on* 60, no. 3, pp.1320-1328, 2012.

[156] E. E. M. Woestenburg, L. Bakker, and M. V. Ivashina, "Experimental results for the sensitivity of a low noise aperture array tile for the SKA," *Antennas and Propag., IEEE Trans. on* 60, no. 2, pp. 915-921, 2012.

[157] Y. Yang, and A. E. Fathy, "Development and implementation of a real-time see-through-wall radar system based on FPGA," *Geoscience and Remote Sensing, IEEE Trans. on* 47, no. 5, pp. 1270-1280, 2009.

[158] G. M. L. Enrique, D. S. Vargas, O. G. Perez, E. U. Munoz, V. G. Posadas, J. M. S. Puente, and J. A. L. Fernandez, "Broadband active differential array for the mid-frequency SKA band," *Antennas and Propag. Magazine, IEEE* 56, no. 2, pp. 27-38, 2014

[159] R. P. Hsia, , W. M. Zhang, C. W. Domier, and N. C. Luhmann, "A hybrid nonlinear delay line-based broad-band phased antenna array system," *Microwave and Guided Wave Lett., IEEE* 8, no. 5, pp. 182-184, 1998.

[160] H. Holter, , T. H. Chio, and D. H. Schaubert, "Experimental results of 144-element dual-polarized endfire tapered-slot phased arrays," *Antennas and Propag., IEEE Trans. on* 48, no. 11, 1707-1718, 2000.

[161] S.-G. Kim and K. Chang, "Ultra wideband 8 to 40 GHz beam scanning phased array using antipodal exponentially-tapered slot antennas," in *IEEE MTT-S Int. Microw. Symp. Dig.*, vol. 3, pp. 1757–1760, Jun. 2004.

[162] W.C. Khor, M.E. Bialkowski, and S. Crozier, "Microwave Imaging Using a Planar Scanning System with Step-Frequency Synthesized Pulse," *Proc. APMC2005*, vol. 1 pp. 358-361, 2005.

[163] A. P. Freundorfer and K. Iizuka, "A study on the scattering of radio waves from buried spherical targets using the step frequency radar," *IEEE Trans. on Geoscience and Remote Sensing*, vol. 31, pp. 1253-1255, 1993.

[164] K. Iizuka, A. P. Freundorfer, and T. Iwasaki, "A method of surface cancellation for an underground CW radar," *IEEE Trans. Elec. Compar.*, Vol. 31, no. 3, pp. 330-332, Aug. 1989.

[165] S. Agarwal, D. Singh, and N. P. Pathak. "Active millimeter wave radar system for non-destructive, non-invasive underline fault detection and multilayer material analysis," *IEEE Intern. In Microwave and RF Conf. (IMaRC),* pp. 369-372, 2014.

[166] J. M. Gracia, "OFF-Axos Holography in Microwave Imaging Systems," *Ph.D. dissertation, Universitat Autònoma de Barcelona*, 2015.

[167] L. Zhang, "Millimetre Wave Imaging for Concealed Target Detection," *Ph.D. dissertation, University of Queen Mary United Kingdom*, 2011.

[168] C. M. Alabaster "The microwave properties of tissue and other lossy dielectrics," *PhD dissertation, Cranfield University*, March 2004.

[169] W. K. Chen, "The electrical engineering handbook," *Academic press, Ch3*, 2004.

[170] N. A. Neely, and P. M. Matthew, "Survival of enterococci and staphylococci on hospital fabrics and plastic," *Journal of clinical microbiology*, Vol. 38, No. 2, pp. 724-726, 2000.

[171] M. D. Sheen, D. L. McMakin, H. D. Collins, T. E. Hall, and R. H. Severtsen, "Concealed explosive detection on personnel using a wideband holographic millimeter-wave imaging system," *Aerospace/Defense Sensing and Controls. Intern. Society for Optics and Photonics*, 1996.

[172] A. K. Dąbrowska, G-M. Rotaru, S. Derler, F. Spano, M. Camenzind, S. Annaheim, R. Stämpfli, M. Schmid, and R. M. Rossi, "Materials used to simulate physical properties of human skin," *Skin Research and Technology*, 2015.

[173] S. W. Harmer, et al. "Determination of the Complex Permittivity of Textiles and Leather in the 14-40 GHz, mm wave band using a Free-W ave Transmittance Only Method," *IEEE Microwaves, Antennas & Propag., ISSN* 8725 (1751): 2008.

[174] W. Ting, T. S. Rappaport, and C. M. Collins, "The Human Body and Millimeter-Wave Wireless Communication Systems: Interactions and Implications," *arXiv preprint arXiv*: 1503.05944 (2015).

[175] A. A. Ibrahim, and K. Sarabandi. "Sub-Terahertz Dielectric Measurement and Its Application to Concealed Object Detection," *IEEE Trans. On Terahertz Science and Technology*, 2015.

[176] R. Appleby, and R. N. Anderton, "Millimeter-wave and submillimeter-wave imaging for security and surveillance," *Proc. IEEE*, Vol. 95, No. 8, pp. 1683-1690, 2007.

[177] R. Appleby, and H. Bruce Wallace, "Standoff detection of weapons and contraband in the 100 GHz to 1 THz region," *IEEE Trans. on antennas and Propag.*, Vol. 55, No. 11, pp. 2944-2956, 2007.

[178] R. Appleby, and A. H. Lettington, "Passive millimetre wave imaging," *Electronics & communication engineering journal*, Vol. 3, No. 1, pp 13-16, 1991.

[179] R. A. Guraliuc, M. Zhadobov, G. Valerio, N. Chahat, and R. Sauleau "Effect of textile on the propagation along the body at 60 GHz," *IEEE Trans. on Antennas and Propag.*, Vol. 62, No. 3, pp. 1489-1494, 2014.

[180] T. Weiland, "A discretization model for the solution of Maxwell's equations for six component fields," Archiv Elektronik und Uebertragungstechnik, vol. 31; pp. 116-120, 1977.

[181] D. M. Pozar, and B. Kaufman. "Comparison of three methods for the measurement of printed antenna efficiency." *IEEE transactions on antennas and propagation* 36, no. 1 (1988): 136-139.

List of Publications

Refereed Journal Papers

[J1] Z. Briqech, A. Sebak, and T. A. Denidni, "60 GHz circular patch-fed high gain transparent lens antenna," *Applied Computational Electromagnetics Society Journal ACES,* 30 (5), May 2015.

[J2] Z. Briqech, A. Sebak, and T. A. Denidn, "High gain 60 GHz antipodal fermi tapered slot antenna with sine corrugation," *Microwave and Optical Technology Letters* 57 (1), 6-9, 2015.

[J3] KD Phalak, Z Briqech, A Sebak, "Ka-band antipodal fermi-linear tapered slot antenna with a knife edge corrugation," *Microwave and Optical Technology Letters* 57 (2), 485-489, 2015.

[J4] Z. Briqech, A. Sebak, and T. A. Denidn, "High-Efficiency 60 GHz printed Yagi antenna array," *Antennas and Wireless Propagation Letters, IEEE,* vol. 12, pp. 1224-1227, 2013.

[J5] I Mohamed, Z. Briqech, A Sebak, "Antipodal Fermi Tapered Slot Antenna for 60-GHz Band Applications," *Antennas and Wireless Propagation Letters, IEEE*, vol. 14, pp.96-99, 2015.

[J6] Z. Briqech, A. Sebak, and T. A. Denidni, "Wideband MMW PET-based phased array with AFTSA-SC antenna," IEEE Trans. Antennas Propagat., 2015, submitted.

[J7] Z. Briqech, A. Sebak, and T. A. Denidni, "57- 64 GHz Imaging/Detection sensor: system setup and experimental evaluations," IEEE Trans. Instrumentation and Measurement (TIM) , 2015, submitted.

[J8] Z. Briqech, A. Sebak, and T. A. Denidni, "Wide-Scan MSC-AFTSC Array-Fed Grooved Spherical Lens Antenna for Millimeter-wave MIMO Applications," IEEE Trans. Antennas Propagat., submitted for publication

Refereed Conference Papers

[C1] Z. Briqech, A. Sebak, and T. A. Denidni, "60 GHz multi sin-corrugations antipodal Fermi tapered slot antenna loaded with a spherical lens," *2015 IEEE AP-S Sympo. on Antennas and Propa. and URSI CNC/USNC,* Presented, July 2015.

[C2] Z. Briqech, A. Sebak, and T. A. Denidni, "60 GHz circularly polarized antipodal Fermi tapered slot antenna with sin- corrugation," 2015 *IEEE AP-S Sympo. on Antennas and Propagation and URSI CNC/USNC,* Presented, July 2015.

[C3] Z. Briqech, J. Robitaille, K. Bishyk, K. Abdo, D. Bhogal, and A. Sebak, "High gain antipodal tapered slot antenna with sine-shaped corrugation and Fermi profile substrate slotted cut-out for MMW 5G," *The 8th Global Symposium on Millimeter-Waves (GSMM 2015), IEEE,* presented, May 2015.

[C4] S. Dorvlo, Z. Briqech and A. Sebak, "3-Element Sectorial Fermi tapered slot antenna with *sin*-corrugation," *The 15th edition of the IEEE International Conference on Ubiquitous Wireless Broadband*, presented, October 2015.

[C5] Z. Briqech, and A. Sebak, and T. A. Denidni, "60 GHz dual-polarized 1× 4 antipodal Fermi tapered slot antenna array," *In Antenna Technology and Applied Electromagnetics (ANTEM), 2014 16th Inter. Symp. IEEE* on, pp. 1-2., 2014.

[C6] I Mohamed, Z. Briqech, A Sebak, "High-gain dielectric-loaded antipodal Fermi tapered slot antenna for MM-wave applications," *In Antenna Technology and Applied Electro. (ANTEM), 2014 16th Inter. Symp. IEEE* on, pp. 1-2 2014.

[C7] KD Phalak, Z Briqech, A Sebak, "Surface integrated waveguide fed Antipodal Fermi-Linear Tapered Slot Antenna at 28 GHz", *In Antenna Technology and Applied Electro. (ANTEM), 2014 16th Inter. Symp. IEEE* on, pp. 1-2 2014.

[C8] Z. Briqech, A. Sebak, and T. A. Denidni, "60 GHz Fermi Tapered Slot Antenna with Sin-Corrugation," *In Antennas and Propagation Society International Symposium (APSURSI), 2013 IEEE*, pp. 160-161., 2013.

[C9] A. Elboushi, Z. Briqech, and A. Sebak, "4-elements MMW array with EBG feeding network," *In Antennas and Propagation Society International Symposium (APSURSI), 2013 IEEE*, pp. 1-2, 2013.

[C10] Z. Briqech, and A. Sebak, "60 GHz microstrip-fed high gain dielectric lens antenna," *In Electrical & Computer Engineering (CCECE), 2012 25th IEEE Canadian Conference on*, pp. 1-4, 2012.

[C11] Z. Briqech, and A. Sebak, "Low-cost 60 GHz printed Yagi antenna array," *In Antennas and Propagation Society International Symposium (APSURSI), 2012 IEEE*, pp. 1-2. 2012.

[C12] Z. Briqech, O. M. Haraz, A. Sebak, and M. R. Abdel-Rahman, "CPW-fed Yagi array with dielectric resonator antenna for W-band and imaging system applications," *In Antennas and Propagation Society International Symposium (APSURSI), IEEE, pp.* 1-2, 2012.